



NTNU – Trondheim
Norwegian University of
Science and Technology

Composition and Surface Modifications of Silica Structures in Diatom Frustules by Incorporation of Functional Oxides and Nitride Formation

Ivar Andre Ødegård

Chemical Engineering and Biotechnology

Submission date: June 2012

Supervisor: Gabriella Tranell, IMTE

Norwegian University of Science and Technology
Department of Materials Science and Engineering

Preface

This Master thesis was written during the spring of 2012 at the Norwegian University of Science and Technology (NTNU) in Trondheim. The problem description leading to this thesis was developed in cooperation with Professor Gabriella Tranell, and is a part of the SOLBIOPTA project group. The SOLBIOPTA group is a Norwegian Research Council supported joint research group between NTNU and SINTEF, which researches the possibility of using silica structures found in diatoms as light harvesting structures in photovoltaic solar cells.

I wish to extend my gratitude towards my supervisor Professor Gabriella Tranell for being a source of inspiration and for all her support through the project. I also wish to extend my gratitude towards Dr. Julien Romann for his input on functionalization of the frustules and for spending countless hours aiding me in the analysis of my samples. My gratitude is also extended towards Professor John Walmsley for his input on chemical analysis of frustules samples along with Professor Arne Røyset and Lyubomir Ahtapodov for their help with photoluminescence spectroscopy. I would also like to thank the people at the Department of Biotechnology for providing numerous samples of frustules as well as the rest of the SOLBIOPTA project group for being a source of inspiration. I would also like to express my gratitude towards the Norwegian Research Council for the economical support which has made this project possible.

I hereby declare that the work in this thesis has been performed independently and in accordance with the examination regulations at the Norwegian University of Science and Technology (NTNU).

Ivar Andre Ødegård

Trondheim June 29th 2012

Sammendrag

Produksjon av fornybar energi ved bruk av silisiumsolceller er av betraktelig interesse for å redusere forurensing og klimaforandringene som følger. Forbedringer i forbindelse med effektivitet og samtidig reduksjon av kostnader er nøkkelbegreper i forhold til storskala implementering av denne teknologien. Noen foreslåtte og til dels utprøvde metoder som kan nevnes i forbindelse med forbedringer i effektivitet kan være: modifisering av bølgelengden til innstrålt lys, som gir lys tilpasset eksisterende båndgap samt overflateteksturering og overflatebehandling med silisiumnitrid. I naturen utviser diatom frustuler svært effektiv lyshøsting som følge av porestrukturene som finnes i frustulene. Inkorporering av disse strukturene i forbindelse med solceller for forbedrede lyshøstingsegenskaper hadde derfor vært svært interessant. Denne oppgaven omhandler modifikasjon av overflateegenskapene til diatom frustuler ved deponering av oksider kjent for opp og ned konvertering av lys samt nitridering av diatom frustuler. Belegging av frustuler med oksider kjent for opp og ned konvertering av lys kombinerer frustulenes lyshøstingsegenskaper med spektral modifikasjon av innstrålt lys. Dette kan forbedre solcelleeffektivitet ved eventuell implementering. Nitridering av diatom frustuler bevarer frustulenes strukturer og utviser forbedrede mekaniske, kjemiske, termiske og antirefleksive egenskaper i forbindelse med mulig videre bruk i solceller.

Diatom frustuler av artene *Coscinodiscus wailesii* og *Coscinodiscus* sp., ble benyttet i alt eksperimentelt arbeid. Innledende temperatur eksponeringsforsøk i området 400°C-1200°C og ved intervaller på 200°C, ble utført for å bestemme frustulenes temperaturfølsomhet. I påfølgende eksperimenter ble frustulene dyppet en, to eller fire ganger i en av to mulige løsninger. Den ene løsningen bestod av erbiumklorid og yttriumklorid løst i en blanding av acetonitril og etylenglykol. Den andre løsningen bestod av manganklorid og sinkklorid oppløst i en blanding av etylenglykol og acetonitril. Etter dypping ble frustulene varmebehandlet ved 800°C i normal atmosfære, hvor kloridene ble dekomponert og dannet oksider. Nitridering av frustuler ble forsøkt ved samtidig metallotermisk reduksjon ved 650°C og 800°C, hvor nødvendig nitrogen kom fra ammoniakk-gass, produsert ved termisk dekomponering av ammoniumklorid blandet med kalsiumoksid. Nitrideringsforsøkene fant sted i en spesialbygget reaktor i rustfritt stål. I etterkant av forsøkene ble frustulene karakterisert vha. scanning elektron mikroskop (SEM) utrustet med energi dispersivt røntgen spektrometer (EDS), fluorescens mikroskopi, fotoluminescens spektroskopi og Raman spektroskopi.

Frustulene i temperatur eksponeringsforsøket ble funnet å utvise små forandringer i porene ved 600°C, større forandringer ble observert ved 800°C, videre ble forandringene funnet å øke i takt med økning av temperaturen. Ved 1200°C var samtlige porestrukturer ødelagte og store strukturelle forandringer ble observert utvendig på frustulene. Frustuler som gjennomgikk en og to dypp sykluser i beleggingseksperimentene ble funnet å mangle fotoluminescens egenskaper. Frustuler dyppet fire ganger, ble i alle tilfeller funnet å inneha svake fotoluminescens egenskaper. Frustuler dyppet fire ganger i Zn/Mn løsning ble funnet å utvise noen større temperaturrelaterte endringer i forhold til frustulene som ble dyppet fire ganger i Y/Er løsning. Frustuler som ble dyppet i Zn/Mn løsning ble funnet å inneholde forhøyede konsentrasjoner av tinn, dette kan muligens påvirke både fotoluminescens og termiske egenskaper. Frustulene som ble eksponert for samtidig metalloterm reduksjon og nitridering ved 650°C ble funnet kun å danne overfladiske og dermed små mengder silisiumnitrid. Frustulene som ble nitrideret ved 800°C utviste større konversjon til silisiumnitrid. Frustuler fra begge forsøk inneholdt forhøyede konsentrasjoner av silisium, som er et resultat av metalloterm reduksjon av silika. Hos frustuler

nitridert ved 800°C ble nitridet bestemt til å være av typen β -silisiumnitrid og resterende silisium ble funnet å være en blanding av nanokrystallinsk og amorf. Nanokrystallinsk silisium ble beregnet å være i størrelsesorden ~2.2 nm.

Summary

Renewable energy production featuring silicon photovoltaic solar cells are of considerable interest to reduce pollution and related environmental changes. Improvements in efficiency along with reductions in cost are key elements to large scale implementation of this technology. Some suggested and attempted methods of improvements that deserves mentioning are: modifying the energy of incident light to better suit the existing band gap along with reduction in losses by applying surface texturing and nitride coatings. Looking to nature for inspiration reveals diatoms and their frustules having pore structures displaying excellent light harvesting abilities. Thus an implementation of such structural features with regards to solar cell improvements would be highly desirable. This thesis was aimed at performing modifications of diatom frustules surfaces by deposition of oxides known to possess properties of up and down-conversion of light as well as attempting to convert diatom frustules to silicon nitride replicas. Coating frustules with oxides possessing properties of up and down-conversion of light combines light harvesting properties of frustules with spectral modifications of incident light. This offers possibilities of solar cell improvements upon implementation. Nitriding of diatom frustules preserves structural features of the frustules and offers increased mechanical, chemical, thermal and anti-reflecting properties for possible solar cell use.

Diatom frustules of the species *Coscinodiscus wailesii* and *Coscinodiscus* sp. were utilized in all experimental work during this thesis. An initial temperature exposure experiment was performed at temperatures ranging from 400°C-1200°C with increments of 200°C, to gauge thermal response of the frustules. In another set of experiments diatom frustules were subjected to one, two and four dip coatings in one of two different precursor solutions. One solution consisted of erbium and yttrium chloride dissolved in a mixture of ethylene glycol and acetonitrile while the other solution consisted of manganese and zinc chloride dissolved in ethylene glycol and acetonitrile. Post dip coating, frustules were annealed at 800°C in normal atmosphere, decomposing chloride precursors to corresponding oxides. Nitriding of frustules was attempted by simultaneous metallothermic reduction in a purpose built reactor vessel where necessary nitrogen was supplied in the form of ammonia at 650°C and 800°C. Ammonia was generated by thermal decomposition of ammonium chloride mixed with calcium oxide. Post experiments, frustules were characterized by use of scanning electron microscope (SEM) featuring energy dispersive x-ray spectrometer (EDS), fluorescence microscopy, photoluminescence spectroscopy and Raman spectroscopy.

Frustules in the temperature exposure experiment were found to display small changes to the pores at 600°C. At 800°C the changes were more severe and the changes were found to increase with increasing temperature until complete destruction of the pores along with visible external changes took place at 1200°C. For the coating experiments, no photoluminescent properties were found to exist for frustules coated once or twice. Frustules coated four times were found to display photoluminescent behavior for both types of coatings. Frustules subjected to four coatings with Zn/Mn solution were found to display more temperature related changes in the pores as compared to frustules coated four times with Y/Er solution. Frustules coated with Zn/Mn solution, were found to be contaminated by elevated levels of tin, possibly influencing both thermal and photoluminescent properties. Frustules subjected to simultaneous metallothermic reduction and nitriding at 650°C were found to suffer low conversion and thus only superficial nitride formation. Frustules nitrided at 800°C were found to display higher conversion to silicon nitride. The formed nitride was determined to be β -silicon nitride by Raman

spectroscopy. The frustules were also found to contain elevated levels of reduced silicon, for the frustules nitrided at 800°C, this silicon was found to be a mixture of amorphous and nanocrystalline. The nanocrystalline silicon was found to have a crystalline size of ~2.2 nm.

Contents

1	Introduction.....	15
1.1	Background.....	15
1.2	Aim of work	17
2	Theory	19
2.1	Diatoms.....	19
2.1.1	Diatom reproduction	20
2.1.2	Diatom frustules	21
2.1.3	Light harvesting in diatom frustules.....	22
2.1.4	Diatom frustules utilized in this thesis	23
2.2	Photovoltaic solar cells.....	24
2.2.1	Silicon solar cells	24
2.2.2	Light harvesting in silicon solar cells.....	25
2.2.3	Improved light harvesting in solar cells by use of frustules properties	27
2.3	Up-conversion of light.....	27
2.3.1	Deposition of up-converting oxides	30
2.4	Down-conversion of light	31
2.4.1	Deposition of down-converting oxides	32
2.5	Nitriding of silicon.....	33
2.6	Simultaneous nitriding and metallothermic reduction of frustules	34
2.6.1	Metallothermic reduction	35
2.6.2	Magnesiothermic reduction.....	35
2.6.3	Simultaneous metallothermic reduction and nitriding of silica frustules	36
3	Experimental/method	40
3.1	Materials	40
3.2	Procedure.....	42
3.2.1	Experimental flowchart	42
3.2.2	Sample acquisition and preparation.....	43
3.2.3	Temperature exposure	44
3.2.4	Coating of frustules with up-converting oxides	44

3.2.5	Coating of frustules with down-converting oxides.....	45
3.2.6	Nitriding of diatom frustules	45
3.3	Characterization.....	47
3.3.1	Original frustules.....	47
3.3.2	Frustules exposed to elevated temperatures	47
3.3.3	Frustules coated with up and down-converting oxides.....	48
3.3.4	Characterization of coated frustules by scanning electron microscope	48
3.3.5	Characterization of coated frustules by fluorescence microscope.....	48
3.3.6	Characterization of coated frustules by photoluminescence spectroscopy	49
3.3.7	Characterization of nitrided frustules by scanning electron microscope	50
3.3.8	Characterization of nitrided frustules by Raman spectroscopy	50
4	Results.....	52
4.1	Original frustules	52
4.2	Characterization of frustules exposed to various temperatures.....	55
4.2.1	Frustules exposed to 400°C for 1hour	55
4.2.2	Frustules exposed to 600°C for 1hour	58
4.2.3	Frustules exposed to 800°C for 1hour	60
4.2.4	Frustules exposed to 1000°C for 1hour	63
4.2.5	Frustules exposed to 1200°C for 1hour	66
4.3	Characterization of frustules coated with up converting oxides	68
4.3.1	Frustules coated once with Er ³⁺ doped Y ₂ SiO ₅ featuring SEM and EDS	68
4.3.2	Frustules coated twice with Er ³⁺ doped Y ₂ SiO ₅ featuring SEM and EDS.....	71
4.3.3	Frustules coated four times by Er ³⁺ doped Y ₂ SiO ₅ featuring SEM and EDS	73
4.3.4	Er ³⁺ doped Y ₂ SiO ₅ coated frustules characterized by fluorescence microscopy	76
4.3.5	Er ³⁺ doped Y ₂ SiO ₅ coated frustules characterization by photoluminescence spectroscopy	77
4.4	Characterization of frustules coated with down converting oxides	78
4.4.1	Frustules coated once with Mn ²⁺ doped Zn ₂ SiO ₄ featuring SEM and EDS	78
4.4.2	Frustules coated twice with Mn ²⁺ doped Zn ₂ SiO ₄ by SEM and EDS.....	81
4.4.3	Frustules coated four times with Mn ²⁺ doped Zn ₂ SiO ₄ featuring SEM and EDS.....	84
4.4.4	Mn ²⁺ doped Zn ₂ SiO ₄ coated frustules characterization by fluorescence microscopy.....	87
4.4.5	Mn ²⁺ doped Zn ₂ SiO ₄ coated frustules characterized by photoluminescence spectroscopy	88

4.5	Characterization of nitrided frustules	89
4.5.1	Frustules nitrided at 650°C	89
4.5.2	Frustules nitrided at 800°C	93
4.5.3	Characterization of frustules nitrided at 800°C by Raman spectroscopy	97
5	Discussion	98
5.1	Starting materials	98
5.2	Original frustules	98
5.3	Frustules exposed to increased temperatures	99
5.3.1	Experimental challenges and issues	99
5.3.2	Effects of temperature exposure on diatom frustules	100
5.4	Frustules coated with up and down converting oxides	102
5.4.1	Experimental issues of coating and characterization of frustules	102
5.4.2	Frustules coated with Er ³⁺ doped Y ₂ SiO ₅	103
5.4.3	Frustules coated with Mn ²⁺ doped Zn ₂ SiO ₄	106
5.5	Nitrided frustules	109
5.5.1	Frustules nitrided at 650°C	110
5.5.2	Frustules nitrided at 800°C	112
6	Conclusion	114
6.1	Temperature exposure characterisation	114
6.2	Coating of frustules with up and down converting oxides	114
6.3	Nitriding of frustules	115
7	Future work	117
8	References	118

List of figures

Figure 1 The diverse shapes of diatoms	19
Figure 2 The habitat of diatoms	19
Figure 3 The three main classes of diatoms	20
Figure 4 Diatom lifecycle and cell division	21
Figure 5 Frustule structure	21
Figure 6 Frustule pore structure	22
Figure 7 <i>Coscinodiscus wailesii</i>	23
Figure 8 Photovoltaic solar cell.....	25
Figure 9 Silicon band gap upon illumination	26
Figure 10 The solar spectrum along with the conversion achieved in silicon PV cells.....	26
Figure 11 Loss mechanisms in a single junction solar cell	27
Figure 12 The three main classes of up-conversion phenomenon.....	28
Figure 13 Up-conversion in Erbium ions	29
Figure 14 Energy transfer between sensitizer and activator ion upon illumination	30
Figure 15 Mechanisms of down-conversion	31
Figure 16 Experimental flowchart.....	42
Figure 17 Frustules on stainless steel grid.....	43
Figure 18 Purpose built reactor chamber	46
Figure 19 Fluorescence microscopy principle.....	49
Figure 20 Photoluminescence spectroscopy.....	49
Figure 21 Typical Raman spectroscopy system	51
Figure 22 Original frustule.....	52
Figure 23 Original frustule pore structure	53
Figure 24 Structural features of the frustule pores at nanoscale.....	53
Figure 25 Original frustule pores inside view	54
Figure 26 Typical EDS spectrum of original frustules.....	54
Figure 27 Frustule exposed to 400°C for 1hour	56
Figure 28 Frustule pores subjected to 400°C for 1 hour.....	56
Figure 29 Frustule pores subjected to 400°C for 1 h at nanoscale.....	57
Figure 30 Frustule pores subjected to 400°C for 1h, inside view.....	57
Figure 31 Frustule subjected to 600°C for 1h.....	58
Figure 32 Frustule pores subjected to 600°C for 1h.....	59
Figure 33 Frustule pores subjected to 600°C for 1h at nanoscale.....	59
Figure 34 Frustule pores subjected to 600 for 1h, inside view	60
Figure 35 Frustule subjected to 800°C for 1h.....	61
Figure 36 Frustule pores subjected to 800°C for 1h.....	61
Figure 37 Frustule pores subjected to 800°C for 1h at nanoscale.....	62
Figure 38 Frustule pores subjected to 800°C for 1h, inside view.....	63
Figure 39 Frustule subjected to 1000°C for 1h.....	63

Figure 40 Frustule pore structure subjected to 1000°C for 1h.....	64
Figure 41 Frustule pores subjected to 1000°C for 1h at nanoscale.....	64
Figure 42 Frustule pores subjected to 1000°C for 1h, inside view.....	65
Figure 43 Frustule subjected to 1200°C for 1h.....	66
Figure 44 Frustule pore structure subjected to 1200°C for 1h.....	66
Figure 45 Frustule pores subjected to 1200°C for 1h at nanoscale.....	67
Figure 46 Frustule subjected to 1200°C for 1h, inside view	67
Figure 47 Frustule coated once with Y/Er.....	68
Figure 48 Frustule coated 1X with Y/Er	69
Figure 49 Frustule coated 1X with Y/Er at nanoscale.....	69
Figure 50 EDS spectrum of (1X) Y/Er coated frustule	70
Figure 51 Frustule coated twice with Y/Er	71
Figure 52 Frustule coated 2X with Y/Er	71
Figure 53 Frustules coated 2X with Y/Er at nanoscale	72
Figure 54 Typical EDS spectrum of (2X) Y/Er coated frustule	72
Figure 55 Frustules coated four times with Y/Er	73
Figure 56 Frustule coated 4X with Y/Er	74
Figure 57 Frustule coated 4X with Y/Er at nanoscale.....	74
Figure 58 Typical EDS spectrum of (4X) Y/Er coated frustule	75
Figure 59 Spectroscopic results from analysis of Er ³⁺ doped Y ₂ SiO ₅ coated frustules.....	77
Figure 60 Frustule coated once with Zn/Mn	78
Figure 61 Surface of frustule coated 1X with Zn/Mn	79
Figure 62 Frustule coated 1X with Zn/Mn at nanoscale	79
Figure 63 Typical EDS spectra of (1X) Zn/Mn coated frustule	80
Figure 64 Frustule coated twice with Zn/Mn	81
Figure 65 Frustule coated 2X with Zn/Mn.....	82
Figure 66 Frustule coated 2X with Zn/Mn at nanoscale	82
Figure 67 Typical EDS spectrum of (2X) coated Zn/Mn.....	83
Figure 68 Frustule coated four times with Zn/Mn	84
Figure 69 Frustule coated 4X with Zn/Mn.....	85
Figure 70 Frustule coated 4X with Zn/Mn at nanoscale	85
Figure 71 Typical EDS spectrum of (4X) Zn/Mn coated frustule.....	86
Figure 72 Spectroscopic results from analysis of Mn ²⁺ doped Zn ₂ SiO ₄ coated frustules.....	88
Figure 73 Frustules nitrided at 650°C overview.....	89
Figure 74 Frustule nitrided at 650°C.....	90
Figure 75 Frustule nitrided at 650°C at nanoscale.....	90
Figure 76 Typical EDS spectrum of frustules nitrided at 650°C, 3keV	91
Figure 77 Typical EDS spectrum of frustules nitrided at 650°C, 15 keV	92
Figure 78 Frustule subjected to nitriding at 800°C.....	93
Figure 79 Front side of frustule subjected to nitriding at 800°C	93

Figure 80 Rear side of frustule subjected to nitriding at 800°C	94
Figure 81 Rear side of frustule subjected to nitriding at 800°C, nanoscale.....	94
Figure 82 Typical EDS spectrum of frustules nitrided at 800°C, 3.00 keV	95
Figure 83 Typical EDS spectrum of frustules nitrided at 800°C, 15.00 keV	96
Figure 84 Raman spectrum of frustules subjected to nitriding at 800°C.....	97

List of tables

Table 1 Equipment	40
Table 2 Reactants/materials	41
Table 3 Average elemental contents of original frustules	55
Table 4 Results of the temperature exposure characterization	55
Table 5 Average elemental content of 1X coated frustules.....	70
Table 6 Average elemental content of (2X) Y/Er coated frustules	73
Table 7 Average elemental content of (4X) Y/Er coated frustules	75
Table 8 Results of the fluorescence microscope analysis of Er ³⁺ doped Y ₂ SiO ₅ coated frustules	76
Table 9 Average elemental contents of (1X) Zn/Mn coated frustules.....	80
Table 10 Average elemental contents of (2X) Zn/Mn coated frustules.....	83
Table 11 Average quantified EDS results of (4X) Zn/Mn coated frustules	86
Table 12 Results of the fluorescence microscope investigation of Mn ²⁺ doped Zn ₂ SiO ₄ coated frustules	87
Table 13 Average elemental contents of frustules nitrided at 650°C, 3keV.....	91
Table 14 Average elemental contents of frustules nitrided at 650°C, 15 keV.....	92
Table 15 Average elemental content of frustules nitrided at 800°C, 3.00 keV	95
Table 16 Average elemental content of frustules nitrided at 800°C, 15.00 keV	96

List of abbreviations

EDS	Energy dispersive x-ray spectrometer.
P.I.D controller	Proportional integral derivative controller.
P.V cells	Photo voltaic cells.
Mitotic	Asexual reproduction.
Meiosis	Sexual reproduction.
SEM	Scanning electron microscope.
Gametes	Cells of opposite sex, can fuse together.
Auxospore	Specialized cell produced at key stage in cell cycle.
EDTA	Ethylenediaminetetraacetic acid.
SDS	Sodium dodecyl sulfate.
Cribellum	Cribal pore.
Cribal pore	Opening in siliceous layer (velum) covering areola.
Cribrum	Velum perforated by cribal pores near interareolar wall.
Areolae	Perforation through valve with internal/external sieve membrane.
Epivalve	Older and larger valve of frustule structure.
Hypovalve	Youngest and smallest valve of frustule structure.
Foramen	Opening of areolae opposite velum.
Velum	Thin usually perforated siliceous layer on frustule surface.
Valve	Siliceous part of frustule containing majority of morphological features that describe diatoms, each valve has two surfaces termed the face and the mantle.
Valve face	Portion of valve, apparent in valve view when oriented to valve plane.

Valve mantle	Portion of valve, sloped, apparent in girdle view.
Raphe	Seam or ridge on diatoms.
PVD	Physical vapor deposition.
PECVD	Plasma enhanced chemical vapor deposition.
CVD	Chemical vapor deposition.
ESA	Excited state up-conversion.
ETU	Energy transfer up-conversion.
PA	Photon avalanche.

1 Introduction

1.1 Background

Global energy demand has been increasing steadily along with the development of modern society and the industrialized world. The fuels that power the world have seen precious few improvements over the last 100 years, and the majority of energy is still supplied from the combustion of fossil fuels like coal and oil. The use of such fuels has long been known to be the source of global pollution and as of recently several studies has pointed out that this pollution may be responsible for global environmental changes [1-3].

In an attempt to reduce pollution and to improve the energy security situation, several technologies have been developed around the world. Some alternative sources of energy that can be mentioned are: Biofuels for use in transportation, hydroelectric energy, wind power, solar energy and geothermal energy.

At present all of the previously mentioned technologies have seen some use, but are either too expensive to compete against the current energy solutions, have low efficiencies or are too regionally bound such as hydroelectric and geothermal power generation.

It should however be mentioned that hydroelectricity is completely competitive with power generation from fossil sources given the required water resources. It is therefore of great importance to improve both the economical and efficiency aspects with regards to all aforementioned technologies.

The development of silicon solar cells have seen a drastic growth over the last decades and along with the improvements in efficiency a substantial decrease in price has been observed. Several reports indicate that close to 20 % of global power demand can be delivered by photovoltaic solar cells by 2050 [4, 5].

To obtain such a large share of the global energy market would necessitate even greater improvements in efficiency as well as a lower price per photovoltaic unit as when compared to what is presently available [6].

The most common photovoltaic solar cells of today are the silicon wafer solar cells and have efficiencies close to 20 %, these types of solar cells are limited to a maximum efficiency of ~ 29 % and this limit is known as the Shockley-Queisser limit.

The Shockley-Queisser limit can be attributed to factors like: a bandgap that only utilize a certain range of the photons in the total incident solar radiation, reflective losses and losses from charge carriers recombining in the photovoltaic material.

In order to improve efficiencies beyond the Shockley-Queisser limit, several strategies are currently explored, some of these strategies may be:

- The use of up and down converting layers at the front and back of the solar cell, this would then transform the energies of incident photons to energies more suited to the existing bandgap of the material, allowing extraction of more energy from incident light.

- The use of highly textured surfaces at the front of the photovoltaic solar cell would allow for more efficient light harvesting by reducing reflective losses as well as improving the path length travelled by light.
- The use of multilayered photovoltaic solar cells featuring several bandgaps that allows for the extraction of more energy from incident solar radiation by being more suited to the various energy levels of the photons found in solar radiation. These types of solar cells are also termed tandem cells.

All of the aforementioned strategies are considered to be improvements with regards to light harvesting properties. Light harvesting properties in photovoltaic solar cells are therefore in this text considered to be processes that involve the capturing of incident solar radiation and the generation of electrical energy from this radiation.

It should be mentioned that several strategies for improving the light harvesting in solar cells are currently implemented, some of these strategies may be: texturing of the surfaces of silicon solar cells by the use of various etchants as well as nitride and oxide coatings to reduce reflection and surface recombination losses [7, 8].

Several studies have pointed out improvements in photovoltaic structures having a large surface area and highly structured surfaces. The surface structures work by interfering and scattering the incident rays, causing the light to have a greater path length in the material and hence improve probability of absorption and charge separation. By use of nanotechnological tools and techniques, structural morphology can be controlled to a high degree. The use of such methods does however come at an increased expense as well as more challenges with regards to industrial use.

Several light harvesting structures do however exist in nature. Diatom frustules are excellent examples of naturally occurring light harvesting structures [9]. Diatoms are some of the most common types of phytoplankton as well as a major group of algae and can be found in almost any aquatic environment on earth [10].

The diatoms are single celled photosynthetic algae consisting of an organic inner cell that is surrounded by a highly porous silica structure termed a frustule. The frustule pores are considered to be photonic structures due to the ability to interfere with light, causing the light to be scattered and hence giving the light a greater path length in the structure [11-13].

The frustule photonic abilities have been proven by utilizing a single frustule as a microlens, the frustule pores were found to focus incident rays of light to a spot the size of a few microns [12, 14]. The function of the pores is similar to that of textured solar cell surfaces but the frustule pores are expected to be much more efficient as light harvesting structures [15].

The highly efficient light harvesting structural features found in diatom frustules would be interesting to implement in photovoltaic solar cells in order to improve efficiency levels as well as possibly reducing the cost of fabrication since these structures exist in nature [16].

Frustules consist of silica, being an insulator in nature, would not be useful as a photovoltaic device in itself. Should however the structural features be coated with oxides that allows for the up and down-conversion of light or being nitrided to give a highly non reflective surface, then these structures could be used in conjunction with existing solar cells to improve efficiency [17].

Earlier attempts at inducing down-conversion in frustules performed by Lee et al. used inkjet printing with dyes containing phosphors known for down converting abilities. Post printing, the frustules were subjected to thermal annealing of several hours at temperatures of 1000°C [18]. This attempt was highly successful in achieving the desired down-conversion [18].

A mixture of halides of zinc and manganese in a solution of ethylene glycol and acetonitrile was used to achieve a coating with possible down-conversion abilities. This mixture was identical to that described by Lee et al. [18]. A dip coating procedure was utilized to deposit the mixture.

No literature was found on up-conversion of light in frustules. Thus a modified version of the coating procedure utilized in previous work by Lee et al. was developed for the deposition of up converting elements [18]. Halides of yttrium and erbium were dissolved in a solution of ethylene glycol and acetonitrile and a dip coating procedure utilized to deposit the mixture.

Due to experimental findings on the student specialization project as well as findings in literature, a temperature of 1000°C was found to cause damages in the frustules pore structures. Changes in pore structure was found to occur at temperatures of 800°C and was found to increase with increasing temperatures, it was therefore decided to limit the annealing temperatures at 800°C in order to limit changes in pore structure .

1.2 Aim of work

In this master thesis the structural features of diatom frustules were subjected to coating with elements from the lanthanide series. The goal of this part of the thesis was to attempt the coating and then characterizing the coating for structural, thermal, chemical and fluorescent abilities. A nitriding procedure to achieve three dimensional nitride replicas of the frustules was also attempted

After coating the frustules were subjected to characterization by scanning electron microscope (SEM) featuring on-board energy dispersive x-ray spectroscopy (EDS) to ensure that micro and nano-structures was preserved post coating. Chemical analysis of the frustules specimens was done at the same time as structural characterization by EDS.

The coated frustules were then characterized by use of fluorescence microscopy and photoluminescence spectroscopy. This gave information about the fluorescent abilities of the coating and the corresponding energy levels responsible for the fluorescence.

A temperature exposure experiment was also performed to investigate and if possible validate previous experiences with thermal behaviour of diatom frustules. In this experiment frustules were exposed to temperatures of 400°C up to 1200°C at increments of 200°C before being characterized in SEM.

Nitriding of the frustules were attempted by utilizing a simultaneous nitriding and metallothermic reduction reaction. This was done in order to lower the temperature of nitriding down to the temperature of metallothermic reduction [19]. The simultaneous metallothermic reduction and nitriding was conducted in a sealed stainless steel vessel featuring an inert argon gas atmosphere at temperatures of 650°C - 800°C, magnesium was used as a reductant and ammonium chloride as a source of nitrogen.

Nitrided frustules were characterized by use of scanning electron microscope (SEM) featuring on board energy dispersive x-ray spectrometer (EDS). This gave structural and chemical information about the nitride frustules. Raman spectroscopy was later used to verify the results of the chemical analysis.

2 Theory

2.1 Diatoms

Diatoms are single-celled algae consisting of an inner organic cell covered by a highly porous silica structure termed a frustule. These microscopic plants can be found in almost all aquatic environments on earth and are considered to be responsible for up to 25 % of all net primary production of organic carbon each year which means that they are highly efficient in performing carbon sequestration [20]. Diatoms are considered to be very important as members of the planktonic food chain [21].



Figure 1 The diverse shapes of diatoms [22]

According to classification based on frustule geometry there are 100 000 different species of diatoms [20]. A great example on the diversity of diatoms can be seen in Figure 1. Most species of diatoms are found in open waters and are termed pelagic, however some species may be found living on the interfaces between water and sediments and are termed benthic [23]. Since most diatoms are photosynthetic they are found in the photic zone of the ocean, this is illustrated in Figure 2. Despite diatoms being unicellular they can be found living in colonies as ribbons or filaments.

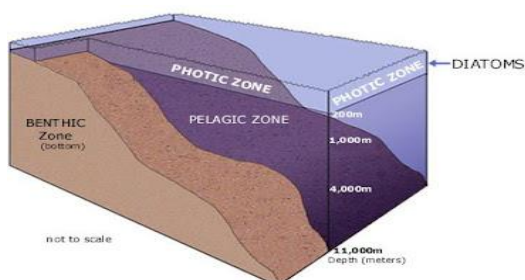


Figure 2 The habitat of diatoms [23]

No form of group symmetry is considered to exist among diatoms, but they are normally divided into centric and pennate types. Centric diatoms have a radial but not necessary circular symmetry. The pennate diatoms are elongated and have a bilateral symmetry. The pennate diatoms are again divided into pennates with and without a raphe. The three main classes of diatoms are illustrated in Figure 3 [21].

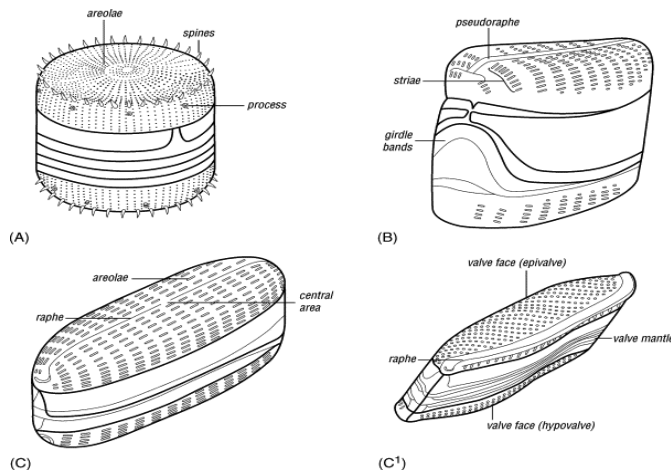


Figure 3 The three main classes of diatoms [21]

In Figure 3, (a) represents a typical centric form, (b) a typical pennate diatom without a raphe, (c) and (d) illustrates typical pennate diatoms with a raphe. In (c) the raphe is central and in (d) the raphe is eccentric [10, 21].

Most diatom species are autotrophic which means that they have the ability to synthesize their own nutrients from simple inorganic molecules like CO_2 by either photosynthesis or chemosynthesis. For this reason autotrophs are considered to be carbon fixating and do not require organic compounds as a source of energy or as a source of carbon. Water is the most common reducing agent used by autotrophs, some may however utilize other hydrogen containing substances like hydrogen sulphide [24].

Some types of diatoms may also be obligate heterotrophs, meaning they consume organic compounds both as a source of energy and as a source of carbon to sustain further growth. Diatoms with the ability to grow heterotrophic often grow faster and achieve a higher number of species than their autotrophic counterparts [25].

2.1.1 Diatom reproduction

Reproduction in diatoms does usually occur via mitotic (asexual) cell division, here one mother cell divides into two daughter cells. Each of the daughter cells keeps one of the halves of the mother cell, these cell halves are termed mother valves and will each become the largest part of the new diatom cell. The largest parts of the daughter cells are termed epivalves. This phase of the diatom lifecycle is termed the vegetative life cycle and for every cell division the average cell size will decrease. Further cell growth will happen as an elongation of the cell by growth of more girdlebands [10].

To avoid the average cell size becoming too small, resulting in death, a phase of sexual reproduction is initiated. During this phase the cells slough their cell walls, forming gametes (cells of opposite sex) which enable cellular expansion. Meiosis (sexual reproduction) takes place during the formation of the gametes. It should be mentioned that not all diatom cells have the ability to differentiate and form gametes. Large cells above a certain critical threshold size are incapable of sexual reproduction.

Important environmental parameters for sexual reproduction are: light, temperature, access to nutrients and the presence of compatible mates. Size restoration happens via formation of a auxospore which is a large structural unit that allows the diatom to grow inside, restoring the original size for the next generation of diatoms [10, 26]. The diatoms life cycle and cell division is illustrated in Figure 4.

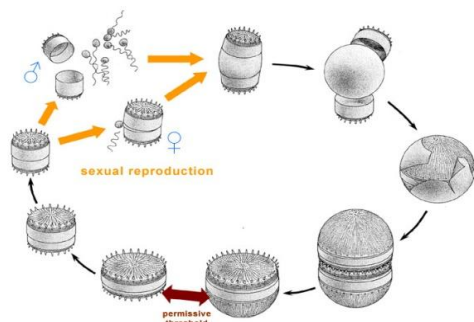


Figure 4 Diatom lifecycle and cell division [10, 26]

2.1.2 Diatom frustules

The frustules are defined as the silica shell that encapsulates the organic parts of the diatom cells and are known for their diverse morphology as well as being highly porous both in the nano and micrometric ranges [10, 22]. A schematic presentation of the various parts of a centric diatom frustule featuring correct terminology is given in Figure 5 [27].

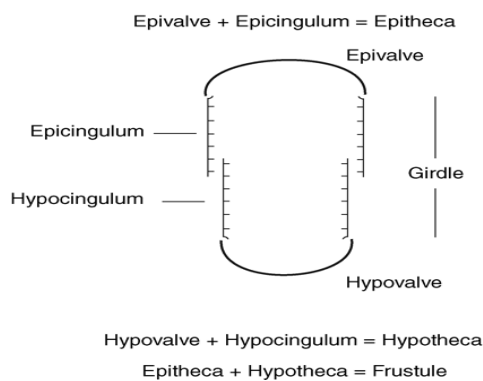


Figure 5 Frustule structure [27]

As indicated in Figure 5, the diatom frustules are consisting of two overlapping, differently sized but identically shaped halves termed thecae. These halves consist of the hypo valve and epivalve which are held together by silica structures termed girdle bands.

The largest side of the frustules structure is named epitheca whereas the smallest part of the structure is named the hypotheca. The silica used in building the frustules are extracted from orthosilicic acid found in seawater and is termed biomineralization.

The frustules porosity can be attributed to a large amount of highly ordered pores, these pores are thought to be efficient light harvesting structures since most diatoms are photosynthetic. The frustules consist of amorphous silica and various organic components [22].

The frustule pore structure is illustrated in Figure 6, schematically (a) and as observed by use of scanning electron microscope (b) [22]. The cribellum pores are found in the velum membrane, and are the pores where the smallest structural features are found. The cribrum are the cavities in the roof of the areola and the foramen is a hole in the floor of the areola towards the inside of the frustule structure.

The pores may be from tens of nanometres to several micrometers in diameter, pore size does not decrease with decreasing frustule size instead the number of pores decreases [11]. Frustules are sturdy and can withstand high pressures for their size and porosity [28].

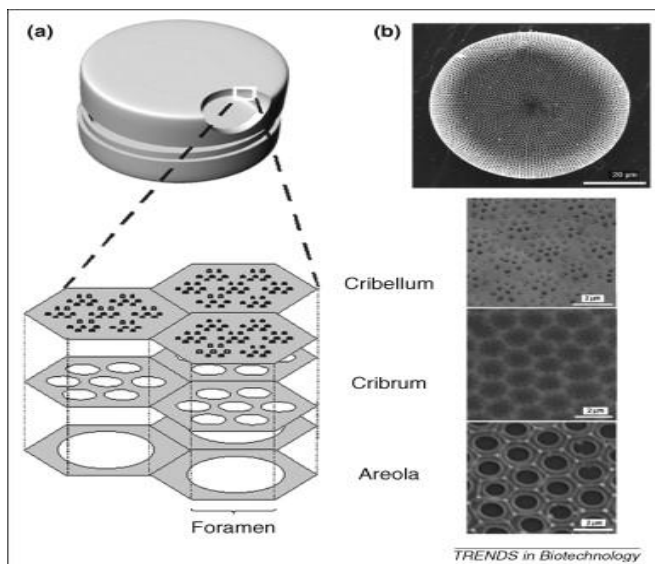


Figure 6 Frustule pore structure [22]

According to Ottesen some differences were observed between pores of frustules that were cultivated as compared to frustules found in net plankton. Cultivated diatoms were found to lack the inner pore structure found in net plankton and differences in placements of the micro sized pores were also observed [29].

2.1.3 Light harvesting in diatom frustules

The light harvesting abilities in frustules are thought to stem from the great number of highly ordered and nanostructured pores. Light entering the three dimensional pore structures will be scattered, causing the light to travel a greater distance within the material, increasing the probability of photon absorption [30].

Frustules of the *Coscinodiscus wailesii* species have also been found to have a microlensing effect. This effect is observed upon illumination by red light, where frustules have the ability to focalize incoming light with a beam diameter of 100 μm to a spot less than 10 μm in diameter at a distance of 104 μm [14, 31]. The focalizing effect takes place towards the center of the frustule and is assumed to be a result of both pore structure as well as total pore pattern along with frustule geometry [14].

Frustules have also been found to give photoluminescence variations in the presence of organic vapors [32]. These effects upon exposure of light have caused frustules to be considered photonic crystals [33]. Photonic crystals can be described as dielectric structures having periodically modulated refractive indices [30, 33].

The photonic effects observed in diatom frustules are highly dependent of the surrounding media. Significant variations in peak placement and intensity have been observed in laser induced fluorescence experiments performed on frustules in different media. These effects are thought to stem from electronic and optical properties in the surrounding media interacting with the properties of the frustules [9].

According to Noren frustules of the species *Coscinodiscus* sp., were found to give slightly lower reflection as when compared to a standard layer of the anti reflecting compound silicon nitride, meaning an improved light harvesting was observed for the frustules [34].

2.1.4 Diatom frustules utilized in this thesis

The type of diatoms used in this thesis was of the genus *Coscinodiscus*, this genus is known for being large in size and having a highly ordered periodic pore pattern. The structure as appearing in light microscope can be seen in Figure 7.

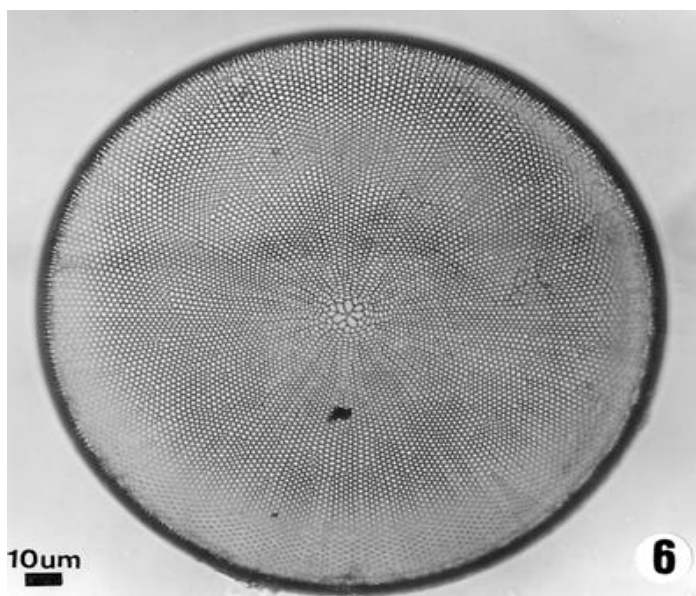


Figure 7 *Coscinodiscus wailesii* [35]

The diatoms in this thesis was cultivated at the institute of biotechnology at NTNU and was of the species *Coscinodiscus wailesii* as well as samples acquired from the Trondeims fjord by use of landing net, exact species of these diatoms were not known and are referred to as *Coscinodiscus* sp.

Coscinodiscus is a large centric diatom with a typical size ranging from 160-400 micrometers in diameter [36]. This species is known to be very robust and handle great variations in temperature, salinity and nutrients, it is therefore considered excellent for cultivation in bioreactors. *C. wailesii* is considered a harmful algae due to the ability to grow fast it will deplete the local area of nutrients required by other organisms [37]. Of the 400 known different species *C. wailesii* is the most extensively researched [38].

In literature *C. wailesii* is reported to complete the first cell division within 48 hours. The diatom is cylindrical in shape giving the impression of being rectangular when viewed from the sides, due to the pervalvar axis being closely dimensioned to the diameter of the cell, this is illustrated in Figure 5 [36].

2.2 Photovoltaic solar cells

Photovoltaic solar cells are electronic devices that enable the conversion of energy in photons to electrical energy. Several approaches are currently in use to achieve this goal, some that deserves mentioning are: silicon wafer solar cells, dye sensitized solar cells (DSSC), polymer/organic solar cells, silicon thin film solar cells and multi junction solar cells [39, 40]. The best known and most developed technology is that of the silicon wafer cells, and will be treated further in this thesis [41].

All of the above mentioned technologies are depending on the separation of charge upon absorption of photons in the photovoltaic material, this separation of charge results in generation of electron hole pairs. In order to prevent spontaneous recombination of the generated holes and electrons, the photovoltaic solar cell utilize an electric field generated by the addition of positive and negative dopants to the semiconductor material [41].

2.2.1 Silicon solar cells

Silicon being a group IV element is an intrinsic semiconductor and is extensively used as a photovoltaic semiconductor material in solar cells, both in monocrystalline and multicrystalline forms. In the fabrication of such solar cells, ingots of high purity silicon are wire sawn into wafers of suitable dimensions and doped with suitable dopants, giving a semiconductor with the desired characteristics.

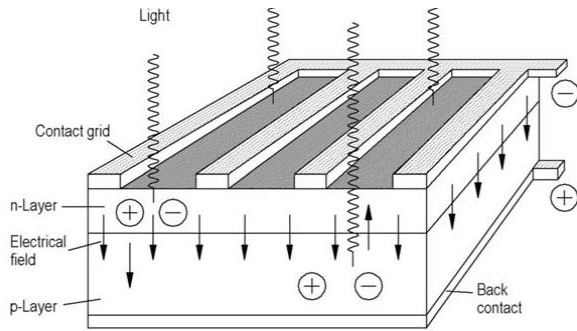


Figure 8 Photovoltaic solar cell [42]

For silicon solar cells the dopants that may be used are phosphorous (P) and boron (B). Phosphorous is a group V element, meaning it has 5 valence electrons whereas silicon (Si) is a group IV element containing 4 valence electrons [43]. The effect of doping silicon with phosphorous is the generation of a semiconductor material with negative (n) characteristics due to the extra valence electron of phosphorous causing an electron donating effect [41].

Upon doping silicon with boron, a semiconductor material featuring positive (p) characteristics is achieved. This effect can be attributed to boron being a group III element, meaning it has one less valence electron than Si and thus would be an electron accepting impurity, creating a positive charge or a hole [41].

The effect of combining semiconductor material featuring both positive and negative characteristics is the creation of a p-n junction. This p-n junction will allow the flow of current in only one direction and thus reducing the probability of holes and electrons spontaneously recombining after generation. A p-n junction is also termed a diode in electronics terminology [40, 41]. The p-n junction is illustrated in Figure 8, depicting a photovoltaic solar cell.

The silicon solar cell has a maximum theoretical efficiency of ~ 29 %, known as the Shockley-Queisser limit [41, 42]. Current solar cells operate in the area of ~14 % for commercial variants and in the area of ~24 % for laboratory variants [44]. The difference in efficiency levels between commercial and laboratory grade solar cells can be attributed to tradeoffs between efficiency and durability as well as price issues, meaning industry has greater demands towards high durability and lower costs than research projects.

2.2.2 Light harvesting in silicon solar cells

Light harvesting in solar cells can be defined as the ability of the solar cell to convert incoming photons to electrical energy. This ability depends on several factors such as: the band gap(s) of the photovoltaic material, reflectivity of the material, resistivity of the material, thickness and structure of the material [40, 41, 45, 46].

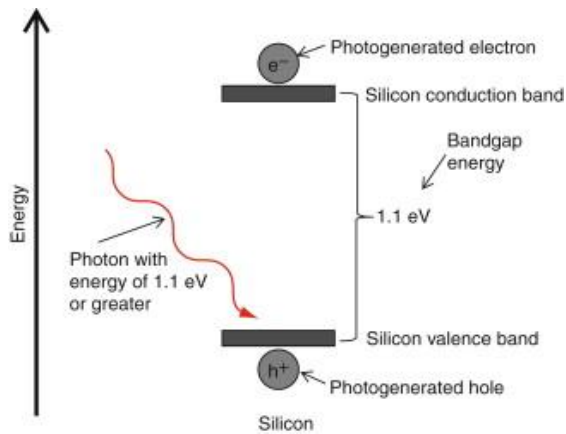


Figure 9 Silicon band gap upon illumination [45]

The p-n junction will have a certain band gap and only photons of equal or greater energy than the band gap can cause a charge separation by exciting electrons from the valence band to the conduction band, leaving positively charged holes behind [39]. Upon completing the circuit, electrons and holes will recombine and thus allow for this energy to be utilized for electrical appliances [46].

A highly simplified illustration of the band gap in silicon is given in Figure 9 and the corresponding parts of the solar spectrum utilized by a silicon solar cell of the same band gap is given in Figure 10.

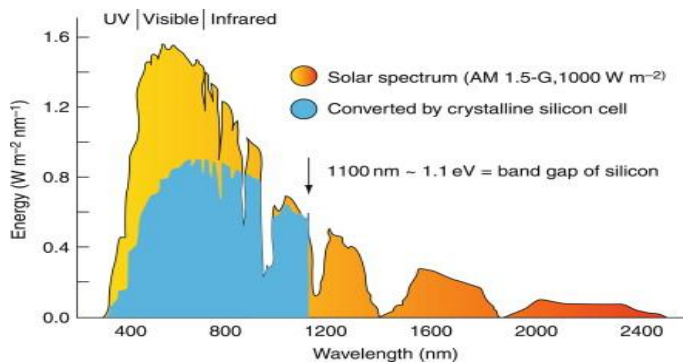


Figure 10 The solar spectrum along with the conversion achieved in silicon PV cells [45]

The band gap has direct meaning to the amount of photons that can be used to excite electrons and give electricity. A large band gap can only use high energy photons, while a smaller band gap can use both high and low energy photons. High energy photons in a small energy band gap loses much energy being converted to heat in a process known as auger recombination [41].

The reflectivity of the material can often pose problems because any reflected light is to be considered lost energy. Reflectivity can be remedied by deposition of a silicon nitride layer along with surface texturing of the front of the solar cell [47, 48].

The thickness of the solar cell is also important since long wavelength light will often pass through the cell and hence will constitute a loss of energy [49]. This situation can be remedied by texturing of the front and rear

surfaces of the photovoltaic device. The texturing will cause the light to transverse the solar cell from side to side and increase the chances of light absorption [50].

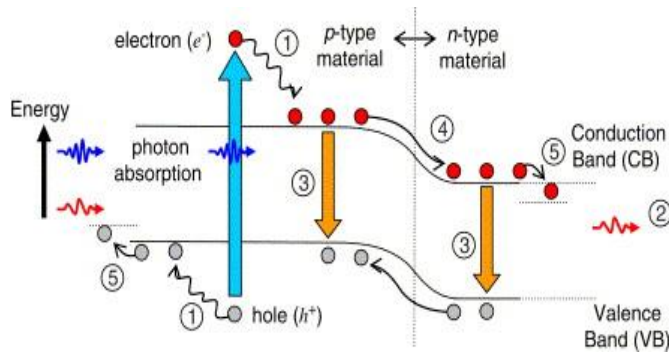


Figure 11 Loss mechanisms in a single junction solar cell [51]

Considering the previous discussion of loss mechanisms and their respective remedies, it becomes clear that a significant part of improved light harvesting would lie in limiting or eliminating the possible loss mechanisms. The various loss mechanisms of a single junction solar cell are summarized in Figure 11.

2.2.3 Improved light harvesting in solar cells by use of frustules properties

Diatom frustules are considered efficient light harvesting structures as a function their great number of highly ordered pores [30]. A close analogy to the efficiency of frustules pores with regards to light harvesting would be the surface texturing of existing solar cells. The texturing was found to give antireflecting properties close to silicon nitride normally used in solar cells which translates to greatly improved light harvesting [34, 52].

According to findings in literature, frustules was found to increase the efficiency of dye sensitized solar cells (DSSC), the increase in efficiency was attributed to the pores of the frustules causing scattering of the incident rays [16].

Frustules were also found to act as efficient light harvesting structures in a report by Lee et al., where frustules of *Pinnularia* sp. were coated with elements of the lanthanide series and annealed [18]. Upon illumination with UV light the frustules was found to down-convert the incident light [18].

No literature describing the direct use of diatom frustules with regards to improvements in silicon solar cells was found.

2.3 Up-conversion of light

Up-conversion of light is a fluorescence phenomenon, and is a term used on processes where low energy incident light is reradiated at a higher wavelength and hence also at a higher energy level. An example of up-conversion would be that of incident red light being reradiated in the green or blue area of the electromagnetic spectrum upon interaction with an up converting material [53, 54].

Up-converting materials are also termed fluorescent materials and phosphors. These materials usually consist of a host lattice doped with impurity ions, these ions are also known as activator ions [53]. The concentrations of impurity ions are usually low since higher concentrations will cause a drop in efficiency of the luminescence efficiency, this effect is termed concentration quenching [53, 55].

The absorbance of energy required for excitation can take place in the host lattice itself or by the impurity ions. Emission of energy takes place at the same impurity ions, if the impurity ions shows too little absorption of light, a second type of impurities is added. These impurities are termed sensitizer ions and have the function of transferring absorbed energy to the ions responsible for up-conversion and emission [53].

The process of up-conversion can be explained by the absorption of two or more low energy photons and the consequent re-radiation of one high energy photon. This process is dependent on long lived intermediate energy levels in the electronic structure of the impurity ions [56].

The intermediate energy level can maintain the energy of one low energy photon for sufficient time to allow the absorption of a second low energy photon and reach a high energy state where the combined energy of the two photons are reradiated as one high energy photon [56, 57].

In materials displaying up converting characteristics, multi-phonon relaxations are non predominant and thus allows several metastable excited states. A good example on this is the rare earth compounds where 4f and 5f electrons are shielded and thus not strongly involved in metal to ligand bonding [58, 59].

The consequences of this shielding are reduced electron-phonon coupling to f-f transitions and therefore less competitive multiphonon relaxation processes. Up-conversion characteristics are therefore usually displayed by materials containing lanthanide ions. There is however transition metal systems and combinations of rare earth and transition metal combinations displaying up-conversion [58, 60].

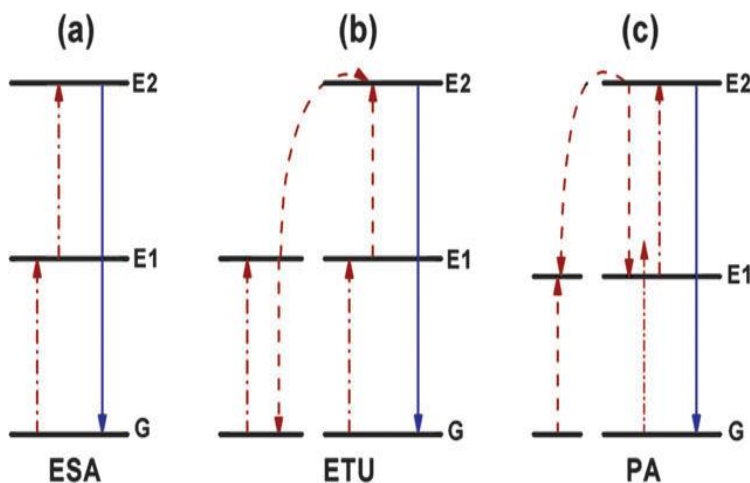


Figure 12 The three main classes of up-conversion phenomenon [59]

The process of up-conversion can be divided into three main classes, these classes are: excited state absorption (ESA), energy transfer up-conversion (ETU) and photon avalanche (PA) [59, 61]. These processes are illustrated in Figure 12.

The energy absorption in ESA occurs in one single ion by the successive absorption of two photons. The first photon absorption happens at ground state (G) and causes an excitation of the ion which populates the long lived intermediate energy level E. The second photon absorption will excite the ion into the energetic state E2, which relaxes back to ground state (G) and emits the energy difference E2-G as a photon of corresponding energy [61].

In the case of ETU, energy absorption is similar but occurs between two adjacent ions. Both ions are excited to the energy level E1 and one of the ions are further excited to energy level E2 by resonant energy transfer from the neighboring donor ion which relaxes back to ground state (G). The acceptor ion in the excited E2 state relaxes back to G, emitting the energy difference E-G as a photon of corresponding energy [59].

Photon avalanche (PA) occurs at a weak non resonant absorption at the ground state (G) and a following resonant excited state absorption (ESA), where one ion is excited to the E2 level. Cross relaxation to an ion in ground state (G) causes both ions to inhibit the intermediate excited state E1. Further resonant ESA and cross relaxation, exponentially increase population of the E2 level and therefore controls up-conversion emission intensity [61].

ESA is the weakest of these processes whereas PA is the most efficient but has a slow response to excitation and is dependent on pump power. ETU is independent of incident pump power and is very fast [61]. Pump power describes the characteristics of the incident light causing excitation [62].

An illustration of the various up-conversion processes in Er^{3+} ions under illumination by 785 nm laser is illustrated in Figure 13 [63]. In this figure the black solid lines represent laser absorption, the colored solid lines represents emitted light and the color of the light. Dotted lines represent nonradiative relaxations.

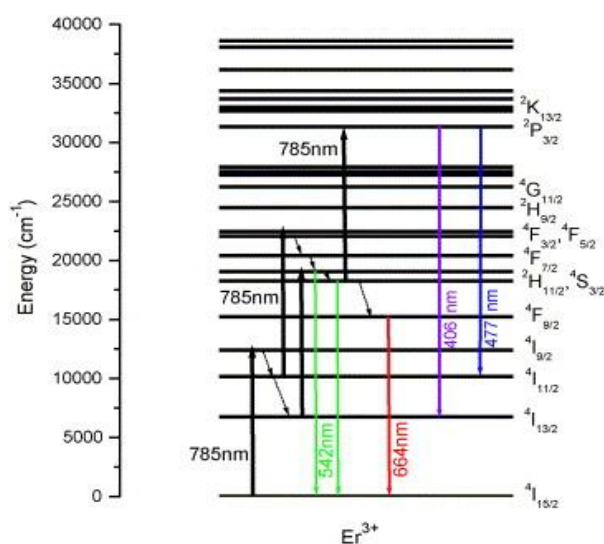


Figure 13 Up-conversion in Erbium ions [63]

It should be mentioned that most lanthanide activator ions exhibit low cross sectional absorption which leads to low pump efficiencies. To increase efficiency, sensitizer ions with greater absorption cross sections in the near infrared region (NIR) are usually co-doped along with the activator ions [59, 64]. The use of a sensitizer ion and the corresponding energy transfer between sensitizer and activator ion upon illumination is illustrated in Figure 14, here ET represents energy transfer and Ln^{3+} represent a lanthanide ion.

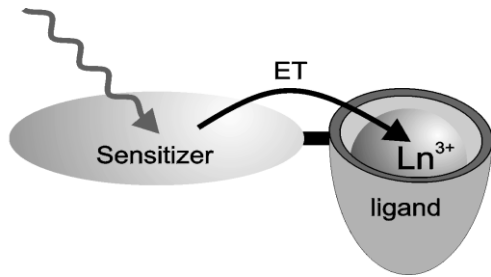


Figure 14 Energy transfer between sensitizer and activator ion upon illumination [64]

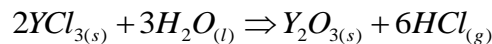
Yttrium doped with rare earth elements are frequently used as an up-converting material due to high chemical stability and high thermal stability. This material also display low phonon energies which increase radiative transmissions and thus results in a higher quantum yield [65].

2.3.1 Deposition of up-converting oxides

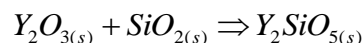
The deposition of up-converting oxides during the experimental parts of this thesis followed a modified method previously outlined by Lee et al. [18, 66]. According to this method, metal halides were dissolved in a mixture of acetonitrile and ethylene glycol before being decomposed at elevated temperatures [18].

However since erbium was not mentioned in the report by Lee et al., and it is an element known to display up-conversion characteristics, the use of erbium chloride was attempted. This was done because erbium (III) chloride displays similar behavior under heating as the europium (III) chloride used in the original article [67].

The decomposition reactions thought to occur during calcining are [18]:



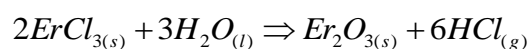
$$\Delta G_{R_x} = -281.502 \text{ kJ/mol at } 800^\circ\text{C [68]}$$



$$\Delta G_{R_x} = \text{No data found [68, 69]}$$

The decomposition reaction which forms Y_2O_3 is thought to occur through a series of intermediate steps such as $Y(OH)_xCl_y$ and YO_aCl_b and at temperatures between $240-700^\circ\text{C}$. The final decomposition and formation of Y_2SiO_5 occurs at temperatures above 700°C [18, 67]. All reactions acquire water by atmospheric absorption due to the chemicals being hygroscopic. Final annealing temperature was set to 800°C .

The decomposition reaction for erbium (III) chloride is [67]:



$$\Delta G_{R_x} = -323.435 \text{ kJ/mol at } 800^\circ\text{C [68]}$$

This reaction occurs at temperatures above 550°C and will occur through intermediates like $\text{ErOCl} \cdot 2\text{ErCl}_3$ and finally ErOCl to Er_2O_3 [67]. The erbium oxide in the final product will exist as an impurity in the final material [18]. Er^{3+} ions function by substituting for Y^{3+} ions in Y_2SiO_5 and are responsible for the photoluminescent behavior. Er^{3+} ions are thus activator ions [70, 71].

2.4 Down-conversion of light

Down-conversion of light is a fluorescence phenomenon, and is in essence just the reverse process of up-conversion. That is upon absorption of one high energy incident photon, two or more low energy photons are emitted [17]. Various mechanisms of down-conversion are illustrated in Figure 15.

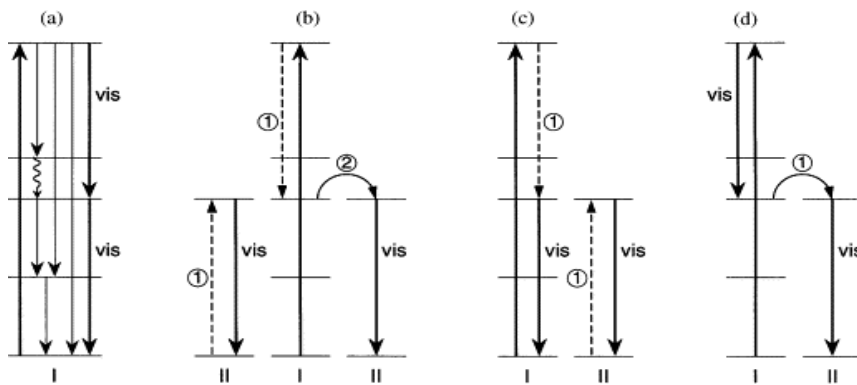


Figure 15 Mechanisms of down-conversion [72]

An example on down-conversion would be absorption of photons in the ultraviolet (UV) spectrum and the emitting of photons in the lower energy visible range (VIS). Another term used on the phenomenon of down-conversion is quantum cutting [17].

According to Figure 15, type I is an ion from which emission from a higher energy level can occur. Type II is an ion to which energy transfer takes place. The situation in (a) describes down-conversion occurring on one single ion and the consequent emission of two photons in the visible range of the electromagnetic spectrum [73, 74].

In the situation described in (b) of Figure 15, down-conversion occurs via a two step energy transfer. In the first step labeled 1, part of the excitation energy is transferred from ion I to II. Ion II relaxes to the ground state by emission of a photon in the visible spectrum. Ion I is still in an excited state and transfers remaining energy to a second type II ion which relaxes back to the ground state by emission of a visible photon [73].

The two last situations in Figure 15 labeled (c) and (d), describe single step energy transfers from ion I to II. In (c), ion I relaxes to an intermediate level by transferring energy to ion II which becomes excited, both ions then relax to the ground state by emission of visible photons [75].

In Figure 15 (d), ion I relaxes to an intermediate energy level by emission of a visible photon and then transfer the remaining energy to ion II which relaxes to the ground state by emission of a visible photon [75].

Similar to the process of up-conversion, down-conversion is usually caused by radiative transitions between electrons in the 4f and 5f regions [17]. Down-conversion characteristics are therefore often displayed by rare

earth elements and some transition metals [17, 59]. The radiative transitions in the 4f and 5f levels occur due to shielding of the electrons in these levels [58].

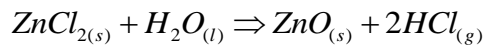
Elements displaying down-conversion characteristics are similar to elements displaying up-conversion in only being added as a dopant of few mole percent to a host lattice. These elements also frequently requires the co-deposition of appropriate sensitizer ions to increase absorption efficiency [76].

2.4.1 Deposition of down-converting oxides

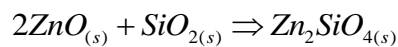
The deposition of down-converting oxides was based on a method developed by Lee et al., and involved dissolution of halides of zinc and manganese in a mixture of ethylene glycol and acetonitrile [18, 66]. This mixture was thought to leave an evenly distributed surface layer of the corresponding halides on the frustules upon heating. The halides are then decomposed at elevated temperatures in a normal atmosphere [18].

The decomposition reactions encountered in the deposition of down-converting elements are:

The decomposition of zinc chloride:



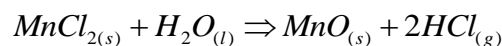
$$\Delta G_{\text{Rx}} = -37.897 \text{ kJ/mol at } 800^\circ\text{C} [68]$$



$$\Delta G_{\text{Rx}} = -34.837 \text{ kJ/mol at } 800^\circ\text{C} [68]$$

The first reaction, forming zinc oxide takes place via formation of zinc hydroxyl chloride at temperatures above 300°C. At temperatures above 400°C, some volatilization of zinc chloride may occur [77]. The final reaction forming zinc silicate occurs above 650° and is completed at 800°C thus final annealing temperature was set to 800°C [18, 77, 78]. All water is absorbed from the atmosphere as these salts are hygroscopic [43].

The decomposition of manganese chloride:



$$\Delta G_{\text{Rx}} = -22.582 \text{ kJ/mol at } 800^\circ\text{C} [68]$$

This reaction will occur at a temperature of 700°C [79]. Some formation of manganese (III) oxide (Mn₂O₃) may occur at high temperatures (~1000°C) [79, 80]. The manganese ions present in the final material will exist only as an impurity [18, 66]. The concentration of impurity is important, since concentration quenching of luminescence may occur at greater concentrations [81].

Mn²⁺ ions functions by substituting for Zn²⁺ ion in Zn₂SiO₄ and is responsible for the color of the photoluminescence. Mn²⁺ ions are thus activator ions [82, 83].

2.5 Nitriding of silicon

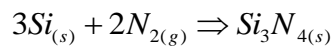
Silicon nitride (Si_3N_4) is formed when silicon is heated in a nitrogen atmosphere. The nitrogen may be present as diatomic N_2 or as ammonia (NH_3), it may also be formed in chemical vapor deposition (CVD) in a reaction between silane (SiH_4) and ammonia [84].

Silicon nitride has a diverse field of use due to a high resistance towards heat, chemical attack and high hardness: it is an important element in lathe and milling tools, it is used as an antireflective coating in solar cells, it forms the base of diesel particulate filters (DPF), it is used in crucibles for melting metal etc. [85-87].

The reaction between silicon and nitrogen requires temperatures around 1300-1400°C. At temperatures above 1800°C Si_3N_4 will decompose into its constituents, this is below the melting point of Si_3N_4 (1900°C) and gives difficulties in producing bulk material [88].

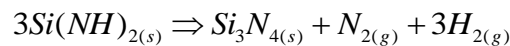
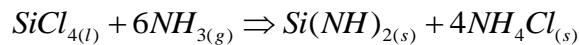
The most common ways of producing silicon nitride are [89, 90]:

Reaction between silicon and nitrogen at 1400°C [89, 90]:

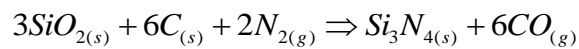


$$\Delta G_{\text{Rx}} = -194.847 \text{ kJ/mol at } 1400^\circ\text{C} [68]$$

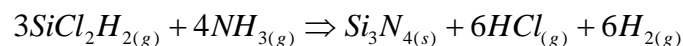
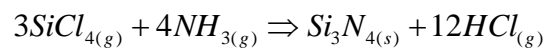
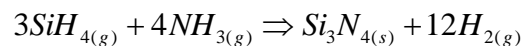
Silicon diimide synthesis from tetrachlorosilane and ammonia at 0°C and thermal decomposition of silicon diimide at 1000°C, silicon diimide being a white solid at room temperature as opposed to gaseous and liquid precursors [90]:



Carbothermal reduction of silica in nitrogen atmosphere at 1450°C [90]:



Deposition of silicon nitride by chemical vapor deposition (CVD) and plasma enhanced vapor deposition (PECVD) at 400-850°C [90]:



All of the above reactions require high temperatures with exemption of the CVD and PECVD processes. Bearing in mind the antireflective properties of silicon nitride and the light harvesting properties of diatom frustules, an

interesting approach to increase frustules light harvesting further would be to convert the porous structures found in diatom frustules to silicon nitride replicas [12, 33, 90].

A complete conversion of silica frustules into silicon nitride replicas would be interesting not only because of the antireflective abilities but also from silicon nitride having a very high tolerance to heat and chemical attack [90]. This would possibly give a replica with a high structural similarity towards the original frustules structure and have chemical and physical features of silicon nitride, meaning a very robust structure would be achieved.

The temperatures usually encountered in conventional methods of nitriding are too severe for the silica structures to endure since diatom frustules show signs of pore changes at 800°C [91, 92]. Coating the structures using CVD or PECVD would seem to be the only viable procedure due to the frustules temperature limits. This would leave the frustules intact and only coated with a layer of silicon nitride [93].

2.6 Simultaneous nitriding and metallothermic reduction of frustules

According to a report by Mazzoni et al. aluminothermic reduction of high silica materials (diatomite and bentonite) in a nitrogen atmosphere resulted in a product mixture within the Si-Al-O-N system [19]. The findings of the study suggests that there may be a possible route to achieve nitriding at lower temperatures compared to temperatures commonly encountered in industry [90].

The findings of Mazzoni et al. are supported by the work of Ma et al. In that study, titanium nitride was synthesized at 650°C by mixing magnesium powder, ammonium chloride and titanium dioxide in an inert gas (Ar) filled autoclave [94]. The synthesis of titanium nitride is similar to the synthesis of silicon nitride by requiring high temperatures (~1200°C) and the low temperature approaches being chemical vapor deposition CVD or physical vapor deposition (PVD) [95].

When considering the temperatures encountered in conventional nitriding of silicon it would seem very unlikely to be able to convert silica frustules to silicon nitride replicas and conserve the structural features of the frustules. A similar analogy would be the reduction of silica frustules to silicon replicas, the temperatures encountered in carbothermic reduction of silica are usually in the range 1900°C to 2000°C which are much higher than the frustules melting point [92, 96].

However in a report by Bao et al., diatom frustules were successfully reduced to silicon replicas at 650°C by utilizing a reaction known as a metallothermic reduction [97]. Structural features of the reduced frustules were found to be conserved to a high degree [97, 98]. It becomes clear that metallothermic reduction of silica occur at modest temperatures when compared to the corresponding carbothermal reduction used in industry [96, 97, 99].

The following subchapters give a description of metallothermic reductions and especially the magnesiothermic reduction due to the possibility of simultaneous nitriding and metallothermic reduction.

2.6.1 Metallothermic reduction

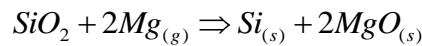
Metallothermic reduction of silica involves mixing a less noble metal with silica and supplying energy by heating above the activation barrier. When this happens the reaction will be self sustaining provided there is enough difference in chemical potential of the reacting species [100]. In order to maintain nano and microscale features of the object to be reduced, metal vapors are often used [97, 99].

The conservation of nano and microscale features are attributed to the resulting metal oxides (MgO, Al₂O₃ etc.) suppressing the formation of volatile species (SiO) and at the same time function as a supporting framework protecting structures exposed to the elevated temperatures of reduction [97].

Metals used in metallothermic reduction of silicon can be: aluminium, magnesium, calcium etc. If magnesium is used it is termed magnesiothermic reduction, if aluminium is used it is termed aluminothermic reduction etc. [101, 102]. These reactions goes very close to completion [103].

2.6.2 Magnesiothermic reduction

Magnesiothermic reduction by use of magnesium vapors in a closed reactor was found to give good results with high reproducibility by both Bao et al. and Sandhage et al. [97, 99]. The magnesiothermic reduction route was therefore attempted in this study. The simultaneous metallothermic reduction and nitriding was attempted at temperatures between 650°C and 800°C, this was done to investigate if higher temperatures related to higher conversions. An example on the magnesiothermic reduction of silica is given below with the corresponding Gibbs energy of reaction:

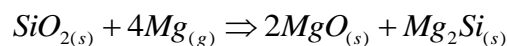


$$\Delta G_{R_x} = -345.852 \text{ kJ/mol at } 650^\circ\text{C} [68]$$

$$\Delta G_{R_x} = -308.060 \text{ kJ/mol at } 800^\circ\text{C} [68]$$

Possible side reactions encountered in magnesiothermic reduction are given below with the corresponding Gibbs energies at the temperatures encountered:

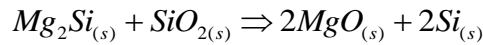
Formation of magnesium silicide and magnesium oxide from magnesium vapor and silica:



$$\Delta G_{R_x} = -502.095 \text{ kJ/mol at } 650^\circ\text{C} [68]$$

$$\Delta G_{R_x} = -430.623 \text{ kJ/mol at } 800^\circ\text{C} [68]$$

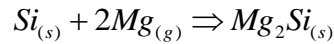
Formation of silicon and magnesium oxide from magnesium silicide and silica:



$$\Delta G_{Rx} = -189.609 \text{ kJ/mol at } 650^\circ\text{C [68]}$$

$$\Delta G_{Rx} = -185.498 \text{ kJ/mol at } 800^\circ\text{C [68]}$$

Formation of magnesium silicide from magnesium vapor and silicon:



$$\Delta G_{Rx} = -156.243 \text{ kJ/mol at } 650^\circ\text{C [68]}$$

$$\Delta G_{Rx} = -122.562 \text{ kJ/mol at } 800^\circ\text{C [68]}$$

The resulting solid oxides from these reactions are removed after the reaction by one or more acid leaching steps. In metallothermic reductions, silicides are inevitably formed, the concentration of silicides is largely determined by the excess of reductant as well as reaction residence time. This means that a greater excess of reductant and/or a greater residence time gives greater concentrations of silicides.

Silicides are removed by an acid leaching step, forming silane gas that combusts spontaneously in contact with oxygen in air [102]. Large concentrations of silicides would be detrimental in conservation of the structures due to their dissolution in the leaching stage. During the acid leaching stage insoluble metal oxides like magnesium oxide are transformed into soluble compounds and removed by rinsing repeatedly in distilled water.

2.6.3 Simultaneous metallothermic reduction and nitriding of silica frustules

In order to initiate both metallothermic reduction and nitriding, an atmosphere of ammonia or nitrogen must be present during the metallothermic reduction.

This is usually solved by passing nitrogen or ammonia through the reactor in conventional nitriding, however gas flow is high and the residence times are long, causing high gas consumption and increased costs [104].

Ammonia can however be prepared by the decomposition of ammonium chloride upon heating, yielding ammonia and hydrochloric acid. The decomposition of ammonium chloride takes place at temperatures above 338°C [94]. The decomposition of ammonium chloride and formation of ammonia and gaseous hydrochloric acid occurs according to:



$$\Delta G_{Rx} = -70.421 \text{ kJ/mol at } 650^\circ\text{C [68]}$$

$$\Delta G_{Rx} = -105.826 \text{ kJ/mol at } 800^\circ\text{C [68]}$$

To remove gaseous hydrochloric acid a reaction with calcium oxide or excess magnesium can be utilized, yielding relatively pure ammonia [94].

The reaction between ammonium chloride and calcium oxide goes according to:



$$\Delta G_{R_x} = -238.308 \text{ kJ/mol at } 650^\circ\text{C [68]}$$

$$\Delta G_{R_x} = -277.205 \text{ kJ/mol at } 650^\circ\text{C [68]}$$

Should the previous reaction occur at temperatures above the decomposition temperature of calcium hydroxide (580°C), the formation of ammonia will be accompanied by calcium oxide and water vapor formation according to [43]:



$$\Delta G_{R_x} = -254.815 \text{ kJ/mol at } 650^\circ\text{C [68]}$$

$$\Delta G_{R_x} = -310.321 \text{ kJ/mol at } 800^\circ\text{C [68]}$$

The reaction between ammonium chloride and magnesium forming ammonia under heating goes according to:



$$\Delta G_{R_x} = -437.153 \text{ kJ/mol at } 650^\circ\text{C [68]}$$

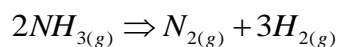
$$\Delta G_{R_x} = -486.126 \text{ kJ/mol at } 800^\circ\text{C [68]}$$

The above reactions must occur within a confined space in the case of nitriding and with a stoichiometric excess of ammonia for the nitride synthesis [94, 105]. Should the synthesis be performed without the use of calcium oxide then the consumption of magnesium to form magnesium chloride must be compensated for by adding more magnesium.

Ammonia is generally considered to be an efficient nitriding agent, the suggested mechanism behind this action is considered to be the dissociation of ammonia to nitrogen and hydrogen at metal gas interfaces [106, 107].

The dissociation of ammonia is thermodynamically feasible at temperatures above 458 K (184.85°C), but is due to kinetic stability only thermally activated at temperatures above 823 K (549.85°C) [106].

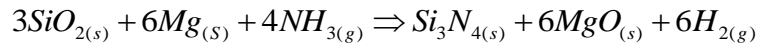
The dissociation of ammonia goes according to:



$$\Delta G_{R_x} = -105.334 \text{ kJ/mol at } 650^\circ\text{C [68]}$$

$$\Delta G_{R_x} = -140.291 \text{ kJ/mol at } 800^\circ\text{C [68]}$$

The simultaneous metallothermic reduction and nitride synthesis reaction at 650 and 800°C may be expressed as:

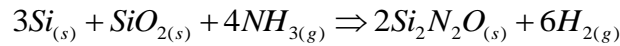


$$\Delta G_{R_x} = -1471.527 \text{ kJ/mol at } 650^\circ\text{C [68]}$$

$$\Delta G_{R_x} = -1459.050 \text{ kJ/mol at } 800^\circ\text{C [68]}$$

Some side reactions may occur, these are: formation of silicon oxynitride, formation of magnesium nitride which consumes magnesium and ammonia, decomposition of magnesium nitride by water, decomposition of magnesium nitride by heating and formation of magnesium oxide by reaction with water. The side reactions listed for magnesiothermic reduction are also likely to occur. These reactions may be expressed as:

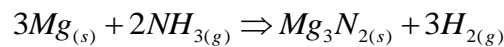
Formation of silicon oxynitride [108]:



$$\Delta G_{R_x} = -712.759 \text{ kJ/mol at } 650^\circ\text{C [68]}$$

$$\Delta G_{R_x} = -725.110 \text{ kJ/mol at } 800^\circ\text{C [68]}$$

The formation of magnesium nitride from ammonia and magnesium metal:

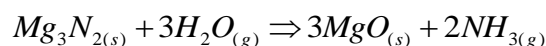


$$\Delta G_{R_x} = -380.391 \text{ kJ/mol at } 650^\circ\text{C [68]}$$

$$\Delta G_{R_x} = -380.814 \text{ kJ/mol at } 800^\circ\text{C [68]}$$

It should be mentioned that there is a possibility of magnesium nitride enhancing the synthesis of silicon nitride by forming reactive intermediates [109]. Should magnesium nitride come in contact with water vapor it will hydrolyze and form magnesium oxide and ammonia [110]. This reaction goes very fast as is indicated by the large negative Gibbs energy of reaction. Magnesium nitride becomes unstable and decomposes above 800°C [43].

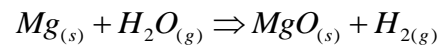
The hydrolysis of magnesium nitride goes according to:



$$\Delta G_{R_x} = -535.876 \text{ kJ/mol at } 650^\circ\text{C [68]}$$

$$\Delta G_{R_x} = -508.254 \text{ kJ/mol at } 800^\circ\text{C [68]}$$

In the case of water vapor reacting with magnesium metal and liberating hydrogen, the reaction can be expressed as:



$$\Delta G_{R_x} = -305.423 \text{ kJ/mol at } 650^\circ\text{C [68]}$$

$$\Delta G_{R_x} = -296.356 \text{ kJ/mol at } 800^\circ\text{C [68]}$$

Oxidation of formed silicon by water vapor will be avoided by using an excess of magnesium reductant according to the above reaction.

3 Experimental/method

3.1 Materials

In Table 1 the equipment used during the experimental parts of this master's thesis are listed, details of their use are given in the subchapters of the procedure.

Table 1 Equipment

Equipment	Notes/type
Scanning Electron Microscope (SEM)	LVFESEM, Zeiss Supra 55 VP
Carbon coating unit	Agar Turbo Carbon Coater, Type 203C
Energy Dispersive X-Ray Spectrometer (EDS/EDX)	EDAX Advanced Microanalysis Solutions
Stainless steel reactor chambers	Made to specifications by author
Inert atmosphere glove box	Unilab M-Braun
Muffle furnace	Bulten Kanthal Super
Fume hood	Kilab
Analytical Scale	Sartorius CP 324 S
Raman spectroscope	Horiba Jobin Yvon HR800UV
Fluorescence microscope	Zeiss axio imager Z2
Photoluminescence Spectrometer	Horiba Jobin Yvon iHR 550

The various reactants used in this master's thesis are listed in Table 2 along with a short description.

Table 2 Reactants/materials

Material/reactant	Purity	Producer
Magnesium powder	< 99 %	Merck
Frustules (<i>Coscinodiscus</i> sp.)/ (<i>Coscinodiscus wailesii</i>)	-	NTNU Dept. of Biotechnology
Hydrochloric acid	37 %	Merck
Argon gas	99.999 %	Yara Praxair
Calcium oxide	99 %	Merck
Yttrium (III) chloride	99.99 %	Sigma-Aldrich
Erbium (III) chloride	99.9 %	Sigma-Aldrich
Manganese (II) chloride	< 99 %	Sigma-Aldrich
Zinc chloride	99.999 %	Sigma-Aldrich
Acetonitrile	99.8 %	Sigma-Aldrich
Ethylene glycol	< 99 %	Sigma-Aldrich
Acetone	< 98 %	Merck
Ammonium chloride	99.5 %	Sigma-Aldrich
Ethanol	absolute	Arcus

3.2 Procedure

Descriptions of the various experimental and characterization procedures are given in the following subchapters.

3.2.1 Experimental flowchart

An overview of the various steps of the experimental work is laid out in the experimental flowchart given in Figure 16.

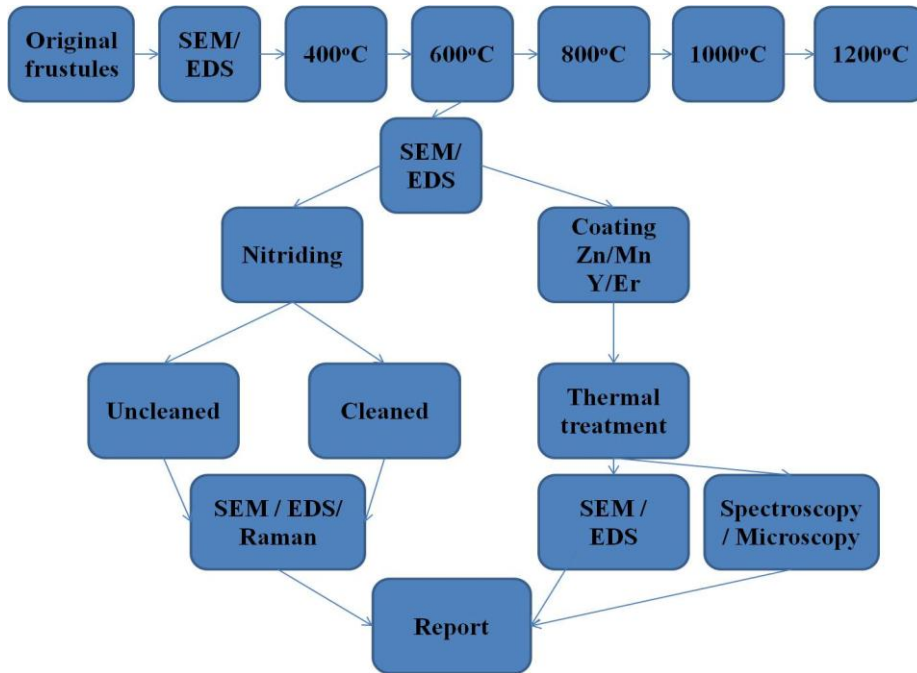


Figure 16 Experimental flowchart

According to the experimental flowchart in Figure 16, the temperature exposure characterization gives the baseline temperature which limits the temperatures at which the remaining experiments are performed. This temperature is determined by comparison of temperature exposed frustules with original frustules, important structural and chemical information are acquired by use of scanning electron microscope (SEM) and energy dispersive x-ray spectroscopy (EDS).

For coated frustules, a thermal treatment step, forming oxides, was performed prior to analysis by use of SEM and EDS. Photoluminescence spectroscopy and fluorescence microscopy gave information on photoluminescent properties of the coated frustules. Frustules subjected to nitriding was characterized in cleaned and un-cleaned form by use of SEM and EDS. Nitrided frustules featuring promising chemical composition in EDS were later analyzed by use of Raman spectroscopy.

All results were then presented and discussed in the following report.

3.2.2 Sample acquisition and preparation

All samples of frustules used during the experimental work in this master's thesis were acquired at NTNU Department of Biotechnology, here the algae had been grown in an enriched seawater medium which was supplied the desired amount of light, nutrients and aeration by compressed air, ensuring optimum growth conditions. The frustules used in all experimental work during this master's thesis were of the species *Coscinodiscus wailesii* and *Coscinodiscus* sp.



Figure 17 Frustules on stainless steel grid

The silica frustules were separated from the organic constituents of the diatom by use of nitric and sulphuric acid as well as hydrogen peroxide. The chemical treatment causes proteins in the girdlebands of the frustules to dissolve, separating the frustules into two halves. Frustules as appearing after being transferred to a stainless steel grid are illustrated in Figure 17.

Other methods of cleaning involve treating diatoms with SDS (sodium dodecyl sulphate) and EDTA (ethylenediaminetetraacetic acid), EDTA being an enzyme inhibitor of metal dependant enzymes and SDS a potent surfactant. The action of SDS and EDTA will dissolve almost all organic components of the cell but will leave proteins in the girdlebands intact and hence cause the frustules to stay in one piece.

Frustules samples acquired for this thesis were found to have damages to the frustules structures and in many cases the frustules units were found to have delaminated into girdleband and valve structures. Pore structures were found to be intact. These features were observed by use of scanning electron microscope since the frustules are so small that they are only observed as white particles to the naked eye.

Post cleaning and centrifugal separation the frustules were stored in methanol (-21°C).

3.2.3 Temperature exposure

Samples of frustules were transferred to a stainless steel grid by use of a pipette. The stainless steel grid was then placed in a ceramic crucible and placed in a muffle furnace. The muffle furnace was then heated to a temperature of 400°C and the frustules were left at this temperature for 1 hour before being extracted and allowed to cool. This procedure was repeated at increments of 200°C to a maximum temperature of 1200°C.

In order to characterize the various micro and nanostructures post heat treatment, the scanning electron microscope (SEM) was used. Characterization by use of scanning electron microscope has been used in several reports encountered in literature and appears to be a convenient technique [11, 18, 22, 111].

A scanning electron microscope featuring on board detectors and software for energy dispersive x-ray spectroscopy (EDS) allows rather precise information (500-5000 ppm) on the elemental composition of the sample, making the SEM an even more attractive tool for characterisation [112].

The temperature where signs of melting or deformation of the frustules pore structures was observed. Was set as a maximum temperature and was not to be exceeded in following experiments.

3.2.4 Coating of frustules with up-converting oxides

Cleaned frustules was placed on a pre-weighed stainless steel grid and then placed in a muffle furnace for annealing (600°C, 20 min.) before being cooled down to room temperature. This was done to ensure complete removal of all organic components.

Erbium (III) chloride was substituted in a 1:1 molar relationship with the Erbium (III) chloride used in the original report of Lee et al. The amount of yttrium (III) chloride used was identical with the original report [18].

A stock solution of erbium (III) chloride (0.015 M) was prepared by carefully weighing out ErCl_3 (0.4104 g) on an analytical scale and transferred to a volumetric flask (100 ml). A solution of acetonitrile (175 ml) and ethylene glycol (325 ml) was prepared in a separate flask and the volumetric flask filled to the graduated mark with this solution. All work featuring solvents was performed in a fume hood.

A stock solution of yttrium (III) chloride (0.015 M) was prepared by weighing out YCl_3 (0.2930 g) on an analytical scale and then transferred to a volumetric flask (100 ml). The volumetric flask was then filled to the graduated mark, using the same solution of acetonitrile and ethylene glycol as above.

After filling the volumetric flasks, a stopper was placed in both bottles and the bottles swirled to ensure proper mixing. From the stock solution of ErCl_3 (0.015 M), a pipette was used to transfer a small volume (3.47 ml) of the solution to a glass bottle (100 ml).

From the stock solution of YCl_3 (0.015 M) a certain volume (85.33 ml) was transferred to the same glass bottle as used above. The bottle was then sealed and swirled to ensure proper mixing of the reactants (0.000052 moles ErCl_3 , 0.00128 moles YCl_3). This bottle was labelled Er/Y coating solution.

The cleaned and annealed frustules residing on the stainless steel grid was then dipped in the Er/Y coating solution before being placed in a clean crucible and heated in a muffle furnace (800°C, 2 hrs.) at normal atmosphere. The coating procedure was performed 1, 2 and 4 times on different samples of annealed frustules. Coated frustules was then stored in glass containers for characterization.

3.2.5 Coating of frustules with down-converting oxides

Like the previous coating procedure, cleaned frustules was placed on a stainless steel grid and annealed in a muffle furnace at normal atmosphere (600°C, 20 min.) before being cooled to room temperature, ensuring removal of organic components.

A stock solution of zinc chloride (0.015 M) was then prepared by weighing out (1.0223 g ZnCl₂) on an analytical scale and transferred to a volumetric flask (500 ml). The flask was then filled to the graduation mark using the previous made solution of acetonitrile and ethylene glycol.

A stock solution of manganese chloride (0.015 M) was prepared by weighing out (0.1888 g MnCl₂) on the same analytical scale used earlier. The chemical was then transferred to a volumetric flask (100 ml) and filled to the graduation mark with a solution of acetonitrile and ethylene glycol.

Both flasks was then sealed and swirled to ensure mixing of the contents. From the stock solution of ZnCl₂, a certain volume (173.33 ml) was transferred to a glass bottle (200 ml) by using a pipette. A certain volume of the ZnCl₂ stock solution (1.73 ml) was then transferred to the same glass bottle using a pipette.

The bottle was then sealed and swirled to ensure proper mixing of the reactants (0.0026 moles ZnCl₂, 0.000026 moles MnCl₂) after this the bottle was labelled Zn/Mn coating solution. Previously annealed frustules were then dipped in this solution before being subjected to heating at normal atmosphere in a muffle furnace on clean crucibles (800°C, 2hrs.).

This coating procedure was performed 1, 2 and 4 times on different samples of frustules. Post heat treatment, the frustules was stored in labelled glass containers for later characterization.

3.2.6 Nitriding of diatom frustules

All descriptions in the following procedure were performed using a stainless steel reactor chamber with a volume of 23.32 cm³. The reactor chamber is illustrated in Figure 18. Samples of frustules were transferred to a previously weighed stainless steel grid and placed in a preheated muffle furnace to soak (650°C, 20 min.). This was done to ensure the complete removal of methanol solvent as well as remaining organic residues surviving the original cleaning procedure.



Figure 18 Purpose built reactor chamber

The frustules were then extracted from the furnace and allowed to cool to room temperature before being weighed out on an analytical scale. The mass of frustules was recorded for later use (0.0070 g).

Calcium oxide (0.10 g) and ammonium chloride (0.05 g) was weighed out separately on an analytical scale and transferred to purpose built stainless steel reactor vessel in a glove box featuring argon atmosphere, where the ingredients were thoroughly mixed.

A bowl shaped stainless steel disc was placed on top of the previously measured chemicals. The bowl shaped disc was then filled with a pre weighed amount of magnesium powder (0.15 g). On top of the bowl shaped stainless steel disc, a hollow pedestal of stainless steel was placed and upon this pedestal the stainless steel grid featuring the dried frustules was placed.

The reactor was then fitted with a new copper ring gasket and the reactor halves sealed by use of a pipe wrench, ensuring a gas tight seal. The reactor was then placed in the glove box antechamber and transferred to the outside by vacuuming and purging of the antechamber by argon gas.

Following this, the reactor was carefully transferred to a muffle furnace and heated (20°C/min) until the desired temperature was reached (650°C and 800°C). The careful handling in transferring the reactor from glove box to furnace was done to ensure no direct contact between frustules and other reactants in the reactor.

After a residence time of 2 hours at the desired temperature level, the furnace was shut down and allowed to cool before the reactor was extracted. Upon extraction, the reactor was opened in normal atmosphere and the contents extracted.

The frustules on the stainless steel grid were then transferred to a glass beaker and cleaned by use of a solution of hydrochloric acid (1M) and ethanol. The frustules were left for 20 minutes in this cleaning solution before being rinsed repeatedly in distilled water and finally rinsed repeatedly in acetone to ensure removal of water.

After drying, the frustules were stored in labelled glass bottles before being transferred to characterization procedures.

3.3 Characterization

The following subchapters give a description of the various procedures and instruments used to characterize the frustules post experimental procedures.

3.3.1 Original frustules

Samples of the original and untreated frustules in methanol were transferred to a scanning electron microscope sample holder by use of pipette and left to evaporate to dryness. After evaporating to dryness for 10 minutes, the sample was transferred to a carbon coating unit.

The graphite rods of the carbon coating unit was sharpened and reinserted in the coating unit before vacuuming the sample chamber until the desired vacuum level was reached and the samples coated (80 A, 12 sec.). The carbon coating unit featured a rotating sample holder which ensured an even coating. Carbon coating was performed to ensure minimal problems with charging of the specimen in SEM.

The samples were then transferred to a scanning electron microscope (SEM) featuring onboard energy dispersive x-ray spectrometer (EDS) and the sample chamber evacuated until the desired vacuum was reached before acceleration voltage was switched on (7.00-15.00 keV). The carbon coated frustules were carefully characterized and the results stored for reporting.

For the EDS analysis, a higher acceleration voltage was used (15.00 keV) along with high current mode of the filament. The EDS spectra were then taken from all relevant samples and the results stored for later analysis and reporting.

After characterization, the sample chamber was pressurized to normal atmosphere before samples were extracted and the microscope shut down.

3.3.2 Frustules exposed to elevated temperatures

Frustules from the temperature exposure investigation were transferred to a carbon tape covered SEM sample holder. The sample holder was of the brass screw type fitted with an adjusting nut.

The sample holder was then placed in a carbon coater with freshly sharpened graphite rods and coated (80 A, 12 sec.). The carbon coating unit featured a rotating sample holder which ensured an even coating. This was done to ensure minimal problems with charging of the specimen.

The sample holder was then transferred to the sample chamber of the electron microscope and the sample chamber evacuated until desired vacuum was reached. The acceleration voltage was then switched on and adjusted along with other parameters of the instrument like working distance and aperture, ensuring the optimum parameters for characterization.

The frustules of the temperature exposure experiment were then characterized according to structural changes at the various temperatures. All results were saved for later analysis and comparison. Elemental analysis of the frustules was performed by use of onboard energy dispersive x-ray spectroscopy (EDS).

When performing EDS analysis, operating parameters were adjusted according to recommendations (15.00 keV, WD =10 mm and an aperture of 120 μm). After acquiring a spectrum it was quantified by the onboard EDS software, giving a chemical analysis of the investigated frustules.

After the characterization session was ended, the sample chamber was pressurized and the sample holders extracted before the microscope was shut down.

3.3.3 Frustules coated with up and down-converting oxides

Since the coated frustules were all identically characterized with respect to luminescence, structural and chemical features, a combined description of their characterization and the equipment utilized will be given in the following subchapters.

3.3.4 Characterization of coated frustules by scanning electron microscope

All frustules samples were transferred to a scanning electron microscope sample holder and fastened using carbon tape before being carbon coated (80 A, 12 sec.) using a carbon coating device. This was done to avoid charging of the specimens upon investigation in SEM.

Sample holders featuring the coated frustules were then transferred to the SEM sample chamber before the chamber was sealed and evacuated. When the desired vacuum level was attained as indicated by the onboard instruments, the acceleration voltage was turned on (4.00-10.00 keV).

A suitable specimen was then located and the structural features zoomed into. Pictures were taken at regular intervals and saved to allow later analysis and comparison between the various specimens. Chemical analysis was undertaken by use of energy dispersive x-ray spectrometer.

For the EDS analysis, a higher acceleration voltage was used (15.00 keV) along with high current mode of the filament. The EDS spectra were then taken from all relevant samples and the results stored for later analysis and reporting. At the end of the session, the system was re-pressurized and all samples extracted before the SEM was shut down.

3.3.5 Characterization of coated frustules by fluorescence microscope

Samples of the coated frustules were transferred to a microscope glass slide and mounted in the fluorescence microscope. The fluorescence microscope was then turned on and transmission mode selected. A low magnification objective lens was chosen to localize a sample. An illustration of the principle of fluorescence microscopy is given in Figure 19.

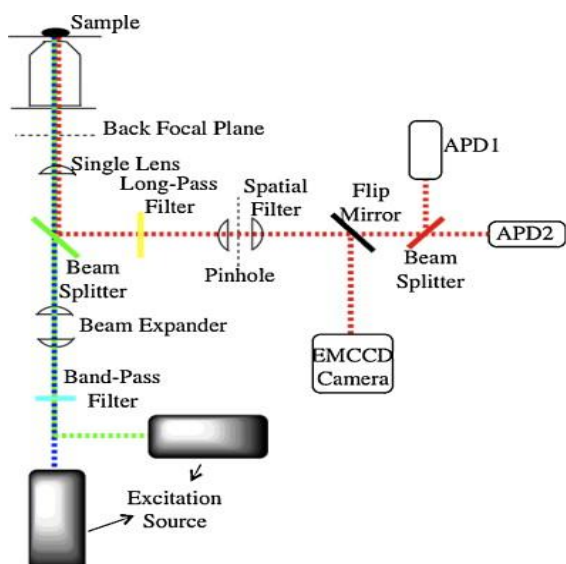


Figure 19 Fluorescence microscopy principle [113]

Having localized a sample, reflection mode was chosen and all other external light sources in the room were turned off. The specimen was then illuminated by a series of increasing wavelength light and the corresponding fluorescence images captured.

For each change in excitation light, pictures were taken to allow for later comparison between the various results. This was done for all the samples of coated frustules. After use the microscope was shut down.

3.3.6 Characterization of coated frustules by photoluminescence spectroscopy

Frustules subjected to the various coating procedures were transferred from the sample containers to microscope glass slides by immersing coated frustules in methanol and using a pipette to transfer the samples. After transfer, the methanol was allowed to evaporate.

The glass slides featuring coated frustules were then placed in the sample chamber of the photoluminescence spectroscope and the chamber sealed and elevated to correct height by adjusting the sample holder table. The laser source was activated and aligned into the spectroscope unit and a filter unit inserted in the beam pathway ($\lambda = 532 \text{ nm}$). The process of photoluminescence spectroscopy is illustrated in Figure 20.

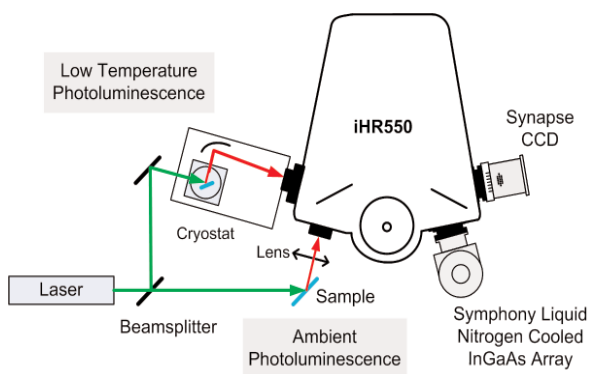


Figure 20 Photoluminescence spectroscopy [114]

A source of white light was then directed into the pathway of the beam, illuminating the sample holder chamber. A microscope lens (50X, 0.65 NA) above the sample holder chamber was adjusted until the glass slide could be detected and the sample holder table moved until a specimen was located. The lens was then focused at the sample and the white light source turned off leaving the sample illuminated by laser light.

The computer system was then adjusted to set up centre of wavelength before performing a series of scans. The power of the laser source was adjusted until a decent spectrum was acquired (10 mW). Several scans were then performed and the results stored for later use. This operation was performed for all samples.

An analysis featuring UV laser ($\lambda=325$ nm) was also attempted. This analysis required insertion of several new mirrors and lenses as well as operating the sample chamber without a lid. A different microscope lens was also used (36X, 0.5 NA). Other parts of this analysis were similar to that already described for the green laser.

3.3.7 Characterization of nitrated frustules by scanning electron microscope

Frustules from the nitrating experiments were transferred to a SEM sample holder featuring carbon tape and carbon coated (80 A, 12 sec.) before being loaded in the SEM sample chamber. The sample chamber was then evacuated until the required vacuum was reached, the acceleration voltage switched on (3.00-15.00 keV) and a proper working distance acquired (3-10 mm.).

Areas of interest were then zoomed into and pictures taken at intervals of increasing magnification, this was done in order to document both micro and nanoscale features of the nitrated frustules structures. All relevant parameters were labelled to each respective image. Every sample was also characterized by EDS. This analysis gave the elemental composition of the sample.

For the EDS analysis, the samples were investigated at two different acceleration voltages (3.00-15.00 keV) but at the same working distance (10 mm) and at high current mode. This was done in order to investigate if the nitride formation was superficial or penetrating as the acceleration voltage determines the depth of the excitation volume. Every EDS spectrum was then quantified by the onboard EDS software and saved for later comparison between the various samples.

3.3.8 Characterization of nitrated frustules by Raman spectroscopy

The frustules from the nitrating experiment were also characterized by use of Raman spectroscopy. Here a small amount of nitrated frustules were transferred from the sample container to a high purity (111) silicon wafer mounted on top of a microscope glass slide. A typical Raman spectroscopy system is illustrated in Figure 21.

The glass slide was mounted in the Raman spectroscopy sample holder along with another glass slide, featuring an identical high purity silicon (111) wafer. The other silicon wafer was kept free of any sample contamination and served as a blank sample.

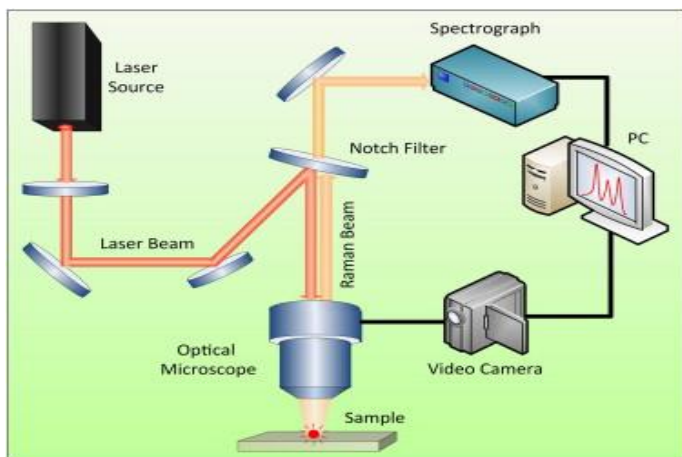


Figure 21 Typical Raman spectroscopy system [115]

In order to avoid the effects of luminescence, a UV laser ($\lambda=325$ nm.) was chosen, a 10 X objective was selected and the instrument focused at the blank silicon sample. A spectrum was acquired and the instrument adjusted according to this spectra.

The sample table was then moved over to the other silicon wafer and the instrument focused on a frustule sample. A series of spectrums were taken (10 seconds sample time and 5 acquisitions). This was repeated on several areas of each frustule and on several different samples.

All spectra were saved for later analysis, and the instrument shut down. Analysis of the spectra was done offline by comparison of the acquired spectra against known spectra of pure compounds suspected to be present in the samples.

4 Results

The results of the various experiments and characterization work are presented in the following subchapters. All results are presented along with a short description.

The results were acquired by use of scanning electron microscope (LVFESEM, Zeiss Supra 55 VP), Raman spectroscopy (Horiba Jobin Yvon HR800UV), fluorescence microscope (Zeiss axio imager Z2), photoluminescence spectroscopy (Horiba Jobin Yvon iHR 550) and energy dispersive x-ray spectrometer (EDAX Advanced Microanalysis Solutions).

4.1 Original frustules

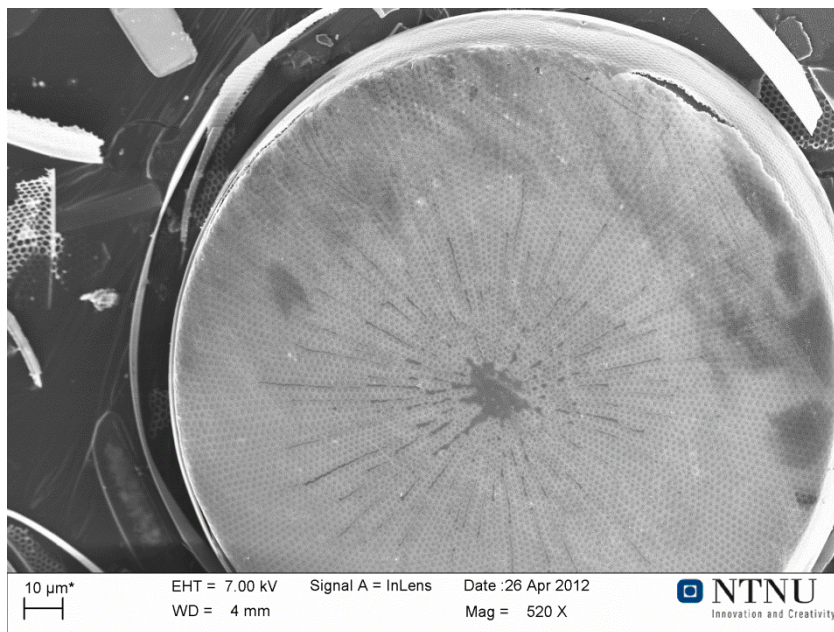


Figure 22 Original frustule

An overview image of an original frustule as appearing at low magnification in scanning electron microscope can be seen in Figure 22. The surrounding debris as well as the damage to the upper part of the structure has most likely occurred during cleaning or during transfer of the sample from container to SEM sample holder. The pores can be seen as the pattern radiating from the centre to the edges of the frustule structure.

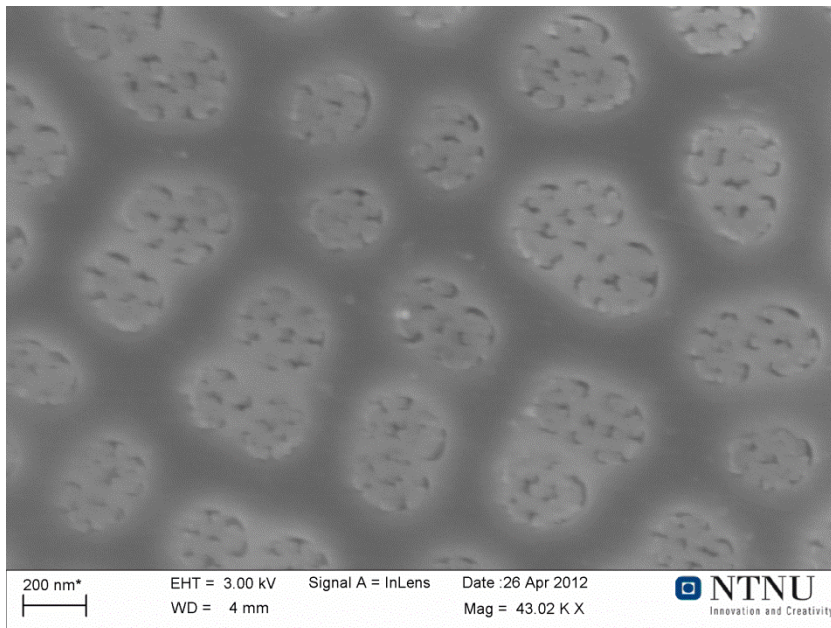


Figure 23 Original frustule pore structure

Figure 23 displays the original pore structure as appearing at higher magnification in SEM. Carbon coating was utilized to avoid charging of the specimen. The thin silica membrane termed velum appear to be intact, this membrane is penetrated by the cribellum pores which covers the larger underlying pores termed the cribrum. A schematic view of the pore structure, explaining terminology and placement is given in Figure 6, important features are also labelled in Figure 24 and Figure 25.

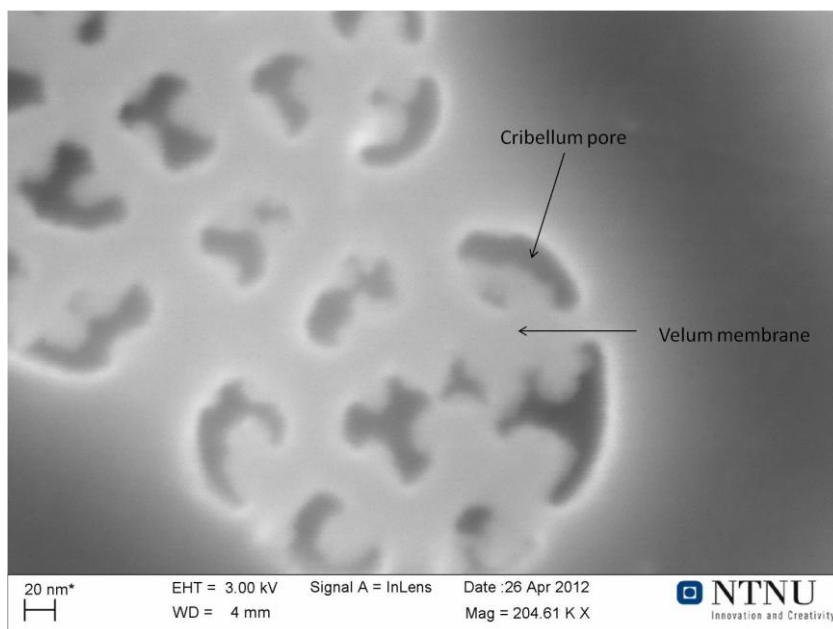


Figure 24 Structural features of the frustule pores at nanoscale

Some impressive structural features becomes visible at very high magnification, this is illustrated in Figure 24. The structural features seen in this picture belong to the cribellum pores of the outer velum membrane found in

the pore, covering the underlying cavities termed the cribrum pores. Some haziness can be seen in the picture, this may be attributed to small vibrations in the room or equipment manifesting itself in the images.

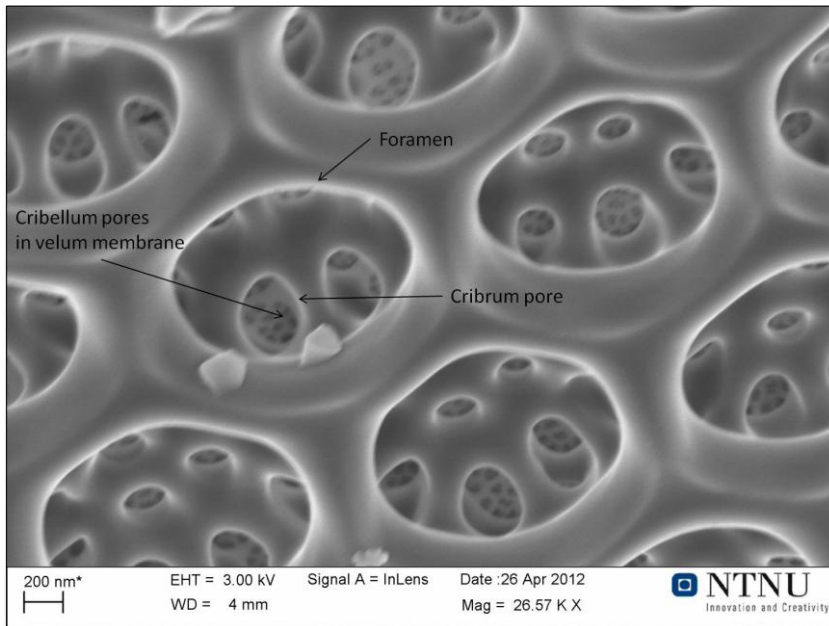


Figure 25 Original frustule pores inside view

In Figure 25 the pores of the original frustule are displayed as it would appear on the inside of the frustule looking through the large foramen opening of the areolae and onto the smaller holes of the cribrum. All the way to the back of the image some parts of the cribellum pores can be seen covering the cribrum openings, important features are labeled in the image.

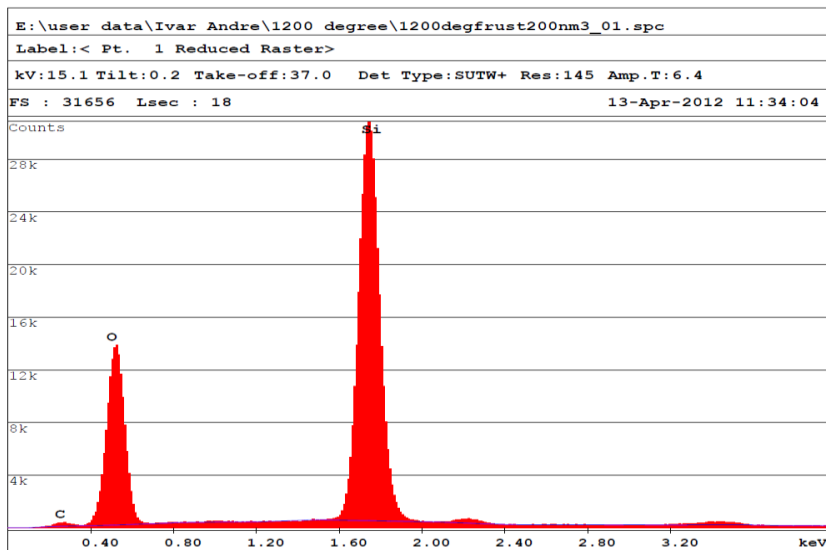


Figure 26 Typical EDS spectrum of original frustules

A typical EDS spectrum representative of original frustules is illustrated in Figure 26. Dominating peaks are identified as oxygen and silicon. A small peak representative of carbon is also detected.

Table 3 Average elemental contents of original frustules

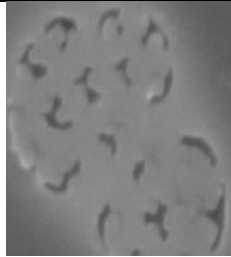
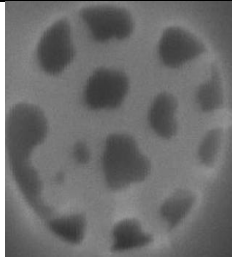
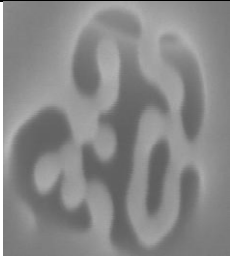
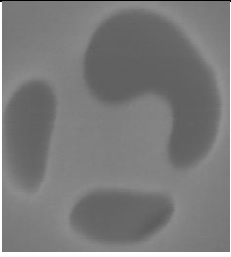
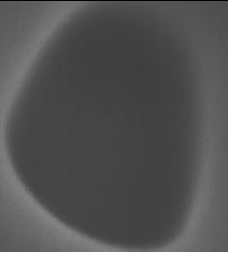
Element	Atomic %	Weight %
C K	3,61	2,21
O K	65,19	53,21
Si K	31,20	44,58
Total	100,00	100,00

The average elemental content of original frustules can be seen in Table 3. These results are based on quantified results from EDS analysis. Dominant species are silicon and oxygen and is expected being that frustules are silica structures. A small amount of carbon also exists within the sample.

4.2 Characterization of frustules exposed to various temperatures

The results of the temperature exposure characterization are summed up in Table 4, the change in size of the pore features can be clearly seen as the temperature increases. Images are taken at the same level of magnification.

Table 4 Results of the temperature exposure characterization

				
400°C	600°C	800°C	1000°C	1200°C

Small changes occur at 600°C. These changes seem to occur in the cribellum pores of the outer velum membrane. At 800°C greater structural changes occur and the velum membrane, the cribellum pores and the cribrum pores appear to be affected. When the temperature reach 1000°C, the holes of the cribrum pores shows sign of melting and appear to widen. At 1200°C no part of the cribrum remains and the pore appear to be a single large hole with surrounding edges slanting inwards.

4.2.1 Frustules exposed to 400°C for 1hour

Figure 27 displays a frustule subjected to a temperature of 400°C for 1 hour, no large structural changes attributable to heat can be detected. Pore pattern and frustule structure appear unchanged as when compared to the features of the original frustule as can be seen in Figure 22. The frustules were carbon coated to minimize problems associated with charging of the specimen.

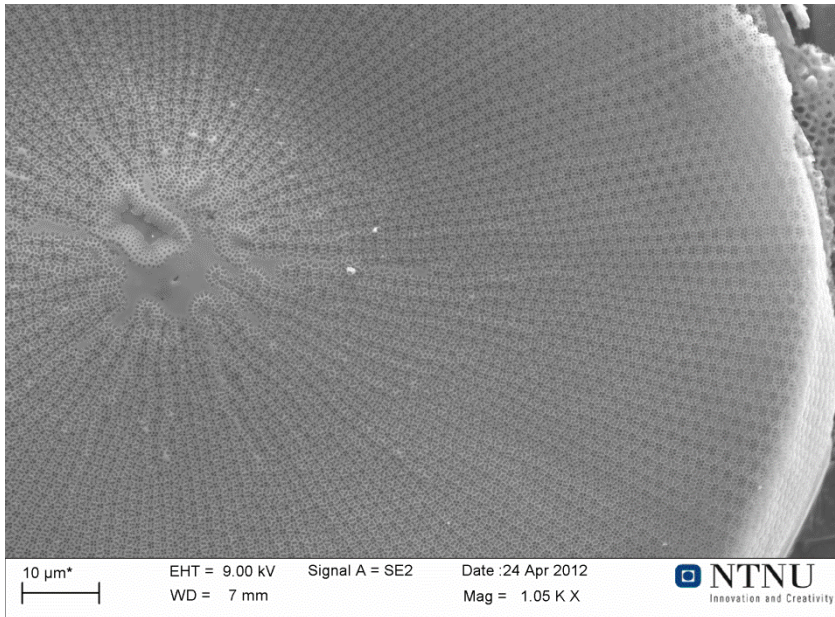


Figure 27 Frustule exposed to 400°C for 1hour

Damages to the edge of the frustule seen in Figure 27 can most likely be attributed to cleaning procedures or damage upon transfer of samples during experimental work.

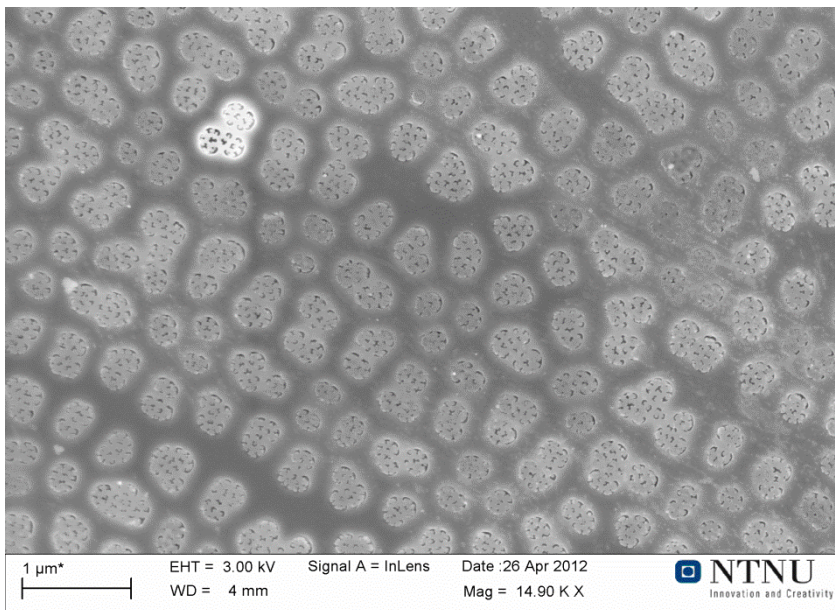


Figure 28 Frustule pores subjected to 400°C for 1 hour

In Figure 28, the corresponding pore structure of the frustule displayed in Figure 27 is shown. The bright area of the frustule pores can be attributed to charging of the specimen. Pore structures appear intact, and nanoscale features of the pores can be seen in Figure 29.

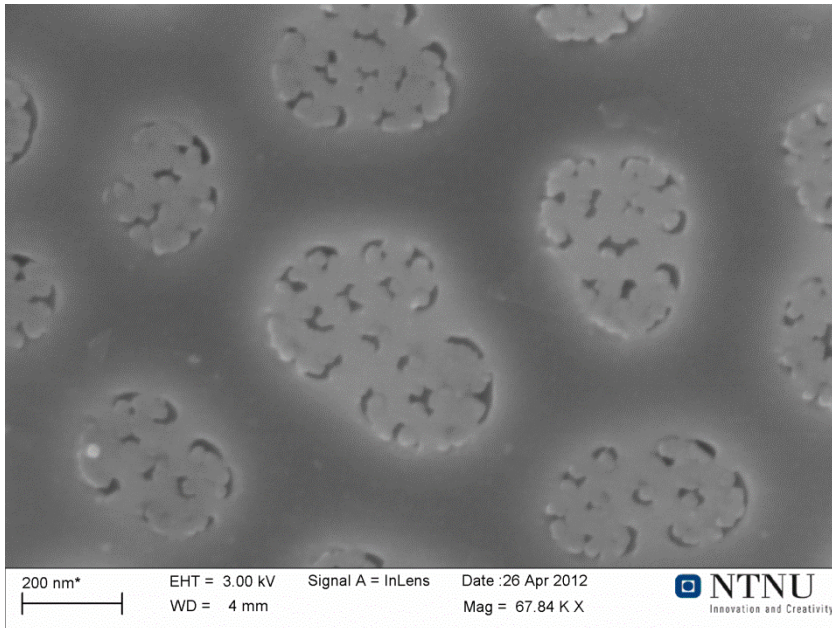


Figure 29 Frustule pores subjected to 400°C for 1 h at nanoscale

In Figure 29 the pores of a frustule subjected to thermal exposure at 400°C is displayed. The picture is taken at high magnification and shows the cribellum pores of the velum membrane to be intact when comparing with the pictures of an original frustule in Figure 23. These structures are all the way to the back of the image.

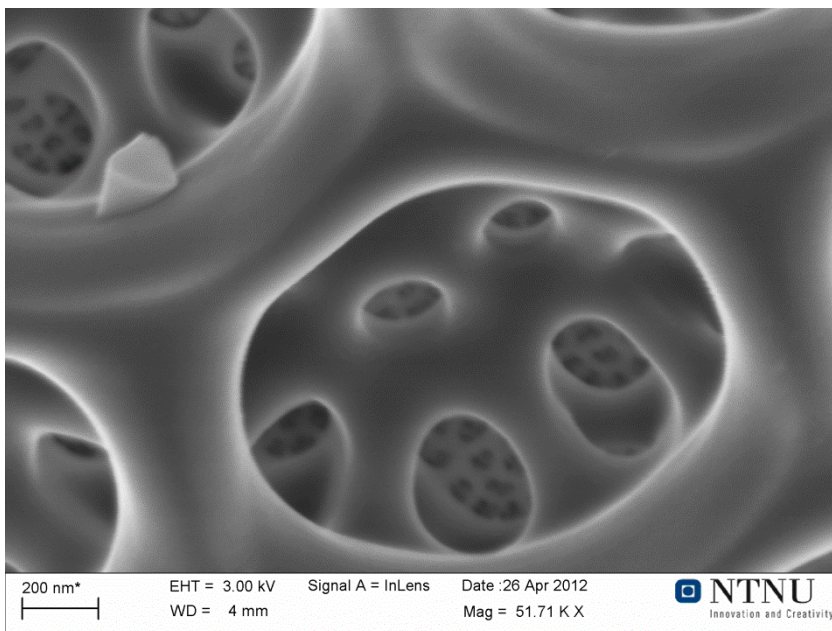


Figure 30 Frustule pores subjected to 400°C for 1h, inside view

Figure 30 displays the structural features as viewed from the inside of the frustule trough the foramen opening in the areolae and towards the cribrum openings of the pores. Bright areas arise as a consequence of charging of the specimen. Nanoscale features appear intact and the cribellum pores of the velum membrane structure can be seen to the rear of the image.

4.2.2 Frustules exposed to 600°C for 1hour

A frustule being subjected to 600°C for 1hour is displayed in Figure 31. The frustule appears to be structurally intact upon comparison with original frustules. The surrounding debris is remains of destroyed frustules and parts of girdleband structures seem to be the dominant species. Carbon coating of the sample was utilized in an attempt to minimize problems related to charging of the specimen.

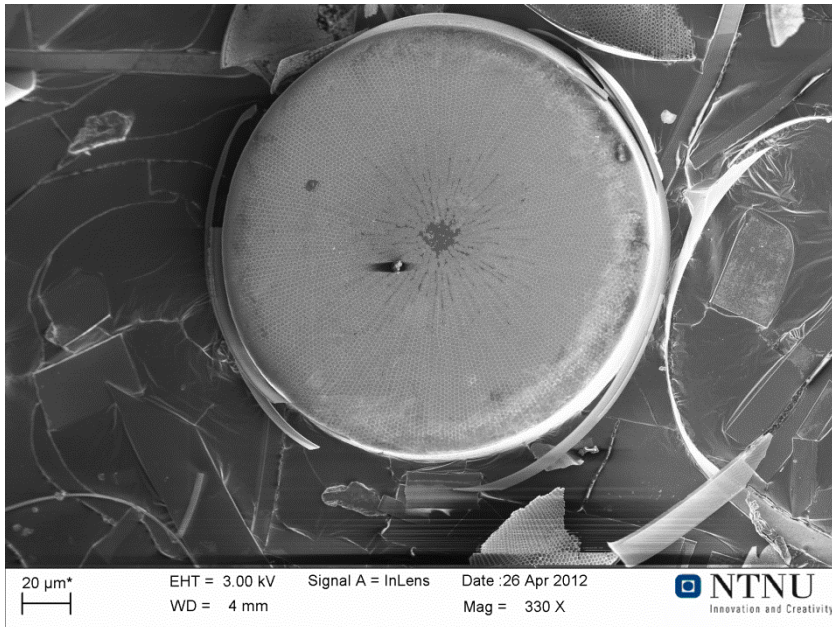


Figure 31 Frustule subjected to 600°C for 1h

The destruction leading to the debris seen in Figure 31 may have arisen both from cleaning procedures as well as sample transfers when performing experimental procedures. Small bright streaks in the lower part of the image are most likely caused by charging of the specimen.

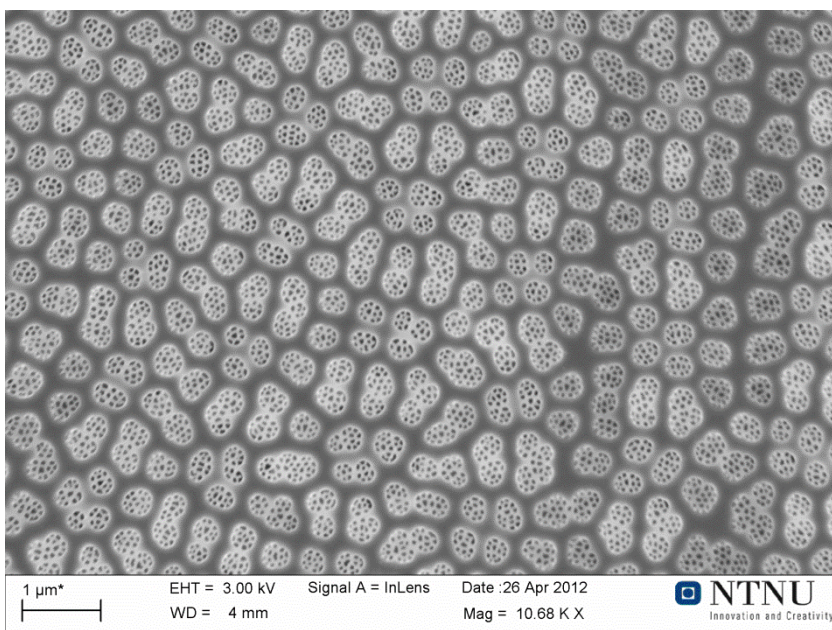


Figure 32 Frustule pores subjected to 600°C for 1h

The pores of a frustule subjected to thermal exposure at 600°C for 1 hour are displayed in Figure 32. Some effects of charging of the specimen may be seen as overly bright areas of the image. Pore structures appear to be more open as when compared to that of the original frustules seen in Figure 23.

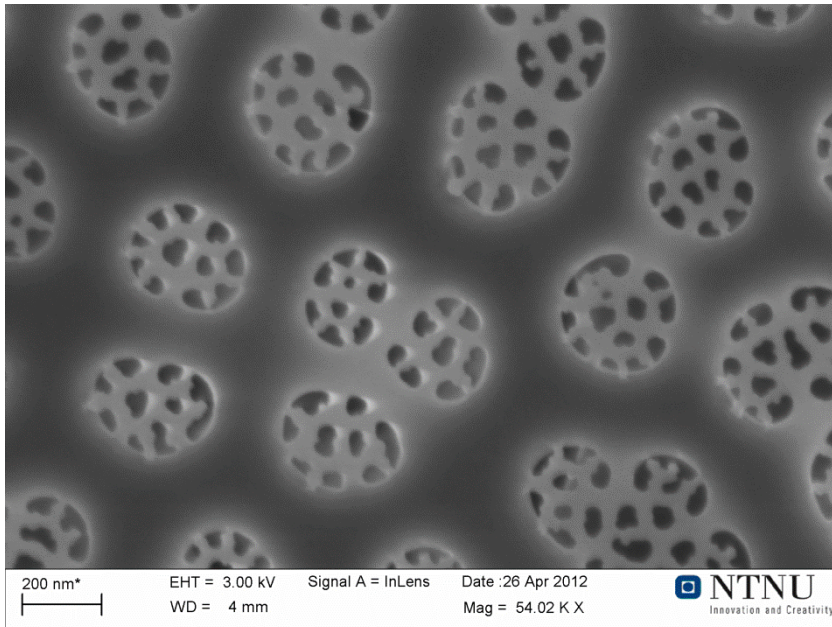


Figure 33 Frustule pores subjected to 600°C for 1h at nanoscale

The pore structures of frustules subjected to thermal exposure for one hour are shown at high magnification in Figure 33. Nanoscale features are still present as when compared to the original frustules seen in Figure 23.

Cribellum pores and velum membrane previously covering the pores seem to have disappeared to some extent, leaving more of the cribrum pores visible. Appearances of small jagged structures around the pores are possible remains of melted velum membrane.

Signs of charging can be observed around the edges of the pores appearing as overly bright areas.

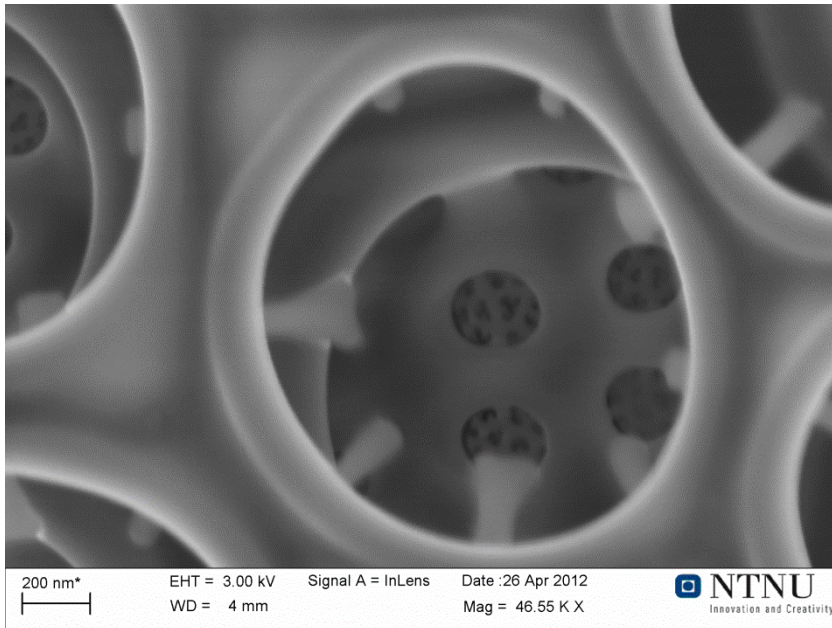


Figure 34 Frustule pores subjected to 600 for 1h, inside view

The pore structure as viewed from the inside through the foramen opening of the areola towards the holes of the cribrum can be seen in Figure 34. Some of the cribellum pores associated with the velum membrane covering these holes can be seen towards the rear of the image.

Minor changes in structure can be seen as when compared to frustules exposed to 400°C illustrated in Figure 30. In this picture there appears to be a delaminated part of a valve featuring the foramen openings placed in front of the original valve of the frustule giving the illusion of a very deep structure.

4.2.3 Frustules exposed to 800°C for 1hour

An overview image of a frustule subjected to thermal exposure at 800°C for one hour can be seen in Figure 35. No structural changes can be seen at this magnification. The pattern of pores can be seen radiating outwards from the centre of the frustule to the edge. The frustules were carbon coated in order to minimize problems related to charging of the specimen.

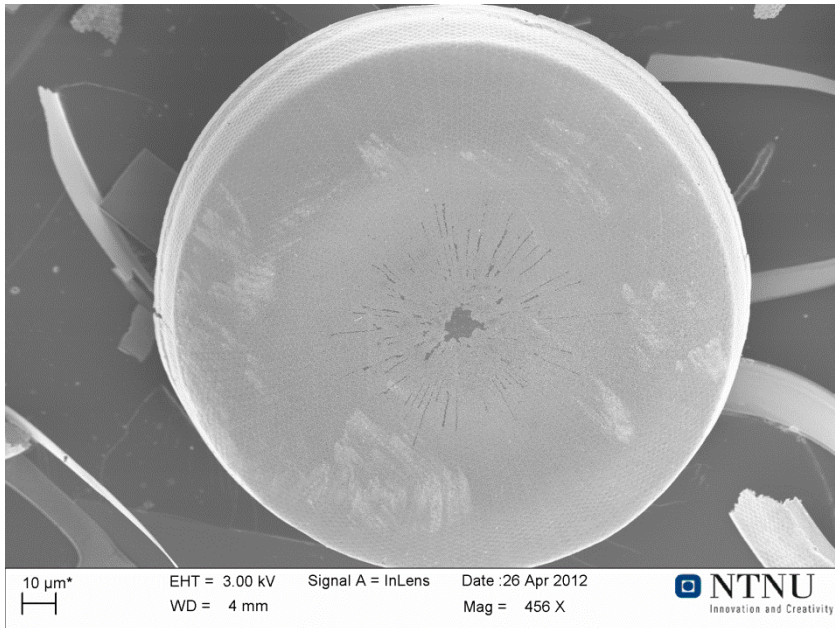


Figure 35 Frustule subjected to 800°C for 1h

As with other pictures, some debris is seen surrounding the frustule. This debris appears to be remains of girdleband structures of destroyed frustules. Parts of a valve can be seen in the lower right corner. Some signs of charging can be seen as bright areas on the frustule valve structure.

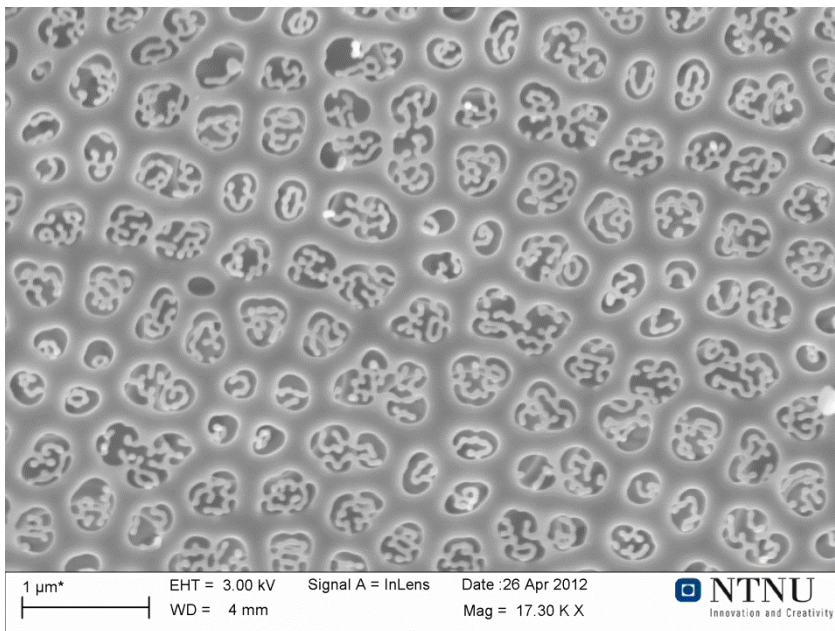


Figure 36 Frustule pores subjected to 800°C for 1h

Frustule pores subjected to 800°C for one hour can be seen in Figure 36. Changes in the pore structures can clearly be seen as when compared to pores of frustules exposed to temperatures of 400°C and 600°C displayed in Figure 28 and Figure 32 respectively.

The changes appear to be related to severe melting of the cribellum pores and associated velum membrane which results in more of the cribrum pores to become visible. Twisted structures seen inside the cribrum pores are thus likely remains of melted cribellum pores and velum membrane.

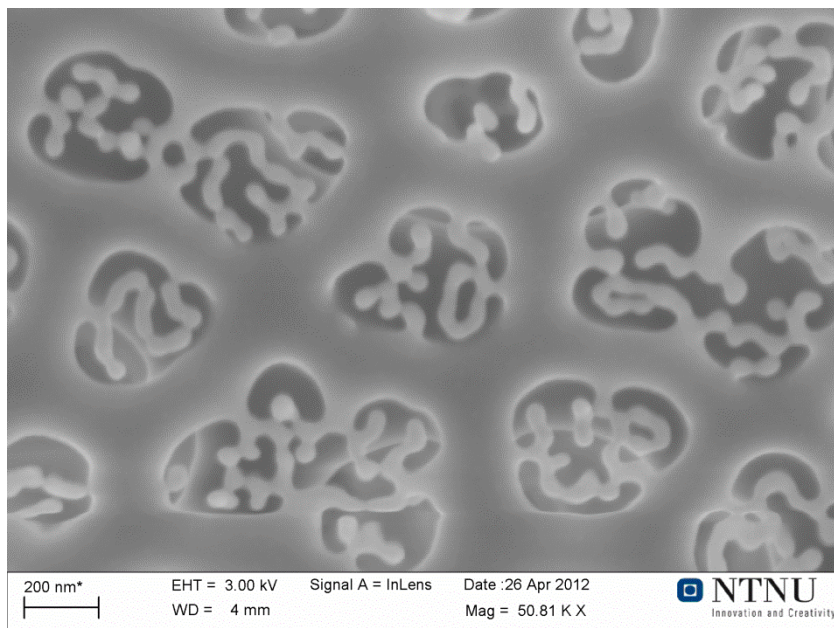


Figure 37 Frustule pores subjected to 800°C for 1h at nanoscale

Figure 37 displays frustule pore structures subjected to 800°C for one hour at high magnification. A clear reduction in nanoscale features can be detected when compared to pores exposed to lower temperatures as can be seen in Figure 29 and Figure 33.

This is likely the result of the cribellum pores and velum membrane melting, revealing more of the underlying cribrum openings in the pores. The cribrum structure can be seen just beneath the twisted structures in the top openings of the pores. Twisted structures are as mentioned earlier probably melted remains of the outermost cribellum pores and velum membrane.

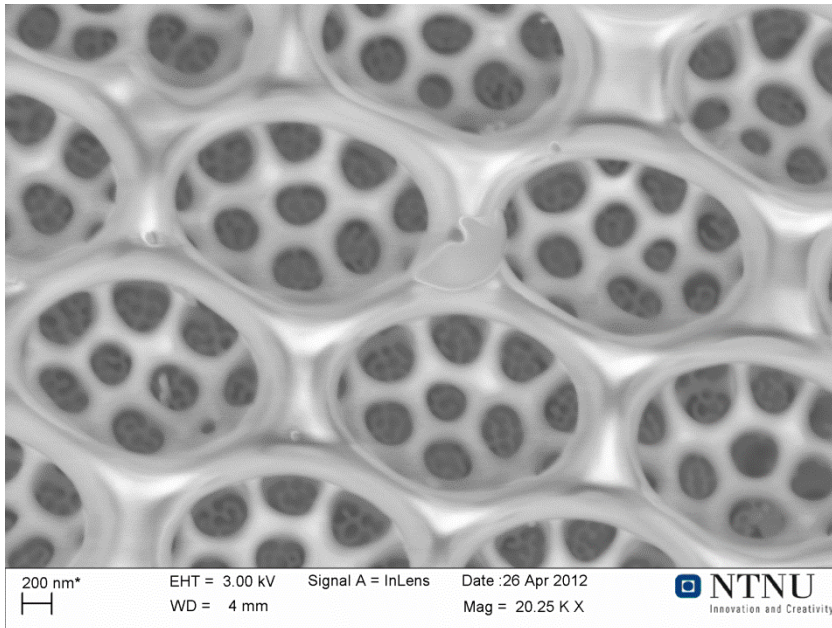


Figure 38 Frustule pores subjected to 800°C for 1h, inside view

An inside view of the frustule exposed to 800°C for one hour, can be seen in Figure 38. Point of view is through the foramen openings in the areolae and towards the cribrum openings of the pores. Remains of the cribellum pores and velum membrane can also here be seen towards the rear of the image. Severe structural changes can be detected when comparing this image to Figure 30 and Figure 34.

4.2.4 Frustules exposed to 1000°C for 1hour

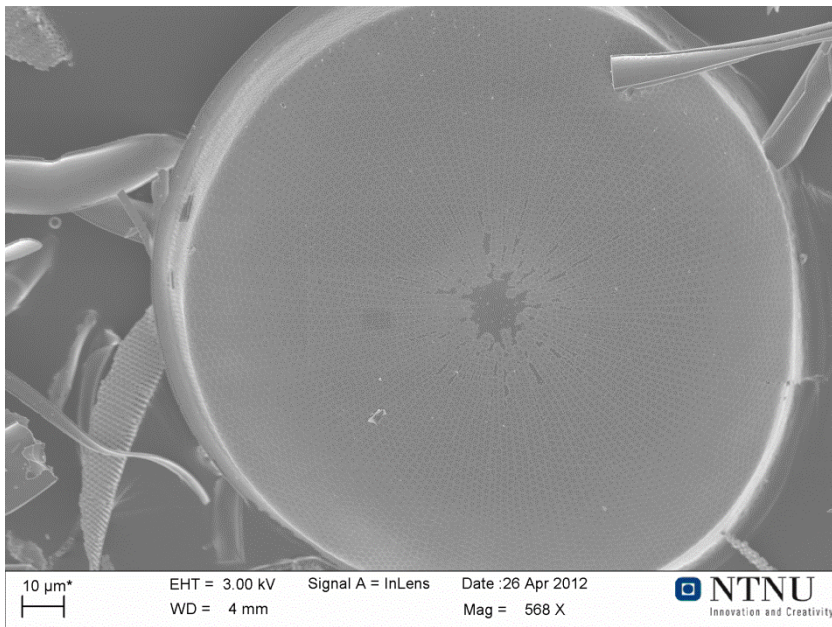


Figure 39 Frustule subjected to 1000°C for 1h

An overview image of a frustule exposed to a temperature of 1000°C for one hour can be seen in Figure 39. A slight elongation of the entire frustule structure can be detected, indicating severe structural changes. Debris surrounding the frustule appears to be a mixture of girdleband structures and parts of valve structures. Some of the debris originating from girdlebands seems slightly deformed.

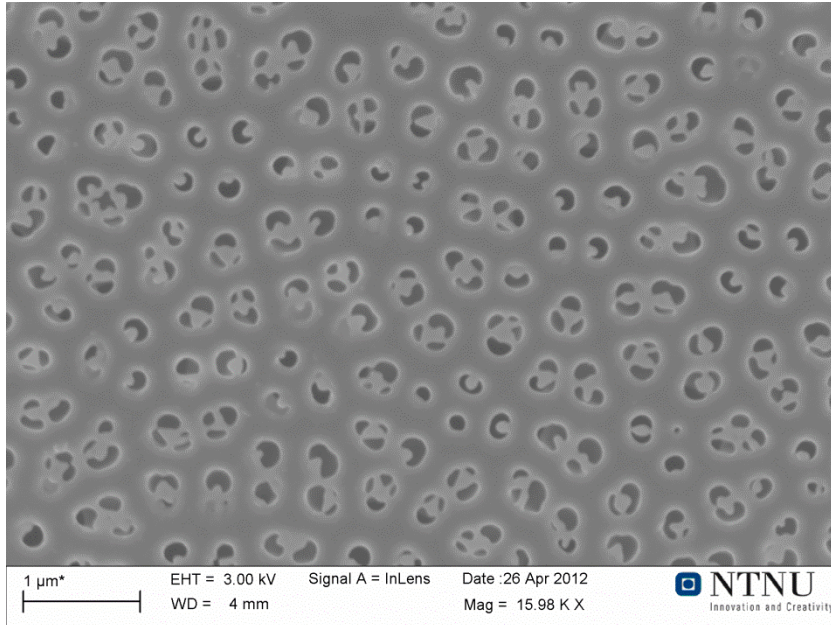


Figure 40 Frustule pore structure subjected to 1000°C for 1h

The corresponding pores of the frustule in Figure 39 can be seen at greater magnification in Figure 40. Severe changes in pore structures are detected as when compared to the frustules exposed to lower temperatures seen in Figure 29 and Figure 32. The changes are presumably a result of the cribellum pores and velum membrane melting severely and exposing the underlying cribrum openings.

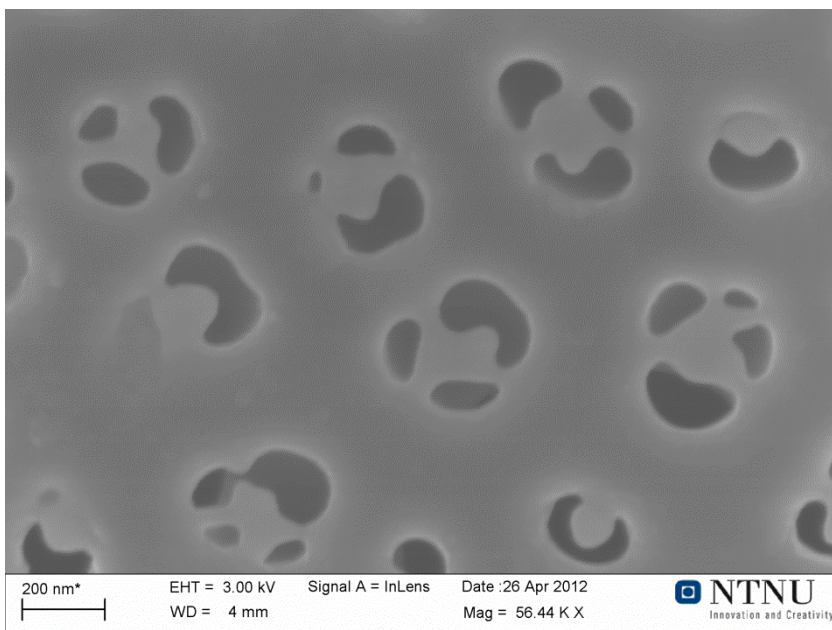


Figure 41 Frustule pores subjected to 1000°C for 1h at nanoscale

The pore structures of Figure 40 can be seen at high magnification in Figure 41, most of the intricate nanoscale structural features previously observed at lower temperatures are melted. Globular protrusions in the sides of the cribrum openings are likely the melted remains of the cribellum pores and velum membrane.

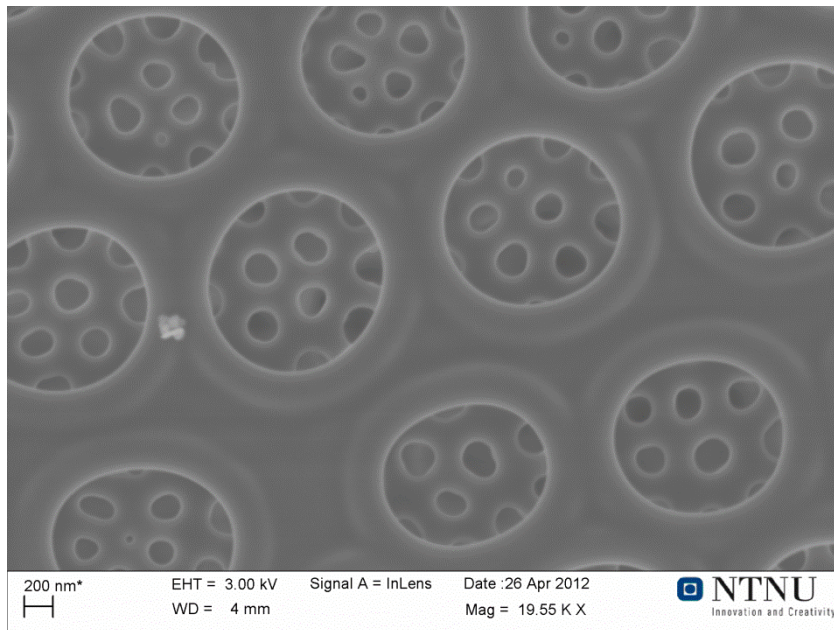


Figure 42 Frustule pores subjected to 1000°C for 1h, inside view

An inside view of the frustule is given in Figure 42. The point of view is through the foramen of the areola and towards the cribrum openings. No cribellum pores or velum membrane structure can be seen towards the rear of the structure and the cribrum openings appear slightly deformed.

The lack of depth in the image as when compared to the inside views presented at lower temperatures (Figure 30 and Figure 34) is probably caused by melting of the frustules structure.

4.2.5 Frustules exposed to 1200°C for 1hour

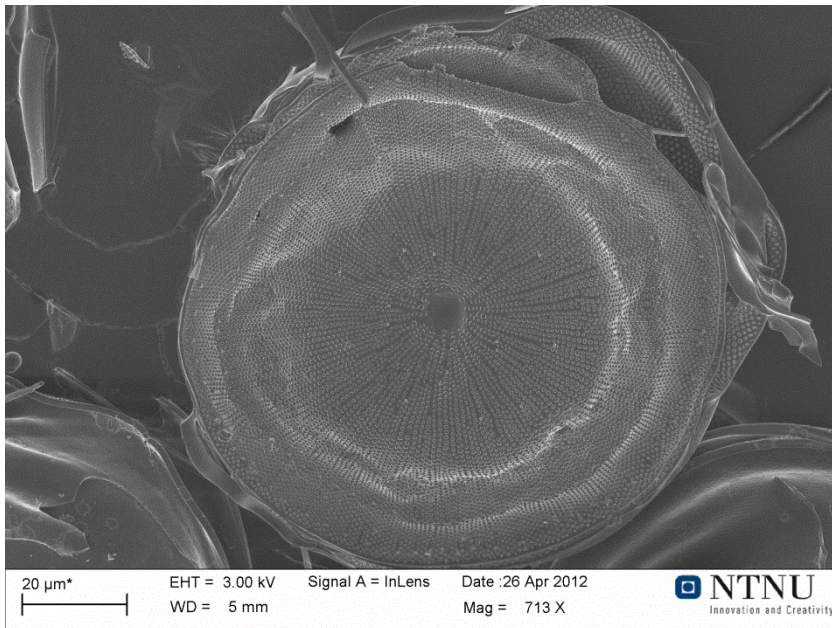


Figure 43 Frustule subjected to 1200°C for 1h

An overview image of a frustule subjected to 1200°C for one hour can be seen in Figure 43. The entire frustule valve structure has adopted a wavy surface and the circumference of the frustules appears asymmetric upon comparison with original frustules. A large gap in the upper right part of the frustule might indicate that the entire structure has delaminated and slid apart under heating. Surrounding debris appears wavy and deformed.

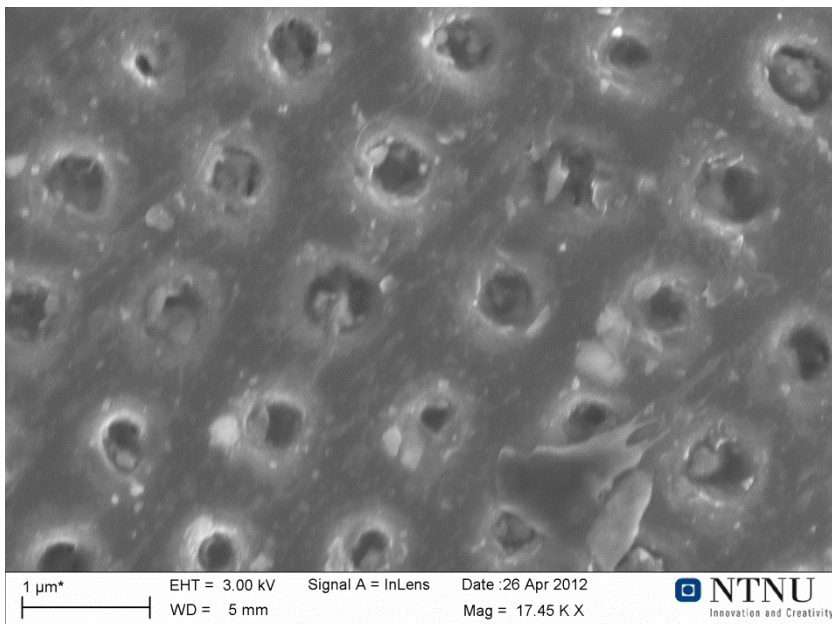


Figure 44 Frustule pore structure subjected to 1200°C for 1h

The corresponding pores of the frustule displayed in Figure 43 can be seen in Figure 44. No structural features of the cribellum pores, velum membrane or the cribrum openings can be discerned within the remains of the pores.

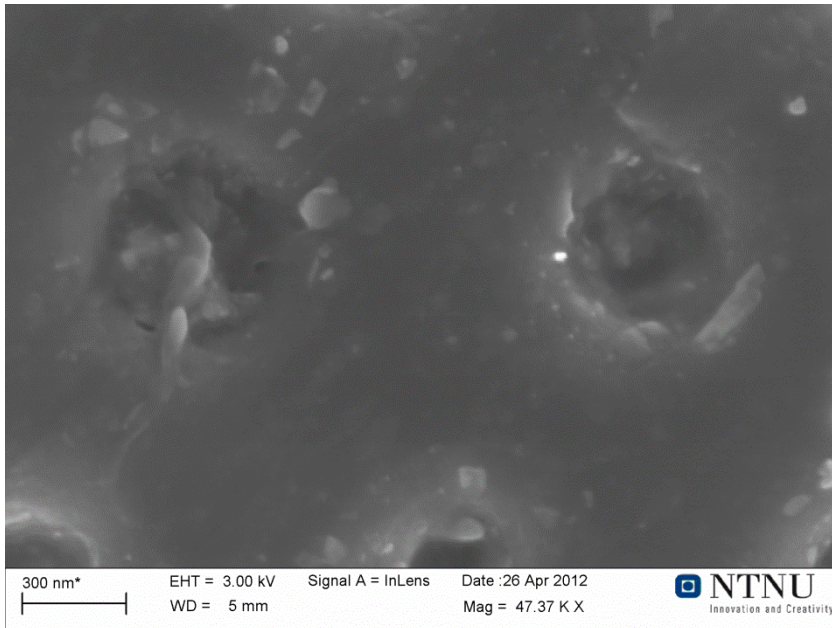


Figure 45 Frustule pores subjected to 1200°C for 1h at nanoscale

A close up view of remaining pore structures at nanoscale is given in Figure 45. No remaining parts of the cribellum pores or velum membrane can be seen. The cribrum openings appear to have collapsed and fused together, in effect closing the entire pore. Edges surrounding the pores slant towards the opening.

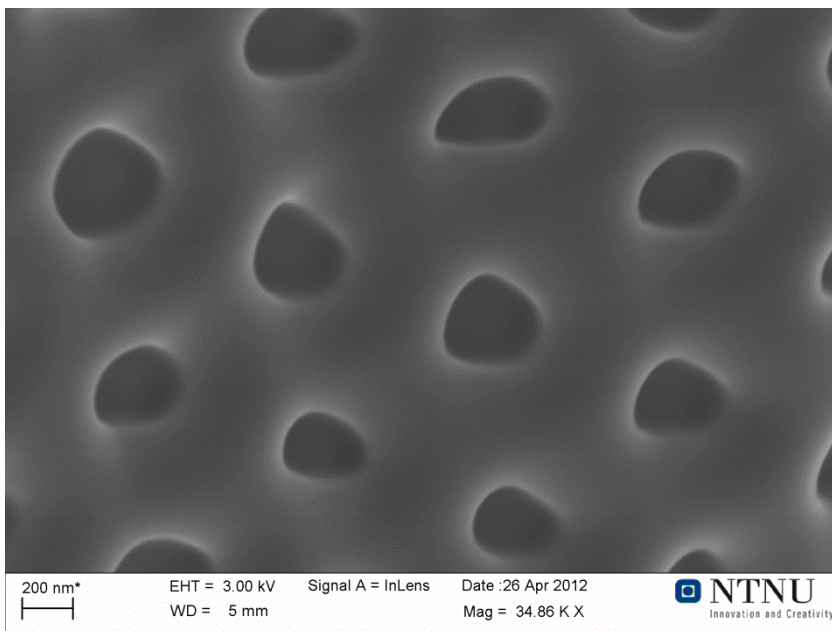


Figure 46 Frustule subjected to 1200°C for 1h, inside view

The inside view of the frustules exposed to 1200°C for one hour is displayed in Figure 46. Point of view is through the foramen opening of the areola. The remaining structure appears to be the foramen. The elevated ridge previously surrounding these openings has seemingly melted and flowed into the cavity. Much like the external pore features, internal pore features have disappeared. The comparison between inside views of pores at lower temperatures versus the current view can be illustrated by comparing Figure 30 with the current figure.

4.3 Characterization of frustules coated with up converting oxides

After coating the frustules with a solution of the desired elements and annealing, the samples were investigated by use of scanning electron microscope (SEM), energy dispersive x-ray spectrometer (EDS), fluorescence microscope and photoluminescence spectroscopy.

4.3.1 Frustules coated once with Er^{3+} doped Y_2SiO_5 featuring SEM and EDS

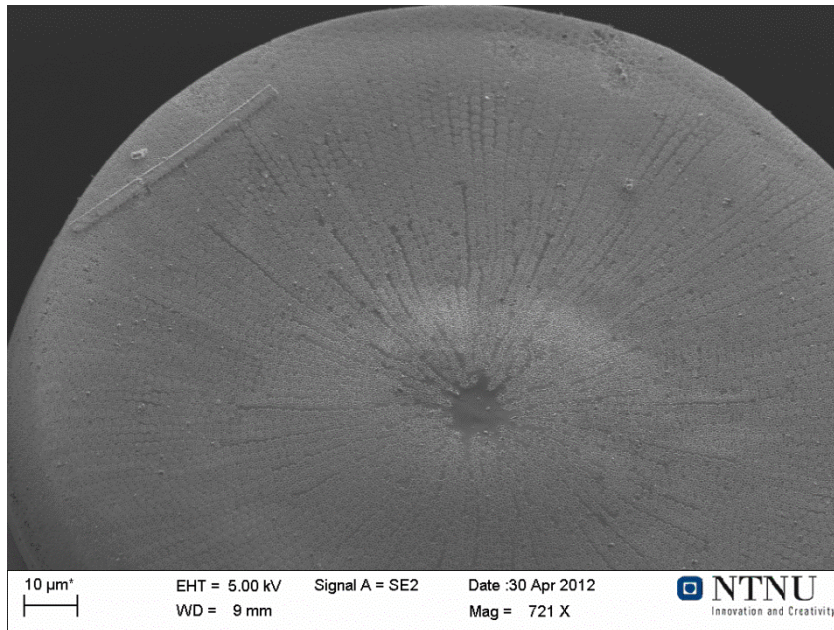


Figure 47 Frustule coated once with Y/Er

An overview picture of a frustule subjected to one coating cycle with Er^{3+} doped Y_2SiO_5 is shown in Figure 47. Structural features of the frustule appear unchanged as when compared to that of original frustules.

The pore pattern can be seen radiating from the centre of the structure towards the extremities. No apparent damages can be seen. In the upper left corner of the frustule a piece of girdleband structure is lying on top of the frustule surface.

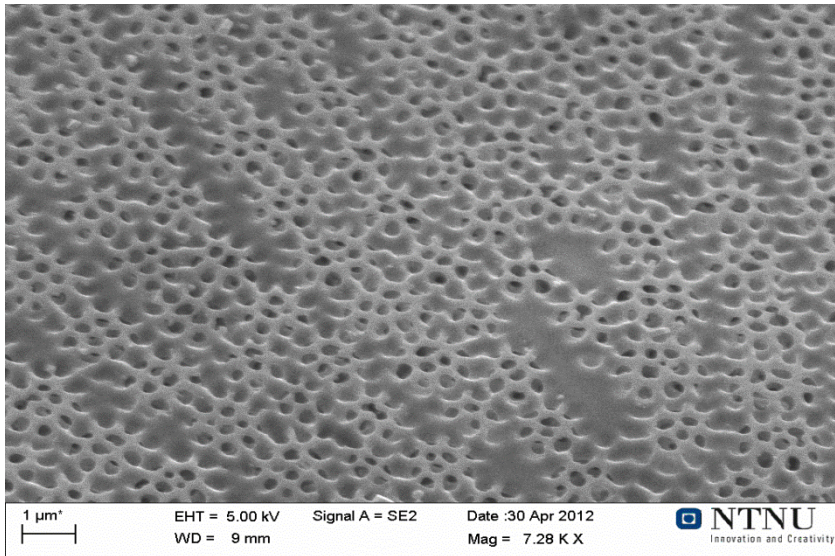


Figure 48 Frustule coated 1X with Y/Er

The structural features of a frustule coated once with Er^{3+} doped Y_2SiO_5 is illustrated in Figure 48. The main features of the surface appear to be the cribellum pores of the velum membrane and the underlying cribrum cavities. The periodic pattern of the pores can be seen radiating from the lower right corner to the upper left corner of the image. The frustules were carbon coated to avoid problems related to charging of the specimen.

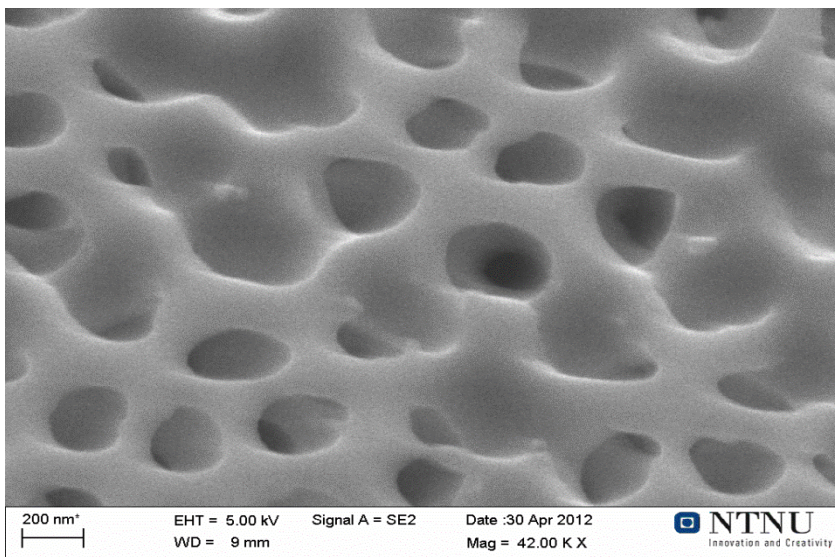


Figure 49 Frustule coated 1X with Y/Er at nanoscale

Figure 49 illustrates the surface features of the frustule at high magnification. At this level of magnification it can clearly be seen that the cribellum pores of the velum membrane are the dominant structural features. Just beneath the cribellum pores, the cavities of the cribrum can be seen. It should be noted that the velum membrane appears less dense as when compared to that of original frustules seen in Figure 23. The cribellum pores and velum membrane still seems more structurally intact than that of frustules just heat treated at the corresponding temperature of 800°C .

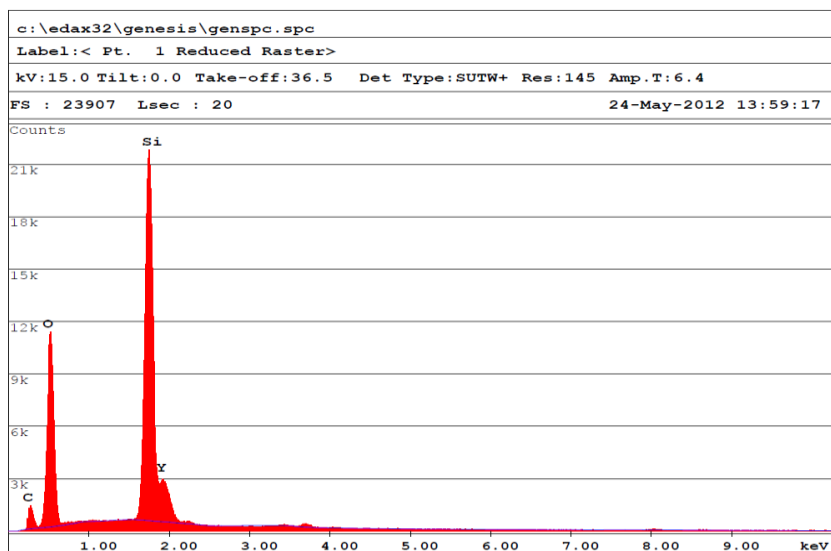


Figure 50 EDS spectrum of (1X) Y/Er coated frustule

An EDS spectrum of a frustule subjected to one coating cycle of Er^{3+} doped Y_2SiO_5 can be seen in Figure 50. The average elemental content of once coated frustules resulting from EDS quantification can be seen in Table 5. The peak representative of yttrium has a small area indicating a low concentration of the element. Erbium cannot be detected, probably due to very low initial concentration.

Table 5 Average elemental content of 1X coated frustules

Element	Atomic %	Weight %
C K	36,25	24,46
O K	43,16	38,13
Si K	18,94	29,37
Y L	1,65	8,03
Mo L	0,00	0,00
Total	100,00	100,00

Average quantified EDS results from the analysis of frustules coated once with Er^{3+} doped Y_2SiO_5 are illustrated in Table 5. As expected from the EDS spectrum, the concentration of yttrium was found to be low. The high concentration of carbon can be attributed to the carbon coating. No chlorine can be detected, meaning the halides have decomposed.

4.3.2 Frustules coated twice with Er^{3+} doped Y_2SiO_5 featuring SEM and EDS

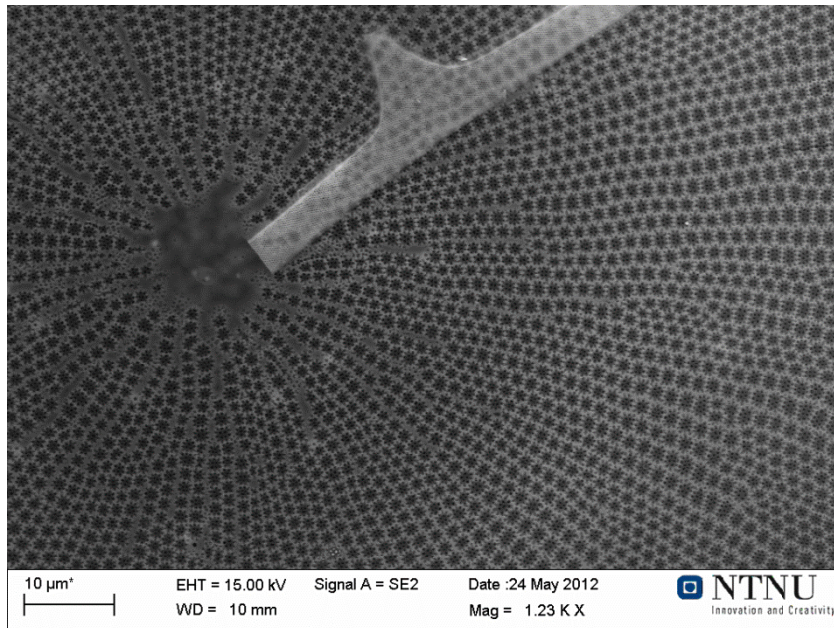


Figure 51 Frustule coated twice with Y/Er

An overview image of a frustule coated twice with Er^{3+} doped Y_2SiO_5 is given in Figure 51. The frustule appears structurally intact and no apparent damages can be seen. A thin piece of girdleband structure can be seen on top.

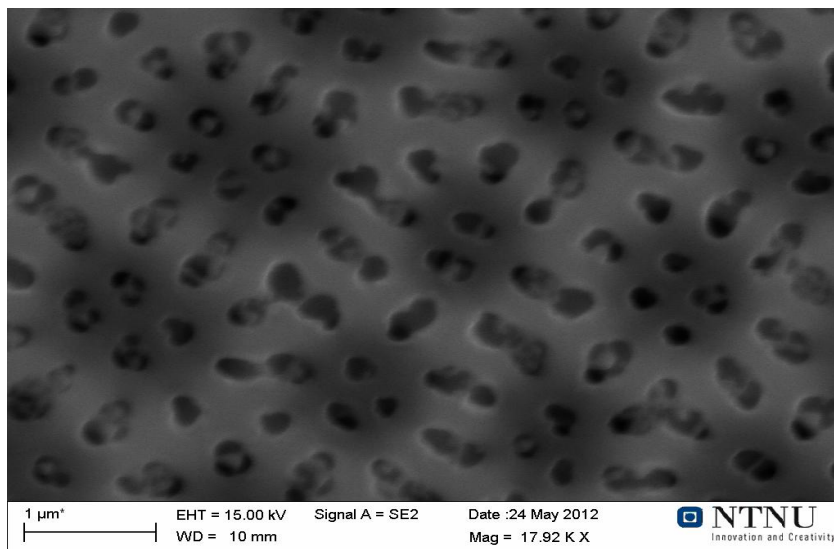


Figure 52 Frustule coated 2X with Y/Er

In Figure 52, the pore structures of a frustule coated 2 times in a solution of yttrium and erbium chlorides in acetonitrile and ethylene glycol can be seen. Picture is taken by SEM and post annealing at 800°C . The frustule is carbon coated to avoid problems related to charging of the specimen. Some bright areas can however be seen around the edges of the pore structures, indicating that some charging still occurs. Dominant features appear to be the cribellum pores of the outer velum membrane and underlying cribrum cavities of the pores.

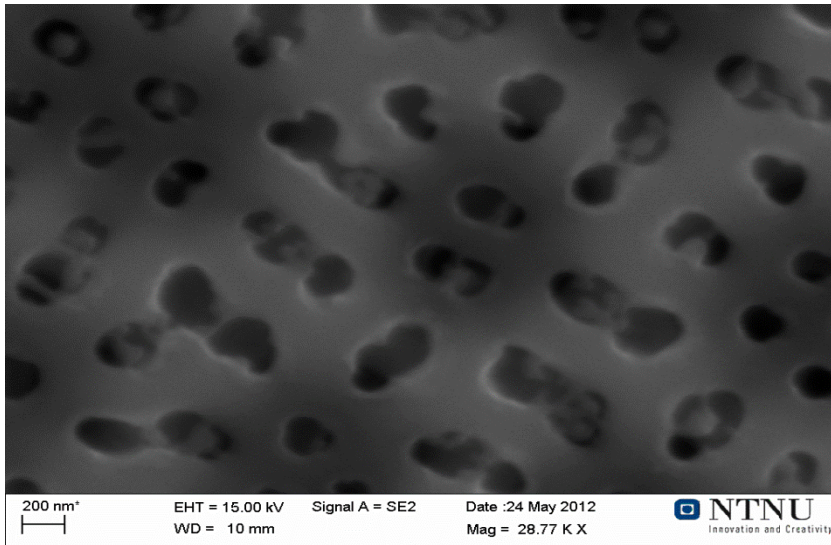


Figure 53 Frustules coated 2X with Y/Er at nanoscale

The frustule displayed in Figure 53 illustrates the surface structures of a frustule twice coated with Er^{3+} doped Y_2SiO_5 , at high magnification. Some melted parts of the cribellum pores and velum membrane can be seen remaining in and around the edges of the cribrum cavities. Surfaces of twice coated frustules appear to suffer greater structural changes than frustules coated once, this can be seen by comparing Figure 53 with Figure 49.

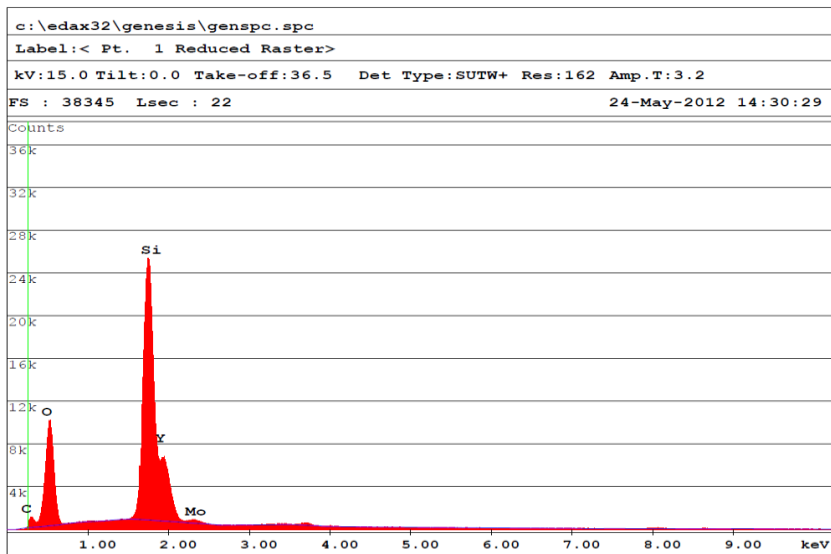


Figure 54 Typical EDS spectrum of (2X) Y/Er coated frustule

A typical EDS spectrum acquired from a twice coated frustule is illustrated in Figure 54 the corresponding list of quantified elements is displayed in Table 6. The area of the yttrium peak has increased markedly when comparing the current EDS spectrum to that of the frustules only subjected to one coating cycle. Erbium cannot be detected, likely due to only being present in very low concentrations. A peak representative of molybdenum (Mo) can be detected. This is likely a contaminant from the stainless steel grid.

Table 6 Average elemental content of (2X) Y/Er coated frustules

Element	Atomic %	Weight %
C K	19,81	11,00
O K	50,96	36,79
Si K	23,72	30,16
Y L	5,10	20,35
Mo L	0,41	1,70
Total	100,00	100,00

Average quantified EDS results from the analysis of frustules coated twice with Er^{3+} doped Y_2SiO_5 can be seen in Table 6. Yttrium concentration has increased as when compared against frustules coated only once, this can be seen by comparing with the quantified EDS results of frustules coated once. Carbon can be attributed to the carbon coating to avoid charging. A presence of molybdenum is detected. This element should not exist in the sample and is as stated earlier likely a contaminant originating from the stainless steel support grid during heat treatment.

4.3.3 Frustules coated four times by Er^{3+} doped Y_2SiO_5 featuring SEM and EDS

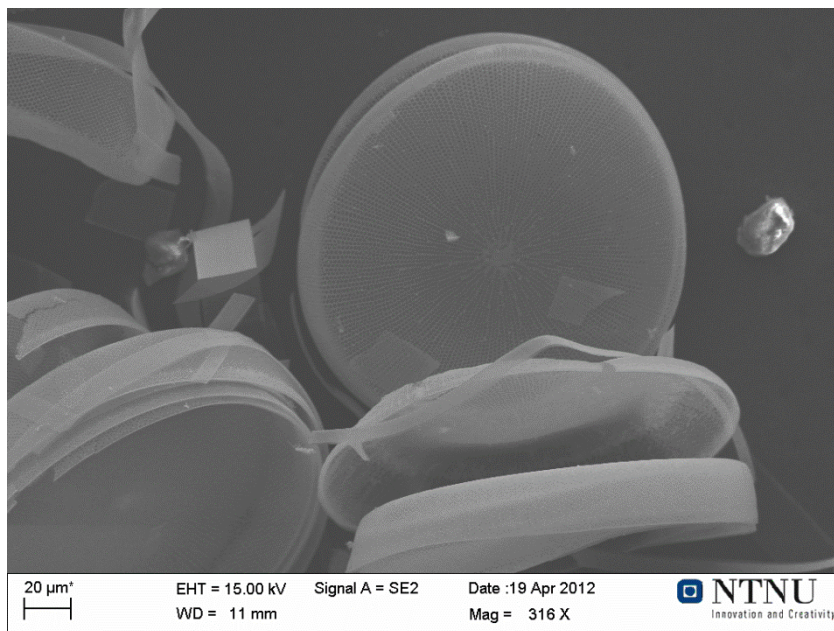


Figure 55 Frustules coated four times with Y/Er

Frustules that have been coated four times with Er^{3+} doped Y_2SiO_5 can be seen in Figure 55. Many of the frustules have delaminated and separated into smaller units like girdleband structures and epi and hypo valves. The pore pattern is clearly visible in the centre frustule. Large solid looking debris on the sides of the centre frustule appears to be parts of the stainless steel grid used during heat treatment.

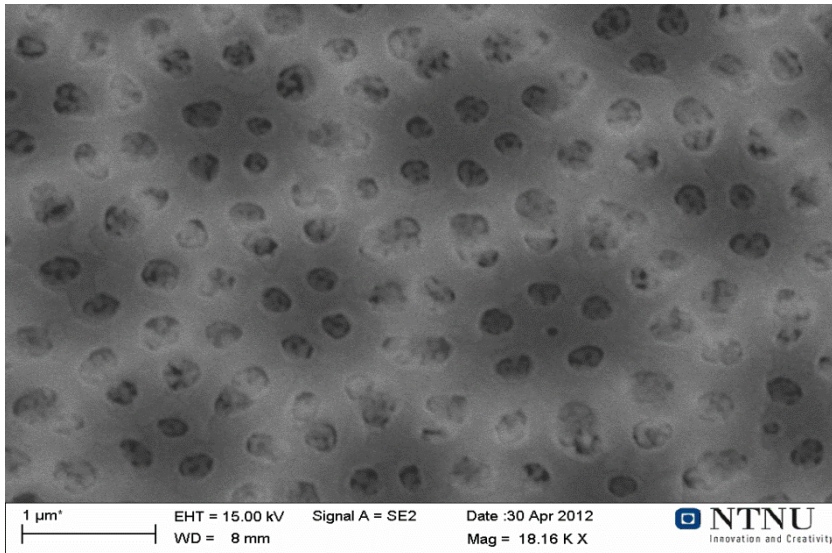


Figure 56 Frustule coated 4X with Y/Er

A frustule that has been subjected to four coating cycles with Er^{3+} doped Y_2SiO_5 is displayed in Figure 56. What appear to be cribellum pores and velum membrane seem to be well conserved. The frustule is carbon coated to avoid charging related problems, what appears to be a hexagonal array of brighter areas might still be signs of charging.

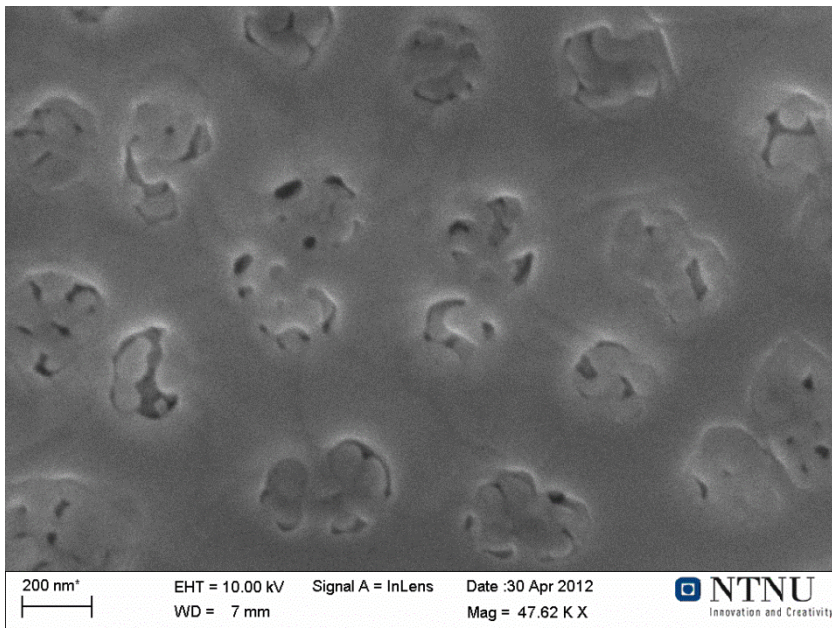


Figure 57 Frustule coated 4X with Y/Er at nanoscale

The frustule subjected to four coating cycles of Er^{3+} doped Y_2SiO_5 is zoomed into at high magnification in Figure 57. The pore structures appear to be remarkably well conserved upon comparison with original frustules.

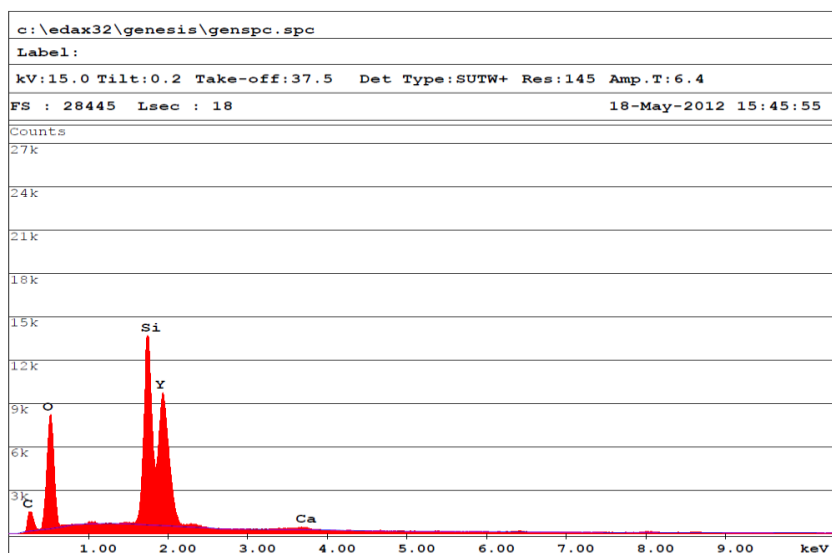


Figure 58 Typical EDS spectrum of (4X) Y/Er coated frustule

An example on a typical EDS spectrum acquired by analysis of a frustule coated four times with erbium doped yttrium (III) oxide is illustrated in Figure 58. The corresponding quantitative results of the EDS analysis are given in Table 7. The area of the yttrium peak is significantly larger than comparative results of frustules subjected to a lower number of coating cycles. This can be seen by comparing the current spectrum with spectrums in Figure 50 and Figure 54. A small peak representative of calcium (Ca) is detected, this element is a contaminant.

Table 7 Average elemental content of (4X) Y/Er coated frustules

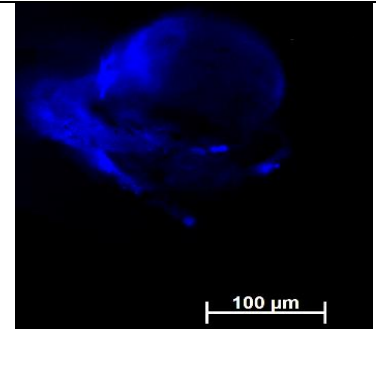
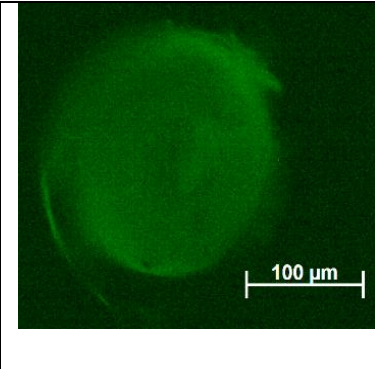
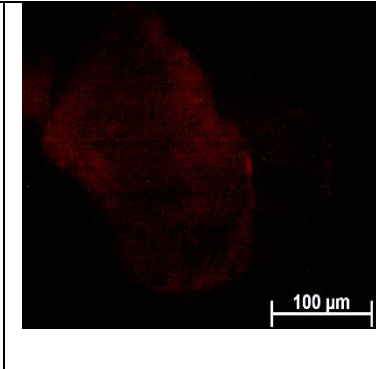
Element	Atomic %	Weight %
C K	30,17	15,44
O K	46,29	31,54
Si K	13,61	16,28
Y L	9,54	36,07
Ca K	0,39	0,67
Total	100,00	100,00

The yttrium content of frustules subjected to four coating cycles is as expected highest when compared to frustules subjected to fewer cycles. The presence of calcium is most likely a result of impurities in the volumetric glassware used to transfer chemicals or a contaminant existing in the frustules. A rather strong concentration of carbon can attributed to the carbon layer coating the frustules to avoid charging.

4.3.4 Er³⁺ doped Y₂SiO₅ coated frustules characterized by fluorescence microscopy

The results from the investigation of Er³⁺ doped Y₂SiO₅ coated frustules is given in Table 8. These results are from the frustules that were subjected to four coating cycles. Frustules subjected to a lesser number of coatings failed to display fluorescent properties.

Table 8 Results of the fluorescence microscope analysis of Er³⁺ doped Y₂SiO₅ coated frustules

		
Excitation = 365 nm Emission = 445-450 nm Filter set 43	Excitation = 440-475 nm Emission = 530-550 nm Filer set 44	Excitation = 630-640 nm Emission = 650-690 nm Filer set 50

According to the results displayed in Table 8, the strongest fluorescence is in the blue region of the spectrum. The blue fluorescence is a result of excitation with light in the ultraviolet region of the electromagnetic region. Some fluorescence can also be seen in the green region of the spectrum and is the consequence of excitation with light in the blue region. The red fluorescence appears to be very weak and is the result of excitation with light in the yellow region of the electromagnetic spectrum.

4.3.5 Er³⁺ doped Y₂SiO₅ coated frustules characterization by photoluminescence spectroscopy

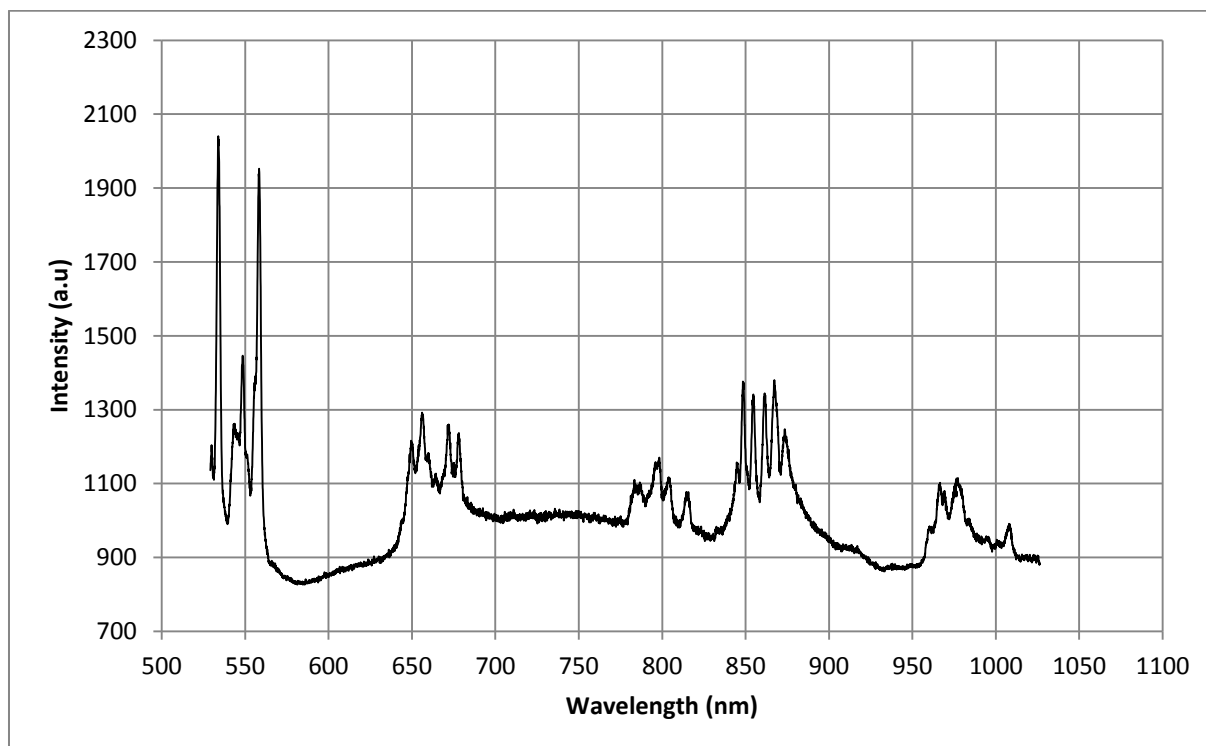


Figure 59 Spectroscopic results from analysis of Er³⁺ doped Y₂SiO₅ coated frustules

The results of the spectroscopic analysis of frustules subjected to four coatings of Er³⁺ doped Y₂SiO₅ are displayed in Figure 59. This spectrum was acquired by excitation with a green laser ($\lambda = 532$ nm). Frustules subjected to a lower number of coating cycles failed to display luminescent properties.

Peaks appear sharp and defined. The cluster of peaks centered around ~540nm, ~660nm, ~800 nm and ~980 nm are all characteristic of Er³⁺ [116]. The presence of the peaks at ~540 nm and ~660 nm are also predicted by the energy diagram of erbium in Figure 13. Peaks centered on ~860 nm were not identified. Peaks at wavelengths below 532 nm are not seen due to a filter inserted in the pathway removing the excitation laser.

4.4 Characterization of frustules coated with down converting oxides

Results of the characterization of frustules coated with elements known to possess the ability of down converting incident light are presented in the following subchapters. Results were acquired by scanning electron microscope (SEM) featuring energy dispersive x-ray spectrometer (EDS), fluorescence microscopy and photoluminescence spectroscopy.

4.4.1 Frustules coated once with Mn^{2+} doped Zn_2SiO_4 featuring SEM and EDS

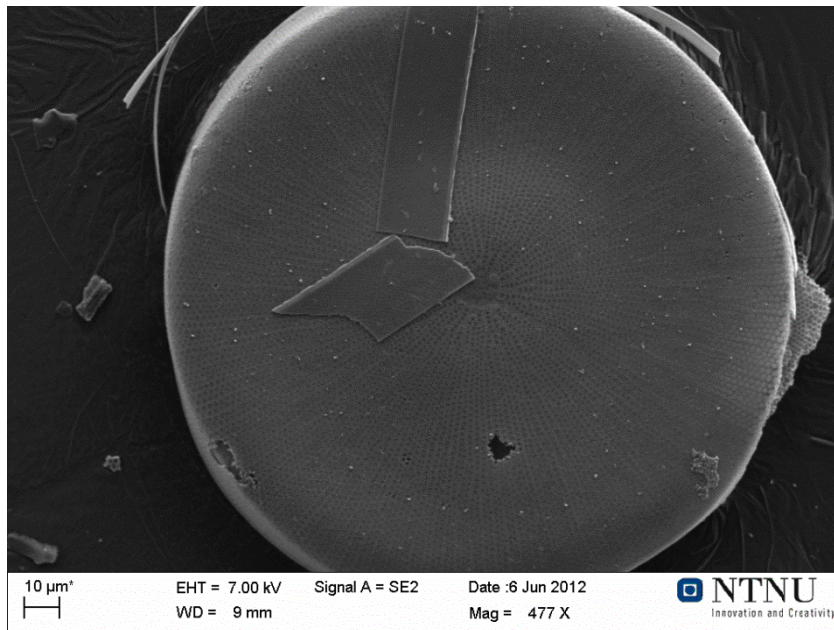


Figure 60 Frustule coated once with Zn/Mn

A frustule coated once with Mn^{2+} doped Zn_2SiO_4 can be seen in Figure 60. The frustule appears mostly structurally intact. Some damages can be seen around the extremities and on the surface of the top valve. Two pieces of girdeband structures adorn the top of the valve surface.

Few pieces of what appears to be broken girdeband structures also can be seen surrounding the frustule. Original frustule pore pattern is clearly visible radiating from the centre to the extremities of the frustule.

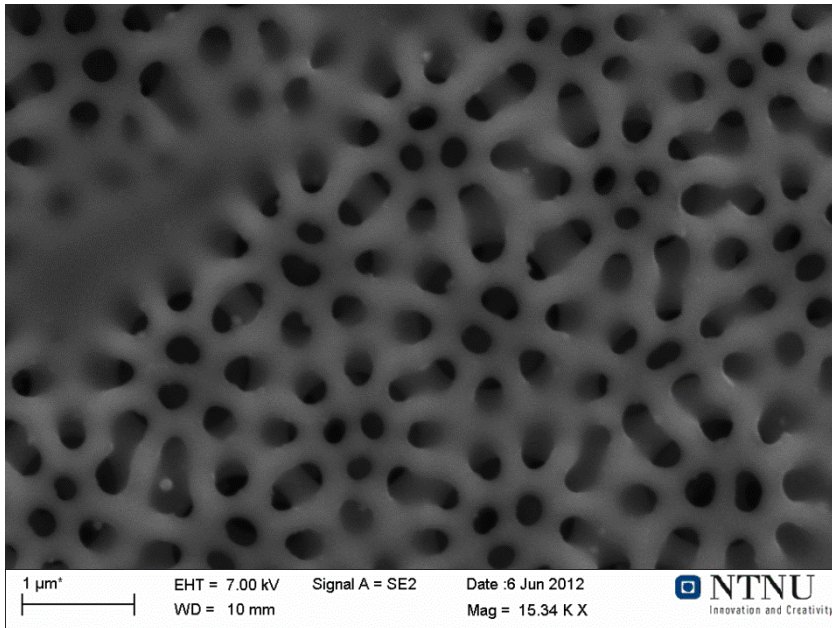


Figure 61 Surface of frustule coated 1X with Zn/Mn

The surface of a frustule subjected to one coating cycle with Mn^{2+} doped Zn_2SiO_4 is displayed in Figure 61. The remaining parts of the cribellum pores and velum membrane can be seen atop of the cribrum cavities. The cribellum pores and velum membrane appears less dense than in the original frustules this can be seen by comparison with Figure 23, this effect can be attributed to melting of the finest velum membrane structures.

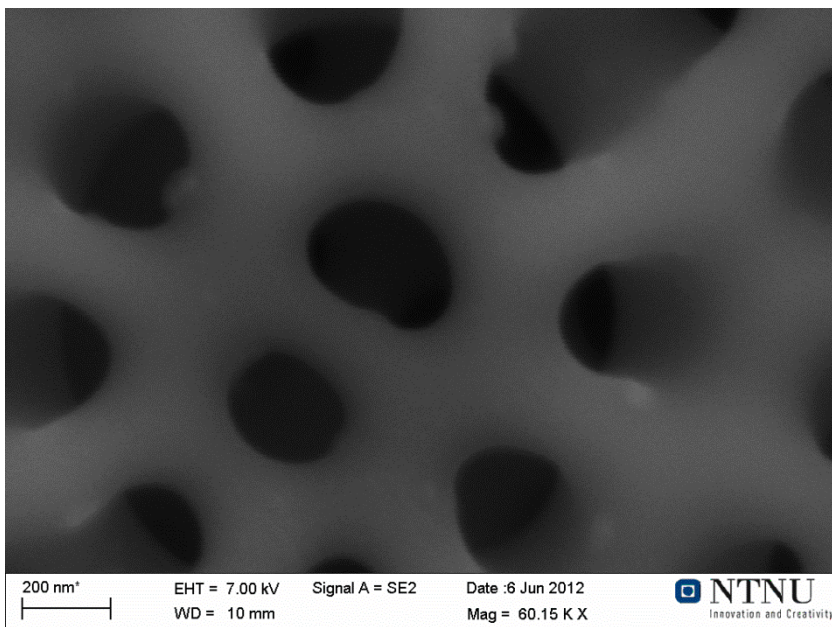


Figure 62 Frustule coated 1X with Zn/Mn at nanoscale

A pore of a frustule subjected to one coating cycle with Zn/Mn is zoomed into in Figure 62. Small bumps in the sides of the remaining cribellum pores are likely remains of the velum membrane. Holes of the cribrum pores can just faintly be seen to the rear underneath the cribellum pores.

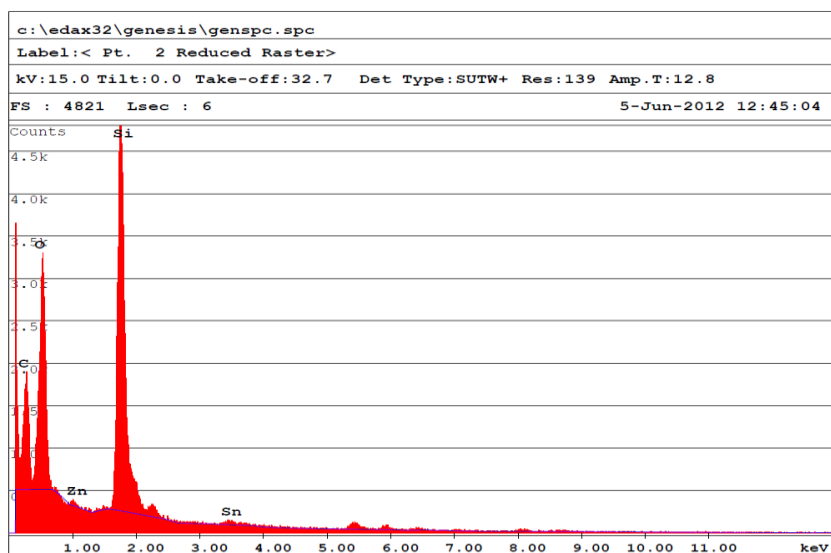


Figure 63 Typical EDS spectra of (1X) Zn/Mn coated frustule

The EDS spectrum of a frustule subjected to one coating cycle is illustrated in Figure 63. Zn peaks have a very low area, indicating a low concentration of the element. No manganese can be detected. A peak representative of tin (Sn) can be seen. The presence of this element is unwanted and is therefore a contaminant.

Table 9 Average elemental contents of (1X) Zn/Mn coated frustules

Element	Atomic %	Weight %
C K	49,70	37,55
O L	35,68	35,40
Zn L	0,12	0,49
Si K	14,25	24,77
Sn L	0,25	1,79
Mn K	0,00	0,00
Total	100,00	100,00

The quantified results of the EDS analysis are shown in Table 9. As indicated by the spectrum in Figure 63, the concentration of Zn is very low. No trace of Mn can be seen, this is most likely the result of Mn concentration being below the detection limit of the EDS system.

The concentration of the pollutant Sn is large compared to the concentration of Zn. The origin of this pollution is likely contaminated reactants, glassware or the stainless steel support grid.

4.4.2 Frustules coated twice with Mn^{2+} doped Zn_2SiO_4 by SEM and EDS

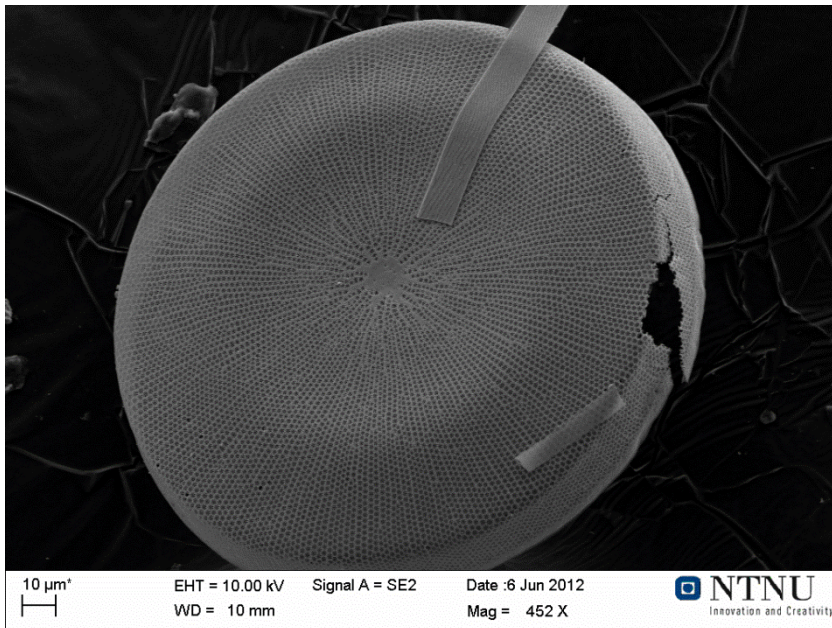


Figure 64 Frustule coated twice with Zn/Mn

A frustule valve that has been coated twice with a solution of Mn^{2+} doped ZnCl_2 in acetonitrile and ethylene glycol is displayed in Figure 64. The frustule appears mostly structurally intact. A large damage can however be seen in the rightmost edge, some large cracks can also be seen in close proximity of this damage.

Few pieces of girdleband structures adorn the surface of the valve. The pattern of pore structures can be seen radiating outwards from the centre of the frustule.

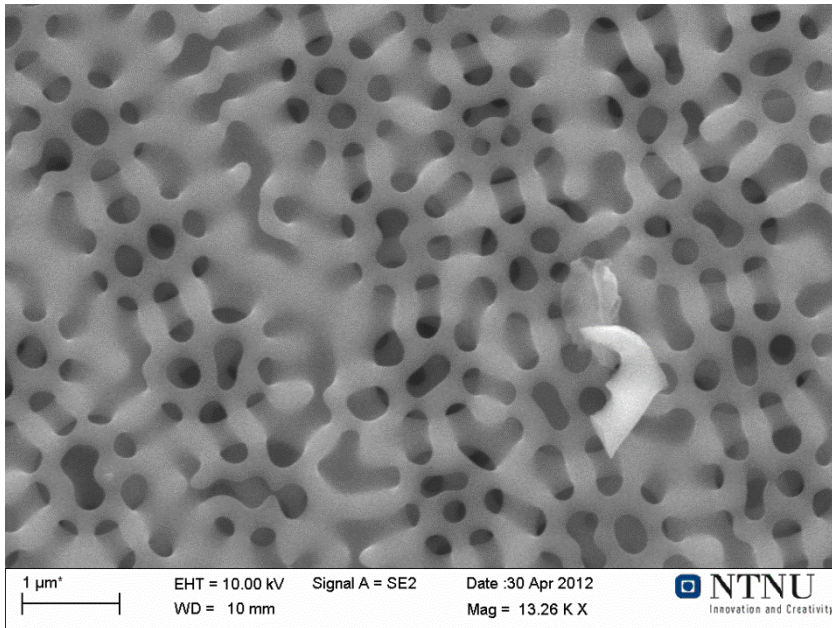


Figure 65 Frustule coated 2X with Zn/Mn

The photo shown in Figure 65 was taken post annealing (800°C, 2 hours) and the frustule was carbon coated. The structural features might be compared to that of frustules in the temperature exposure characterization at 800°C, seen in Figure 37. Holes of the cribrum appear underneath the remaining parts of the cribellum pores associated with the outer velum membrane. Structures appear slightly more irregular as when compared to frustules coated only once. Central pores appear to have fused together forming larger units.

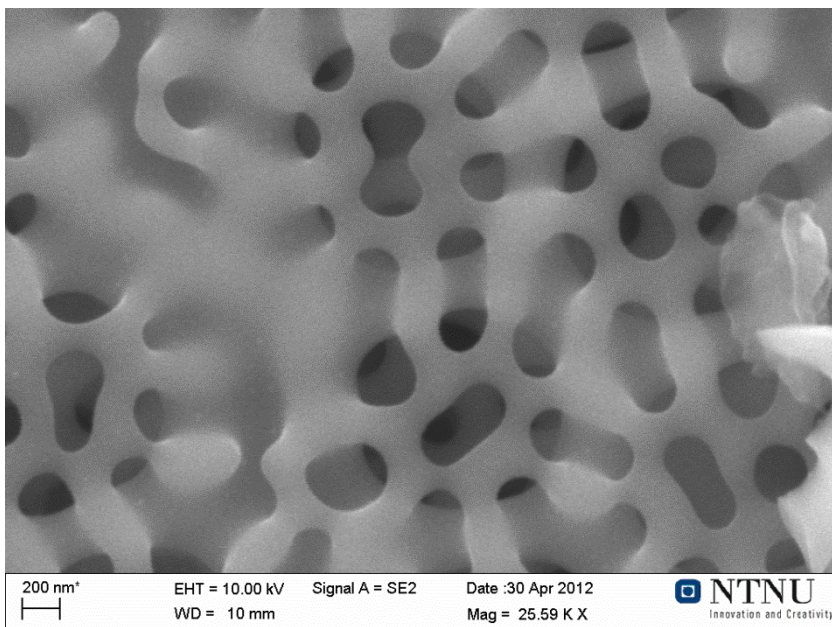


Figure 66 Frustule coated 2X with Zn/Mn at nanoscale

Figure 66 displays structural features of the frustule that has been coated twice with Mn^{2+} doped Zn_2SiO_4 at high magnification. Remains of the thin velum membrane can be seen covering parts of the underlying cribrum cavities leading to the internals of the frustule. Some unidentifiable debris adorns the surface of the lower right

parts of the image. Pores in the middle of the circular structures appear to have increased in size, this is likely caused by several pores fusing and forming larger entities.

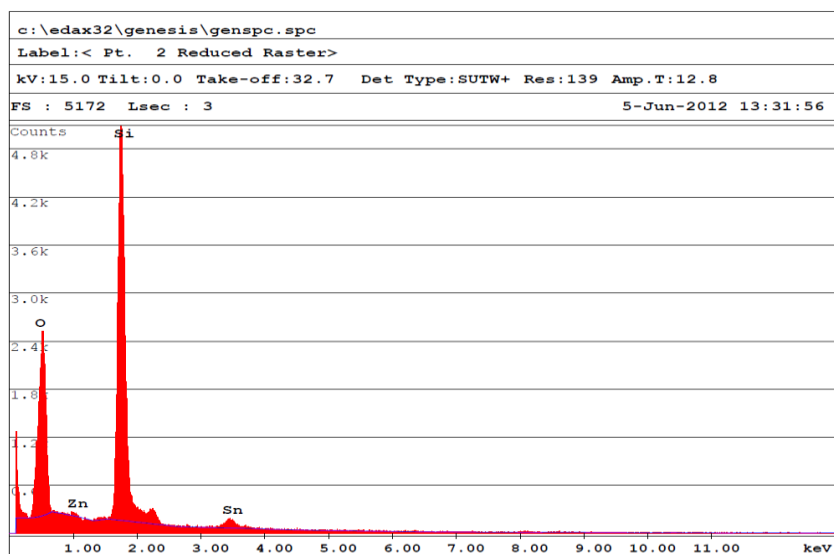


Figure 67 Typical EDS spectrum of (2X) coated Zn/Mn

A typical EDS spectrum representative of frustules coated twice with Mn^{2+} doped Zn_2SiO_4 is illustrated in Figure 67. The peak identifying Zn appears to be small, indicative of low concentrations of the element. A somewhat larger peak representative of tin (Sn), is also detected.

Table 10 Average elemental contents of (2X) Zn/Mn coated frustules

Element	Atomic %	Weight %
C K	0,00	0,00
O L	60,59	44,14
Zn L	0,23	0,68
Si K	37,95	48,53
Sn L	1,23	6,65
Mn K	0,00	0,00
Total	100,00	100,00

The average quantified results of the EDS analysis of frustules subjected to two coating cycles with Mn^{2+} doped Zn_2SiO_4 is displayed in Table 10. As expected from the small peak representing Zn in the EDS spectrum shown in Figure 67, the concentration of the element is low.

As for the other samples of Mn/Zn coated frustules, tin (Sn) is found in the elemental analysis. The presence of this element is likely due to contaminated reactants, glassware or cross contamination from the grid supporting frustules during coating and annealing.

4.4.3 Frustules coated four times with Mn^{2+} doped Zn_2SiO_4 featuring SEM and EDS

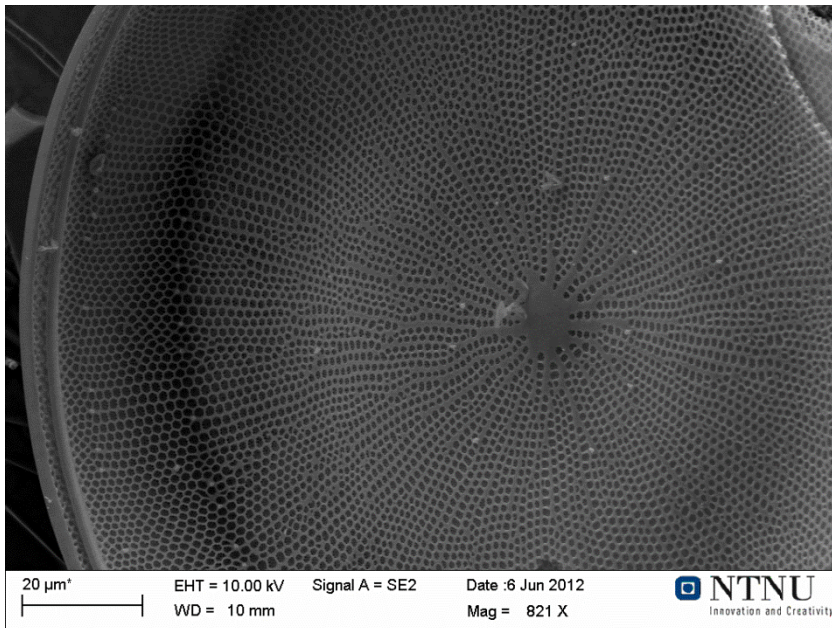


Figure 68 Frustule coated four times with Zn/Mn

A frustule coated four times with Mn^{2+} doped ZnO can be seen in Figure 68. The point of view is from inside of the frustule towards the foramen of the areolae. This is why the pores appear very large when compared to the outside view given in other images.

A large damage can be seen in the upper right parts of the image. The frustule pore structure is clearly seen radiating towards the extremities. Few traces of unidentifiable debris can be seen towards the centre of the structure. The frustules were carbon coated.

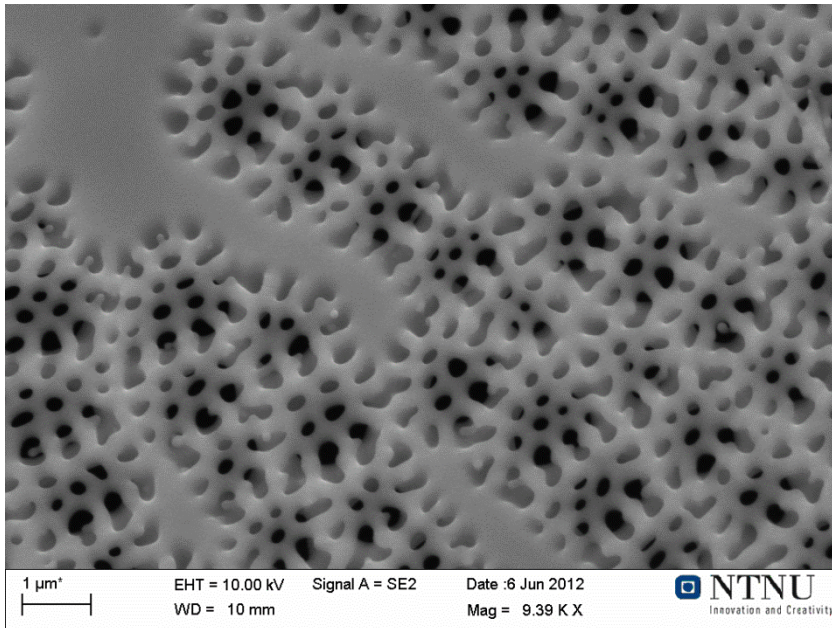


Figure 69 Frustule coated 4X with Zn/Mn

A frustule subjected to four coating cycles with Mn^{2+} doped Zn_2SiO_4 is displayed in Figure 69. The image appears bright in selected areas. This is likely some effect of the specimen charging and occurs despite carbon coating applied to avoid this effect. Dominant structural feature appears to be the cribellum pores of the velum membrane as well as the underlying cribrum cavities. The cribrum cavities can be seen as dark areas beneath the cribellum pores.

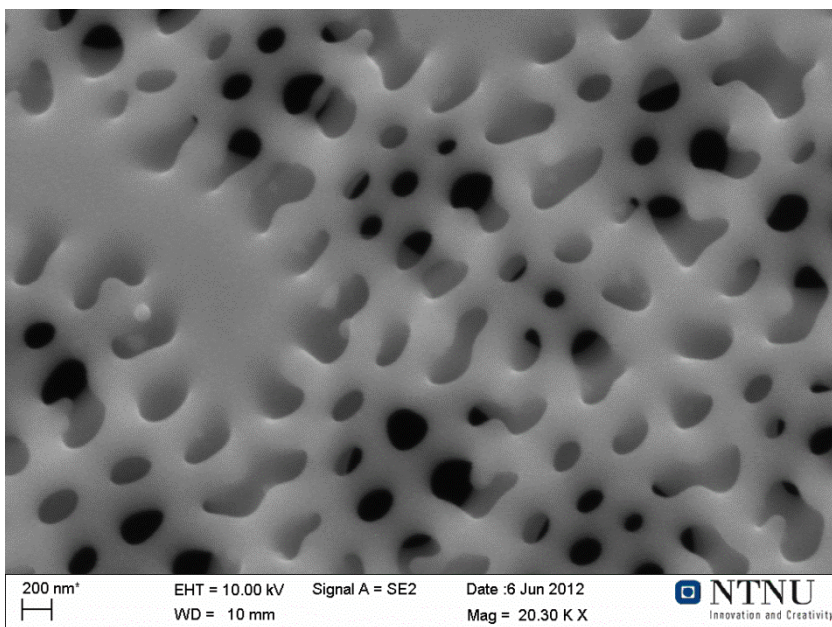


Figure 70 Frustule coated 4X with Zn/Mn at nanoscale

A frustule subjected to four coating cycles with Mn^{2+} doped Zn_2SiO_4 is displayed at high magnification in Figure 70. Bright areas in the image are likely the effect of the specimen charging. Cribrum cavities are clearly visible beneath the outer remains of the cribellum pores and associated velum membrane.

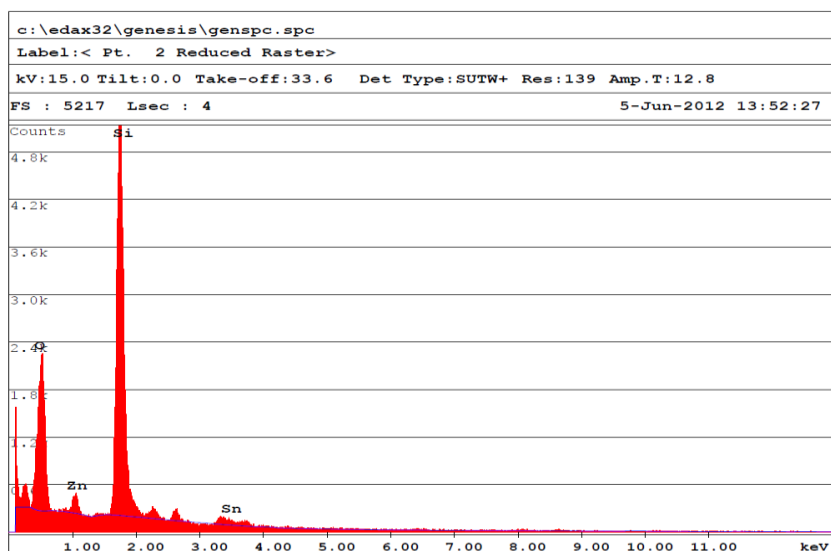


Figure 71 Typical EDS spectrum of (4X) Zn/Mn coated frustule

A typical EDS spectrum representative of frustules subjected to four coating cycles with Mn^{2+} doped Zn_2SiO_4 is illustrated in Figure 71. The peak representative of Zn appears significantly larger than when compared to equivalent peaks of frustules subjected to a lesser number of coatings. This can be seen by comparing Figure 63, Figure 67 and Figure 71. A peak representative of tin (Sn), can also be detected in these frustules.

Table 11 Average quantified EDS results of (4X) Zn/Mn coated frustules

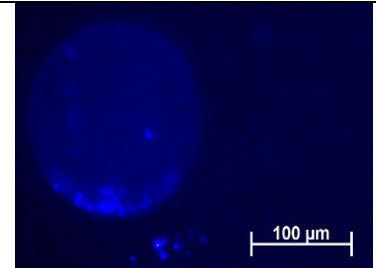
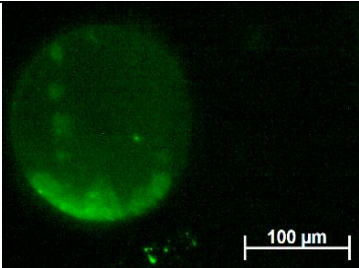
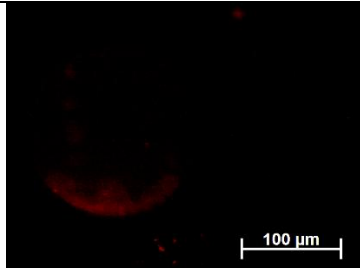
Element	Atomic %	Weight %
C K	0,00	0,00
O L	55,61	38,98
Zn L	1,04	2,95
Si K	42,16	51,86
Sn L	1,20	6,22
Mn K	0,00	0,00
Total	100,00	100,00

The average quantified EDS results acquired upon analysis of frustules subjected to four coating cycles of Mn^{2+} doped Zn_2SiO_4 are illustrated in Table 11. The increased concentration of Zn as suspected from the large representative peak in the EDS spectrum of Figure 71 is confirmed by this analysis. A certain concentration of tin appears to be present. This is however considered to be the result of a contamination of the sample or precursors.

4.4.4 Mn²⁺ doped Zn₂SiO₄ coated frustules characterization by fluorescence microscopy

The results of the fluorescence microscope investigation of Mn²⁺ doped Zn₂SiO₄ coated frustules are illustrated in Table 12. It should be noted that these are the results from the frustules had been subjected to four coating cycles as frustules subjected to a lower number of coating cycles failed to display fluorescent properties.

Table 12 Results of the fluorescence microscope investigation of Mn²⁺ doped Zn₂SiO₄ coated frustules

		
Excitation = 365 nm Emission = 445-450 nm Filter set 43	Excitation = 440-475 nm Emission = 530-550 nm Filer set 44	Excitation = 630-640 nm Emission = 650-690 nm Filer set 50

The results shown in Table 12 illustrate the fluorescent properties of Zn/Mn coated frustules along with the relevant data with regards to excitation wavelength and the corresponding filter set.

The green fluorescence appears to be the brightest whereas the blue appears to be very faint and is barely visible against the background. The red fluorescence is also very weak. The fluorescence phenomenon seems to be unevenly distributed on the frustules and is likely the result of uneven coating.

4.4.5 Mn^{2+} doped Zn_2SiO_4 coated frustules characterized by photoluminescence spectroscopy

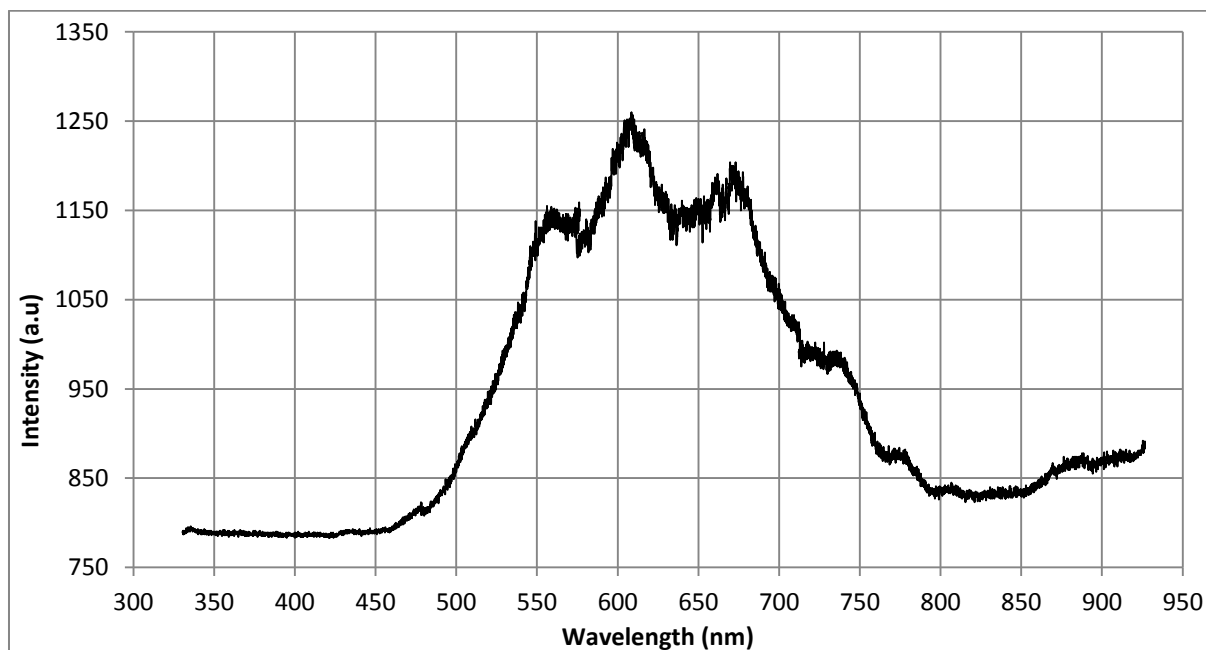


Figure 72 Spectroscopic results from analysis of Mn^{2+} doped Zn_2SiO_4 coated frustules

The spectroscopic results from investigation of frustules subjected to four coating cycles are displayed in Figure 72. Frustules subjected to a lesser number of coating cycles failed to display luminescence. The above spectrum was acquired by excitation with a UV laser ($\lambda = 325$ nm). Three peaks stand out and are located at ~ 570 nm, ~ 610 nm and ~ 670 nm.

The peak at 570 nm is likely a result of the Mn^{2+} doped Zn_2SiO_4 [117]. Other peaks are not described in literature on Mn^{2+} doped Zn_2SiO_4 and are likely results of impurities. Presence of tin impurity is also confirmed by EDS, thus it is likely that the peaks from 610-670 nm have arisen as a consequence of tin forming zinc stannate (Zn_2SnO_4) [118].

Presence of impurities might also account for lack of distinct and sharp peaks as were found in the analysis of Er/Y coated frustules seen in Figure 59.

4.5 Characterization of nitrided frustules

Frustules that had been subjected to a simultaneous metallothermic reduction and nitriding were investigated by use of scanning electron microscope (SEM) featuring energy dispersive x-ray spectrometer (EDS). Raman spectroscopy was later used to verify the EDS results of the most promising samples.

4.5.1 Frustules nitrided at 650°C

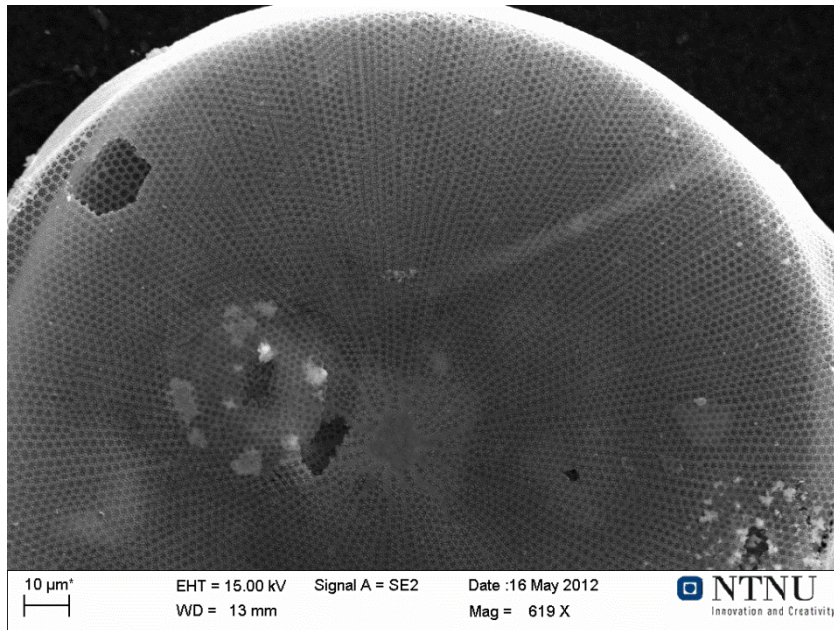


Figure 73 Frustules nitrided at 650°C overview

An overview image of a frustule subjected to simultaneous metallothermic reduction and nitriding is displayed in Figure 73. External features of the frustules appear to be intact. Some damages can be seen close to the center and towards the extremities of the structure.

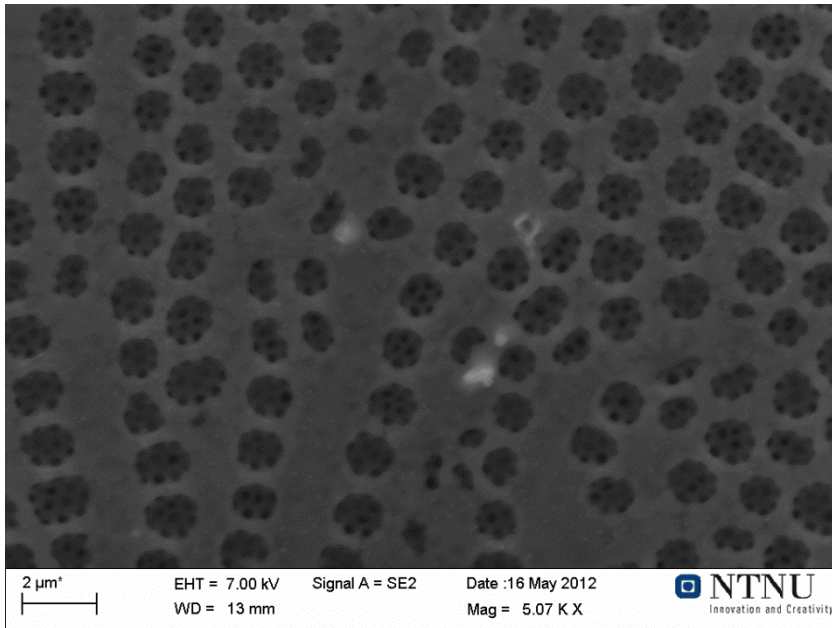


Figure 74 Frustule nitrided at 650°C

A frustule subjected to nitriding at 650°C is illustrated in Figure 74. Point of view is from the inside of the frustule through the foramen and towards the cribrum pores to the rear of the image.

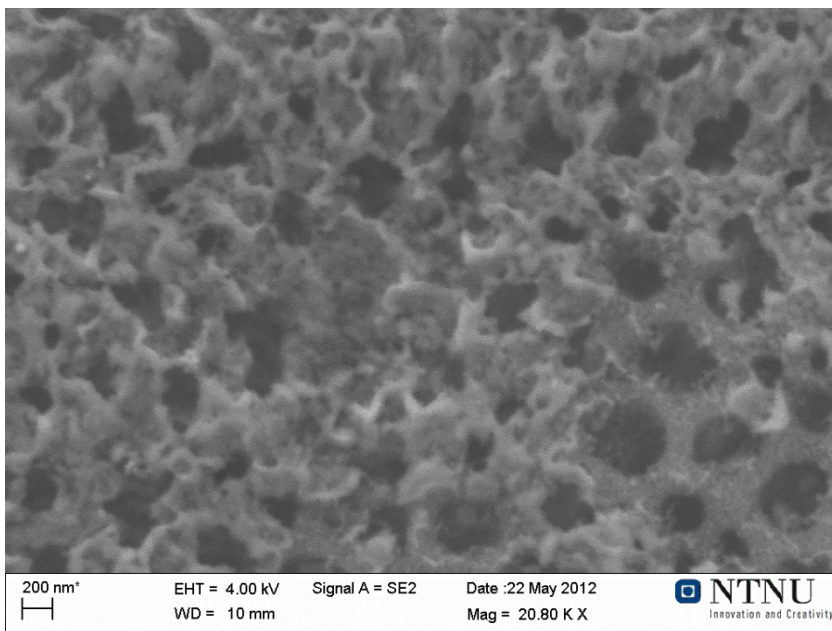


Figure 75 Frustule nitrided at 650°C at nanoscale

In Figure 75, a frustule subjected to nitriding at 650°C is illustrated. Point of view is from outside the frustule towards the cribellum pores. The surface appears to be partly covered in remains from the reduction and nitriding reactions which have survived the cleaning procedures.

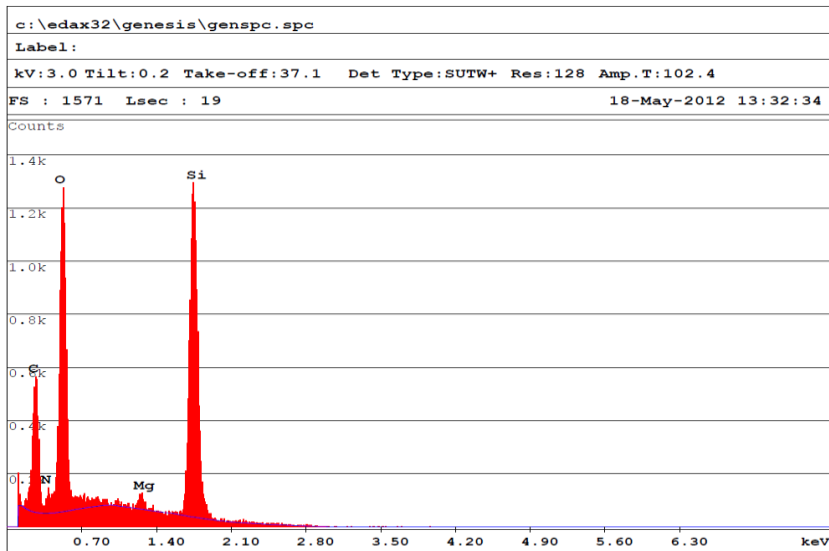


Figure 76 Typical EDS spectrum of frustules nitrated at 650°C, 3keV

A typical EDS spectrum of a frustule nitrated at 650°C is illustrated in Figure 76. Dominant peaks are representative of silicon (Si), oxygen (O) and carbon (C). Peaks representing nitrogen and magnesium are very small compared to the others, indicating a low concentration of the elements.

Table 13 Average elemental contents of frustules nitrated at 650°C, 3keV

Element	Atomic %	Weight %
C K	10,09	5,13
N K	2,26	1,34
O K	20,59	13,98
Mg K	1,94	2,00
Si K	65,13	77,54
Total	100,00	100,00

The average elemental contents of frustules subjected to simultaneous metallothermic reduction and nitrating at 650°C is illustrated in Table 13. The information in this table was acquired by quantification of the EDS software. As expected from the EDS diagrams dominant species are Si, O, and C whereas concentrations of Mg and N are low as compared to concentrations of other elements. This is indicative of a low conversion to nitride.

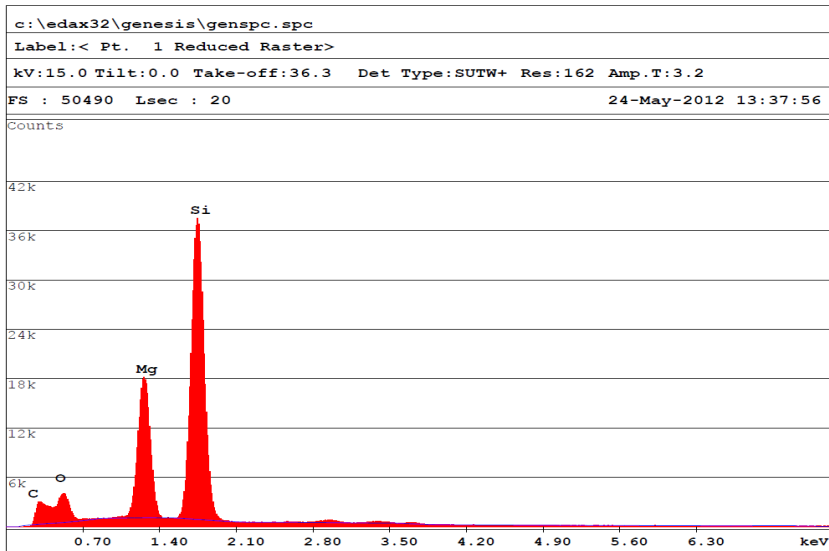


Figure 77 Typical EDS spectrum of frustules nitrated at 650°C, 15 keV

An EDS spectrum typical to frustules nitrated at 650°C is illustrated in Figure 77. Dominant peaks are silicon (Si) and magnesium (Mg). Peaks representative of carbon (C) and oxygen (O) have a significantly smaller area. Nitrogen (N) has disappeared.

Table 14 Average elemental contents of frustules nitrated at 650°C, 15 keV

Element	Atomic %	Weight %
C K	32,20	19,05
N K	0,00	0,00
O K	16,17	12,54
Na K	0,30	0,32
Mg K	6,87	8,44
Si K	44,45	59,65
Total	100,00	100,00

The average elemental composition of frustules subjected to nitriding at 650°C is illustrated in Table 14. Dominant elements appear to be: Si, O and C. No nitrogen was detected using the EDS onboard auto detect mode. Some magnesium appears to have survived the cleaning process. Traces of sodium can also be seen and is likely due to cross contamination from glass ware or a contaminant inherent to the frustules.

4.5.2 Frustules nitrated at 800°C

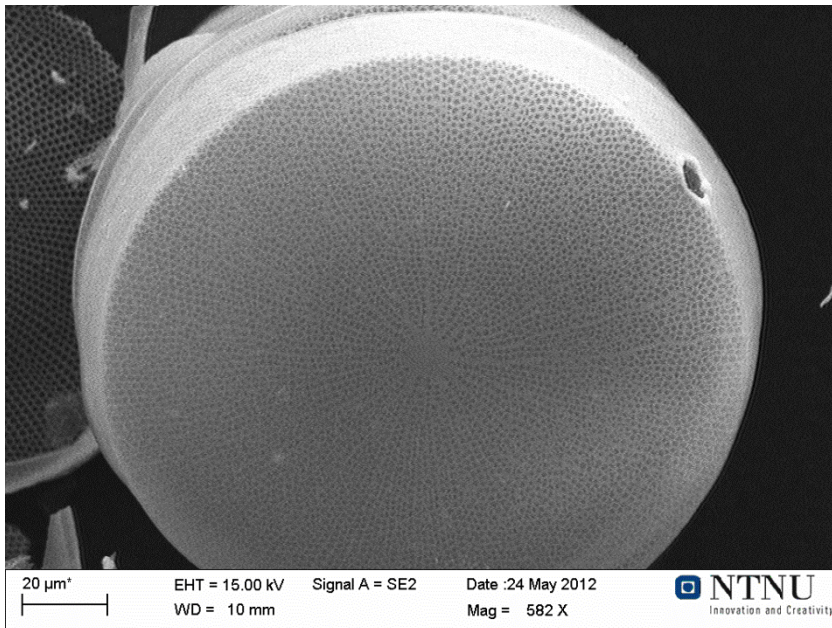


Figure 78 Frustule subjected to nitrating at 800°C

An overview image of a frustule that has been nitrated during simultaneous metallothermic reduction can be seen in Figure 78. The frustule appears to be structurally intact with the exception of damage to the upper right extremity. Part of a frustule valve can be seen to the left behind the main frustule. Pores are seen radiating from the centre of the frustule towards the extremities.

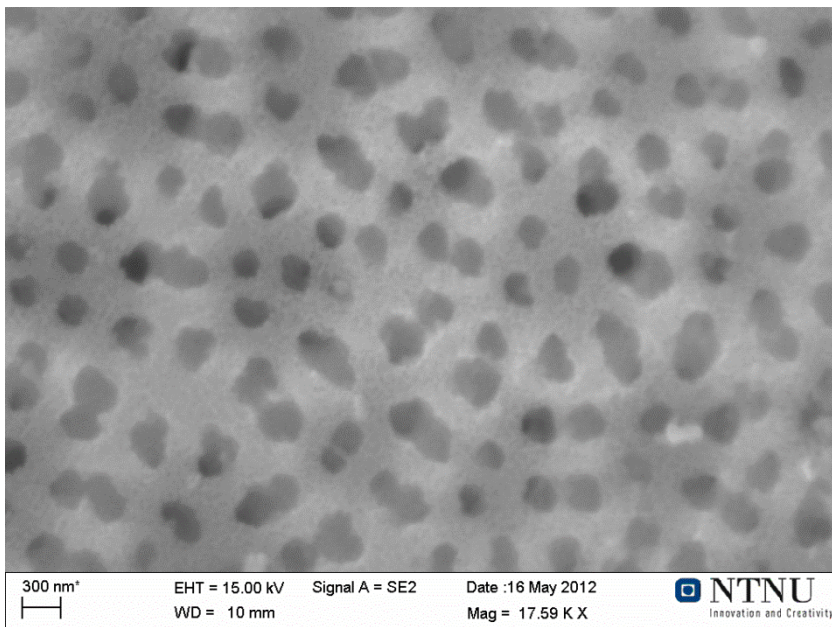


Figure 79 Front side of frustule subjected to nitrating at 800°C

The front side of a frustule nitrated at 800°C can be seen in Figure 79. Much of the cribellum pores and velum membrane appears to be intact, but the structures appear to be highly porous as when compared to original

frustules. Cribrum cavities can be seen as darker areas beneath the cribellum pores of the outer velum membrane. The cribrum cavities do however not appear as large as in original frustules.

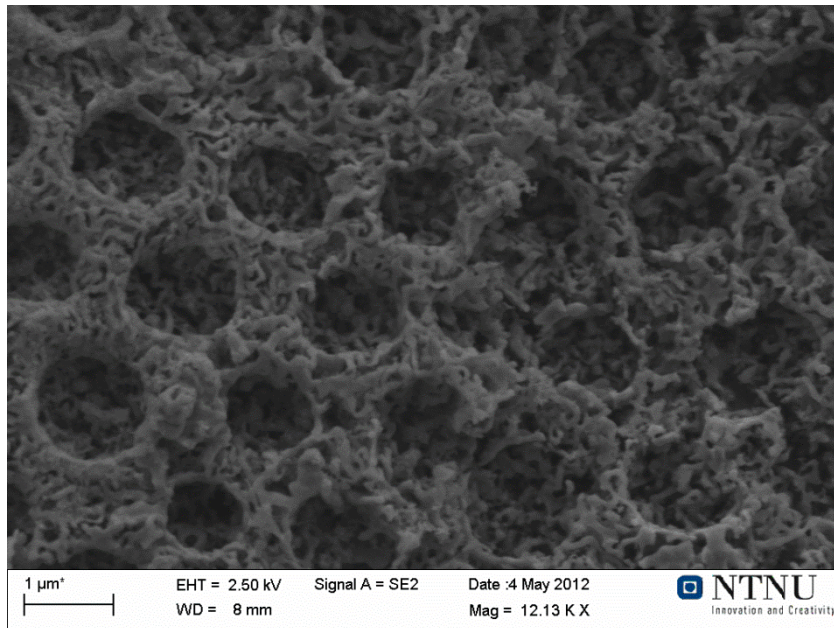


Figure 80 Rear side of frustule subjected to nitriding at 800°C

A frustule subjected to simultaneous metallothermic reduction and nitriding is displayed in Figure 80. The picture is taken post cleaning and point of view is from inside of the frustule towards the foramen holes of the areolae. The structure appears to be highly porous and several structural features of the original frustule appear to be conserved. This can be seen by comparing the images of the original frustules with the above image.

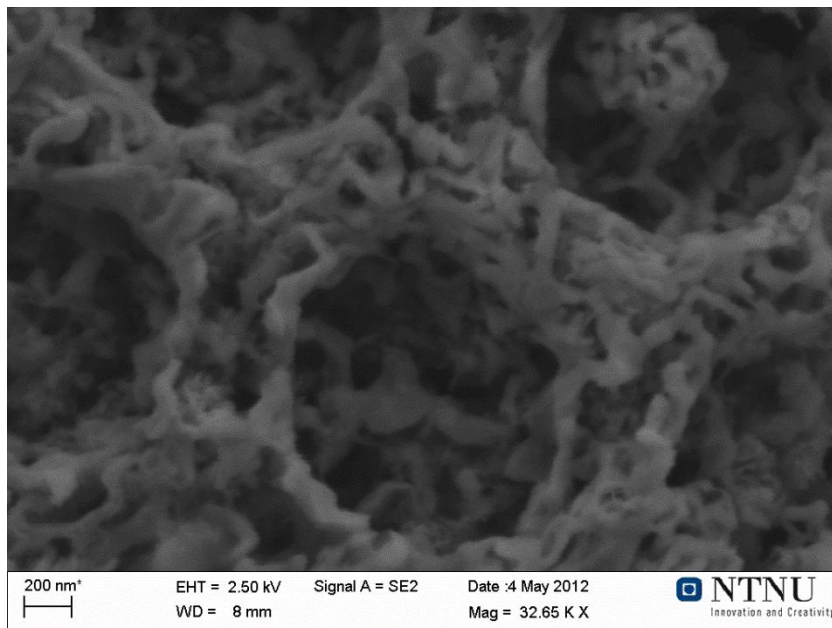


Figure 81 Rear side of frustule subjected to nitriding at 800°C, nanoscale

A frustule subjected to simultaneous metallothermic reduction and nitriding at 800°C is displayed at high magnification in Figure 81. The image represents a frustule as viewed from the inside of the frustule through the hole in the foramen and towards the cribrum. The structure appears to be highly porous as when compared to original frustules. The cribrum cavities appear partially closed.

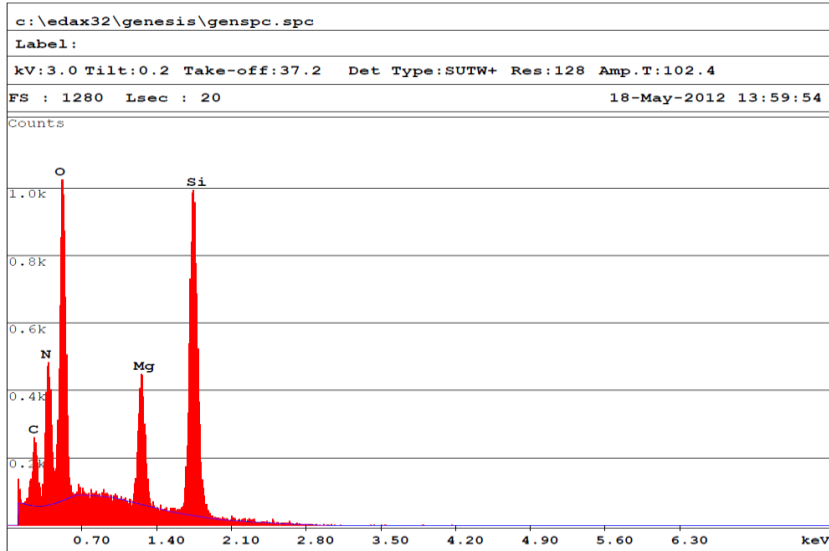


Figure 82 Typical EDS spectrum of frustules nitrided at 800°C, 3.00 keV

A typical EDS spectrum of frustules subjected to simultaneous metallothermic reduction and nitriding at 800°C, is illustrated in Figure 82. Major peaks are representative of silicon (Si), oxygen (O), nitrogen (N), carbon (C) and magnesium (Mg). The above spectrum was acquired at 3.00 keV.

Table 15 Average elemental content of frustules nitrided at 800°C, 3.00 keV

Element	Atomic %	Weight %
C K	7,97	4,35
N K	17,91	11,44
O K	12,20	8,78
Mg K	15,53	17,22
Si K	46,39	58,21
Total	100,00	100,00

The average elemental content of frustules subjected to simultaneous metallothermic reduction and nitriding at 800°C, is illustrated in Table 15. Numbers are based on quantified EDS results acquired at 3.00 keV. Quantified results are in agreement with the dominant peaks illustrated in Figure 82. The elements existing in highest concentration appear to be Si, Mg and N.

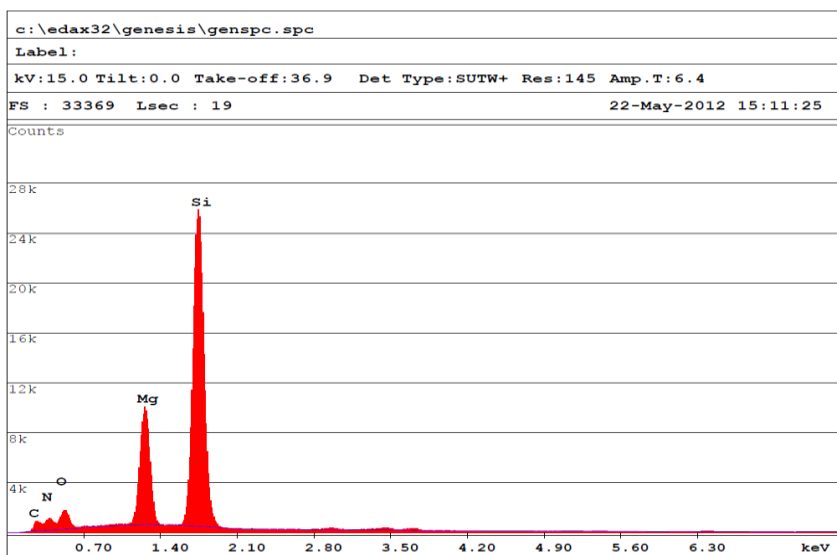


Figure 83 Typical EDS spectrum of frustules nitrated at 800°C, 15.00 keV

A typical EDS spectrum acquired upon analysis of frustules subjected to simultaneous metallothermic reduction and nitriding acquired at 15.00 keV is illustrated in Figure 83. Dominant peaks are silicon (Si) and magnesium (Mg). Peaks representative of oxygen (O), nitrogen (N) and carbon (C) are significantly smaller.

Table 16 Average elemental content of frustules nitrated at 800°C, 15.00 keV

Element	Atomic %	Weight %
C K	23,79	14,46
N K	16,91	12,08
O K	14,18	11,37
Mg K	9,64	11,97
Si K	35,48	50,12
Total	100,00	100,00

The average elemental content based upon quantified EDS results of frustules analyzed at 15.00 keV can be seen in Table 16. There appear to be only small differences with regards to nitrogen content between EDS results acquired at 15.00keV and EDS results acquired at 3.00 keV as seen in Table 15. Dominant species are Si and C followed closely by N, Mg and O.

4.5.3 Characterization of frustules nitrated at 800°C by Raman spectroscopy

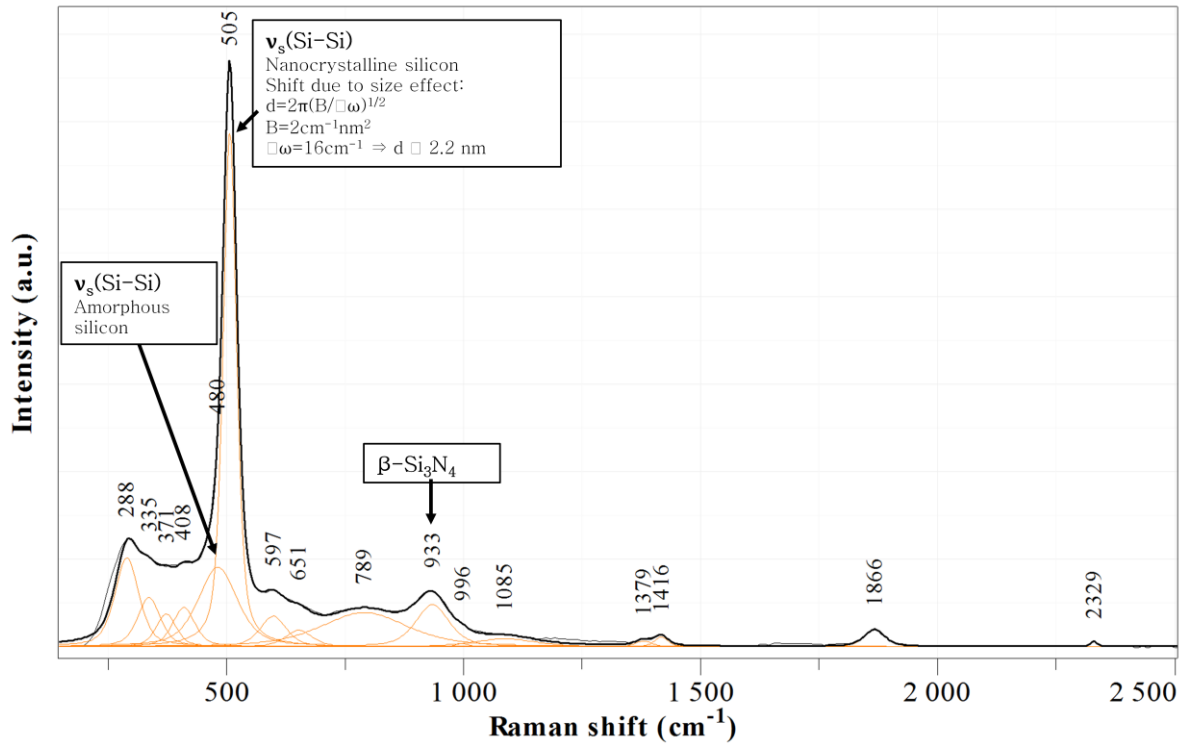


Figure 84 Raman spectrum of frustules subjected to nitriding at 800°C

The resulting spectrum resulting from the analysis of frustules subjected to simultaneous metallothermic reduction and nitriding at 800°C, is illustrated in Figure 84. The black coloured curve is the resultant curve as received from the Raman spectroscope and the orange curves are the result of deconvolution of the black curve.

The peak located at 480 cm^{-1} corresponds to the presence of amorphous silicon [119]. The peak at 505 cm^{-1} corresponds to the presence of nanocrystalline silicon with a crystalline size of 2.2 nm [119, 120]. The peak at 933 cm^{-1} corresponds to the presence of β -Silicon nitride [121].

5 Discussion

In the following subchapters, the results of the characterization and experimental work are discussed.

5.1 Starting materials

Samples acquired from NTNU Department of Biotechnology generally had a low concentration of frustules. This necessitated that either several samples had to be used for each experiment or that the volumetric size of each experiment was kept low. The frustules were of the species *Coscinodiscus wailesii* and *Coscinodiscus* sp.

The small sample sizes were found to be problematic whenever cleaning procedures had to be undertaken as chances of losing materials were greatly increased. Chemicals utilized in the experiments were of reasonable purity as is illustrated in Table 2.

The stainless steel grid used to support frustules in experimental work may be a source of contamination since expected contents of the grid (Mo, Sn) can be seen appearing in EDS analyses of frustules post experiments.

The glassware utilized was from a public metallographic laboratory (metallographic lab, A. Getz way) meaning that the glassware may be a source of contaminants. To avoid problems with such issues, every piece of glassware used was extensively cleaned in distilled water.

The stainless steel reactor featuring copper gaskets was found to give of a dark scale on areas exposed to normal atmosphere. This scaling could easily get onto the copper gaskets and thus break the seal from external atmosphere which necessitated cleaning of all surfaces between experimental runs.

5.2 Original frustules

In order to form a comparative basis with respect to chemical, fluorescent and structural features, original frustules were subjected to characterization with scanning electron microscope (SEM) featuring onboard energy dispersive x-ray spectrometer (EDS) and fluorescence microscope.

The original frustules were carbon coated to ensure minimal problems with charging of the specimen. This was done based on earlier experiences when investigating frustules structures. The problems with charging of the specimen can be attributed to accumulation of charge on the frustule surface as a consequence of silica being an insulator.

The carbon coating might hide some structural features, but such an event would seem unlikely. Initial observation upon zooming into the sample area was rather large concentrations of debris resulting from destroyed frustules. A good example on this debris would be the area surrounding the frustule in Figure 22.

The debris from destroyed frustules can probably be attributed to damages occurring during cleaning procedures and then especially the end centrifugal separation post chemical cleaning. Another possibility for the observed damages is the handling of samples during experiments and characterization. The aforementioned reasons might also be the cause of some damages that were observed in more structurally intact frustule units.

The original frustules displayed impressive nanoscale features and the majority of such features were found to exist in the pores. An example on such features can be seen in Figure 24. Despite damages observed to many frustules, the pore structures were in most cases found to be intact, thus it appears the cleaning procedures have been successful in maintaining pore structure.

Elemental analysis featuring EDS showed the constituents of the frustules to be silicon and oxygen, which is expected due to frustules being silica structures. The small amount of carbon can be attributed to carbon coating as well as the electron beam penetrating the frustules structure, giving chemical information about the underlying carbon support tape.

Original cleaned frustules were not found to possess any form of fluorescent properties upon investigation with fluorescence microscope.

5.3 Frustules exposed to increased temperatures

In order to assess the effect of heat treatment on structural aspects of the frustules, a temperature exposure experiment was set up. Here the frustules were exposed to temperatures from 400°C and up to 1200°C at increments of 200°C.

The experiment gave a comparative basis with respect to both the coating and nitriding experiments and allowed for determination of possible structural changes to be expected at elevated temperatures. This allowed for future differentiation between features that could be attributable to chemical reactions or heat related changes.

5.3.1 Experimental challenges and issues

All experiments were undertaken in normal atmosphere using a muffle furnace and a stainless steel support grid upon which the frustules were placed. Similarly all experiments were performed for the same duration of time (1h) to circumvent possible issues of unequal residence times.

All transfers of samples between the various experiments and analytical equipment were sought to be performed as carefully as possible. This was done to avoid inflicting damages to the brittle frustules, since such damages can easily be erroneously attributed to effects of temperature.

Damages sustained during initial cleaning procedures were also found to be plentiful. Such damages can also erroneously be attributed to effects of temperature exposure. Thus, comparison with data collected on original frustules gave important information on pre-existing damages to be expected that could be neglected in the temperature exposure experiments.

No photoluminescence spectroscopy or fluorescence microscopy were performed to heat treated frustules, since original frustules failed to display photoluminescence and no photoluminescent properties are thought to occur during heat treatment.

Post heat treatment the frustules were allowed to cool to room temperature before being characterized with scanning electron microscope (SEM). No elemental analysis featuring energy dispersive x-ray spectrometer (EDS) was undertaken, since no changes to the elemental makeup were thought to occur from the investigation of the original frustules.

All frustules subjected to the temperature exposure characterization were carbon coated before characterization with SEM. This was done to avoid problems with charging of the specimen. Charging of the specimen causes drift in the image as well as hazy and/or excessively bright images.

Problems related to charging of the specimen can be attributed to charge accumulating on the surface of insulating objects. Since silica is an insulator such problems were expected. Despite carbon coating some effects of charging could still be seen around edges and at slow scan speeds of the SEM. Examples of charging can be seen in Figure 28 and Figure 32 and then as bright areas within the pores.

A quick summary of the structural changes occurring to the pore structures at increased temperatures is given in Table 4. Here, changes are seen taking place at temperatures of 600°C and gradually increasing at every temperature interval, until the entire pore structure is destroyed at 1200°C.

To complete the results of this table, a more thorough discussion of the results at the respective temperatures follows in the next chapter.

5.3.2 Effects of temperature exposure on diatom frustules

No structural changes of any sort could be detected in the frustules exposed to 400°C for one hour. This was true both for pores as well as total structural integrity. This could be seen by comparison of external structures of the original frustules with corresponding features of frustules heat treated at 400°C. The structural features apparent in pores of frustules subjected to 400°C were the cribellum pores of the outer velum membrane.

The inside view of frustules subjected to 400°C, gave good three dimensional view of the pore structure. No differences could be detected between the original and heat treated sample from this angle of view. Damages observed to some frustules exposed to 400°C were thought to be resulting from cleaning procedures or handling issues upon sample transfers in experimental and characterization work.

For frustules exposed to a temperature of 600°C for one hour, no changes in outer structure could be detected. Small structural changes occurring in the pores can however be detected upon comparison with original frustules. The observed changes in pore structure were likely resulting from melting of the thin silica velum membrane causing an increase in the cribellum pore size.

Debris surrounding the frustules exposed to 600°C was found to be slightly more plentiful than what was expected to occur as a result of cleaning and handling based on experiences from the original frustules. This could likely be attributed to proteins existing in the girdlebands and valves decomposing at high temperature, resulting in some delaminating of the frustules structures.

When observing the inside view of a frustule pore subjected to 600°C, the three dimensional structure of the pore appeared to suffer no changes when compared to that of original frustules.

Frustules exposed to a temperature of 800°C for one hour, displayed rather large changes in pore structures when compared to frustules subjected to lower temperatures and original frustules. No obvious structural changes in total external frustules structure could be detected.

The twisted and curled structures witnessed in the pores of frustules subjected to 800°C, appeared to be the melted remains of cribellum pores and associated velum membrane. Just below these structures the cribrum cavities leading into the areola was seen.

Inside view of frustules valves exposed to 800°C, displayed no changes in the three dimensional structure of the cribrum pores, foramen or areola. This could be seen by comparison with images of frustules subjected to lower temperatures and original frustules. Melted remains of cribellum pores and velum membrane could be seen adorning the outermost parts of the cribrum pores.

Frustules subjected to a temperature of 1000°C for one hour suffered severe structural changes, especially to the pores. Structural changes with regards to the external frustule structure could also be seen as the frustules appeared slightly elongated when compared to frustules subjected to lower temperatures.

Much of the surrounding debris exposed to 1000°C, also appeared deformed upon comparison with debris found surrounding frustules subjected to lower temperatures. Major structural features seen in the pores appeared to be cribrum pores. Melted remains of the velum membrane could be seen as smooth bumps in the sides of the cribrum cavities.

Upon comparison of inside views of frustules exposed to 1000°C with inside views of frustules subjected to lower temperatures, it became apparent that structural features surrounding the foramen hole appeared to have diminished. This was probably a sign of the main mass of the frustule approaching melting temperature.

Frustules exposed to 1200°C for one hour displayed the most severe structural changes. Here the external features of the frustules were clearly deformed. The surface appeared wavy and the respective parts of the frustules halves appeared to have delaminated and slid apart. Surrounding debris appeared twisted and deformed.

No distinguishable features previously seen the pores of frustules subjected to lower temperatures were remaining, this could be seen by comparison with frustules exposed to temperatures below 1000°C. Most of the pores seems to have melted shut and is likely caused by collapsing of the outermost parts of the cribrum pores along with melting of the velum membrane.

The inside view of the frustules exposed to 1200°C revealed that the only remaining structural features present appeared to be parts of the cribrum pores. All other details previously seen at this point of view were gone.

These results indicated that the frustules should not be exposed to temperatures higher than 800°C to avoid excessive damage both to overall frustules structure as well as pore structure.

5.4 Frustules coated with up and down converting oxides

The coating method utilized in this thesis was devised by way of modification of a coating procedure previously developed by Lee et al., where erbium was substituted for europium and dip coating was substituted for spray coating [18]. Manganese doped zinc chloride deposition was identical in every way to that previously described by Lee et al., with the exception of dip coating being utilized instead of spray coating [18].

Erbium was utilized due to findings in literature describing up-conversion processes in ions of the element and hence being an interesting material with regards to improvements in efficiency for photovoltaic solar cells [17, 60, 63].

It should be mentioned that no attempt was made to characterize possible up-conversion phenomenon, nor the investigation of any efficiencies with regards to up and down-conversion of light. The intent of this work was to devise a way to coat diatom frustules with the desired oxides and to characterize these oxides with regards to conservation of the frustules pores, chemical composition, photoluminescence and completeness of the coating layer.

The information acquired from this work allowed for the evaluation of the coating method. Characterization of up and down-conversion abilities and related efficiencies along with possible improvements to the coating method were thus moved to future work.

5.4.1 Experimental issues of coating and characterization of frustules

All experimental procedures were sought to be replicated as closely as possible for each coating cycle. This was done to minimize sources of error and to increase the probability of observed changes between samples subjected to different coating cycles being the consequence of different coating thicknesses.

Frustules were deposited on a stainless steel grid and annealed at 600°C in air by using a muffle furnace before being subjected to one, two or four dip coatings in a solution containing chlorides of erbium and yttrium dissolved in ethylene glycol and acetonitrile. Between each dip the coated frustules were heated to remove the solvents of the dye before being annealed at 800°C in air for two hours.

For frustules coated with down converting oxides, an identical procedure to that described above was utilized. The dye would in this case consist of chlorides of zinc and manganese dissolved in ethylene glycol and acetonitrile.

The dip coating method can possibly cause uncoated areas to arise, this might occur when intimate contact between frustules prevent the diffusion of coating solution to the contact areas. In order to avoid such situations the frustules were swirled upon dipping in the coating solution.

Post annealing the frustules were allowed to cool to room temperature before being characterized by use of scanning electron microscope (SEM) featuring energy dispersive x-ray spectroscopy (EDS), fluorescence microscopy and photoluminescence spectroscopy.

In order to acquire good images and avoid charging of the specimens, dip coated frustules were carbon coated before characterization in SEM and EDS. Frustules investigated by photoluminescence spectroscopy and fluorescence microscopy were transferred to glass microscope slides before investigation. Frustules in the photoluminescence spectroscopy and fluorescence microscopy were not carbon coated.

The characterization of coated frustules by fluorescence microscope did not give spectroscopic information about the fluorescent light, but allowed for imaging of the frustules upon excitation and the corresponding fluorescent light emitted. Pictures acquired by this method would thus be complemented by spectroscopic information. Fluorescence microscopy also allowed for the detection of areas featuring less or no photoluminescence as a possible consequence of uneven coating.

Upon analysis featuring photoluminescence spectroscopy, a green laser with a wavelength of 532 nm was utilized as an excitation source for the Er^{3+} doped species and a UV laser of 325 nm was used for the Mn^{2+} doped species. A filter blocking out the above laser wavelengths was inserted between the sample and spectroscope. Spectroscopic information was thus only acquired from photoluminescence at longer wavelengths.

The photoluminescence spectroscopy gave information about the electronic energy states of the excited atoms and allowed for comparison between the acquired results and results described in literature.

A detailed discussion pertaining to the results of the respective coatings and their properties are given in the following chapters.

5.4.2 Frustules coated with Er^{3+} doped Y_2SiO_5

Frustules subjected to one dip coating cycle were found to suffer small structural changes to the pores as when compared to pores of frustules in the temperature exposure experiment subjected to equivalent temperatures.

These changes would be expected as the residence time of frustules during annealing post coating is two hours, versus one hour in the temperature exposure experiment, meaning that signs of melting would likely be exaggerated for the specimens subjected to the longest residence times.

Frustules coated twice, were however found to develop less structural changes as when compared to the frustules coated once. For the frustules subjected to four coatings, the structural features were remarkably well conserved and had a striking similarity to pores of frustules only subjected to annealing at 400°C in the temperature exposure experiment. It would thus appear that the frustules became increasingly heat resistant upon increased dip cycles.

All aforementioned changes were observed to occur in the cribellum pores and the associated velum membrane of the frustules pores. These are the areas of the frustules displaying the finest and most delicate structural features and thus heat related changes are most likely to manifest in such areas. No changes in external frustules structure were observed.

The observations of improved structural conservation were followed by an increase in yttrium concentration for frustules subjected to increased dip cycles as indicated by EDS analysis. In every EDS analysis, no traces of

chlorine were detected, meaning that the desired decomposition reactions were taking place and forming oxides. Frustules subjected to four coating cycles were found to contain small levels of calcium.

The presence of calcium should not affect the melting temperature of the frustules since it was present only in low concentrations compared to the concentration of yttrium.

According to the proposed chemical reactions taking place upon deposition of the oxides, there is formation of an yttrium silicate (Y_2SiO_5). According to Sarkisov et al., the melting points of yttrium silicates (Y_2SiO_5 , $Y_2Si_2O_7$) are higher than the melting point of silica [122]. The melting point would however be dependent on the yttrium concentration [122, 123].

Assuming that the yttrium silicate forming reactions are taking place only at surfaces, the result would be a thin external layer of yttrium silicate on the frustules surfaces. In case of the very small structural features found in the pores, the relative yttrium silicate concentration as when compared to thicker structures, would be higher.

The expected results of elevated concentrations of yttrium silicate would be more heat resistance as when compared to original frustules pores. For the frustules subjected to one coating cycle, this means that the concentration of yttrium silicate is too low for any significant effects to occur. At increased numbers of coating cycles the increased concentration of heat resistant yttrium silicate can likely be attributed to the observed increases in conservation of the most delicate pore structures.

Frustules subjected to one and two dip coating cycles were not found to display any photoluminescent properties upon investigation by fluorescence microscopy and photoluminescence spectroscopy. This was likely an effect of low concentrations of yttrium silicate and erbium dopant, forming a very thin film on the frustules surface.

Film thickness has been found to have a significant effect on photoluminescent phenomenon, as low film thickness was found to give less intensity and in some cases no photoluminescence [124, 125].

According to Ouyang et al., the luminescence of rare earth doped yttrium silicate increases 5-10 times if subjected to annealing temperatures above 800°C , the increase was attributed to higher levels of crystallinity in the samples [70].

High temperature annealing was however not performed in the experimental work during coating of frustules due to fear of damages to the pores, as were found in the temperature exposure experiment. The lack of heat treatment at such temperatures might also to some extent contribute to the observed lack of photoluminescent properties in frustules coated once and twice.

Small levels of molybdenum (Mo) could also be detected in the frustules coated twice with Y/Er solution. The presence of this element can likely be attributed to the stainless steel grid upon which the frustules were coated and annealed [126]. This indicates that some cross contamination between support and sample has occurred.

Presence of molybdenum should however not have detrimental effects on photoluminescence. According to Dong et al., four fold improvements in photoluminescence properties were observed upon co-doping molybdenum with erbium in Er-Yb oxide systems [127].

Frustules subjected to four coating cycles were found to possess photoluminescent properties during investigations in fluorescence microscope and photoluminescence spectroscopy. The strongest fluorescence was found to exist for excitation with blue light at 440-475 nm resulting in bright green fluorescence at 530-550 nm.

Upon excitation with UV light at 365 nm the resulting fluorescence was found to be in the blue region at 440-470 nm. The weakest fluorescence was found upon excitation with 630-640 nm light which resulted in red fluorescence at 650-690 nm. The fluorescence appeared to be evenly distributed on the frustules structures in terms of intensity.

The fluorescent emission of light from the frustules was found to behave similar to the expected emission lines of Er^{3+} given in Figure 13. Upon investigation of frustules coated four times with Y/Er solution featuring photoluminescence spectroscopy, a green laser ($\lambda = 532 \text{ nm}$, 10 mW) was utilized as an excitation source and a filter inserted in the pathway to avoid laser light entering the spectroscopy analytical unit.

This filter would then effectively block any observation of photoluminescence at lower wavelengths. Thus any activity in the blue end of the electromagnetic spectrum was not observed for investigation with photoluminescence spectroscopy.

According to the spectroscopic results presented in Figure 59, three groups of peaks were found centered on ~540 nm (green), ~660 nm (red) and ~800 nm (IR). These peaks are described by Stanley et al. as belonging to the Er^{3+} ion [116, 128]. Peaks centered at ~540 nm can be attributed to the $^4\text{S}_{3/2}$ to $^4\text{I}_{15/2}$ transition. Peaks at ~660 nm arise from the $^4\text{F}_{9/2}$ to $^4\text{I}_{15/2}$ transition whereas peaks at ~800 nm stem from the $^4\text{F}_{9/2}$ to $^4\text{I}_{15/2}$ transition [63, 129].

The other peaks presented in Figure 59, centered on ~980 nm (IR) are described by Tkachuk et al., as belonging to the $^4\text{I}_{9/2}$ to $^4\text{I}_{15/2}$ transition of Er^{3+} [129]. Peaks centered on ~860 nm (IR) are unidentified and the author did not find any references to these emission peaks in literature upon comparison with emission spectra of the elements present in the EDS analysis.

Regarding traces of calcium being detected in frustules subjected to four coating cycles, the presence of this element was likely a result of contaminants found in the frustules used in this experiment since no other samples displayed a concentration of the element. The existence of calcium should not have any detrimental effects with regards to photoluminescence since it is described as a constituent of several phosphors in literature [130, 131].

The erbium dopant, which was also introduced in the dye, is responsible for the color of the photoluminescence and works by substituting a Y^{3+} ion with an Er^{3+} ion in Y_2SiO_5 [70, 71]. No trace of the erbium dopant could be detected by use of EDS, this is likely the result of the dopant existing in concentrations below the detection level of the EDS system [112].

The presence of the peaks in the photoluminescence spectrogram and the colors of the fluorescent light still confirm the existence of the element within the frustules [63, 116].

Since no traces of erbium could be detected, and this likely can be attributed to the element existing in concentrations below the detection limit of the EDS system, there is some uncertainty about the decomposition of the chloride precursor.

However, given the high temperatures of annealing combined with findings in literature describing this decomposition reaction along with a very large negative Gibbs energy of reaction at the annealing temperatures, it is highly likely that such a decomposition reaction occurs.

Since a green laser with a wavelength of 532 nm was utilized as an excitation source, the down-conversion of light was not observed as this would require light in the IR region. It is however likely that the presences of energy levels required for down-conversion are existent as a natural consequence of the presence of erbium ions in the material [132].

5.4.3 Frustules coated with Mn²⁺ doped Zn₂SiO₄

Frustules coated once, twice and four times with Zn/Mn solution was found to be structurally intact with respect to external features. No major external differences could be detected upon comparison with frustules subjected to an equivalent coating procedure featuring Y/Er dye. This would also be true in comparison with original frustules only subjected to similar temperatures.

Pore structures of frustules subjected to one coating cycle with Zn/Mn solution, were found to be well conserved as when compared to pores of frustules subjected to identical temperature less chemicals. However some effects of what probably can be attributed to heat related damages can be seen as a lack of some of the more detailed features in the pores of once coated frustules, when compared to pores of frustules only subjected to heat treatment at 800°C.

No significant structural changes with respect to pore features was detected upon comparison with frustules subjected to an equivalent coating cycle featuring Y/Er solution. This means that structural behaviour is still determined by the silica of the frustules rather than the deposited oxides at one coating cycle.

As mentioned earlier, effects of heat related damages will likely be exaggerated in the specimens subjected to longer residence times at elevated temperatures and thus the effects will appear more visible in pores of frustules that were coated due to the extended exposure time in high temperatures.

Frustules subjected to two and four coating cycles featuring Zn/Mn solution, were found to have developed some more extensive heat related changes as when compared to frustules coated only once. There was however no observed increases in heat related changes from the twice coated frustules to the four times coated frustules.

In this case the results started to differ from what was observed upon comparison with frustules coated two and four times with the Y/Er solution. Since frustules coated with Y/Er were found to have increased conservation of pore structures and frustules coated with Zn/Mn solution were found to have slightly decreased conservation of pore structures.

What is termed structural changes does in this case refer to heat related changes in size of the cribellum pores as a result of the associated velum membrane melting. These structures are the dominant features of the frustules surfaces. In some cases several cribellum pores were found to have formed larger holes by this melting action, exposing the underlying cribrum pores.

According to findings in literature, zinc silicate has a lower melting point as when compared to silica which frustules consists of [133]. This would mean that the previously observed improvements to pore structures, as were the case for Y/Er coated frustules, are not expected to occur. Rather, due to the lower melting temperature of zinc silicate, a reduced conservation of pore structure would be expected. This is however dependent on zinc silicate concentration [133].

Effects of the lower temperature resistance would likely be observed in the pores due to the fine features being coated with Zn/Mn dye, forming zinc silicate. The relative concentration of Zn_2SiO_4 in the pores would be higher as when compared to the rest of the frustules structures, since the surface area available for reaction is much greater in the pores.

According to results of EDS analysis, zinc concentration was found to increase with increased numbers of dip coating cycles as was expected. No traces of chlorine could be detected which means that all decomposition reactions have occurred and formed the corresponding silicates.

Concentration of zinc was found to double from the once coated frustules to the twice coated frustules and was found to be over eight times higher in frustules subjected to four coating cycles versus frustules coated once. This sudden increase in zinc concentration might be attributed to evaporation of solvents from the coating solution, in effect causing a more concentrated solution.

Surprisingly, all samples of frustules coated with Zn/Mn precursor solution, were found to contain large concentrations of tin as indicated by EDS analysis. In every case concentration of the contaminant (Sn) was found to exceed the concentration of zinc.

To find such levels of contaminants in one of the chemical precursors would be highly unlikely, since all chemicals were purchased new and unopened, in addition no other than the author handled the chemicals. Contamination remaining in the frustules post cleaning could be a possible explanation but upon comparison of Table 9, Table 10 and Table 11, the concentration of the element is found to increase, whereas the amount of frustules in each experiment was kept constant.

Thus only two possible explanations would remain:

1. Contaminants surviving the cleaning process of the glassware and thereby entering the precursors which would ultimately reveal itself as an increased concentration of pollutant upon increased dip cycles.
2. Elements found in the stainless steel grid forming soluble intermediates dissolving into the precursors, being transferred to the frustules and thus increasing concentration of the contaminant upon increased dip cycles.

It should be mentioned that the concentration of tin was found to increase dramatically from the once coated frustules to the twice coated frustules. No increase in tin concentration was however detected from the twice coated frustules to the four times coated frustules.

Given the fact that no increase in concentration of the contaminant was detected despite increased number of dip cycles for the twice and four times coated frustules, it would be tempting to attribute the presence of the contaminant to leeching from the stainless steel support grid.

An interesting observation with regards to the above stated scenario was the disintegration upon handling of the stainless steel grids supporting the frustules subjected to two and four coating cycles featuring Zn/Mn solution post annealing. Since this behaviour was not observed during dip coating of frustules with Y/Er solution, it is very likely that some reaction has affected the stainless steel grid.

Given the fact that few heat related changes could be observed between twice and four times coated frustules along with the fact that concentration of zinc was found to have increased whereas the concentration of tin was virtually unchanged. It is very probable that the concentration of tin is responsible for the observed heat related changes since presence of tin in silica will cause a depression in the melting point [134].

Formation of zinc stannate (Zn_2SnO_4) can thus not be eliminated, due to the high concentration of the contaminant (Sn). No information was found in literature with respect to thermodynamics of formation for such a compound, thus any thermodynamic considerations with respect to probability of formation between zinc silicate and zinc stannate cannot be made.

The presence of the contaminant is nevertheless highly undesirable and if time permitted the entire experiment should have been attempted again, but such an event would also require the finding of a completely inert support for the dip coating procedure as well as purchasing new precursors and is thus moved to future work.

A high concentration of carbon as indicated by EDS analysis, can be attributed to the carbon coating process which was performed to avoid problems related to charging of the samples.

Frustules subjected to one and two coating cycles featuring the Zn/Mn precursor solution, were not found to possess any photoluminescent properties upon investigation with fluorescence microscopy and photoluminescence spectroscopy. This can likely be attributed to low concentrations of the precursors in the coating solution resulting in low concentrations of the Mn^{2+} doped Zn_2SiO_4 on the frustules surfaces.

According to Ma et al. the presence of tin was found to increase luminescence in Si rich silica films [135]. It should however be mentioned that tin was only present as a dopant in that study. What occurs at the much higher concentrations observed in this work was not found described in literature.

No traces of manganese could be detected during the EDS investigation. This is likely the result of Mn^{2+} existing in concentrations below the EDS detection limit [112]. Manganese would be substituted for one Zn^{2+} ion in the Zn_2SiO_4 species and should be responsible for the photoluminescent behaviour. Manganese is thus an activator centre [82, 83].

Since no traces of manganese could be detected, and this likely can be attributed to the element existing in concentrations below the detection limit of the EDS system one cannot be entirely certain about the decomposition of the chloride precursor.

However, given the high temperatures of annealing combined with findings in literature describing this decomposition reaction, along with a negative Gibbs energy of reaction at the annealing temperatures, it is highly likely that such a reaction occurs.

Frustules coated four times with the Zn/Mn dye were found to inhabit fluorescent abilities upon investigation with fluorescence microscopy. The frustules were found to give off weak blue light at 445-450 nm when excited by 365 nm light, a more intense green light at 530-550 nm upon excitation by 440-475 nm light and a weak red light at 650-690 nm when excited by 630-640 nm light. The fluorescence was found to be rather weak and unevenly distributed with respect to the frustules structure.

The cause of the unevenly distributed fluorescence is unclear as no literature was found with regards to concentration quenching caused by tin. Another possibility is the chance of uneven coating in areas of intimate contact between the frustules. The samples were however swirled to reduce the probability of such events occurring.

Upon investigation with photoluminescence spectrometry, emission was found to emanate from three peaks positioned on top of a broad emission section stretching from ~470 nm to ~800 nm. The three peaks were centred at ~570 nm, ~610 nm and ~680 nm. These peaks correspond to yellow, orange and red emission.

Formation of Zn_2SnO_4 can possibly be a cause of the broad orange and red emissions centred on 610 nm and 670 nm [118]. Whereas the yellow emission centred on 570 nm can both be attributed to the Mn^{2+} doped Zn_2SiO_4 as well as emission from Zn_2SnO_4 [117, 118]. In the case of emission from manganese, 3d shell transitions are responsible for the yellow luminescence [136].

Since a UV laser with a wavelength of 325 nm was utilized as an excitation source, and the observed photoluminescence was found to be in the yellow, orange and red part of the electromagnetic spectrum, the incident light was down converted.

5.5 Nitrided frustules

Frustules were subjected to simultaneous metallothermic reduction and nitriding experiments to determine the feasibility of producing three dimensional frustule replicas consisting of silicon nitride. The experiments were undertaken by use of a stainless steel reactor chamber featuring threaded end caps that was built by the author.

The reactor vessel had a volume of 23.32 cm³. All experimental procedures along with all amounts of specimens and chemicals were sought to be performed as identically as possible for each experiment. This was done to avoid problems with differences in procedure possibly leading to differences in results.

The samples were investigated by use of scanning electron microscope (SEM) featuring energy dispersive x-ray spectroscopy. Samples displaying the most interesting features were investigated by use of Raman spectroscopy to verify nitride formation as indicated in EDS.

The simultaneous metllothermic reduction and nitridding reactions were performed at 650°C and 800°C. This was done to investigate if increased temperatures could be attributed to increased formation of silicon nitride or oxynitride.

5.5.1 Frustules nitrided at 650°C

After exposure to a temperature of 650°C for two hours the reactor was extracted and allowed to cool to room temperature before the samples were extracted. A strong smell of ammonia followed immediately after opening the reactor chamber. Upon visual inspection of these samples, a slight colour change towards yellow was observed in the frustule mass and the area surrounding the frustules were coated in a fine yellow to greenish powder.

The underlying magnesium powder in the stainless steel bowl also had a slight greenish to yellow appearance to it. Upon cleaning the frustules in a mixture of HCl (1M) and ethanol, there was bubbling and apparent evolution of gas immediately upon immersion. The evolution of gas subsided after a short time (~1-1.5 min). The frustules were then rinsed repeatedly in distilled water before being rinsed in acetone and dried. After cleaning, the frustules had a rather dark colour.

The frustules were then carbon coated before investigation by SEM featuring EDS. Upon investigation of the frustules using an acceleration voltage of 3.0 keV, small peaks of nitrogen became apparent. This is illustrated in Figure 76.

According to the quantified EDS results nitrogen could only be found in average concentrations of 2.26 atomic percent which was equivalent to 1.34 weight %, this is illustrated in Table 13. The numbers indicate the presence of silicon nitride (Si_3N_4) or an oxynitride (SiO_xN_y) in low concentrations.

Even if magnesium was present according to the elemental analysis, there was very little probability that the nitrogen could exist as magnesium nitride. This could be attributed to magnesium nitride being highly unstable with regards to hydrolysis as can be seen from the large negative Gibbs energies of reaction [68]. Thus it is highly unlikely that such a compound can survive prolonged acid cleaning procedures utilized in this work.

Silicon was by far the most dominant element and was found to exist in average concentrations of 65.13 atomic percent according to quantified EDS results. Upon comparison with the concentration of oxygen it became clear that much of this silicon actually existed in the elemental state instead of being chemically bound to oxygen as silica.

This became clear upon considering the stoichiometric relations between the atoms found in silica (SiO_2), which indicated that for every atomic percent silicon there should be twice the number atomic percent monoatomic

oxygen. As an example, for silica this would then be ~33.33 atomic percent silicon and ~66.67 atomic percent oxygen.

Since silicon is found to exist in concentrations three times higher than what was expected for silica, the conclusion must be that much of the silica had been reduced in contact with magnesium vapour at the elevated temperatures. Bearing the previous observations in mind, it would therefore be very likely that the magnesium found to exist in the frustules post reaction actually exists as magnesium oxide.

Given the acid cleaning regime and the observed evolution of gas upon contact between acid and frustules, there is an even greater probability of magnesium existing in oxide form. Due to the low concentration of nitrogen as found upon investigation with an acceleration voltage of 3.0 keV, there is a possibility of silicon nitride only existing as a thin film at the surface of the frustules.

An acceleration voltage of 15.00 keV was then chosen in the SEM and the frustules subjected to EDS analysis. In these analyses the nitrogen peaks had disappeared and the dominant elements were found to be silicon (Si), oxygen (O) and carbon (C). A trace of sodium could also be detected along with a slightly higher concentration of magnesium (Mg) as when compared to the analyses at 3.00 keV.

Presence of sodium can probably be attributed to cross contamination from impurities found in glass ware used during cleaning procedures or as an impurity inherent to just that sample of frustules. Carbon can be attributed to the carbon coating procedure utilized to avoid problems related to charging of the specimen in SEM.

Again silicon were found to exist in higher concentration than oxygen, but this time at a slightly lower ratio as the higher excitation voltage utilized gave information about the chemical environment deep beneath the surfaces of the frustules.

This was also expected, since the metallothermic reduction of silicon and nitride forming reactions likely would be more complete at or near the surfaces as a function of temperature, diffusion length, formation of oxide layers etc. [100]. Thus the concentration of reduced silicon and nitride would diminish somewhat over a distance below the surface of the frustules.

Given the disappearance of the nitride peaks upon increasing the acceleration voltage in SEM, it would be probable that the silicon nitride or silicon oxynitride has formed only at the surface of the frustules at this temperature. Thus no further attempts were made with regards to nitriding at this temperature. No further analysis was attempted due to the low concentration of the nitride or oxynitride.

Frustules subjected to nitriding at 650°C were found to have developed some superficial porosity which was visible upon high magnification as can be seen in Figure 75. The cause of the porosity is likely related to sintering effects occurring during nitride formation. Several of the frustules subjected to nitriding at 650°C were found to have smaller damages to the external structure.

The reason for these damages might be the initial cleaning process to remove all organic matter as performed by NTNU Department of Biotechnology. Another possibility is the formation of gas upon contact with acid cleaning media, generating enough pressure to cause damages in the frustules structures.

5.5.2 Frustules nitrated at 800°C

In order to assess the effect of reaction temperature on the nitride formation, a second set of nitriding experiments were carried out at 800°C. All other parameters were kept identical to the experiments carried out at 650°C. The temperature of 800°C was chosen because magnesium nitride becomes unstable and decomposes at this temperature [43].

Magnesium nitride is a possible side reaction in the simultaneous metallothermic reduction and nitriding reaction as indicated in the theoretical section. Should the compound only exist as an intermediate it could enhance the formation of other nitrides upon decomposition [109].

After being exposed to 800°C for two hours the reactor was extracted and allowed to cool to room temperature before being opened. The immediate difference observed between the experiment at 650°C and the present one was the lack of ammonia smell upon extraction of the samples as were experienced previously.

The frustules had taken a deep grey to bluish colour and the surrounding grid was covered in a fine yellow to greenish powder. After a short time in normal atmosphere a smell of ammonia was evolved from the samples. This might be an indication to the presence of magnesium nitride being hydrolyzed by atmospheric moisture.

Upon cleaning in dilute hydrochloric acid (1 M) and ethanol, gas bubbles were evolved from the frustules for a short time (1.5-2 minutes). After acid cleaning the frustules were rinsed repeatedly in distilled water and acetone before being dried.

All frustules samples were then carbon coated prior to investigation in SEM featuring EDS. Initially an acceleration voltage of 3.00 keV was chosen. Upon investigation with EDS the dominant peaks was found to be silicon (Si) and oxygen (O) closely followed by nitrogen (N), magnesium (Mg) and carbon (C).

When compared against frustules nitrated at 650°C, the peaks representative of nitrogen had significantly more area for the frustules at 800°C. This can be seen by comparing the EDS spectrums acquired at 3.00 keV for frustules nitrated at 800°C seen in Figure 82 and frustules nitrated at 650°C seen in Figure 76.

As expected from the EDS spectrums, the nitrogen concentration was found to be 17.91 atomic percent. This is nearly eight times higher than for the frustules nitrated at 650°C.

This nitrogen was likely present as either nitride or oxynitride due to the very low probability of nitrogen existing in the form of magnesium nitride, given the acid cleaning procedure and the ease of hydrolysis with respect to magnesium nitride.

The presence of β -silicon nitride was later determined by use of Raman analysis and comparison of the acquired results with literature [121]. The result of this analysis is given in Figure 84. The presence of large concentrations of silicon in comparison with monoatomic oxygen was also detected.

This means that silicon must exist in a reduced elemental state, since the atomic distribution with regards to stoichiometric distribution in silica (SiO_2) would be expected to be ~33.33 atomic percent silicon and ~66.67 atomic percent oxygen.

In this case the silicon exists in concentrations 2.5 times greater than oxygen. As discussed for the case of frustules nitrided at 650°C, this is likely the cause of metallothermic reduction of silica upon contact with magnesium vapour at elevated temperatures.

A rather high concentration of magnesium can likely be attributed to the presence of magnesium oxide. This would be very likely because of the acid cleaning process and the large negative Gibbs energy of reaction upon hydrolysis with acid. Another reason for the formation of magnesium oxide would be the large negative Gibbs energy of reaction for the metallothermic reduction process.

The presence of rather large concentrations of magnesium oxide would still mean that the cleaning process could be improved. Presence of carbon in the samples can be attributed to the carbon coating performed to avoid problems related to charging of the specimen in SEM.

In order to increase the depth of the emission volume, the acceleration voltage was increased to 15.00 keV. This allowed for the detection of silicon nitride at some distance into the frustules material. According to the quantified results, a small decrease of 1 atomic percent in the nitrogen concentration could be detected upon comparison with the results acquired at 3.00 keV.

This could be compared to the results found in analysis of the frustules nitrided at 650°C where nitrogen was found to disappear at analysis with 15.00 keV given in Table 14. Such results might substantiate that the nitride formation at 650°C is only superficial, whereas nitride formation at 800°C is more complete.

A slight decrease in silicon content could also be detected upon increasing the acceleration voltage, this was also observed for the frustules nitrided at 650°C. The decrease in concentration of silicon along with the increase in concentration of oxygen can likely be attributed to a higher rate of reaction at the frustules surfaces as when compared to the bulk [100]. The observed decrease in magnesium concentration can likely be attributed to the same effect.

According to the results of the Raman spectroscopy given in Figure 84 and the subsequent analysis of these results upon comparison with findings in literature, revealed that reduced silicon was found to consist of amorphous and nanocrystalline silicon [119]. The nanocrystalline silicon was found to have a size of ~2.2 nm [120].

Structural features of frustules nitrided at 800°C were found to be extremely porous as compared to the original frustules structures. This effect can likely be attributed to sintering effects occurring during nitride forming reactions [137, 138].

6 Conclusion

6.1 Temperature exposure characterisation

By utilizing a muffle furnace and subjecting frustules to a series of increasing temperatures the thermal behaviour of frustules was determined.

- At temperatures of 400°C, no changes in pore structures were found. No changes were found with regards to external features of the frustules structure.
- Small changes were found occurring to frustules pore structures subjected to 600°C. At 800°C the structural changes had increased significantly. The changes were found to be caused by a gradual increase in cribellum pore size as a function of the outer velum membrane melting. No changes in external structural features were observed.
- Frustules exposed to 1000°C were found to suffer significant structural damages to the pores. These changes were attributed to severe melting of outer velum membrane and cribellum pores accompanied with some changes to the underlying cribrum pores. External structural features of the frustules were found to have changed as the frustules were found to appear slightly elongated.
- At temperatures of 1200°C all structural features previously seen in the pores were found to have melted, leaving cavities that were melted shut. Severe deformation of the frustules external structural features were found to have occurred as frustules had delaminated and adopted a wavy structure to the valve surfaces.

6.2 Coating of frustules with up and down converting oxides

Upon dip coating frustules with oxides known for the up and down-conversion of light and the subsequent characterization of the coated frustules, the thermal, structural, photoluminescent and chemical features of the frustules were determined.

- Frustules subjected to one and two dip coating cycles in a solution of erbium and yttrium chlorides dissolved in a mixture of acetonitrile and ethylene glycol, were not found to possess photoluminescent properties.
- Frustules subjected to four coating cycles were found to give of photoluminescent light with peaks centred on 540 nm, 660 nm, 800 nm, 860 nm and 980 nm upon excitation with a green laser of 532 nm, during investigation with photoluminescence spectroscopy. Upon investigation in fluorescence microscope the four times coated frustules were found to give of bright blue light of 445-450 nm upon excitation with light of 365 nm, strong green light of 530-550 nm when excited by 440-475 nm light and a weak red light at 650-690 nm upon excitation with 630-640 nm light.
- Pore structures of frustules subjected to four dip coatings in Y/Er solution, were found to display very few temperature related changes as when compared to frustules subjected to a lesser number of coatings. This effect was found to be caused by increased formation of temperature resistant yttrium silicate on surfaces of frustules subjected to the highest number of dip coating cycles. Concentration of

yttrium was found to increase with increasing dip cycles by use of EDS analysis. No traces of erbium could be detected in any of the coated frustules and was attributed to the element existing in concentrations below the detection limit of the EDS equipment.

- Frustules subjected to one and two dip coating cycles in a solution of manganese and zinc chlorides dissolved in a mixture of acetonitrile and ethylene glycol, were not found to display any photoluminescent properties.
- Frustules subjected to four coating cycles were however found to give of photoluminescent light centred on 570 nm, 610 nm and 680 nm upon excitation with a laser of 325 nm. Frustules coated four times examined in fluorescence microscope were found to give of weak blue light at 445-450 nm when excited by 365 nm light, a more intense green light at 530-550 nm upon excitation by 440-475 nm light and a weak red light at 650-690 nm when excited by 630-640 nm light.
- A slight increase in temperature related changes was observed for frustules coated twice by Zn/Mn solution as compared to frustules only coated once. No increase in heat related changes was observed for frustules subjected to four coating cycles upon comparison to frustules coated twice. According to EDS analysis, zinc concentration was found to increase with increasing dip cycles. Presence of tin, a contaminant was found to exist in all frustules samples coated with Zn/Mn solution. For twice and four times coated frustules the concentrations of tin were found to have increased drastically but to similar levels. The temperature related changes were thus attributed to the presence of the tin contaminant. No traces of manganese were detected which was attributed to the element existing in concentrations below the detection limit of the EDS equipment.

6.3 Nitriding of frustules

The simultaneous metallothermic reduction and nitriding of frustules allowed for the production of silicon nitride frustules replicas and the characterisation of such replicas with respect to chemical and structural features.

- Attempted nitriding of frustules at 650°C resulted in the formation of a thin layer of silicon nitride on the surfaces of the frustules. At increased acceleration voltages, no presence of nitrogen was found. High magnification in SEM revealed increased porosity of the frustules surfaces.
- Frustules nitrided at 650°C were found to contain significant amounts of reduced silicon by EDS analysis. This was seen as a higher atomic concentration of silicon as compared to atomic concentration of oxygen. Elevated levels of reduced silicon were found to be resulting from metallothermic reduction of silica by magnesium vapour. At increased acceleration voltages concentration of silicon was found to decline. This was found to be caused by higher rates of reaction at the frustules surfaces.
- Attempted nitriding of frustules at 800°C were found to result in increased formation of silicon nitride. The results were collaborated by Raman spectroscopy, suggesting that β -silicon nitride was present. Upon increased acceleration voltage in EDS, a slight but insignificant decrease in nitrogen concentration was detected along with a decrease in reduced silicon concentration. This was found to be consistent with a more complete formation of nitride in the bulk of the samples. The slight decrease in concentration of nitrogen and reduced silicon was attributed to more efficient reaction parameters at the frustules surfaces as compared to bulk parameters.

- Frustules nitrided at 800°C were found to contain high concentrations of reduced silicon by EDS analysis. Presence of reduced silicon was based upon detection of significantly higher atomic concentrations of silicon as compared to atomic concentrations of oxygen. The presence of reduced silicon was found to be resulting from magnesiothermic reduction of silica. The reduced silicon was determined to be a mixture of amorphous and nanocrystalline silicon, having a crystalline size of ~2.2 nm according to results of Raman spectroscopy.
- Frustules nitrided at 800°C were found to have developed an extreme porosity as when compared to frustules nitrided at 650°C and original frustules. The porosity was found to be caused by sintering effects during silicon nitride forming reactions.
- Major structural features of the frustules nitrided at 800°C were found to be well preserved meaning silicon nitride frustules replicas were produced successfully.

7 Future work

The results of the experimental work performed during the course of this master's thesis, have shown that diatom frustules may be successfully coated with up and down converting elements. It was also shown that diatom frustules can be nitrated and that the 3 dimensional nitrate replicas were found to have preserved both micro and nanoscale structural features. Future work can thus be extended in several directions.

- Since increasing the thickness of the coating layer was found to give better photoluminescence, it would be interesting to determine the optimum thickness of this layer.
- Thickness of the current layer should be determined.
- The experimental procedure with regards to the Zn/Mn coating procedure should be attempted on a completely inert support, featuring new precursors due to the presence of contaminants experienced in this work.
- Given the interesting physical and chemical aspects of the possible contaminant zinc stannate, an interesting aspect would be the intentional coating of frustules with zinc stannate and the consequent doping to achieve luminescence.
- The existence of up and down-conversion phenomenon in diatom frustules would be highly interesting to incorporate in photovoltaic solar cells.
- The characterization of the up and down-conversion phenomenon with regards to frustules coated in a similar manner to this thesis would be interesting.
- Parameters determining the optimum coating efficiency should be defined.
- Chemical, thermal and mechanical stability of coated diatom frustules should be investigated with respect to future photovoltaic use.
- The parameters determining formation of the nitrate should be optimized.
- The chemical, thermal and mechanical stability of nitrated frustules should be examined.
- The potential use of nitrated frustules as a catalyst support for use in chemical engineering should be investigated.
- The use of nitrated frustules as an antireflective coating should be examined.
- The incorporation of doped silicon into the nitrated frustules structure, forming a small photovoltaic unit should be attempted.

8 References

1. Lonngren, K.E. and E.-W. Bai, *On the global warming problem due to carbon dioxide*. Energy Policy, 2008. 36(4): p. 1567-1568.
2. Baranzini, A., M. Chesney, and J. Morisset, *The impact of possible climate catastrophes on global warming policy*. Energy Policy, 2003. 31(8): p. 691-701.
3. Nordell, B., *Thermal pollution causes global warming*. Global and Planetary Change, 2003. 38(3-4): p. 305-312.
4. Peters, M., et al., *Shedding light on solar technologies—A techno-economic assessment and its policy implications*. Energy Policy, 2011. 39(10): p. 6422-6439.
5. Dincer, F., *The analysis on photovoltaic electricity generation status, potential and policies of the leading countries in solar energy*. Renewable and Sustainable Energy Reviews, 2011. 15(1): p. 713-720.
6. Rockett, A.A., *The future of energy – Photovoltaics*. Current Opinion in Solid State and Materials Science, 2010. 14(6): p. 117-122.
7. Kerr, M.J., et al., *Surface recombination velocity of phosphorus-diffused silicon solar cell emitters passivated with plasma enhanced chemical vapor deposited silicon nitride and thermal silicon oxide*. Journal of Applied Physics, 2001. 89(7): p. 3821-3826.
8. Salman, K.A., K. Omar, and Z. Hassan, *The effect of etching time of porous silicon on solar cell performance*. Superlattices and Microstructures, 2011. 50(6): p. 647-658.
9. De Stefano, L., et al., *Marine diatoms as optical biosensors*. Biosensors and Bioelectronics, 2009. 24(6): p. 1580-1584.
10. Round, F.E., R.M. Crawford, and D.G. Mann, *The Diatoms: Biology & Morphology of the Genera*. 1990: Cambridge University Press.
11. De Stefano, L., et al., *Nano-biosilica from marine diatoms: A brand new material for photonic applications*. Superlattices and Microstructures, 2009. 46(1-2): p. 84-89.
12. De Tommasi, E., et al., *Multi-wavelength study of light transmitted through a single marinecentric diatom*. Opt. Express, 2010. 18(12): p. 12203-12212.
13. Gogoi, A., et al., *Laboratory measurements of light scattering by tropical fresh water diatoms*. Journal of Quantitative Spectroscopy and Radiative Transfer, 2009. 110(14-16): p. 1566-1578.
14. De Tommasi, E., et al. *Light micro-lensing effect in biosilica shells of diatoms microalgae*. 2008. Strasbourg, France: SPIE.
15. Sattler, K.D., *Handbook of Nanophysics: Nanoparticles and Quantum Dots*. 2010: Taylor and Francis.
16. Jeffryes, C., et al., *The potential of diatom nanobiotechnology for applications in solar cells, batteries, and electroluminescent devices*. Energy & Environmental Science, 2011. 4(10): p. 3930-3941.
17. Trupke, T., P. Würfel, and M.A. Green. *Up-and down-conversion as new means to improve solar cell efficiencies*. in *Photovoltaic Energy Conversion, 2003. Proceedings of 3rd World Conference on*. 2003.
18. Lee, D.-h., et al., *Biogenic silica based Zn₂SiO₄:Mn²⁺ and Y₂SiO₅:Eu³⁺ phosphor layers patterned by inkjet printing process*. Journal of Materials Chemistry, 2008. 18(31): p. 3633-3635.
19. Mazzoni, A.D. and E.F. Aglietti, *Aluminothermic reduction and nitriding of high silica materials (diatomite and bentonite) minerals*. Applied Clay Science, 2000. 17(3-4): p. 127-140.
20. Parkinson, J. and R. Gordon, *Beyond micromachining: the potential of diatoms*. Trends in Biotechnology. 17(5): p. 190-196.
21. Jones, V., *DIATOM INTRODUCTION*, in *Encyclopedia of Quaternary Science*, A.E. Editor-in-Chief: Scott, Editor. 2007, Elsevier: Oxford. p. 476-484.
22. Gordon, R., et al., *The Glass Menagerie: diatoms for novel applications in nanotechnology*. Trends in Biotechnology, 2009. 27(2): p. 116-127.
23. Santos-Hofschneider, F., *Diatom*, in *Marine Biology - Shine*. 2007.
24. Perez-Garcia, O., et al., *Heterotrophic cultures of microalgae: Metabolism and potential products*. Water Research, 2011. 45(1): p. 11-36.
25. Pahl, S.L., et al., *Heterotrophic growth and nutritional aspects of the diatom Cyclotella cryptica (Bacillariophyceae): Effect of some environmental factors*. Journal of Bioscience and Bioengineering, 2010. 109(3): p. 235-239.
26. Chepurinov, V.A., et al., *Experimental Studies on Sexual Reproduction in Diatoms*, in *International Review of Cytology*. 2004, Academic Press. p. 91-154.
27. Austin, W.E.N., R. James, and G.S.o. London, *Biogeochemical controls on palaeoceanographic environmental proxies*. 2008: Geological Society.

28. Lopez, P.J., et al., *Prospects in diatom research*. *Current Opinion in Biotechnology*, 2005. 16(2): p. 180-186.
29. Ottesen, P., *Processing and Characterization of Diatoms for Light Harvesting Materials in Solar Cells*, in *Department of Materials Science and Engineering*. 2011, Norwegian University of Science and Technology: Trondheim. p. 92.
30. Nassif, N. and J. Livage, *From diatoms to silica-based biohybrids*. *Chemical Society Reviews*, 2011. 40(2): p. 849-859.
31. De Stefano, L., et al., *Lensless light focusing with the centric marinediatom *Coscinodiscus walesii**. *Opt. Express*, 2007. 15(26): p. 18082-18088.
32. Bismuto, A., et al., *Marine diatoms as optical chemical sensors: A time-resolved study*. *Sensors and Actuators B: Chemical*, 2008. 130(1): p. 396-399.
33. Fuhrmann, T., et al., *Diatoms as living photonic crystals*. *Applied Physics B: Lasers and Optics*, 2004. 78(3): p. 257-260.
34. Noren, A.K., *Characterization of Structure and Optical Properties of Diatoms for improved Solar Cell Efficiency*, in *Department of Materials Science and Engineering*. 2011, Norwegian University of Science and Technology: Trondheim. p. 80.
35. Fernandes, L.F., L. Zehnder-Alves, and J.C. Bassfeld, *The recently established diatom *Coscinodiscus walesii* (*Coscinodiscales*, *Bacillariophyta*) in Brazilian waters. I: Remarks on morphology and distribution*. *Phycological Research*, 2001. 49(2): p. 89-96.
36. Hasle, G.R. and E.E. Syvertsen, *Chapter 2 - Marine Diatoms*, in *Identifying Marine Diatoms and Dinoflagellates*, R.T. Carmelo, et al., Editors. 1996, Academic Press: San Diego. p. 5-385.
37. Manabe, T. and S. Ishio, *Bloom of *Coscinodiscus walesii* and DO deficit of bottom water in Seto Inland Sea*. *Marine Pollution Bulletin*, 1991. 23(0): p. 181-184.
38. Guiry, M.D.G., *AlgaeBase*. World-wide electronic publication, 2011.
39. Fraas, L.M. and L.D. Partain, *Solar Cells and Their Applications*. 2010: John Wiley & Sons.
40. Chen, C.J., *Physics of Solar Energy*. 2011: John Wiley & Sons.
41. Green, M.A., *Solar cells: operating principles, technology, and system applications*. 1982: Prentice-Hall.
42. Pfisterer, F., *Photovoltaic Cells*, in *Ullmann's Encyclopedia of Industrial Chemistry*. 2000, Wiley-VCH Verlag GmbH & Co. KGaA.
43. Aylward, G.H. and T.J.V. Findlay, *SI Chemical Data*. 2007: John Wiley & Sons Australia.
44. Vikrant A. Chaudhari, C.S.S., *A Seminar Report On Losses In Solar Cells*. *Energy Systems Engg Indian Institute of Technology Bombay*, 2006.
45. Tvrdy, K. and P.V. Kamat, *4.09 - Quantum Dot Solar Cells*, in *Comprehensive Nanoscience and Technology*, L.A. Editors-in-Chief: David, D.S. Gregory, and P.W. Gary, Editors. 2011, Academic Press: Amsterdam. p. 257-275.
46. Markvart, T., *Light harvesting for quantum solar energy conversion*. *Progress in Quantum Electronics*, 2000. 24(3-4): p. 107-186.
47. Kim, J., et al., *Surface texturing of single-crystalline silicon solar cells using low density SiO₂ films as an anisotropic etch mask*. *Solar Energy Materials and Solar Cells*, 2010. 94(12): p. 2091-2093.
48. Gangopadhyay, U., et al., *Comparative study of different approaches of multicrystalline silicon texturing for solar cell fabrication*. *Solar Energy Materials and Solar Cells*, 2007. 91(4): p. 285-289.
49. Müller, J., et al., *TCO and light trapping in silicon thin film solar cells*. *Solar Energy*, 2004. 77(6): p. 917-930.
50. Söderström, K., et al., *Highly reflective nanotextured sputtered silver back reflector for flexible high-efficiency n-i-p thin-film silicon solar cells*. *Solar Energy Materials and Solar Cells*, 2011. 95(12): p. 3585-3591.
51. Richards, B.S., *Enhancing the performance of silicon solar cells via the application of passive luminescence conversion layers*. *Solar Energy Materials and Solar Cells*, 2006. 90(15): p. 2329-2337.
52. Parker, A.R. and H.E. Townley, *Biomimetics of photonic nanostructures*. *Nat Nano*, 2007. 2(6): p. 347-353.
53. Ronda, C.R., *Luminescence: From Theory to Applications*. 2004: John Wiley & Sons.
54. Zijlmans, H.J.M.A.A., et al., *Detection of Cell and Tissue Surface Antigens Using Up-Converting Phosphors: A New Reporter Technology*. *Analytical Biochemistry*, 1999. 267(1): p. 30-36.
55. Dai, S., et al., *Concentration quenching in erbium-doped tellurite glasses*. *Journal of Luminescence*, 2006. 117(1): p. 39-45.
56. Auzel, F., *Upconversion and anti-Stokes Processes with f and d Ions in Solids*. *ChemInform*, 2004. 35(16): p. no-no.
57. Goetzberger, A. and V.U. Hoffmann, *Photovoltaic Solar Energy Generation*. 2005: Springer.

58. Güdel, H.U., *New Light-Emitting Inorganic Materials*. CHIMIA International Journal for Chemistry, 1998. 52(10): p. 561-565.
59. Wang, F. and X. Liu, *Recent advances in the chemistry of lanthanide-doped upconversion nanocrystals*. Chemical Society Reviews, 2009. 38(4): p. 976-989.
60. Polman, A., *Erbium as a probe of everything?* Physica B: Condensed Matter, 2001. 300(1-4): p. 78-90.
61. Achatz, D., R. Ali, and O. Wolfbeis, *Luminescent Chemical Sensing, Biosensing, and Screening Using Upconverting Nanoparticles, Luminescence Applied in Sensor Science*, L. Prodi, M. Montalti, and N. Zaccheroni, Editors. 2011, Springer Berlin / Heidelberg. p. 29-50.
62. Pliska, T., et al., *Wavelength stabilized 980 nm uncooled pump laser modules for erbium-doped fiber amplifiers*. Optics and Lasers in Engineering, 2005. 43(3-5): p. 271-289.
63. Wang, D., et al., *Synthesis and NIR-to-violet, blue, green, red upconversion fluorescence of Er³⁺:LaOBr*. Journal of Alloys and Compounds, 2005. 397(1-2): p. 1-4.
64. Hebbink, G.A., *Luminescent materials based on lanthanide ions. Basic properties and application in NIR-LEDs and optical amplifiers*. 2002: Enschede. p. 163.
65. Qin, X., T. Yokomori, and Y. Ju, *Flame synthesis and characterization of rare-earth (Er³⁺, Ho³⁺, and Tm³⁺) doped upconversion nanophosphors*. Applied Physics Letters, 2007. 90(7): p. 073104-3.
66. Lee, D.H., et al., *Nanofabrication of Green Luminescent Zn₂SiO₄:Mn Using Biogenic Silica*. Electrochemical and Solid-State Letters, 2007. 10(7): p. K13-K16.
67. Wendlandt, W.W., *The thermal decomposition of the heavier rare earth metal chloride hydrates*. Journal of Inorganic and Nuclear Chemistry, 1959. 9(2): p. 136-139.
68. Roine, A., *HSC Chemistry 7.0*. 2006.
69. K.J Hubbard, D.J.S., *Thermodynamic stability of binary oxides in contact with silicon*. Journal of Materials Research, 1996. 11(11): p. 2757-2776.
70. Ouyang, X., A.H. Kitai, and R. Siegele, *Rare-earth-doped transparent yttrium silicate thin film phosphors for colour displays*. Thin Solid Films, 1995. 254(1-2): p. 268-272.
71. Robertson, J.M. and M.W. van Tol, *Cathodoluminescent garnet layers*. Thin Solid Films, 1984. 114(1-2): p. 221-240.
72. Wegh, R.T., et al., *Visible quantum cutting in Eu³⁺-doped gadolinium fluorides via downconversion*. Journal of Luminescence, 1999. 82(2): p. 93-104.
73. Zhang, Q.Y. and X.Y. Huang, *Recent progress in quantum cutting phosphors*. Progress in Materials Science, 2010. 55(5): p. 353-427.
74. Wegh, R.T., et al., *Quantum cutting through downconversion in rare-earth compounds*. Journal of Luminescence, 2000. 87-89(0): p. 1017-1019.
75. Oskam, K.D., et al., *Downconversion: a new route to visible quantum cutting*. Journal of Alloys and Compounds, 2000. 300-301(0): p. 421-425.
76. Richards, B.S., *Luminescent layers for enhanced silicon solar cell performance: Down-conversion*. Solar Energy Materials and Solar Cells, 2006. 90(9): p. 1189-1207.
77. Lee, D.H., et al., *A General Route to Printable High-Mobility Transparent Amorphous Oxide Semiconductors*. Advanced Materials, 2007. 19(6): p. 843-847.
78. Takesue, M., et al., *Phase formation of Mn-doped zinc silicate in water at high-temperatures and high-pressures*. The Journal of Supercritical Fluids, 2007. 43(2): p. 214-221.
79. Chao, R.E., *Thermochemical Water Decomposition Processes*. Product R&D, 1974. 13(2): p. 94-101.
80. Mohamed, M.A., *Non-isothermal dehydration and decomposition of manganese(II) malonate dihydrate*. Journal of Analytical and Applied Pyrolysis, 1994. 30(1): p. 59-72.
81. Lu, Q., P. Wang, and J. Li, *Structure and luminescence properties of Mn-doped Zn₂SiO₄ prepared with extracted mesoporous silica*. Materials Research Bulletin, 2011. 46(6): p. 791-795.
82. Sohn, K.-S., B. Cho, and H.D. Park, *Photoluminescence Behavior of Manganese-Doped Zinc Silicate Phosphors*. Journal of the American Ceramic Society, 1999. 82(10): p. 2779-2784.
83. Copeland, T.S., et al., *Synthesis and luminescent properties of Mn²⁺-doped zinc silicate phosphors by sol-gel methods*. Journal of Luminescence, 2002. 97(3-4): p. 168-173.
84. Balland, B. and A. Glachant, *Chapter 1 Silica, silicon nitride and oxynitride thin films: An overview of fabrication techniques, properties and applications*, in *Instabilities in Silicon Devices*, B. Gérard and V. André, Editors. 1999, North-Holland. p. 3-144.
85. Li, C.X. and T. Bell, *Potential of plasma nitriding of polymer for improved hardness and wear resistance*. Journal of Materials Processing Technology, 2005. 168(2): p. 219-224.
86. Riofano, R.M.M., et al., *Improved wear resistance of P/M tool steel alloy with different vanadium contents after ion nitriding*. Wear, 2008. 265(1-2): p. 57-64.

87. Yoo, J., et al., *Study on hydrogenated silicon nitride for application of high efficiency crystalline silicon solar cells*. *Solar Energy Materials and Solar Cells*, 2011. 95(1): p. 7-10.
88. Bao, Y., et al., *Quantitative model for the viscous flow and composition of two-phase silicon nitride-based particles in plasma-spray deposition*. *Journal of the European Ceramic Society*, 2009. 29(8): p. 1521-1528.
89. Carter, C.B. and G. Norton, *Ceramic Materials*. 2007: Springer.
90. Riley, F.L., *Silicon Nitride and Related Materials*. *Journal of the American Ceramic Society*, 2000. 83(2): p. 245-265.
91. Umemura, K., et al., *Diatom Cells Grown and Baked on a Functionalized Mica Surface*. *Journal of Biological Physics*, 2008. 34(1): p. 189-196.
92. Umemura, K., et al., *Morphology and Physical-Chemical Properties of Baked Nanoporous Frustules*. *Journal of Nanoscience and Nanotechnology*, 2010. 10(8): p. 5220-5224.
93. Nishi, Y. and R. Doering, *Handbook of Semiconductor Manufacturing Technology*. 2000: Marcel Dekker.
94. Ma, J., et al., *Synthesis of nanocrystalline titanium nitride at low temperature and its thermal stability*. *Journal of Alloys and Compounds*, 2009. 476(1-2): p. 603-605.
95. Pierson, H.O., *Handbook of Refractory Carbides and Nitrides: Properties, Characteristics, Processing, and Applications*. 1996: Noyes Publications.
96. Schei, A., J. Tuset, and H. Tveit, *Production of High Silicon Alloys*. 1997: Tapir.
97. Bao, Z., et al., *Chemical reduction of three-dimensional silica micro-assemblies into microporous silicon replicas*. *Nature*, 2007. 446(7132): p. 172-175.
98. Bao, Z., et al., *Syntheses of Porous Self-Supporting Metal-Nanoparticle Assemblies with 3D Morphologies Inherited from Biosilica Templates (Diatom Frustules)*. *Advanced Materials*, 2009. 21(4): p. 474-478.
99. Sandhage, K., *Materials "alchemy": Shape-preserving chemical transformation of micro-to-macroscopic 3-D structures*. *JOM Journal of the Minerals, Metals and Materials Society*, 2010. 62(6): p. 32-43.
100. Borissov, A.A., L.D. Luca, and A.G. Merzhanov, *Self-propagating high-temperature synthesis of materials*. 2002: Taylor & Francis.
101. Mishra, P., A. Chakraverty, and H.D. Banerjee, *Production and purification of silicon by calcium reduction of rice-husk white ash*. *Journal of Materials Science*, 1985. 20(12): p. 4387-4391.
102. Won, C.W., H.H. Nersisyan, and H.I. Won, *Solar-grade silicon powder prepared by combining combustion synthesis with hydrometallurgy*. *Solar Energy Materials and Solar Cells*, 2011. 95(2): p. 745-750.
103. Barati, M., et al., *Recovery of silicon from silica fume*. *Journal of Non-Crystalline Solids*, 2011. 357(1): p. 18-23.
104. Jong, B.W., G.J. Slavens, and D.E. Traut, *Synthesis of silicon and silicon nitride powders by vapour-phase reactions*. *Journal of Materials Science*, 1992. 27(22): p. 6086-6090.
105. Sjöberg, J. and R. Pompe, *Nitridation of Amorphous Silica with Ammonia*. *Journal of the American Ceramic Society*, 1992. 75(8): p. 2189-2193.
106. Jacob, K.T., R. Verma, and R.M. Mallya, *Nitride synthesis using ammonia and hydrazine—a thermodynamic panorama*. *Journal of Materials Science*, 2002. 37(20): p. 4465-4472.
107. Kim, D.-W., et al., *Synthesis of nanocrystalline magnesium nitride (Mg₃N₂) powder using thermal plasma*. *Applied Surface Science*, 2011. 257(12): p. 5375-5379.
108. Riedel, R. and I.W. Chen, *Ceramics Science and Technology: Structures*. 2008: Wiley-VCH.
109. Pawelec, A., et al., *Preparation of silicon nitride powder from silica and ammonia*. *Ceramics International*, 2002. 28(5): p. 495-501.
110. Vissokov, G.P. and P.S. Pirgov, *Preparation of ultradispersed magnesium nitride by the electric-arc low-temperature plasma technique*. *Journal of Materials Science*, 1996. 31(14): p. 3685-3690.
111. Cai, Y., et al., *3-D Microparticles of BaTiO₃ and Zn₂SiO₄ Via the Chemical (Sol-Gel, Acetate, or Hydrothermal) Conversion of Biological (Diatom) Templates*, in *Synthesis and Processing of Nanostructured Materials: Ceramic Engineering and Science Proceedings*. 2008, John Wiley & Sons, Inc. p. 49-56.
112. Hjelen, J., *Scanning elektron-mikroskopi*. 1989: p. 46-47.
113. Sahoo, H., *Förster resonance energy transfer – A spectroscopic nanoruler: Principle and applications*. *Journal of Photochemistry and Photobiology C: Photochemistry Reviews*, 2011. 12(1): p. 20-30.
114. Yvon, H.J., *IHR Series Imaging Spectrometers*. 2012, Horiba Scientific. p. 1-6.
115. Tu, Q. and C. Chang, *Diagnostic applications of Raman spectroscopy*. *Nanomedicine: Nanotechnology, Biology and Medicine*, 2012. 8(5): p. 545-558.

116. Stanley, D.A., et al., *SEM-mapped micro-photoluminescence studies of highly luminescent micro-clusters in erbium-doped silicon-rich silicon oxide*. *Journal of Luminescence*, 2011. 131(1): p. 72-77.
117. Takesue, M., et al., *Formation mechanism and luminescence appearance of Mn-doped zinc silicate particles synthesized in supercritical water*. *Journal of Solid State Chemistry*, 2008. 181(6): p. 1307-1313.
118. Lin, H.-F., et al., *Thermal plasma synthesis and optical properties of Zn₂SnO₄ nanopowders*. *Materials Chemistry and Physics*, 2009. 117(1): p. 9-13.
119. Wu, X.L., et al., *Raman scattering of alternating nanocrystalline silicon/amorphous silicon multilayers*. *Applied Physics Letters*, 1996. 69(4): p. 523-525.
120. Romann, J., *Size of crystals in nanocrystalline silicon*, I.A. Oedegaard, Editor. 2012: Trondheim.
121. Honda, K., S. Yokoyama, and S.-i. Tanaka, *Assignment of the Raman active vibration modes of beta-Si₃N₄ using micro-Raman scattering*. *Journal of Applied Physics*, 1999. 85(10): p. 7380-7384.
122. Sarkisov, P., et al., *Structure formation in production of yttrium-silicate materials by the sol-gel method*. *Glass and Ceramics*, 2007. 64(1): p. 3-6.
123. Toropov, N.A. and I.A. Bondar, *Silicates of the rare earth elements*. *Russian Chemical Bulletin*, 1961. 10(4): p. 502-508.
124. Cuff, S., et al., *Thickness-dependent optimization of Er³⁺ light emission from silicon-rich silicon oxide thin films*. *Nanoscale Research Letters*, 2011. 6(1): p. 1-6.
125. Fang, Y.C., et al., *Photoluminescence from SiO_x thin films: effects of film thickness and annealing temperature*. *Nanotechnology*, 2004. 15(5): p. 494.
126. Ilevbare, G.O. and G.T. Burstein, *The role of alloyed molybdenum in the inhibition of pitting corrosion in stainless steels*. *Corrosion Science*, 2001. 43(3): p. 485-513.
127. Dong, B., et al., *Temperature Sensing and In Vivo Imaging by Molybdenum Sensitized Visible Upconversion Luminescence of Rare-Earth Oxides*. *Advanced Materials*, 2012. 24(15): p. 1987-1993.
128. Anders, K., et al., *Emission properties of polymer composites doped with Er³⁺:Y₂O₃ nanopowders*. *Optical Materials*, (0).
129. Tkachuk, A.M., et al., *Upconversion processes in Er³⁺:KPb₂Cl₅ laser crystals*. *Journal of Luminescence*, 2007. 125(1-2): p. 271-278.
130. Sampaio, J.A., et al., *Thermo-optical properties of OH-free erbium-doped low silica calcium aluminosilicate glasses measured by thermal lens technique*. *Journal of Non-Crystalline Solids*, 2001. 284(1-3): p. 210-216.
131. Kojima, Y., M. Numazawa, and T. Umegaki, *Fluorescent properties of a green- to red-emitting Eu³⁺, Tb³⁺ codoped amorphous calcium silicate phosphor*. *Journal of Luminescence*, 2012. 132(10): p. 2648-2652.
132. de Wild, J., et al., *Towards upconversion for amorphous silicon solar cells*. *Solar Energy Materials and Solar Cells*, 2010. 94(11): p. 1919-1922.
133. Takesue, M., H. Hayashi, and R.L. Smith Jr, *Thermal and chemical methods for producing zinc silicate (willemite): A review*. *Progress in Crystal Growth and Characterization of Materials*, 2009. 55(3-4): p. 98-124.
134. Risbud, S.H., *Non-ideality and immiscibility in tin oxide-silica glasses*. *Materials Science and Engineering*, 1978. 34(1): p. 97-99.
135. Ma, C., L. Bi, and J.Y. Feng, *Tin-induced enhancement of photoluminescence and crystal growth in Si-rich silica films*. *Journal of Crystal Growth*, 2007. 305(1): p. 30-35.
136. Georgobiani, A. and A. Gruzintsev, *Effect of surface morphology on manganese ion luminescence kinetics in ZnS:Mn²⁺ films*. *Inorganic Materials*, 2011. 47(2): p. 107-111.
137. Park, Y.-J.S., In-Hyuck ; Kim, Hai-Doo, *Characterization of Pore Structures for Porous Sintered Reaction-Bonded Silicon Nitrides with Varied Pore-Former Content*. *Journal of the Korean Ceramic Society*, 2008. 45(11): p. 675-680.
138. Yang, J.-F., et al., *Microstructure and Mechanical Properties of Silicon Nitride Ceramics with Controlled Porosity*. *Journal of the American Ceramic Society*, 2002. 85(6): p. 1512-1516.

Appendix

Original frustules

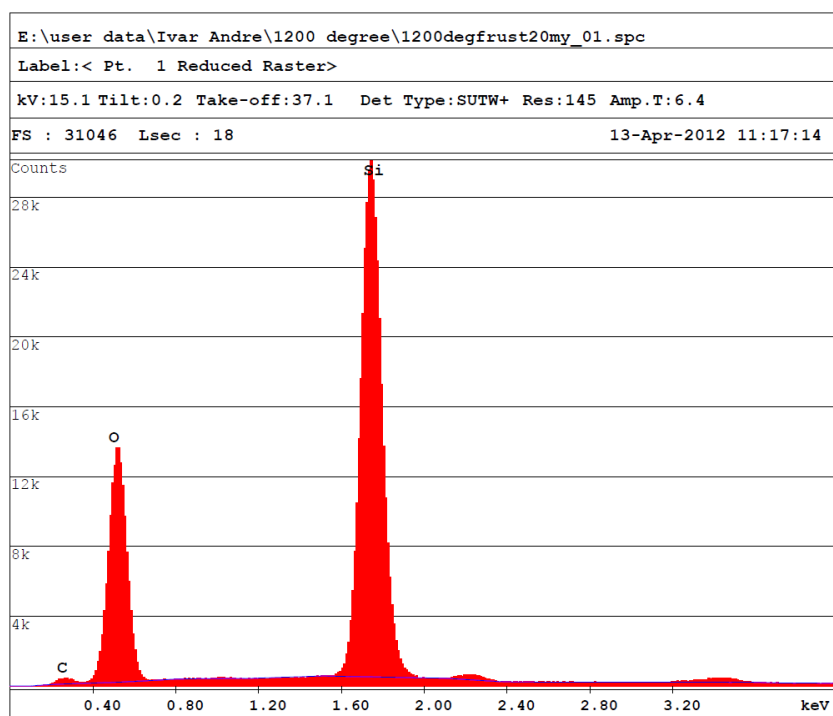


Figure 85 EDS spectrum of original frustules, sample 1

Table 17 Original frustules sample1, quantification

EDAX ZAF Quantification (Standardless)
 Element Normalized
 SEC Table : Default
 Coating Correction Used : Element : C , Factor : 14.00

Element	Wt %	At %	Z	A	F
C K	2.46	4.01	1.0400	0.1502	1.0005
O K	53.51	65.36	1.0203	0.4555	1.0004
SiK	44.03	30.63	0.9671	0.8961	1.0000
Total	100.00	100.00			

Element	Net Inte.	Bkgd Inte.	Inte. Error	P/B
C K	140.48	56.96	2.64	2.47
O K	6051.33	120.73	0.30	50.12
SiK	14724.40	320.17	0.20	45.99

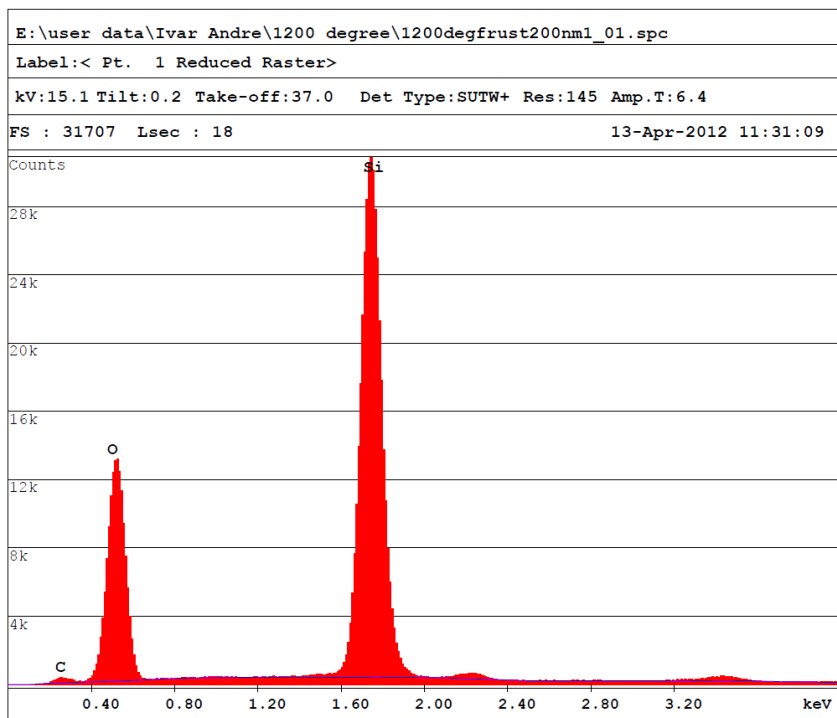


Figure 86 EDS spectrum of original frustules, sample 2

Table 18 Original frustules sample 2, quantification

```

EDAX ZAF Quantification (Standardless)
Element Normalized
SEC Table : Default
Coating Correction Used : Element : C , Factor : 14.00

```

Element	Wt %	At %	Z	A	F
C K	2.16	3.54	1.0407	0.1472	1.0005
O K	52.57	64.72	1.0210	0.4505	1.0004
SiK	45.27	31.74	0.9679	0.8977	1.0000
Total	100.00	100.00			

Element	Net Inte.	Bkgd Inte.	Inte. Error	P/B
C K	121.88	52.12	2.89	2.34
O K	5936.50	111.00	0.31	53.48
SiK	15336.34	262.84	0.19	58.35

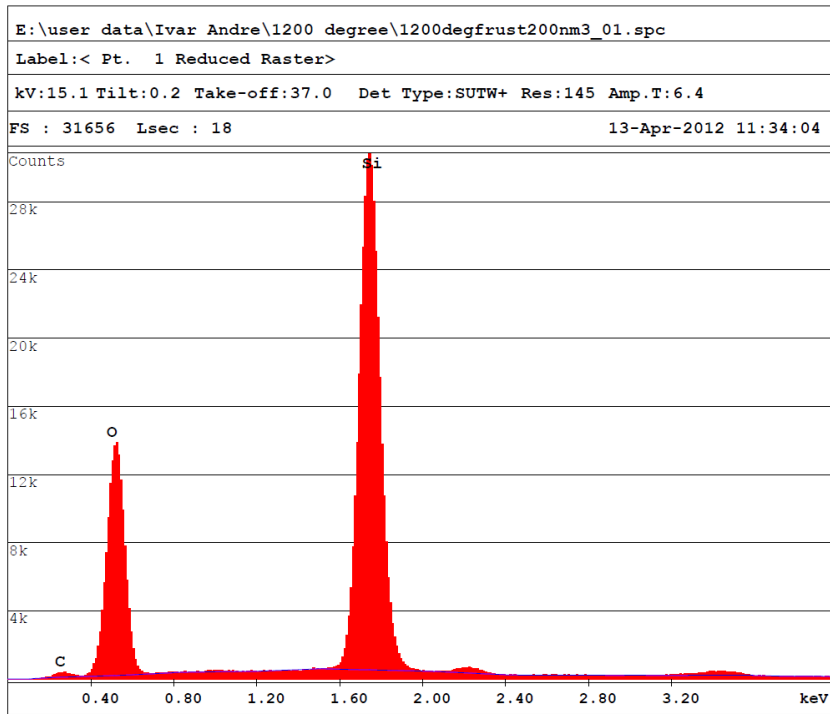


Figure 87 EDS spectrum of original frustules, sample 3

Table 19 Original frustules sample 3, quantification

```

EDAX ZAF Quantification (Standardless)
Element Normalized
SEC Table : Default
Coating Correction Used : Element : C , Factor : 14.00

```

Element	Wt %	At %	Z	A	F
C K	2.01	3.28	1.0404	0.1485	1.0005
O K	53.34	65.49	1.0207	0.4554	1.0004
SiK	44.65	31.23	0.9676	0.8963	1.0000
Total	100.00	100.00			

Element	Net Inte.	Bkgd Inte.	Inte. Error	P/B
C K	116.27	54.60	3.04	2.13
O K	6195.24	115.83	0.30	53.49
SiK	15368.26	332.45	0.19	46.23

Table 20 Average weight % elemental content of original frustules

Weight %					
Element	Sample 1	Sample 2	Sample 3	Average	Std. Dev.
C K	2,46	2,16	2,01	2,21	0,23
O K	53,51	52,57	53,54	53,21	0,55
Si K	44,03	45,27	44,45	44,58	0,63
Total	100,00	100,00	100,00	100,00	

Table 21 Average atomic % elemental content of original frustules

Atomic %					
Element	Sample 1	Sample 2	Sample 3	Average	Std. Dev.
C K	4,01	3,54	3,28	3,61	0,37
O K	65,36	64,72	65,49	65,19	0,41
Si K	30,63	31,74	31,23	31,20	0,56
Total	100	100	100	100	

Table 22 Average elemental constituents of the original frustules

Element	Atomic %	Weight %
C K	3,61	2,21
O K	65,19	53,21
Si K	31,20	44,58
Total	100,00	100,00

Frustules coated 1X with Y/Er

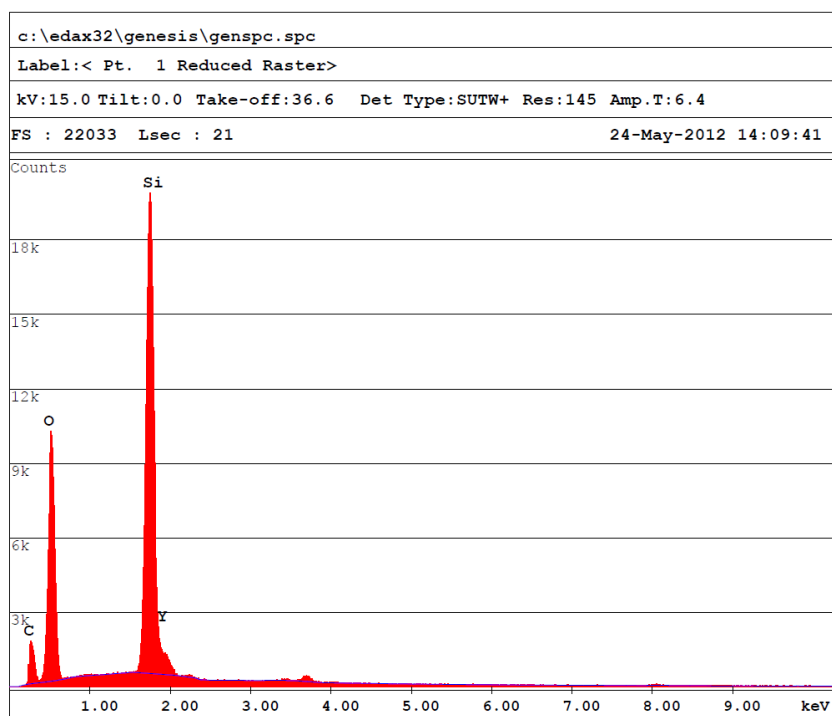


Figure 88 EDS spectrum of frustules coated once with Y/Er, sample1

Table 23 Frustules coated once with Y/Er sample 1, quantification

EDAX ZAF Quantification (Standardless)
 Element Normalized
 SEC Table : Default

Element	Wt %	At %	Z	A	F
C K	22.95	34.01	1.0395	0.1804	1.0003
O K	40.22	44.74	1.0198	0.3296	1.0003
SiK	32.00	20.28	0.9667	0.9068	1.0016
Y L	4.83	0.97	0.7630	0.8391	1.0000
Total	100.00	100.00			

Element	Net Inte.	Bkgd Inte.	Inte. Error	P/B
C K	540.52	48.25	1.00	11.20
O K	3776.69	102.38	0.36	36.89
SiK	8161.88	276.30	0.25	29.54
Y L	411.00	253.43	1.58	1.62

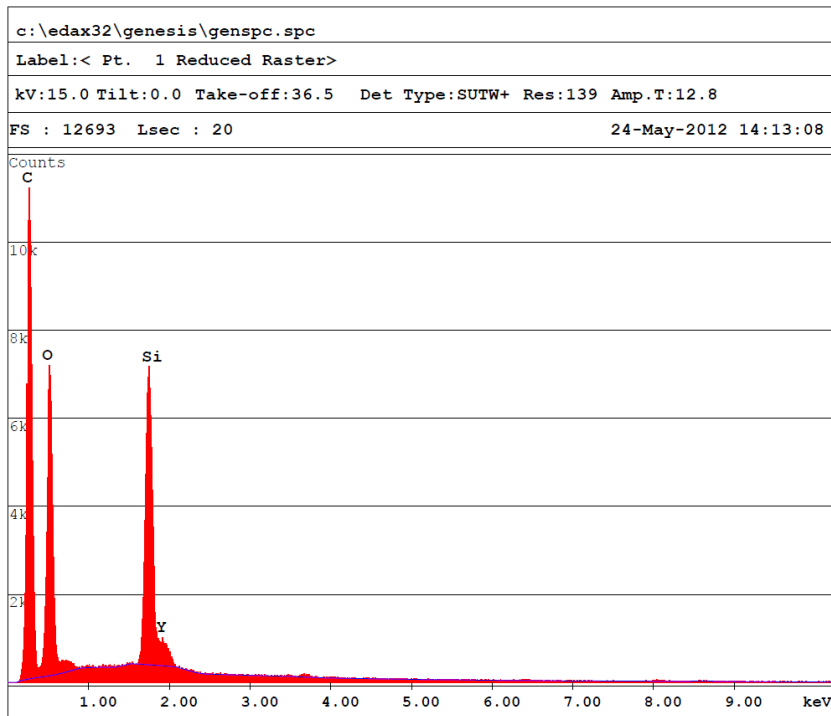


Figure 89 EDS spectrum of frustules coated once with Y/Er, sample 2

Table 24 Frustules coated once with Y/Er sample 2, quantification

```

EDAX ZAF Quantification (Standardless)
Element Normalized
SEC Table : Default

```

Element	Wt %	At %	Z	A	F
C K	59.79	70.02	1.0163	0.3915	1.0002
O K	28.17	24.76	0.9972	0.2534	1.0001
SiK	9.67	4.84	0.9417	0.9235	1.0012
Y L	2.38	0.38	0.7436	1.0133	1.0000
Total	100.00	100.00			

Element	Net Inte.	Bkgd Inte.	Inte. Error	P/B
C K	3465.48	32.79	0.37	105.67
O K	2308.25	60.90	0.47	37.90
SiK	2839.58	221.58	0.44	12.82
Y L	277.03	207.57	2.08	1.33

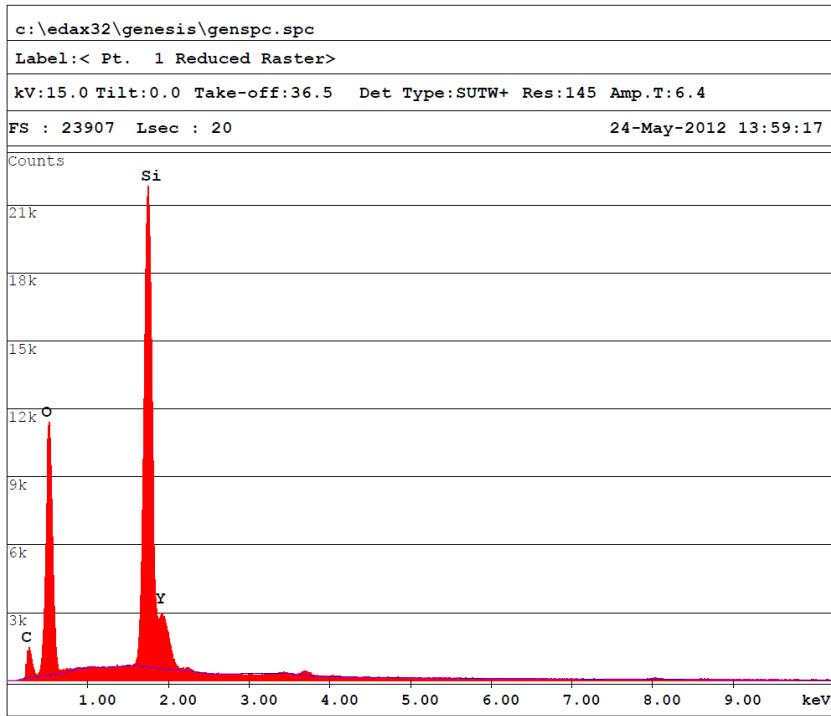


Figure 90 EDS spectrum of frustules coated once with Y/Er, sample 3

Table 25 Frustules coated once with Y/Er sample 3, quantification

```

EDAX ZAF Quantification (Standardless)
Element Normalized
SEC Table : Default

```

Element	Wt %	At %	Z	A	F
C K	16.99	27.28	1.0540	0.1648	1.0003
O K	40.59	48.93	1.0340	0.3223	1.0003
SiK	31.05	21.32	0.9826	0.8969	1.0038
Y L	11.37	2.47	0.7753	0.8391	1.0000
Total	100.00	100.00			

Element	Net Inte.	Bkgd Inte.	Inte. Error	P/B
C K	441.80	55.97	1.19	7.89
O K	4507.58	118.88	0.34	37.92
SiK	9514.40	329.95	0.24	28.84
Y L	1173.02	293.24	0.80	4.00

Table 26 Average weight % elemental content of frustules coated once with Y/Er

Weight %					
Element	Sample 1	Sample 2	Sample 3	Average	Std. Dev.
C K	33,43	16,99	22,95	24,46	8,32
O K	33,59	40,59	40,22	38,13	3,94
Si K	25,07	31,05	32,00	29,37	3,76
Y L	7,90	11,37	4,83	8,03	3,27
Mo L	0,00	0,00	0,00	0,00	0,00
Total	99,99	100,00	100,00	100,00	

Table 27 Average atomic % elemental content of frustules coated once with Y/Er

Atomic %					
Element	Sample 1	Sample 2	Sample 3	Average	Std. Dev.
C K	47,46	27,28	34,01	36,25	10,27
O K	35,80	48,93	44,74	43,16	6,71
Si K	15,22	21,32	20,28	18,94	3,26
Y L	1,52	2,47	0,97	1,65	0,76
Mo L	0,00	0,00	0,00	0,00	0,00
Total	100,00	100,00	100,00	100,00	

Table 28 Average elemental constituents of frustules coated once with Y/Er

Element	Atomic %	Weight %
C K	36,25	24,46
O K	43,16	38,13
Si K	18,94	29,37
Y L	1,65	8,03
Mo L	0,00	0,00
Total	100,00	100,00

Frustules coated 2X with Y/Er

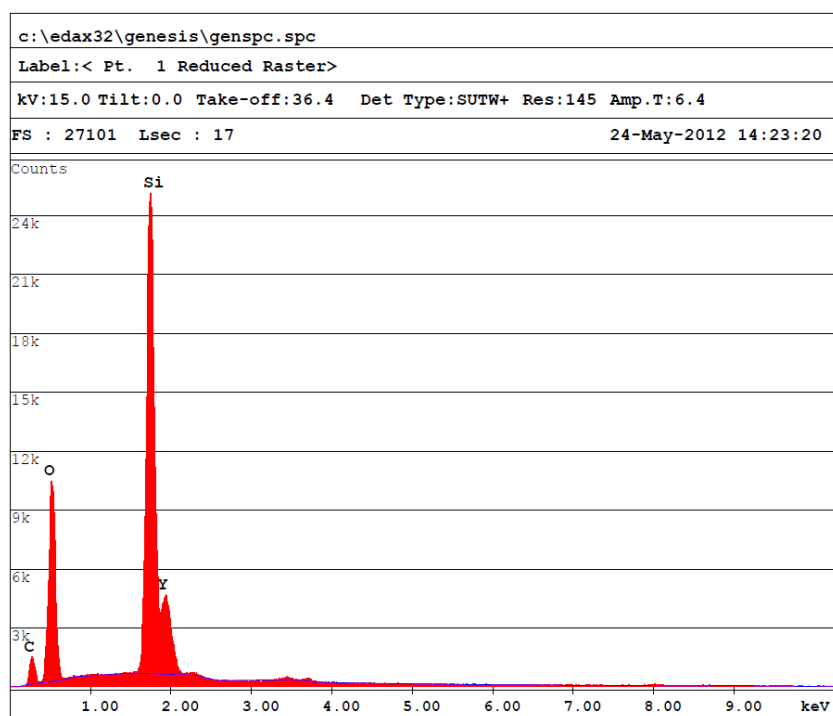


Figure 91 EDS spectrum of frustules coated twice with Y/Er, sample 1

Table 29 Frustules coated twice with Y/Er sample 1, quantification

EDAX ZAF Quantification (Standardless)
 Element Normalized
 SEC Table : Default

Element	Wt %	At %	Z	A	F
C K	17.02	28.81	1.0655	0.1537	1.0003
O K	35.27	44.83	1.0451	0.2937	1.0003
SiK	31.19	22.58	0.9951	0.8979	1.0054
Y L	16.52	3.78	0.7850	0.8391	1.0000
Total	100.00	100.00			

Element	Net Inte.	Bkgd Inte.	Inte. Error	P/B
C K	525.12	72.27	1.17	7.27
O K	4543.01	153.37	0.36	29.62
SiK	12230.26	416.47	0.22	29.37
Y L	2174.17	400.31	0.59	5.43

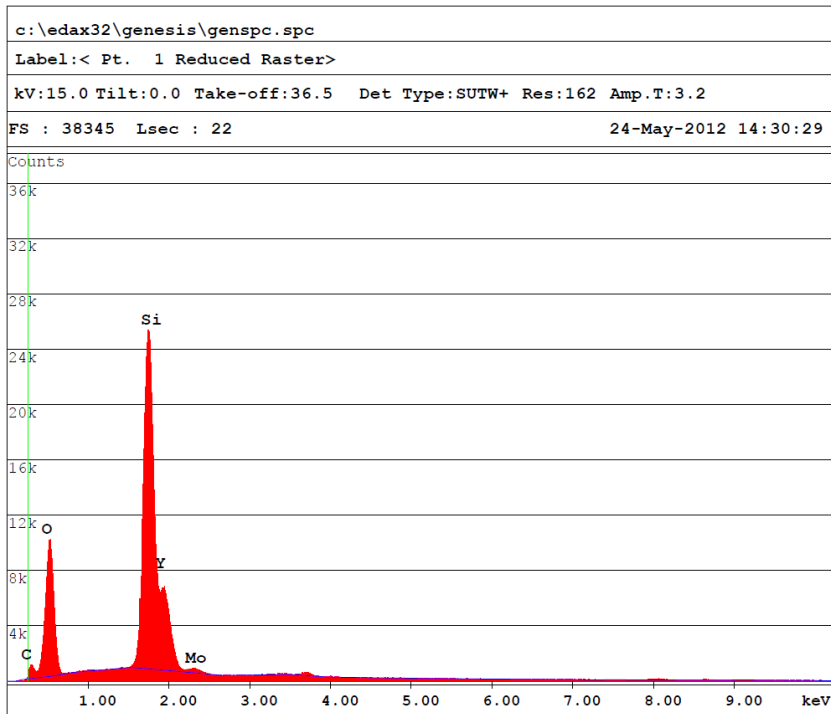


Figure 92 EDS spectrum of frustules coated twice with Y/Er, sample 2

Table 30 Frustules coated twice with Y/Er sample 2, quantification

```

c:\edax32\genesis\genspc.spc
Label : < Pt. 1 Reduced Raster>
Acquisition Time : 14:30:29 Date:24-May-2012
kV : 15.00 Tilt: 0.00 Take-off:36.49 AmpT : 3.2
Detector Type:SUTW, Sapphire Resolution:161.79 Lsec:22

```

EDAX ZAF Quantification (Standardless)
Element Normalized
SEC Table : Default

Element	Wt %	At %	Z	A	F
C K	9.50	18.15	1.0864	0.1396	1.0003
O K	35.33	50.70	1.0655	0.2841	1.0003
SiK	30.28	24.75	1.0179	0.8851	1.0078
Y L	23.35	6.03	0.8026	0.8369	1.0003
MoL	1.54	0.37	0.8051	0.8047	1.0000
Total	100.00	100.00			

Element	Net Inte.	Bkgd Inte.	Inte. Error	P/B
C K	257.44	96.72	1.73	2.66
O K	4255.29	181.80	0.33	23.41
SiK	11377.88	511.59	0.21	22.24
Y L	2972.79	459.35	0.44	6.47
MoL	163.62	375.32	3.87	0.44

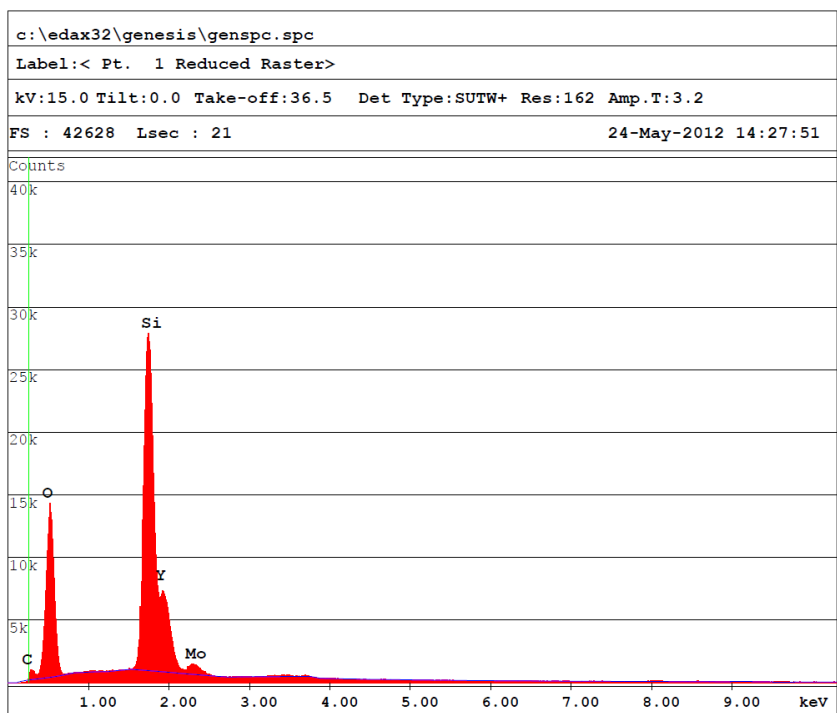


Figure 93 EDS spectrum of frustules coated twice with Y/Er, sample 3

Table 31 Frustules coated twice with Y/Er, sample 3, quantification

```

EDAX ZAF Quantification (Standardless)
Element Normalized
SEC Table : Default

```

Element	Wt %	At %	Z	A	F
C K	6.49	12.47	1.0860	0.1422	1.0003
O K	39.76	57.34	1.0652	0.2977	1.0003
SiK	29.01	23.83	1.0176	0.8768	1.0075
Y L	21.17	5.49	0.8024	0.8392	1.0007
MoL	3.57	0.86	0.8048	0.8169	1.0000
Total	100.00	100.00			

Table 32 Average weight % elemental content of frustules coated twice with Y/Er

Weight %					
Element	Sample 1	Sample 2	Sample 3	Average	Std. Dev.
C K	17,02	9,50	6,49	11,00	5,42
O K	35,27	35,33	39,76	36,79	2,58
Si K	31,19	30,28	29,01	30,16	1,09
Y L	16,52	23,35	21,17	20,35	3,49
Mo L	0,00	1,54	3,57	1,70	1,79
Total	100,00	100,00	100,00	100,00	

Table 33 Average atomic % elemental content of frustules coated twice with Y/Er

Atomic %					
Element	Sample 1	Sample 2	Sample 3	Average	Std. Dev.
C K	28,81	18,15	12,47	19,81	8,30
O K	44,83	50,70	57,34	50,96	6,26
Si K	22,58	24,75	23,83	23,72	1,09
Y L	3,78	6,03	5,49	5,10	1,17
Mo L	0	0,37	0,86	0,41	0,43
Total	100	100	99,99	100,00	

Table 34 Average elemental content of frustules coated twice with Y/Er

Element	Atomic %	Weight %
C K	19,81	11,00
O K	50,96	36,79
Si K	23,72	30,16
Y L	5,10	20,35
Mo L	0,41	1,70
Total	100,00	100,00

Frustules coated 4X with Y/Er

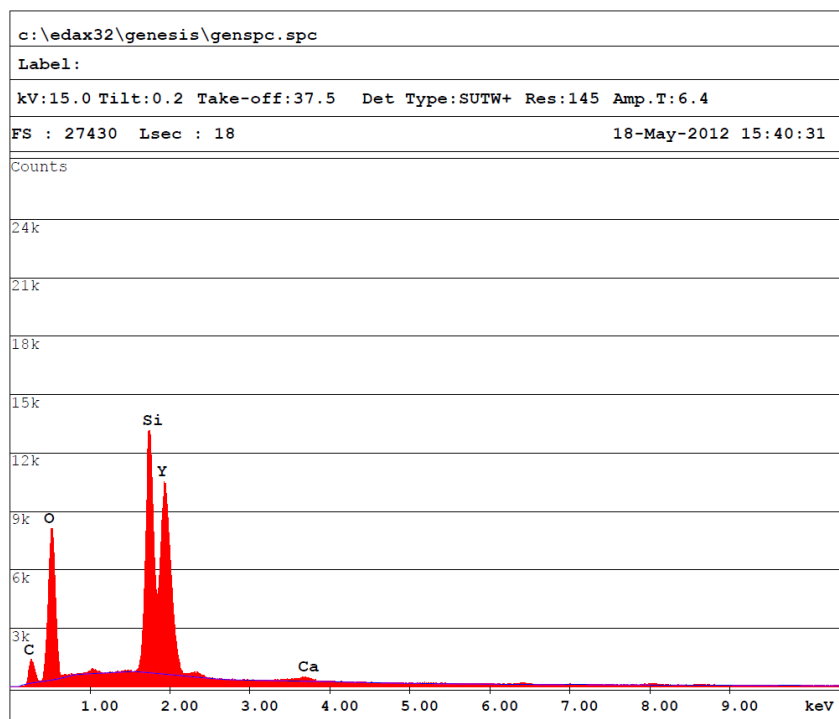


Figure 94 EDS spectrum of frustules coated four times with Y/Er, sample 1

Table 35 Frustules coated four times with Y/Er, sample 1, quantification

EDAX ZAF Quantification (Standardless)					
Element Normalized					
SEC Table : Default					
Element	Wt %	At %	Z	A	F
C K	14.70	29.03	1.1064	0.1523	1.0002
O K	31.85	47.21	1.0851	0.2511	1.0002
SiK	16.04	13.54	1.0400	0.8740	1.0141
Y L	36.67	9.78	0.8197	0.9239	1.0001
CaK	0.74	0.44	1.0027	0.9097	1.0000
Total	100.00	100.00			
Element	Net Inte.	Bkgd Inte.	Inte. Error	P/B	
C K	435.83	85.83	1.32	5.08	
O K	3380.66	182.09	0.42	18.57	
SiK	5952.66	426.33	0.32	13.96	
Y L	5133.80	385.19	0.35	13.33	
CaK	144.00	205.12	3.82	0.70	

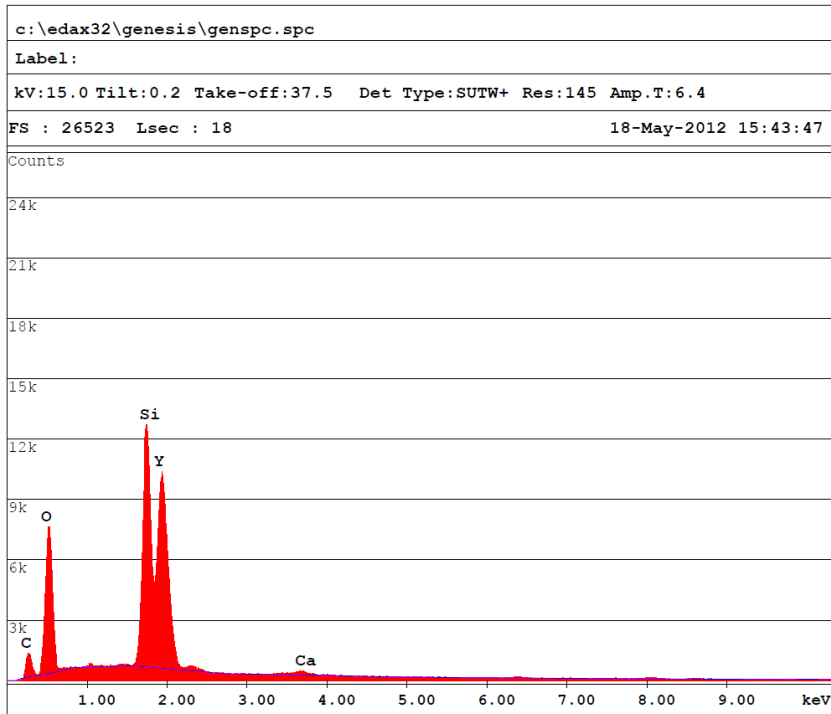


Figure 95 EDS spectrum of frustules coated four times with Y/Er, sample 2

Table 36 Frustules coated four times with Y/Er, sample 2, quantification

EDAX ZAF Quantification (Standardless)
Element Normalized
SEC Table : Default

Element	Wt %	At %	Z	A	F
C K	15.03	29.83	1.1080	0.1513	1.0002
O K	31.01	46.21	1.0866	0.2485	1.0003
SiK	15.98	13.56	1.0416	0.8745	1.0144
Y L	37.34	10.02	0.8210	0.9247	1.0001
CaK	0.65	0.39	1.0042	0.9084	1.0000
Total	100.00	100.00			

Element	Net Inte.	Bkgd Inte.	Inte. Error	P/B
C K	433.54	89.61	1.33	4.84
O K	3191.03	190.22	0.44	16.78
SiK	5816.38	406.91	0.33	14.29
Y L	5127.63	370.57	0.35	13.84
CaK	122.94	210.86	4.43	0.58

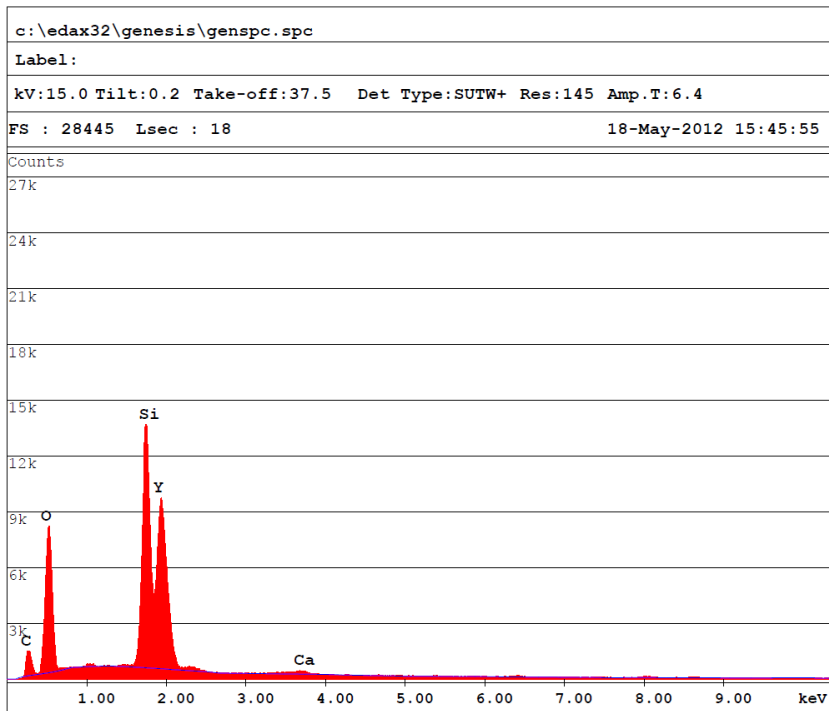


Figure 96 EDS spectrum of frustules coated four times with Y/Er, sample 3

Table 37 Frustules coated four times with Y/Er, sample 3, quantification

EDAX ZAF Quantification (Standardless)
 Element Normalized
 SEC Table : Default

Element	Wt %	At %	Z	A	F
C K	16.60	31.66	1.1000	0.1557	1.0002
O K	31.75	45.45	1.0788	0.2536	1.0002
SiK	16.82	13.72	1.0329	0.8778	1.0131
Y L	34.21	8.82	0.8142	0.9213	1.0001
CaK	0.62	0.35	0.9965	0.9142	1.0000
Total	100.00	100.00			

Element	Net Inte.	Bkgd Inte.	Inte. Error	P/B
C K	491.58	84.39	1.21	5.82
O K	3324.44	178.99	0.42	18.57
SiK	6115.15	354.25	0.31	17.26
Y L	4662.91	325.18	0.36	14.34
CaK	117.07	193.65	4.42	0.60

Table 38 Average weight % elemental content of frustules coated four times with Y/Er

Weight %					
Element	Sample 1	Sample 2	Sample 3	Average	Std. Dev.
C K	16,60	15,03	14,70	15,44	1,02
O K	31,75	31,01	31,85	31,54	0,46
Si K	16,82	15,98	16,04	16,28	0,47
Y L	34,21	37,33	36,67	36,07	1,64
Ca K	0,62	0,65	0,74	0,67	0,06
Total	100,00	100,00	100,00	100,00	

Table 39 Average atomic % elemental content of frustules coated four times with Y/Er

Atomic %					
Element	Sample 1	Sample 2	Sample 3	Average	Std. Dev.
C K	31,66	29,83	29,03	30,17	1,35
O K	45,45	46,21	47,21	46,29	0,88
Si K	13,72	13,56	13,54	13,61	0,10
Y L	8,82	10,01	9,78	9,54	0,63
Ca K	0,35	0,39	0,44	0,39	0,05
Total	100	100	100	100	

Table 40 Average elemental content of frustules coated four times with Y/Er

Element	Atomic %	Weight %
C K	30,17	15,44
O K	46,29	31,54
Si K	13,61	16,28
Y L	9,54	36,07
Ca K	0,39	0,67
Total	100,00	100,00

Frustules coated 1X with Zn/Mn

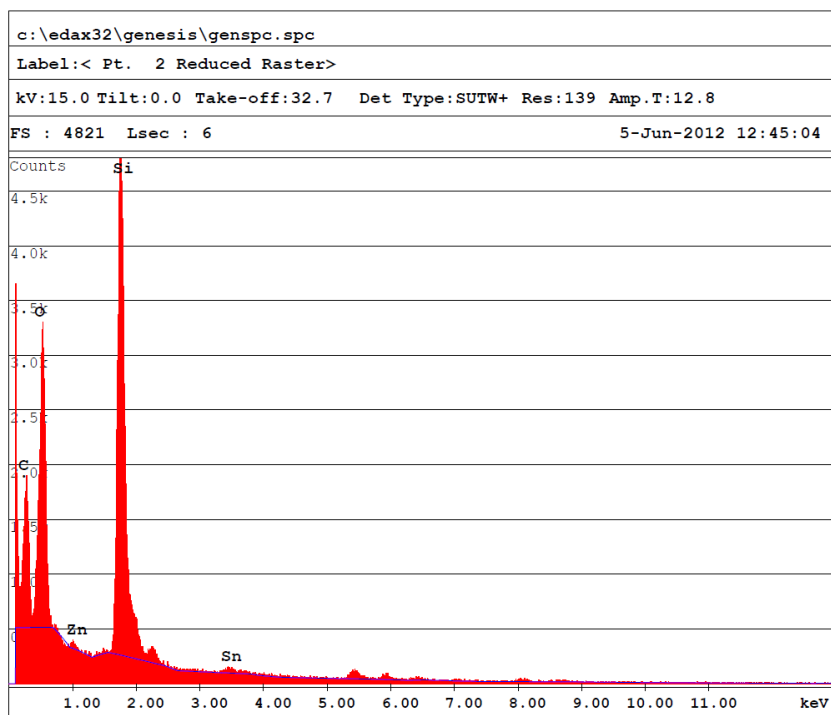


Figure 97 EDS spectrum of frustules coated once with Zn/Mn, sample 1

Table 41 Frustules coated once with Zn/Mn, sample 1, quantification

EDAX ZAF Quantification (Standardless)
 Element Normalized
 SEC Table : User E:\user data\Fengliu\MnO2.sec

Element	Wt %	At %	Z	A	F
C K	41.84	54.27	1.0249	0.2436	1.0003
O K	33.79	32.90	1.0056	0.2743	1.0002
ZnL	0.58	0.14	0.8291	0.6894	1.0020
SiK	22.59	12.53	0.9510	0.9023	1.0001
SnL	1.20	0.16	0.7215	1.0605	1.0000
Total	100.00	100.00			

Element	Net Inte.	Bkgd Inte.	Inte. Error	P/B
C K	1393.76	623.96	1.44	2.23
O K	2833.86	623.96	0.88	4.54
ZnL	62.85	483.72	19.87	0.13
SiK	6290.93	437.53	0.52	14.38
SnL	71.79	176.28	11.17	0.41

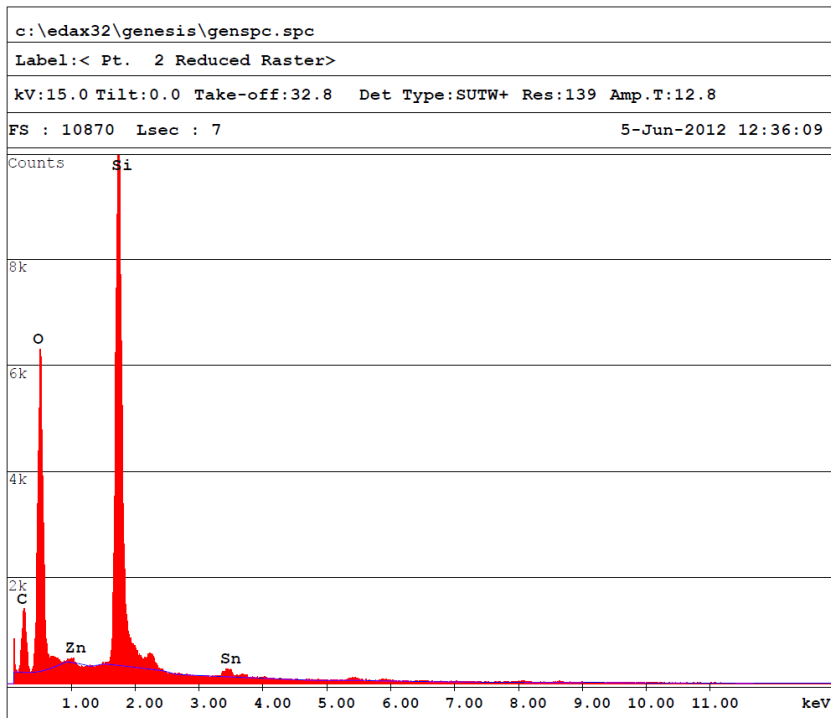


Figure 98 EDS spectrum of frustules coated once with Zn/Mn, sample 2

Table 42 Frustules coated once with Zn/Mn, sample 2, quantification

EDAX ZAF Quantification (Standardless)
 Element Normalized
 SEC Table : User E:\user data\Fengliu\MnO2.sec

Element	Wt %	At %	Z	A	F
C K	26.86	38.28	1.0344	0.1967	1.0003
O K	40.20	43.01	1.0149	0.3112	1.0002
ZnL	0.51	0.13	0.8366	0.6602	1.0025
SiK	29.87	18.20	0.9613	0.8871	1.0003
SnL	2.56	0.37	0.7287	1.0424	1.0000
Total	100.00	100.00			

Element	Net Inte.	Bkgd Inte.	Inte. Error	P/B
C K	1136.19	249.39	1.31	4.56
O K	6012.79	275.65	0.50	21.81
ZnL	83.13	586.39	15.72	0.14
SiK	12858.91	557.55	0.34	23.06
SnL	237.28	226.53	4.08	1.05

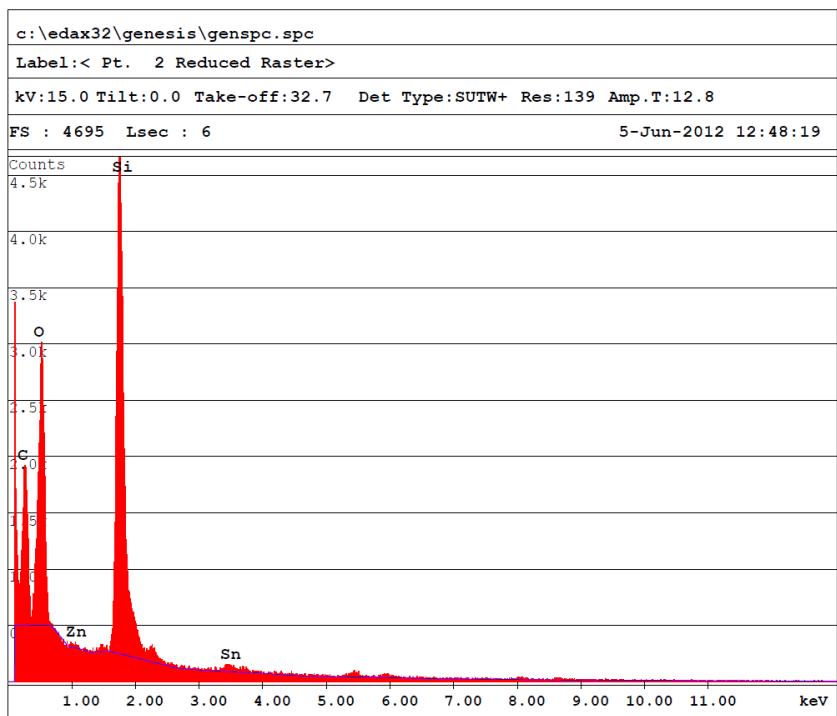


Figure 99 EDS spectrum of frustules coated once with Zn/Mn, sample 3

Table 43 Frustules coated once with Zn/Mn, sample 3, quantification

```

EDAX ZAF Quantification (Standardless)
Element Normalized
SEC Table : User E:\user data\Fengliu\MnO2.sec

```

Element	Wt %	At %	Z	A	F
C K	43.96	56.56	1.0247	0.2510	1.0003
O K	32.21	31.12	1.0053	0.2664	1.0002
ZnL	0.38	0.09	0.8289	0.6908	1.0019
SiK	21.85	12.02	0.9507	0.9043	1.0002
SnL	1.60	0.21	0.7213	1.0624	1.0000
Total	100.00	100.00			

Element	Net Inte.	Bkgd Inte.	Inte. Error	P/B
C K	1536.57	614.63	1.34	2.50
O K	2674.13	614.63	0.91	4.35
ZnL	42.17	470.17	29.11	0.09
SiK	6215.15	420.33	0.53	14.79
SnL	97.84	162.86	8.24	0.60

Table 44 Average weight % elemental content of frustules coated once with Zn/Mn

Weight %					
Element	Sample 1	Sample 2	Sample 3	Average	Std. Dev.
C K	41,84	26,86	43,96	37,55	9,32
O L	33,79	40,20	32,21	35,40	4,23
Zn L	0,58	0,51	0,38	0,49	0,10
Si K	22,59	29,87	21,85	24,77	4,43
Sn L	1,20	2,56	1,60	1,79	0,70
Mn K	0,00	0,00	0,00	0,00	0,00
Total	100,00	100,00	100,00	100,00	

Table 45 Average atomic % elemental content of frustules coated once with Zn/Mn

Atomic %					
Element	Sample 1	Sample 2	Sample 3	Average	Std. Dev.
C K	54,27	38,28	56,56	49,70	9,96
O L	32,90	43,01	31,12	35,68	6,41
Zn L	0,14	0,13	0,09	0,12	0,03
Si K	12,53	18,20	12,02	14,25	3,43
Sn L	0,16	0,37	0,21	0,25	0,11
Mn K	0,00	0,00	0,00	0,00	0,00
Total	100,00	99,99	100,00	100,00	

Table 46 Average elemental content of frustules coated once with Zn/Mn

Element	Atomic %	Weight %
C K	49,70	37,55
O L	35,68	35,40
Zn L	0,12	0,49
Si K	14,25	24,77
Sn L	0,25	1,79
Mn K	0,00	0,00
Total	100,00	100,00

Frustules coated 2X with Zn/Mn

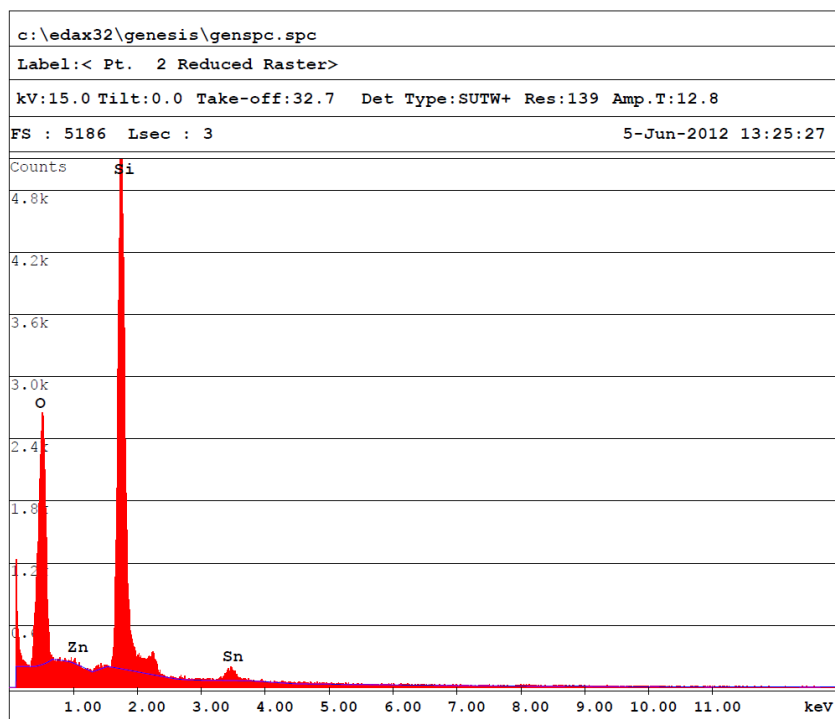


Figure 100 EDS spectrum of frustules coated twice with Zn/Mn, sample 1

Table 47 Frustules coated twice with Zn/Mn, sample 1, quantification

EDAX ZAF Quantification (Standardless)					
Element Normalized					
SEC Table : User E:\user data\Fengliu\MnO2.sec					
Element	Wt %	At %	Z	A	F
O K	44.69	60.97	1.0385	0.3641	1.0004
ZnL	0.39	0.13	0.8559	0.6279	1.0039
SiK	48.55	37.73	0.9877	0.8652	1.0005
SnL	6.38	1.17	0.7470	1.0008	1.0000
Total	100.00	100.00			
Element	Net Inte.	Bkgd Inte.	Inte. Error	P/B	
O K	4867.15	482.29	0.81	10.09	
ZnL	37.31	622.38	49.72	0.06	
SiK	12758.72	535.43	0.48	23.83	
SnL	354.27	211.22	4.08	1.68	

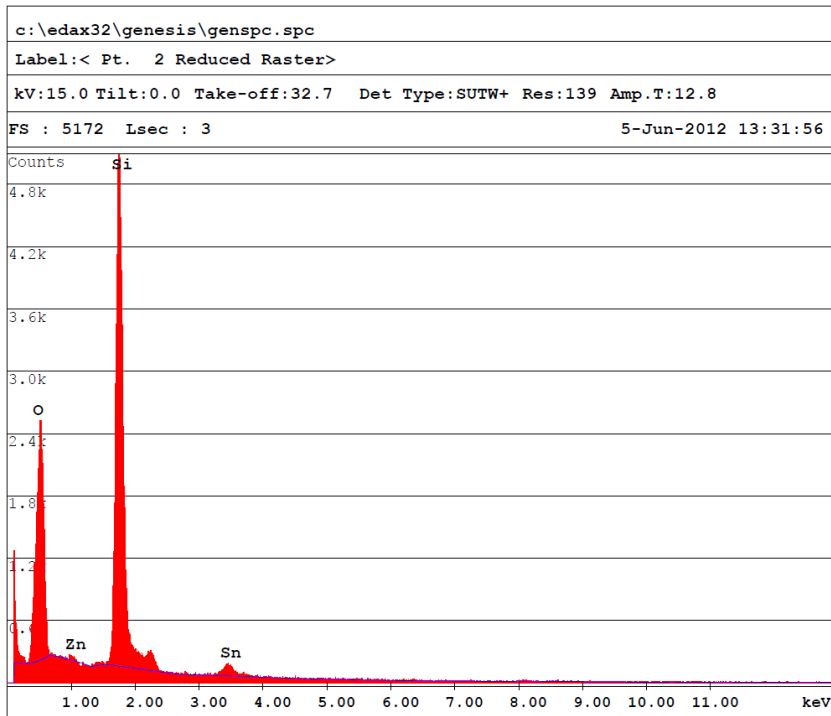


Figure 101 EDS spectrum of frustules coated twice with Zn/Mn, sample 2

Table 48 Frustules coated twice with Zn/Mn, sample 2, quantification

EDAX ZAF Quantification (Standardless)
 Element Normalized
 SEC Table : User E:\user data\Fengliu\MnO2.sec

Element	Wt %	At %	Z	A	F
O K	43.89	60.23	1.0392	0.3622	1.0004
ZnL	0.90	0.30	0.8565	0.6332	1.0039
SiK	49.03	38.33	0.9885	0.8634	1.0005
SnL	6.18	1.14	0.7475	0.9995	1.0000
Total	100.00	100.00			

Element	Net Inte.	Bkgd Inte.	Inte. Error	P/B
O K	4734.71	494.99	0.84	9.57
ZnL	87.04	604.56	21.81	0.14
SiK	12802.28	498.89	0.48	25.66
SnL	341.49	222.75	4.33	1.53

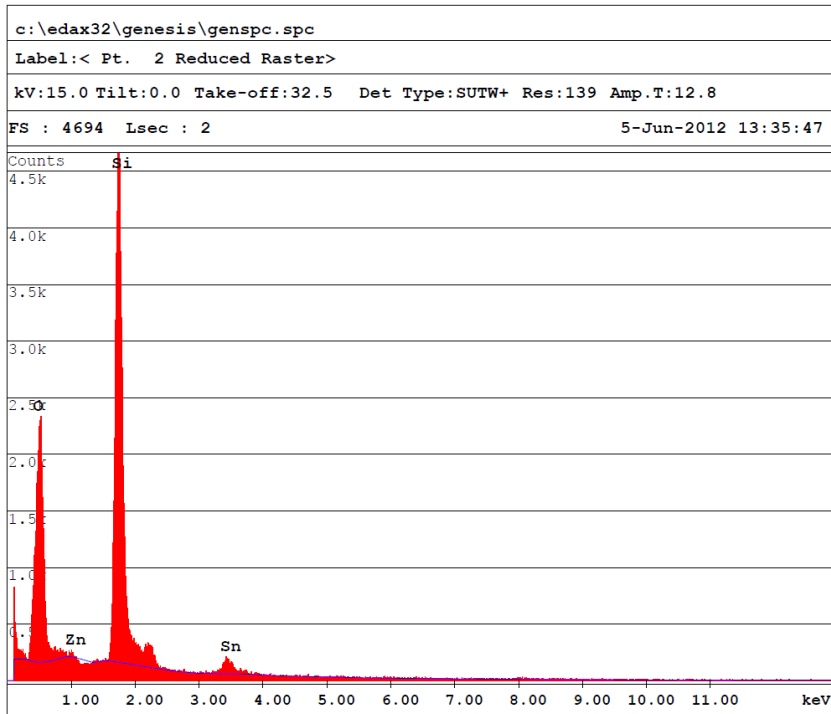


Figure 102 EDS spectrum of frustules coated twice with Zn/Mn, sample 3

Table 49 Frustules coated twice with Zn/Mn, sample 3, quantification

```

EDAX ZAF Quantification (Standardless)
Element Normalized
SEC Table : User E:\user data\Fengliu\MnO2.sec

```

Element	Wt %	At %	Z	A	F
O K	43.83	60.57	1.0413	0.3560	1.0004
ZnL	0.75	0.25	0.8582	0.6219	1.0038
SiK	48.02	37.80	0.9909	0.8578	1.0006
SnL	7.40	1.38	0.7492	1.0004	1.0000
Total	100.00	100.00			

Element	Net Inte.	Bkgd Inte.	Inte. Error	P/B
O K	5329.37	441.88	0.86	12.06
ZnL	80.90	705.98	27.85	0.11
SiK	14312.71	601.63	0.51	23.79
SnL	470.09	238.95	3.82	1.97

Table 50 Average weight % elemental content of frustules coated twice with Zn/Mn

Weight %					
Element	Sample 1	Sample 2	Sample 3	Average	Std. Dev.
C K	0,00	0,00	0,00	0,00	0,00
O L	44,69	43,89	43,83	44,14	0,48
Zn L	0,39	0,90	0,75	0,68	0,26
Si K	48,54	49,03	48,02	48,53	0,51
Sn L	6,38	6,18	7,40	6,65	0,65
Mn K	0,00	0,00	0,00	0,00	0,00
Total	100,00	100,00	100,00	100,00	

Table 51 Average atomic % elemental content of frustules coated twice with Zn/Mn

Atomic %					
Element	Sample 1	Sample 2	Sample 3	Average	Std. Dev.
C K	0,00	0,00	0,00	0,00	0,00
O L	60,97	60,23	60,57	60,59	0,37
Zn L	0,13	0,30	0,25	0,23	0,09
Si K	37,73	38,33	37,80	37,95	0,33
Sn L	1,17	1,14	1,38	1,23	0,13
Mn K	0,00	0,00	0,00	0,00	0,00
Total	100,00	100,00	100,00	100,00	

Table 52 Average elemental content of frustules coated twice with Zn/Mn

Element	Atomic %	Weight %
C K	0,00	0,00
O L	60,59	44,14
Zn L	0,23	0,68
Si K	37,95	48,53
Sn L	1,23	6,65
Mn K	0,00	0,00
Total	100,00	100,00

Frustules coated 4X with Zn/Mn

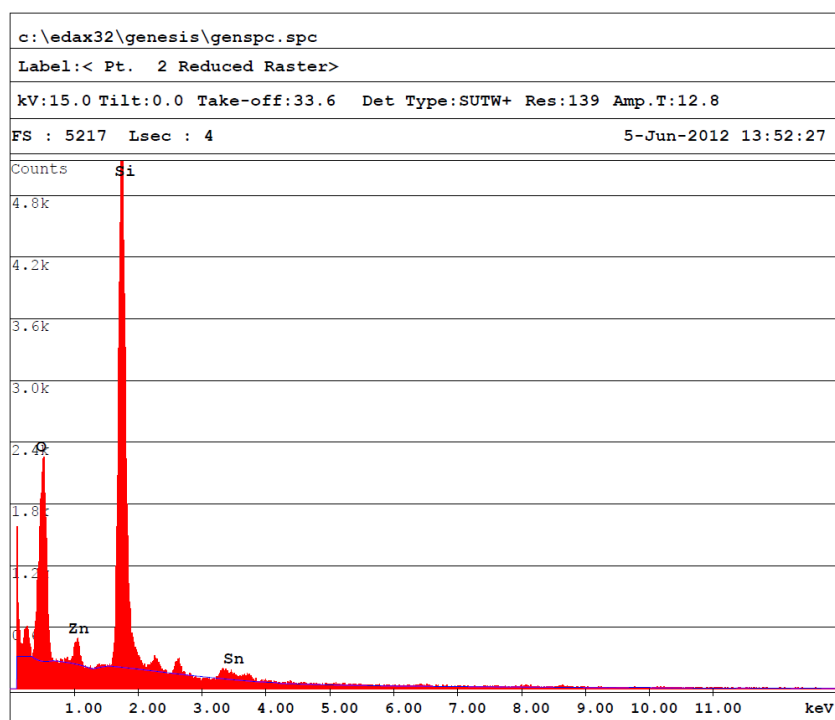


Figure 103 EDS spectrum of frustules coated four times with Zn/Mn, sample 1

Table 53 Frustules coated four times with Zn/Mn, sample 1, quantification

EDAX ZAF Quantification (Standardless)
 Element Normalized
 SEC Table : User E:\user data\Fengliu\MnO2.sec

Element	Wt %	At %	Z	A	F
O K	38.49	54.90	1.0434	0.3586	1.0005
ZnL	4.95	1.73	0.8598	0.6824	1.0041
SiK	52.39	42.57	0.9929	0.8528	1.0003
SnL	4.17	0.80	0.7507	0.9905	1.0000
Total	100.00	100.00			

Element	Net Inte.	Bkgd Inte.	Inte. Error	P/B
O K	2992.39	443.51	0.94	6.75
ZnL	374.56	500.10	4.49	0.75
SiK	9770.32	476.85	0.48	20.49
SnL	165.05	222.68	6.79	0.74

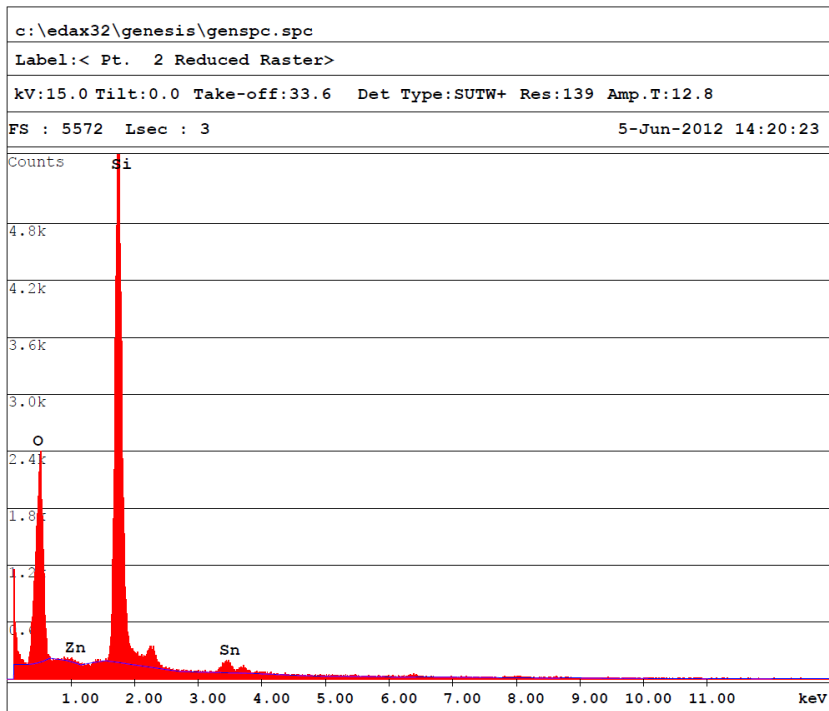


Figure 104 EDS spectrum of frustules coated four times with Zn/Mn, sample 2

Table 54 Frustules coated four times with Zn/Mn, sample 2, quantification

```

EDAX ZAF Quantification (Standardless)
Element Normalized
SEC Table : User E:\user data\Fengliu\MnO2.sec

```

Element	Wt %	At %	Z	A	F
O K	40.26	56.53	1.0416	0.3504	1.0004
ZnL	0.59	0.20	0.8584	0.6498	1.0043
SiK	52.52	42.01	0.9912	0.8733	1.0006
SnL	6.64	1.26	0.7494	0.9941	1.0000
Total	100.00	100.00			

Element	Net Inte.	Bkgd Inte.	Inte. Error	P/B
O K	4179.47	386.15	0.87	10.82
ZnL	57.67	482.35	28.78	0.12
SiK	13706.55	518.73	0.46	26.42
SnL	360.55	213.15	4.04	1.69

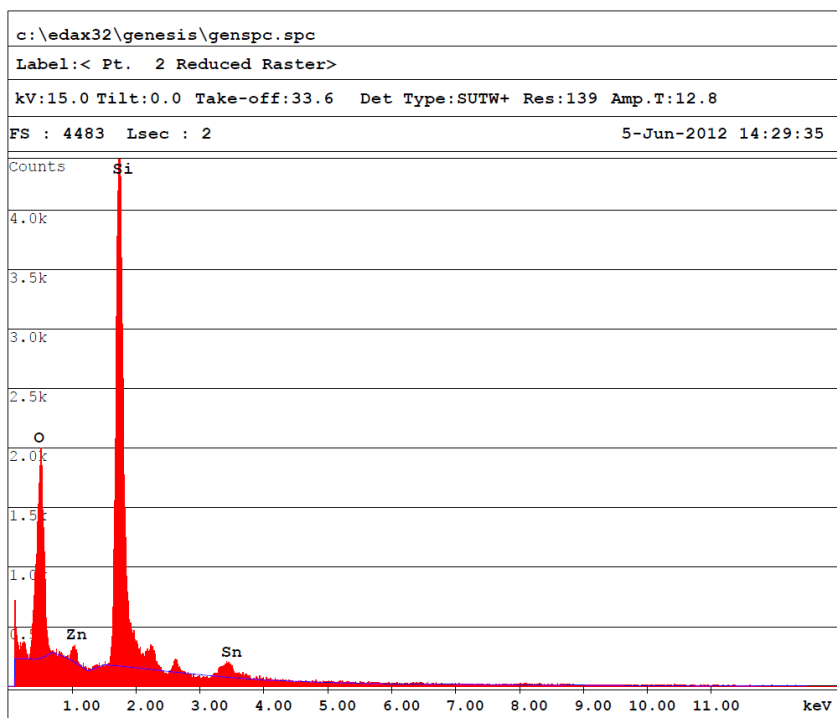


Figure 105 EDS spectrum of frustules coated four times with Zn/Mn, sample 3

Table 55 Frustules coated four times with Zn/Mn, sample 3, quantification

```

EDAX ZAF Quantification (Standardless)
Element Normalized
SEC Table : User E:\user data\Fengliu\MnO2.sec

```

Element	Wt %	At %	Z	A	F
O K	38.18	55.40	1.0485	0.3410	1.0004
ZnL	3.31	1.18	0.8640	0.6485	1.0039
SiK	50.67	41.89	0.9989	0.8479	1.0006
SnL	7.84	1.53	0.7547	0.9926	1.0000
Total	100.00	100.00			

Element	Net Inte.	Bkgd Inte.	Inte. Error	P/B
O K	4187.20	661.05	1.04	6.33
ZnL	353.06	722.64	7.05	0.49
SiK	13964.56	646.25	0.52	21.61
SnL	462.15	309.70	4.17	1.49

Table 56 Average weight % elemental content of frustules coated four times with Zn/Mn

Weight %					
Element	Sample 1	Sample 2	Sample 3	Average	Std. Dev.
C K	0,00	0,00	0,00	0,00	0,00
O L	38,49	40,26	38,18	38,98	1,12
Zn L	4,95	0,59	3,31	2,95	2,20
Si K	52,39	52,51	50,67	51,86	1,03
Sn L	4,17	6,64	7,84	6,22	1,87
Mn K	0,00	0,00	0,00	0,00	0,00
Total	100,00	100,00	100,00	100,00	

Table 57 Average atomic % elemental content of frustules coated four times with Zn/Mn

Atomic %					
Element	Sample 1	Sample 2	Sample 3	Average	Std. Dev.
C K	0,00	0,00	0,00	0,00	0,00
O L	54,90	56,53	55,40	55,61	0,84
Zn L	1,73	0,20	1,18	1,04	0,78
Si K	42,57	42,01	41,89	42,16	0,36
Sn L	0,80	1,26	1,53	1,20	0,37
Mn K	0,00	0,00	0,00	0,00	0,00
Total	100,00	100,00	100,00	100,00	

Table 58 Average elemental content of frustules coated four times with Zn/Mn

Element	Atomic %	Weight %
C K	0,00	0,00
O L	55,61	38,98
Zn L	1,04	2,95
Si K	42,16	51,86
Sn L	1,20	6,22
Mn K	0,00	0,00
Total	100,00	100,00

Frustules nitrated at 650°C, 3 keV

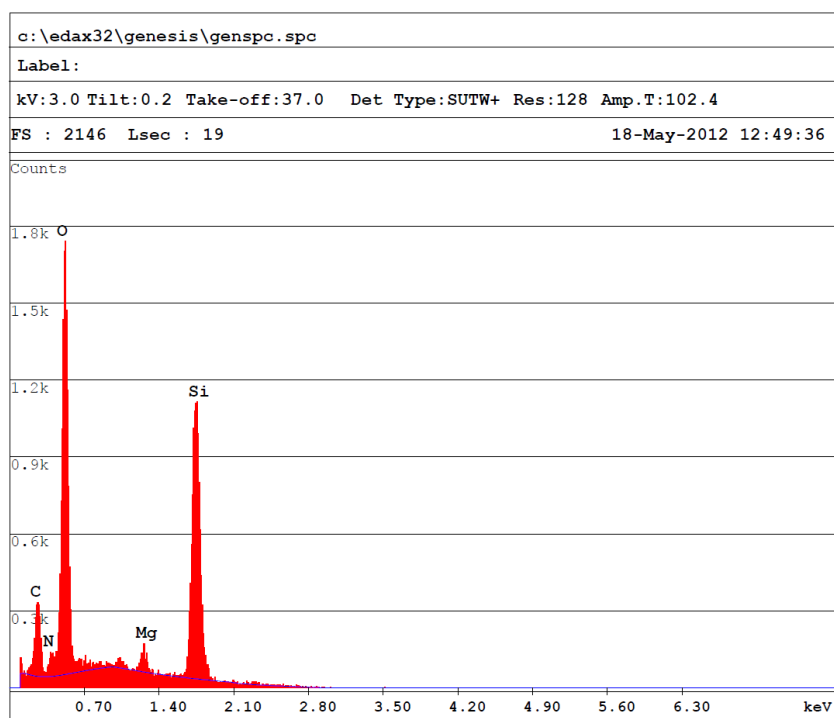


Figure 106 EDS spectrum of frustule nitrated at 650°C, sample 1

Table 59 Frustules nitrated at 650°C quantified, sample 1

EDAX ZAF Quantification (Standardless)
 Element Normalized
 SEC Table : Default

Element	Wt %	At %	Z	A	F
C K	4.40	8.65	1.1233	0.6271	1.0001
N K	1.39	2.34	1.1099	0.7923	1.0002
O K	14.94	22.05	1.0833	0.8935	1.0001
MgK	2.29	2.22	0.9954	0.9907	1.0083
SiK	76.99	64.74	0.9746	0.9981	1.0000
Total	100.00	100.00			

Element	Net Inte.	Bkgd Inte.	Inte. Error	P/B
C K	69.37	11.71	3.13	5.92
N K	24.19	13.95	6.72	1.73
O K	434.56	16.38	1.12	26.53
MgK	30.68	26.07	6.68	1.18
SiK	408.54	16.68	1.16	24.49

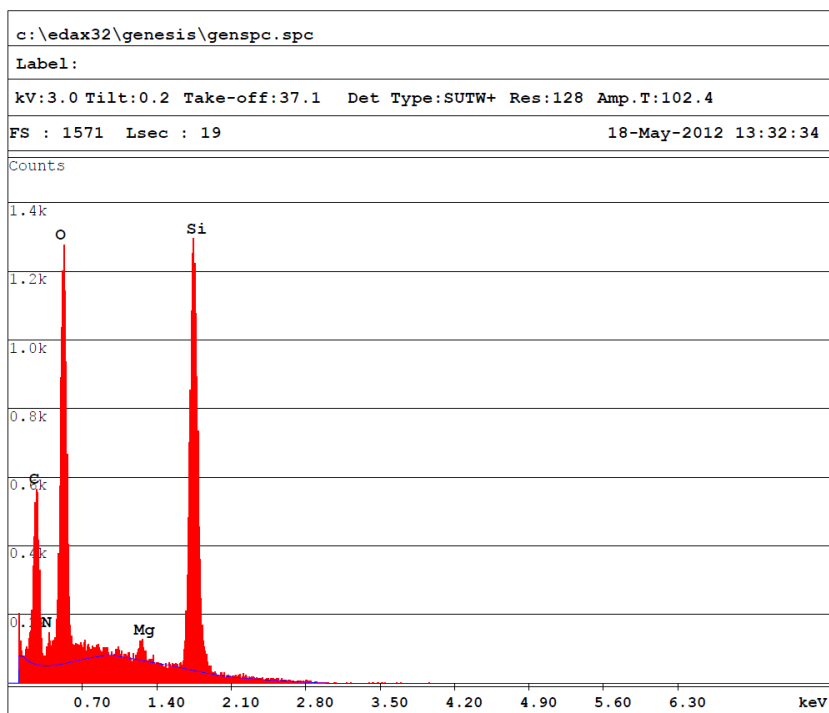


Figure 107 EDS spectrum of frustule nitrated at 650°C, sample 2

Table 60 Frustules nitrated at 650°C quantified, sample 2

```

EDAX ZAF Quantification (Standardless)
Element Normalized
SEC Table : Default

```

Element	Wt %	At %	Z	A	F
C K	6.91	13.64	1.1251	0.6204	1.0000
N K	1.19	2.02	1.1119	0.7799	1.0001
O K	10.34	15.32	1.0852	0.8868	1.0001
MgK	1.18	1.15	0.9970	0.9917	1.0094
SiK	80.38	67.87	0.9762	0.9988	1.0000
Total	100.00	100.00			

Element	Net Inte.	Bkgd Inte.	Inte. Error	P/B
C K	115.16	13.95	2.33	8.26
N K	21.83	15.61	7.50	1.40
O K	318.65	17.48	1.33	18.23
MgK	16.93	27.13	11.20	0.62
SiK	455.79	16.83	1.09	27.09

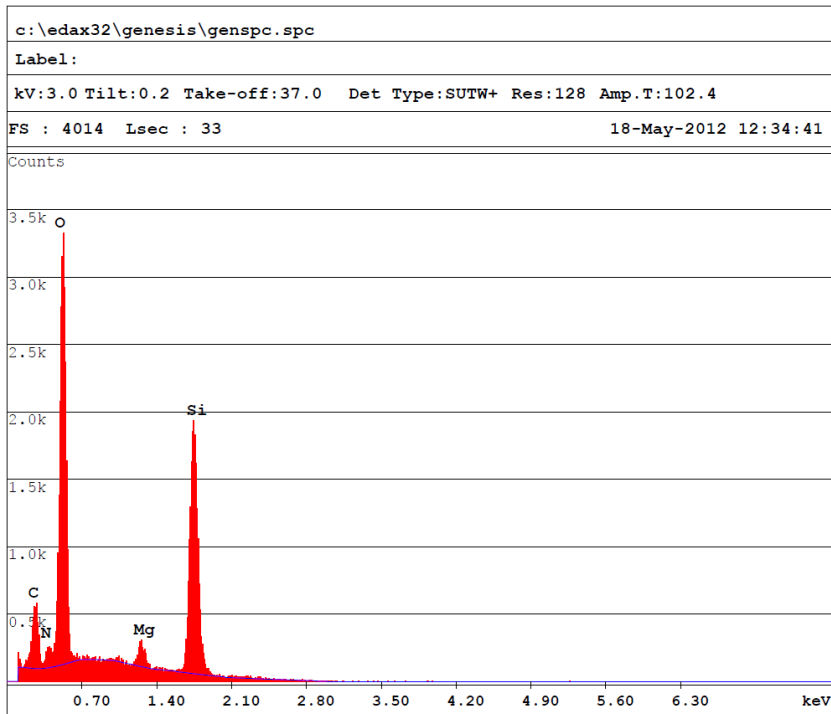


Figure 108 EDS spectrum of frustule nitrated at 650°C, sample 3

Table 61 Frustules nitrated at 650°C quantified, sample 3

EDAX ZAF Quantification (Standardless)
 Element Normalized
 SEC Table : Default

Element	Wt %	At %	Z	A	F
C K	4.09	7.97	1.1216	0.6317	1.0001
N K	1.44	2.42	1.1081	0.7963	1.0002
O K	16.66	24.40	1.0816	0.8957	1.0001
MgK	2.54	2.45	0.9939	0.9903	1.0079
SiK	75.26	62.77	0.9731	0.9979	1.0000
Total	100.00	100.00			

Element	Net Inte.	Bkgd Inte.	Inte. Error	P/B
C K	65.53	14.63	2.58	4.48
N K	25.53	18.75	5.40	1.36
O K	490.32	23.03	0.82	21.29
MgK	34.41	26.67	4.72	1.29
SiK	402.90	15.71	0.90	25.64

Table 62 Average weight % elemental content of frustules nitrated at 650°C

Weight %					
Element	Sample 1	Sample 2	Sample 3	Average	Std. Dev.
C K	4,09	6,91	4,40	5,13	1,55
N K	1,44	1,19	1,39	1,34	0,13
O K	16,66	10,34	14,93	13,98	3,27
Mg K	2,54	1,18	2,29	2,00	0,72
Si K	75,26	80,38	76,99	77,54	2,60
Total	99,99	100,00	100,00	100,00	

Table 63 Average atomic % elemental content of frustules nitrated at 650°C

Atomic %					
Element	Sample 1	Sample 2	Sample 3	Average	Std. Dev.
C K	7,97	13,64	8,65	10,09	3,10
N K	2,41	2,02	2,34	2,26	0,21
O K	24,40	15,32	22,05	20,59	4,71
Mg K	2,45	1,15	2,22	1,94	0,69
Si K	62,77	67,87	64,74	65,13	2,57
Total	100,00	100,00	100,00	100,00	

Table 64 Average elemental content of frustules nitrated at 650°C

Element	Atomic %	Weight %
C K	10,09	5,13
N K	2,26	1,34
O K	20,59	13,98
Mg K	1,94	2,00
Si K	65,13	77,54
Total	100,00	100,00

Frustules nitrated at 650°C, 15 keV

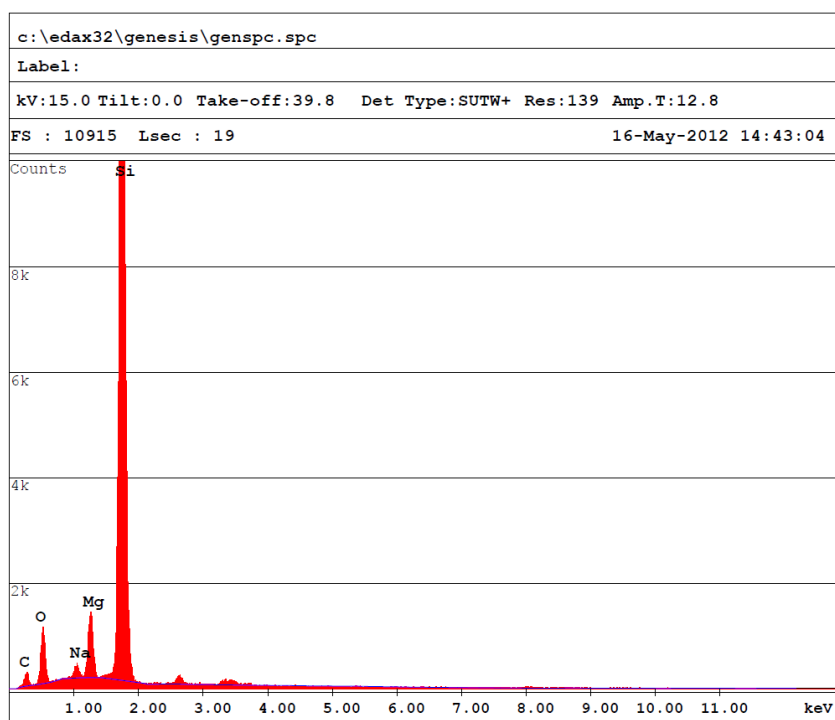


Figure 109 EDS spectrum of frustule nitrated at 650°C, sample 1, 15 keV

Table 65 Frustules nitrated at 650°C quantified, sample 1, 15 keV

EDAX ZAF Quantification (Standardless)
Element Normalized
SEC Table : Default

Element	Wt %	At %	Z	A	F
C K	13.79	25.38	1.0543	0.1086	1.0001
O K	10.19	14.09	1.0342	0.2903	1.0007
NaK	0.95	0.91	0.9649	0.7405	1.0104
MgK	4.35	3.96	0.9882	0.8489	1.0200
SiK	70.72	55.67	0.9823	0.9432	1.0000
Total	100.00	100.00			

Element	Net Inte.	Bkgd Inte.	Inte. Error	P/B
C K	85.70	22.21	3.00	3.86
O K	363.69	41.33	1.31	8.80
NaK	97.31	100.20	3.99	0.97
MgK	521.75	116.02	1.18	4.50
SiK	7948.83	95.33	0.26	83.38

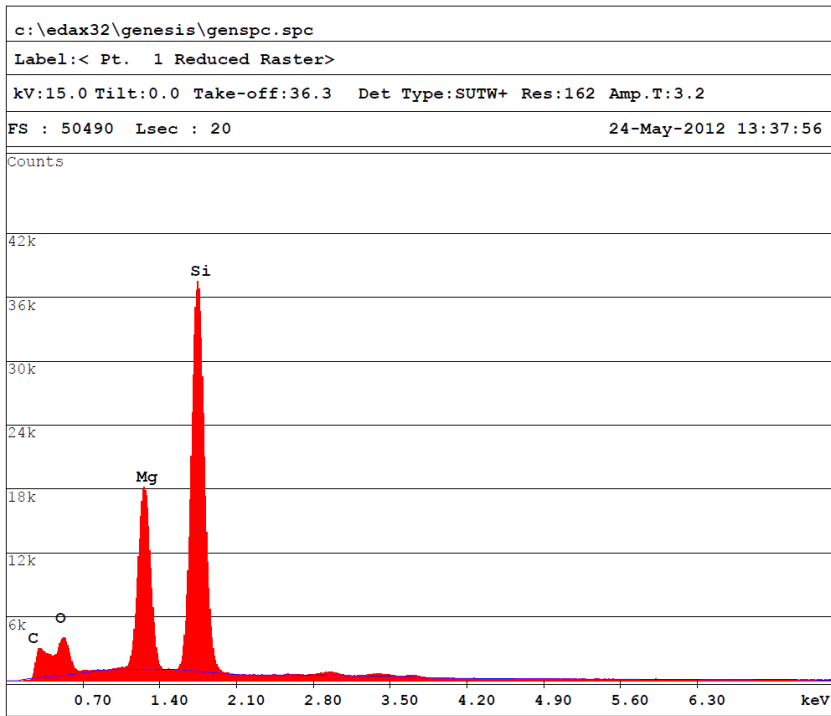


Figure 110 EDS spectrum of frustule nitrated at 650°C, sample 2, 15 keV

Table 66 Frustules nitrated at 650°C quantified, sample 2, 15 keV

```

EDAX ZAF Quantification (Standardless)
Element Normalized
SEC Table : Default

```

Element	Wt %	At %	Z	A	F
C K	26.87	42.48	1.0429	0.1373	1.0001
O K	12.21	14.50	1.0231	0.2778	1.0006
MgK	17.41	13.60	0.9779	0.8421	1.0095
SiK	43.51	29.42	0.9699	0.8519	1.0000
Total	100.00	100.00			

Element	Net Inte.	Bkgd Inte.	Inte. Error	P/B
C K	871.61	156.54	0.87	5.57
O K	1752.98	294.34	0.61	5.96
MgK	8760.51	682.05	0.25	12.84
SiK	18895.56	559.32	0.16	33.78

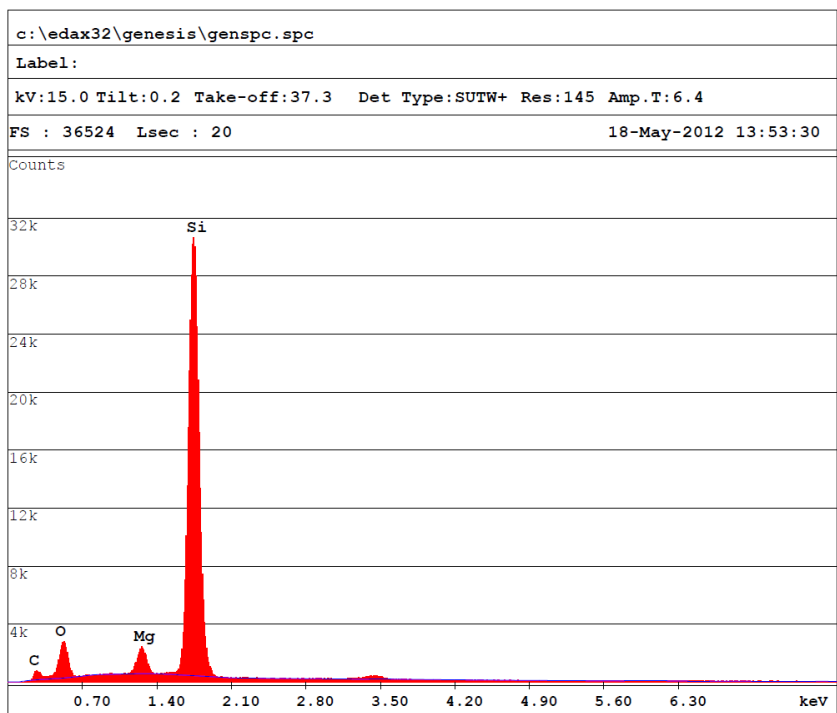


Figure 111 EDS spectrum of frustule nitrated at 650°C, sample 3, 15 keV

Table 67 Frustules nitrated at 650°C quantified, sample 3, 15 keV

EDAX ZAF Quantification (Standardless)
Element Normalized
SEC Table : Default

Element	Wt %	At %	Z	A	F
C K	16.49	28.75	1.0494	0.1147	1.0002
O K	15.23	19.93	1.0295	0.2869	1.0006
MgK	3.56	3.07	0.9838	0.8289	1.0178
SiK	64.72	48.25	0.9771	0.9404	1.0000
Total	100.00	100.00			

Element	Net Inte.	Bkqd Inte.	Inte. Error	P/B
C K	192.18	61.75	2.04	3.11
O K	965.74	130.87	0.80	7.38
MgK	757.13	302.92	1.08	2.50
SiK	13216.26	229.37	0.20	57.62

Table 68 Average weight % elemental content of frustules nitrated at 650°C, 15 keV

Weight %					
Element	Sample 1	Sample 2	Sample 3	Average	Std. Dev.
C K	26,87	13,79	16,49	19,05	6,91
N K	0,00	0,00	0,00	0,00	0,00
O K	12,21	10,19	15,23	12,54	2,54
Na K	0,00	0,95	0,00	0,32	0,55
Mg K	17,41	4,35	3,56	8,44	7,78
Si K	43,51	70,72	64,72	59,65	14,30
Total	100,00	100,00	100,00	100,00	

Table 69 Average atomic % elemental content of frustules nitrated at 650°C, 15 keV

Atomic %					
Element	Sample 1	Sample 2	Sample 3	Average	Std. Dev.
C K	42,48	25,38	28,75	32,20	9,06
N K	0,00	0,00	0,00	0,00	0,00
O K	14,50	14,09	19,93	16,17	3,26
Na K	0,00	0,91	0,00	0,30	0,53
Mg K	13,60	3,95	3,07	6,87	5,84
Si K	29,42	55,67	48,25	44,45	13,53
Total	100,00	100,00	100,00	100,00	

Table 70 Average elemental content of frustules nitrated at 650°C, 15 keV

Element	Atomic %	Weight %
C K	32,20	19,05
N K	0,00	0,00
O K	16,17	12,54
Na K	0,30	0,32
Mg K	6,87	8,44
Si K	44,45	59,65
Total	100,00	100,00

Frustules nitrated at 800°C, 3 keV

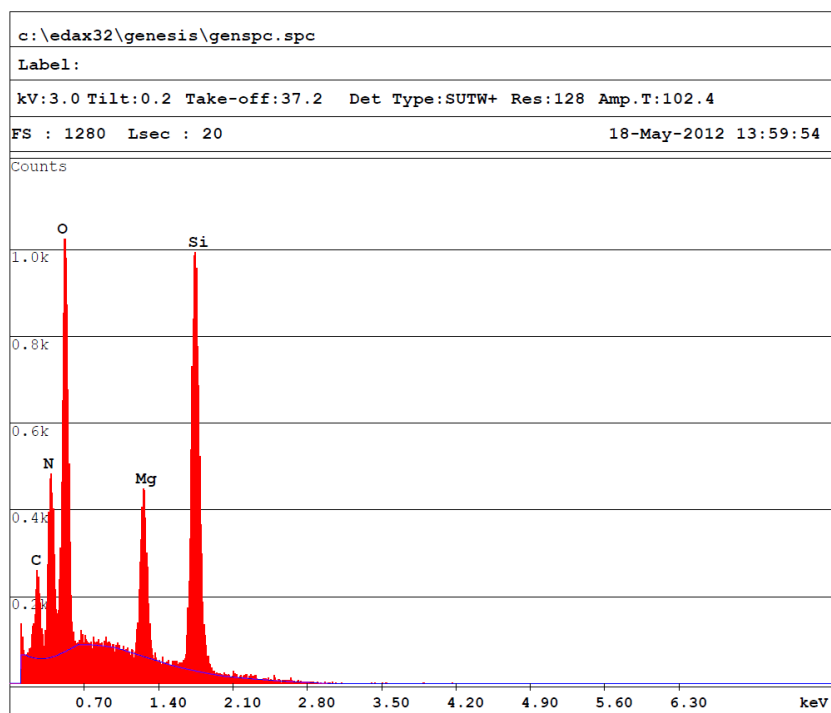


Figure 112 EDS spectrum of nitrated frustules, sample 1, 3 keV

Table 71 Nitrated frustules, sample 1, quantified, 3 keV

EDAX ZAF Quantification (Standardless)
 Element Normalized
 SEC Table : Default

Element	Wt %	At %	Z	A	F
C K	2.91	5.72	1.1236	0.6322	1.0001
N K	6.75	11.37	1.1101	0.8005	1.0001
O K	8.96	13.22	1.0836	0.8847	1.0001
MgK	9.87	9.59	0.9956	0.9919	1.0069
SiK	71.51	60.10	0.9748	0.9962	1.0000
Total	100.00	100.00			

Element	Net Inte.	Bkgd Inte.	Inte. Error	P/B
C K	43.27	14.85	4.39	2.91
N K	111.02	18.80	2.44	5.91
O K	241.24	22.90	1.56	10.54
MgK	123.70	25.61	2.37	4.83
SiK	353.89	13.32	1.22	26.56

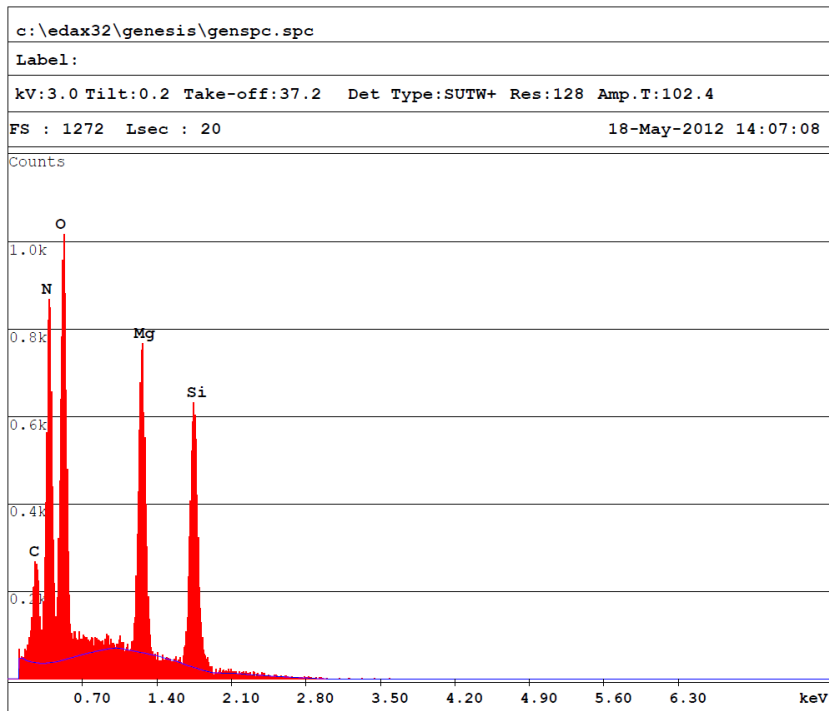


Figure 113 EDS spectrum of nitrated frustules, sample 2, 3 keV

Table 72 Nitrated frustules, sample 2, quantified, 3 keV

EDAX ZAF Quantification (Standardless)
 Element Normalized
 SEC Table : Default

Element	Wt %	At %	Z	A	F
C K	3.89	6.97	1.1069	0.6811	1.0001
N K	14.13	21.70	1.0923	0.8287	1.0002
O K	10.55	14.18	1.0671	0.8821	1.0001
MgK	20.72	18.33	0.9810	0.9912	1.0039
SiK	50.70	38.82	0.9603	0.9927	1.0000
Total	100.00	100.00			

Element	Net Inte.	Bkgd Inte.	Inte. Error	P/B
C K	54.04	9.50	3.52	5.69
N K	208.39	11.43	1.62	18.23
O K	245.31	13.46	1.50	18.22
MgK	224.28	24.94	1.64	8.99
SiK	216.76	12.17	1.59	17.80

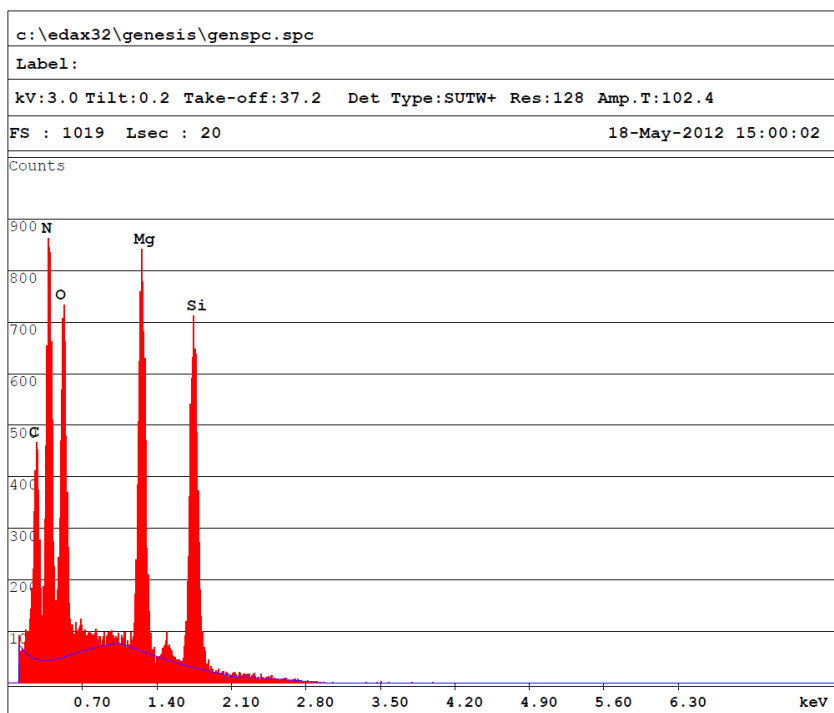


Figure 114 EDS spectrum of nitrated frustules, sample 3, 3 keV

Table 73 Nitrated frustules, sample 3, quantified, 3 keV

EDAX ZAF Quantification (Standardless)
 Element Normalized
 SEC Table : Default

Element	Wt %	At %	Z	A	F
C K	6.25	11.21	1.1082	0.6758	1.0001
N K	13.43	20.66	1.0937	0.8174	1.0001
O K	6.82	9.19	1.0684	0.8779	1.0001
MgK	21.07	18.68	0.9822	0.9921	1.0042
SiK	52.43	40.25	0.9616	0.9929	1.0000
Total	100.00	100.00			

Element	Net Inte.	Bkgd Inte.	Inte. Error	P/B
C K	89.35	11.25	2.63	7.94
N K	202.77	12.88	1.66	15.75
O K	163.94	14.70	1.88	11.15
MgK	237.01	24.03	1.58	9.86
SiK	232.77	12.98	1.53	17.94

Table 74 Average weight % elemental content of nitrified frustules, 3 keV

Weight %					
Element	Sample 1	Sample 2	Sample 3	Average	Std. Dev.
C K	2,91	3,89	6,25	4,35	1,72
N K	6,75	14,14	13,43	11,44	4,08
O K	8,96	10,55	6,82	8,78	1,87
Mg K	9,87	20,72	21,07	17,22	6,37
Si K	71,51	50,70	52,43	58,21	11,55
Total	100,00	100,00	100,00	100,00	

Table 75 Average atomic % elemental content of nitrified frustules, 3 keV

Atomic %					
Element	Sample 1	Sample 2	Sample 3	Average	Std. Dev.
C K	5,72	6,97	11,21	7,97	2,88
N K	11,37	21,70	20,66	17,91	5,69
O K	13,22	14,18	9,19	12,20	2,65
Mg K	9,59	18,33	18,68	15,53	5,15
Si K	60,10	38,82	40,26	46,39	11,89
Total	100,00	100,00	100,00	100,00	

Table 76 Average elemental content of nitrified frustules 3 keV

Element	Atomic %	Weight %
C K	7,97	4,35
N K	17,91	11,44
O K	12,20	8,78
Mg K	15,53	17,22
Si K	46,39	58,21
Total	100,00	100,00

Frustules nitrated at 800°C, 15 keV

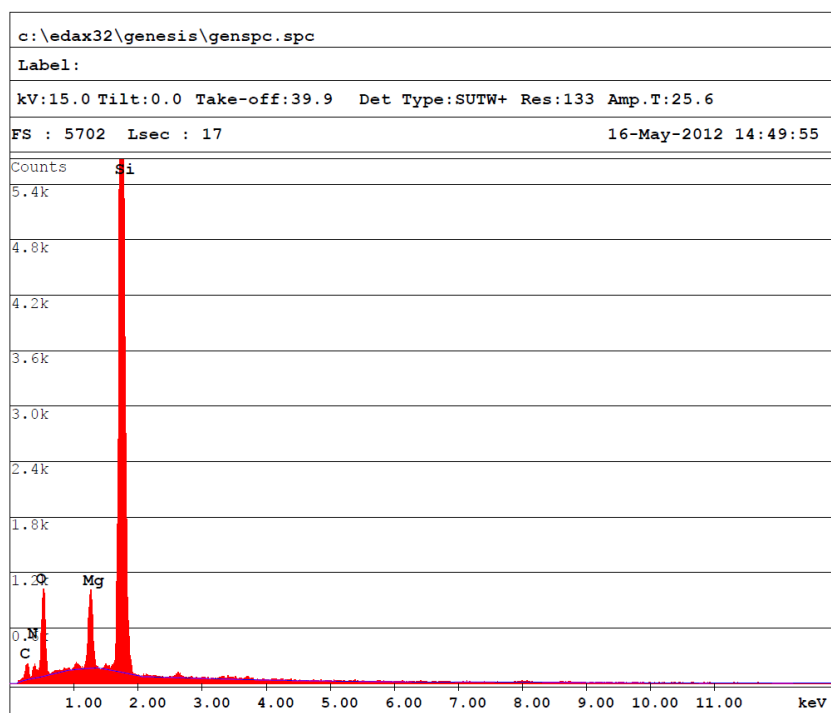


Figure 115 EDS spectrum of nitrated frustules, sample 1, 15 keV

Table 77 Nitrated frustules, sample 1, quantified, 15 keV

EDAX ZAF Quantification (Standardless)					
Element Normalized					
SEC Table : Default					
Element	Wt %	At %	Z	A	F
C K	13.04	22.31	1.0476	0.1237	1.0002
N K	6.50	9.53	1.0371	0.1810	1.0005
O K	15.79	20.28	1.0277	0.2844	1.0006
MgK	4.85	4.10	0.9821	0.8246	1.0157
SiK	59.82	43.77	0.9751	0.9289	1.0000
Total	100.00	100.00			
Element	Net Inte.	Bkgd Inte.	Inte. Error	P/B	
C K	53.67	15.81	4.06	3.39	
N K	44.43	22.21	5.01	2.00	
O K	320.69	34.02	1.45	9.43	
MgK	327.10	82.29	1.60	3.97	
SiK	3844.11	60.02	0.39	64.05	

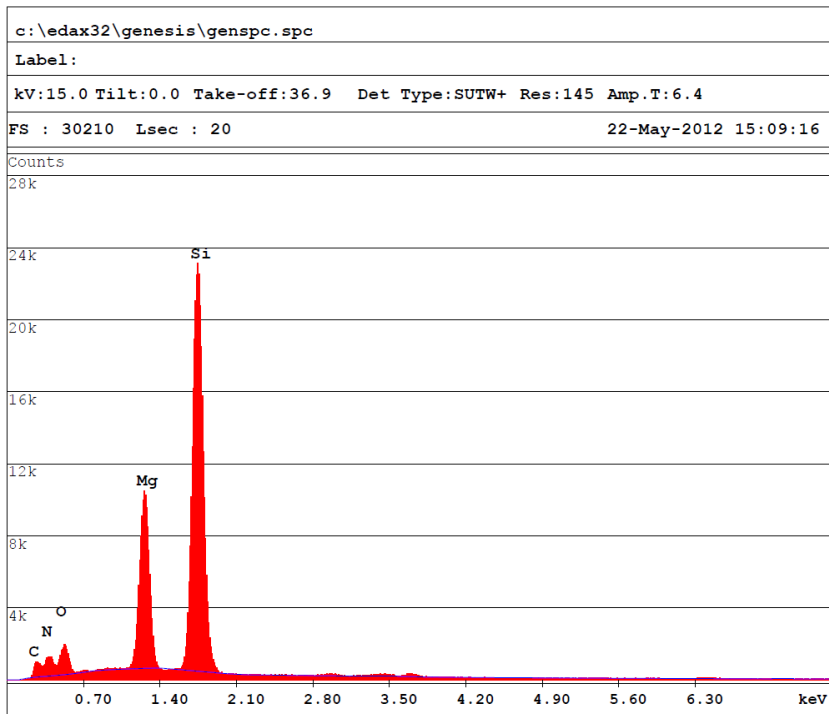


Figure 116 EDS spectrum of nitrified frustules, sample 2, 15 keV

Table 78 Nitrified frustules, sample 2, quantified, 15 keV

EDAX ZAF Quantification (Standardless)
 Element Normalized
 SEC Table : Default

Element	Wt %	At %	Z	A	F
C K	15.55	24.80	1.0427	0.1401	1.0003
N K	16.03	21.93	1.0323	0.1881	1.0004
O K	9.53	11.41	1.0229	0.2430	1.0006
MgK	15.93	12.56	0.9777	0.8260	1.0093
SiK	42.96	29.30	0.9697	0.8555	1.0000
Total	100.00	100.00			

Element	Net Inte.	Bkgd Inte.	Inte. Error	P/B
C K	282.74	67.70	1.61	4.18
N K	448.35	108.05	1.28	4.15
O K	655.00	143.50	1.04	4.56
MgK	4293.13	354.84	0.37	12.10
SiK	10222.77	268.61	0.23	38.06

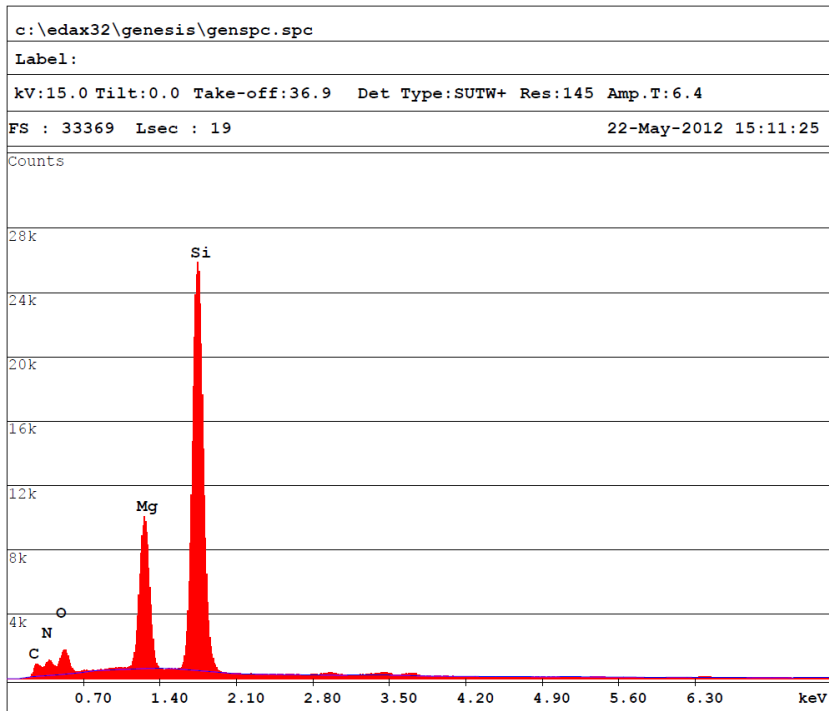


Figure 117 EDS spectrum of nitrified frustules, sample 3, 15 keV

Table 79 Nitrified frustules, sample 3, quantified, 15 keV

EDAX ZAF Quantification (Standardless)
 Element Normalized
 SEC Table : Default

Element	Wt %	At %	Z	A	F
C K	14.79	24.26	1.0451	0.1318	1.0002
N K	13.71	19.28	1.0347	0.1821	1.0004
O K	8.80	10.84	1.0252	0.2472	1.0006
MgK	15.11	12.24	0.9799	0.8337	1.0106
SiK	47.58	33.37	0.9723	0.8639	1.0000
Total	100.00	100.00			

Element	Net Inte.	Bkgd Inte.	Inte. Error	P/B
C K	259.04	66.31	1.73	3.91
N K	380.06	105.78	1.45	3.59
O K	630.27	140.72	1.08	4.48
MgK	4213.76	356.12	0.38	11.83
SiK	11715.85	287.72	0.21	40.72

Table 80 Average weight % elemental content of nitrified frustules, 15 keV

Weight %					
Element	Sample 1	Sample 2	Sample 3	Average	Std. Dev.
C K	15,55	14,79	13,04	14,46	1,29
N K	16,03	13,71	6,50	12,08	4,97
O K	9,53	8,80	15,79	11,37	3,84
Mg K	15,93	15,12	4,85	11,97	6,18
Si K	42,96	47,58	59,82	50,12	8,71
Total	100,00	100,00	100,00	100,00	

Table 81 Average atomic % elemental content of nitrified frustules, 15 keV

Atomic %					
Element	Sample 1	Sample 2	Sample 3	Average	Std. Dev.
C K	24,80	24,26	22,31	23,79	1,31
N K	21,93	19,28	9,53	16,91	6,53
O K	11,41	10,84	20,28	14,18	5,29
Mg K	12,56	12,25	4,11	9,64	4,79
Si K	29,30	33,37	43,77	35,48	7,46
Total	100,00	100,00	100,00	100,00	

Table 82 Average elemental content of nitrified frustules, 15 keV

Element	Atomic %	Weight %
C K	23,79	14,46
N K	16,91	12,08
O K	14,18	11,37
Mg K	9,64	11,97
Si K	35,48	50,12
Total	100,00	100,00